Modeling of ductile fracture using local approach : reliable simulation of crack extension

Youbin Chen

To cite this version:

Youbin Chen. Modeling of ductile fracture using local approach : reliable simulation of crack extension. Mechanics [physics.med-ph]. Université Paris sciences et lettres, 2019. English. NNT : 2019PSLEM038 . tel-02439257

HAL Id: tel-02439257
https://pastel.hal.science/tel-02439257

Submitted on 14 Jan 2020

THÈSE DE DOCTORAT
DE L'UNIVERSITÉ PSL
Préparée à MINES ParisTech

Modélisation de la rupture ductile par approche locale : Simulation robuste de la déchirure

Modeling of ductile fracture using local approach: Reliable simulation of crack extension

Soutenue par
Youbin CHEN
Le 20 Novembre 2019

Ecole doctorale n° 621
ISMME : Ingénierie des Systèmes, Matériaux, Mécanique, Energétique

Spécialité
MÉCANIQUE

Composition du jury :

Jonas, FALESKOG Professeur, KTH	*Président*
Jean-Jacques, MARIGO Professeur, Ecole Polytechnique	*Rapporteur*
Zhiliang, ZHANG Professeur, NTNU	*Rapporteur*
Sylvia, FELD-PAYET Ingénieur de recherche, ONERA	*Examinateur*
Renaud, MASSON HDR, CEA	*Examinateur*
Gilles, PERRIN HDR, Framatome	*Examinateur*
Jacques, BESSON Directeur de recherche, Mines Paristech	*Directeur de thèse*
Eric, LORENTZ HDR, EDF R&D	Co-*directeur de thèse*

Preface

The doctoral dissertation has been written to fulfill the graduation requirements and to obtain the doctor's degree of the PSL Research University. I was engaged in writing it from March to August, 2019.

The title of the dissertation is “Modeling of ductile fracture using local approach: reliable simulation of crack extension”. From this title, you can see two key words: “ductile fracture” and “local approach”. These two key words had already accompanied me for three years before starting the PhD study. Indeed, my master project, which was realized at Zhongshan University (also called Sun Yat-sen University) in China, centers on the extension of the GTN model to low triaxiality. The GTN model belongs to the category of local approach. This experience motivated me to pursue a PhD study in the field of ductile fracture.

This PhD is a CIFRE thesis, a special PhD system set up by ANRT (Association Nationale de la Recherche et de la Technologie) in France. ANRT provides a part of financial support for PhD students. This kind of PhD system consists in carrying out the PhD work at an academic university and at a company at the same time. The name of My PhD University is PSL Research University, which was formed in 2010 and is located in Paris, France. My company is a French electric utility company named EDF (Electricité De France) from which I received another part of my financial support. The current work has been undertaken in the laboratories of *Centre des matériaux* (PSL) and EDF from November 2016 to October 2019.

The dissertation provides some comprehensive ways to solve the uncontrolled strain localization issue induced by classical local approach (GTN model in this work) and several numerical issues appeared in finite element simulation. Theoretical knowledge and practical applications are both covered in detail. This dissertation is suitable as a literature review in different fields (Chapter 1): (1) Resolution of the physical issue of uncontrolled strain localization induced by classical local approach by means of different nonlocal models; (2) Treatment of some numerical issues such as mesh sensitivity, volumetric-locking, material failure and adaptive mesh refinement. This selected portion (Chapter 1) should appeal to a relatively wide audience. The dissertation is also suitable for readers who would like to implement the same model as mine in their in-house finite element software. I provide you the description (Chapter 2), the numerical implementation details (Appendices A2-A4), as well as some test-cases (Chapter 2) of the present nonlocal GTN model. For the more advanced reader, some applications of the model are also included (Chapter 3-5, Appendices A5-A6). To know more about the structure of the dissertation, you can read the “introduction” part in which the basic organization and underlying philosophy are described in detail.

Enjoy your reading.

Acknowledge

I am pleased to acknowledge all those individuals who helped make this PhD thesis possible.

Firstly, I would like to express my sincere gratitude to my advisors Jacques Besson and Eric Lorentz for the continuous support of my PhD study and related research, for their humor, patience and immense knowledge. Their guidance helped me a lot in research and writing of this thesis. I will never forget that they spent a lot of time reading and revisiting this thesis sentence by sentence. I could not have imagined having two such excellent mentors for my PhD study. I cannot thank them enough nor express with such few words how grateful I truly am.

My sincere thanks also goes to the jury members of my thesis defense. I thank Professor Jean-Jacques Marigo and Professor Zhiliang Zhang for having accepted to read this thesis from A to Z, as well as for their suggestions for the improvement of this thesis. I thank also other jury members, i.e., Professor Jonas Faleskog (president of the thesis defense), Mrs. Sylvia Feld-Payet, Mr. Renaud Masson and Mr. Gilles Perrin for their questions and comments during my thesis defense which incented me to widen my research from various perspectives.

I would like to thank Mr. Christophe Varé, my advisor of the Bachelor’s project, for having given me the opportunity to pursue a PhD study in EDF in France.

I am very thankful for the support given by Yi Zhang, a very kind person who has provided me lots of useful documents to start this PhD study. I am indebted to my EDF colleague Anna Dahl who has provided me the experimental results of ATLAS+ project.

I am grateful to my very kind office colleague Astrid Filiot with whom I had lots of discussions on different topics (research, culture, language, etc.). I want to express my heartfelt thanks to all other EDF colleagues who have given me some precious supports to conduct this research. I felt very happy to stay with them and I will keep in mind all the fun we have had in the last three years.

Last but not the least, I would like to express my sincere thanks to my parents and my girlfriend Liyao Zhang for supporting me spiritually throughout writing this thesis and my life in general. Even if they were not physically with me during these three years, I could still feel their love. They were there for me every step of the way. I love them more than anything in the universe and outside it!

写到此处，我的心情十分激动。我想用中文再次对我的导师 Jacques Besson 和 Eric Lorentz 表示感谢，能遇到如此优秀且友好的导师是我这三年博士生涯中最大的幸运之一。另外，感谢我的父母从小对我无微不至的关心与毫无条件的支持，使我能够一路走到今天。最后，我要感谢我的未婚妻张丽瑶的鼓励与陪伴，我相信我们会一辈子在一起。

脱离学生时代的我，缓缓步入了而立之年，崭新的生活与挑战即将开始。站在时空交汇的十字路口，有了你们对我的帮助与关爱，我不会彷徨与迷惘，我将坚定信念，继续踏上旅程，走向未知的未来，追逐那个最初的梦想。

Contents

Introduction

Industrial and scientific background

Methodological and numerical needs

As we know, when it comes to the design of industrial facilities such as nuclear reactors, pipelines, planes, cars, rockets, it is important to well understand the damage phenomena to produce high-quality components by controlling material resistance. Besides aging effects (temperature, corrosion, irradiation, etc.), the initial component quality has a direct impact on the service life of these facilities. Besides, when these facilities are put to use, it is crucial to be able to predict the potential damage and fracture of the materials under normal or accidental loading conditions so as to lower the risk of accidents and thus to ensure safety. For instance, in nuclear power plants, for nuclear safety, it is necessary to avoid pipe fracture which may occur due to the existence and the growth of defects (crack, notch, etc.) in the case of severe loading conditions.

Numerical simulations including the description of damage of material are increasingly used to predict the behavior of structures, especially in industrial cases where the experiments at real scale cannot be realized. For instance, in view of high cost and representativeness, it is difficult, even impossible to replicate operating conditions (pressure, temperature, etc.) and aging effects in some nuclear power components (reactor pressure vessel, stream generator, etc.).

Under the background of these methodological and numerical needs, the EDF R&D's project named MODERN (Mode de Ruine) aims at studying the mechanical strength of various nuclear reactor components. One of the sub-projects centers on ductile fracture in metallic structures. Nowadays, the modeling and numerical simulation of ductile fracture remain complex due to the existence of finite strains and softening phenomena.

"Global" and "Local" approach

At present, the "global" approach to fracture is commonly used for the assessment of the mechanical integrity of mechanical structures. This approach is based on the concepts of linear elastic fracture mechanics (LEFM) and nonlinear fracture mechanics (NLFM). The fracture resistance is assumed to be measurable in terms of one (K or J) or several ($K-T$ or $J-Q$) parameters (Anderson, 2017). This approach is simple and useful, but it has lots of limitations. For instance, this approach cannot be easily used in large-scale yielding or non-isothermal conditions. Moreover, the quantity which is commonly used for the prediction of crack initiation, i.e., critical toughness J_c is actually a specimen size/geometry dependent parameter, consequently, the transferability of the laboratory experimental results to large-scale structures remains problematic.

Another approach, referred to as "local" approach to fracture, can overcome some limitations of "global" approach. The local approach was initially proposed in (McClintock, 1968, 1963). The local models are often derived from micromechanical models. Using the local approach requires to well estimate the stress-strain distribution in the neighborhood of defects (crack or notches) for both the initiation and propagation stages. The stress/strain field can be obtained using analytical or numerical (for instance, using the finite element method) solutions. The local approach is devoted to deal with complex situations (unknown crack path, non-proportional loading conditions, presence of welds, etc.).

Modeling of ductile fracture using "local" approach

For ductile damage/fracture, the local approach relies on constitutive models for plasticity and damage which describe the three main stages of ductile fracture: micro void nucleation, growth and coalescence. The development of porous plasticity models traces back to the seminal work of (Rice and Tracey, 1969) in which the growth of a single void was studied. The Gurson model (Gurson, 1977) allowed accounting for a finite porosity and developing the first micro-mechanically based constitutive equations for porous plasticity. This first development was followed by the work of (Needleman and Tvergaard, 1984; Tvergaard and Needleman, 1984) who developed the so-called GTN model which is a pragmatic modification of the Gurson model allowing accounting for void nucleation, growth and coalescence as well as work hardening. The model was in particular successful in capturing "cup and cone" fracture. Almost at the same time, the more phenomenological but thermodynamically consistent Rousselier model was also proposed (Rousselier, 1981). These works paved the way for the application of porous plasticity models to simulate crack initiation and growth in structures. They also led to the development of numerous porous plasticity models which, over the years, have allowed accounting for an increasing number of phenomena affecting ductile damage. Most of these models can be seen as extensions of the Gurson and GTN models. The models can first phenomenologically be extended to the case of rate-dependent materials (Besson et al., 2001) but a micro-mechanical approach can also be adopted (Leblond et al., 1994). The initial models were developed assuming a matrix following a von-Mises flow rule. It was then extended to account for a Hill-type matrix (Benzerga and Besson, 2001), a Tresca matrix (Cazacu et al., 2014), a matrix exhibiting tension-compression asymmetry (Cazacu and Stewart, 2009) or a complex Barlat-type (Bron and Besson, 2004; Kim et al., 2007) anisotropic matrix (Shinohara et al., 2016). Many extensions address the fact that voids cannot be considered as spheres and are in fact closer to ellipsoids. The first extensions (Gologanu et al., 1994, 1993) considered axisymmetric voids (oblate or prolate) but the model was later further extended to describe arbitrary ellipsoids including the description of the rotation of their main axes (Cao et al., 2013; Danas and Aravas, 2012; Madou et al., 2013; Madou and Leblond, 2013). The combined effects of plastic anisotropy and void shape were studied in (Keralavarma and Benzerga, 2010; Monchiet et al., 2008). Coalescence is also largely investigated based on the initial approach proposed in (Thomason, 1985a, 1985b) which described void coalescence as internal necking. The modeling approach was then improved by combining it with the Gurson model (Benzerga, 2002; Gologanu et al., 2001; Pardoen and Hutchinson, 2000; Zhang et al., 2000). The resulting model can be formulated as a multi-surface model which can be used to perform finite element simulations (Besson, 2009; Reddi et al., 2019). This approach was also used in the case of anisotropic matrices (Keralavarma and Chockalingam, 2016; Shinohara et al., 2016). Further developments include the description of coalescence under combined tension and shear (Torki et al., 2015). More recent developments concern single crystals containing voids for which a yield surface was first proposed by (Han et al., 2013). In that case, the activation of each slip system depends on a GTN-like yield surface. An approximate treatment of the model was proposed in (Paux et al., 2015) so that only one surface can be considered. To account for the size effect due to the size of voids, the matrix can be assumed to be a strain gradient plasticity material (Monchiet and Bonnet, 2013) or one can also assume interfacial residual stresses at the interface between the matrix and the cavity (Monchiet and Kondo, 2013). Internal pressure inside voids can also be taken into account (Vincent et al., 2014a, 2014b). Models for void nucleation have been less developed even though attempts to describe these damage mechanisms have been made (see for instance (Hannard et al., 2018)). Finally the effect of the Lode parameter can be described by adding a nucleation-like term in the model as in (Chen et al., 2017; Morgeneyer and Besson, 2011; Nahshon and Hutchinson, 2008; Xue, 2008). A detailed review of the applications, the advantages and the shortcomings of such continuum damage models can be found in (Besson, 2010).

In the last years, these models have been successfully applied to model crack extension, see for instance (Besson et al., 2013; Hütter et al., 2013; Xia and Shih, 1995). However, due to the complexity of some of the extensions, most applications involving large crack propagation are restricted to the GTN model or its simplest extensions. That is why in this work, for the sake of simplicity, we focus our attention on the isotropic GTN model while proposing new solutions to tackle numerical problems linked to the use of these models.

Limitation of "local" approach

Damage at the continuum level results in strain-softening, i.e. the drop of the stress carrying capability with increasing damage. At the structure scale where constitutive behavior is combined with mechanical equilibrium, strain-softening is responsible for the spatial localization of strain, plastic strain and damage, in agreement with experimental evidences (Morgeneyer et al., 2014). The scale of the macroscopic field variations becomes comparable to the microstructure scale (micro-void spacing, for instance). This is in contradiction to the length scale separation assumption which underlies the derivation of local constitutive relations, i.e. models that only depend on the point-wise state variables (strain, damage, plasticity, hardening and so on). Besides, such local models would lead to ill-posed boundary value problems resulting from loss of ellipticity of the rate operator (Benallal et al., 1993; Rudnicki and Rice, 1975), spurious mesh-sensitivity and unrealistic physical predictions (Besson et al., 2003).

Problems with the finite element simulations of ductile failure

Diverse problems appear when the local damage models are used in finite element simulations:

- Mesh-sensitivity: strain/damage localization occurs with the use of constitutive law including softening. Numerically, spurious mesh-sensitivity and unrealistic physical predictions may be observed when this kind of constitutive law is used in the finite element analysis. Indeed, as the mesh is refined, the localization zone narrows and finally vanishes. Thus, the dissipated energy also tends to zero. This is in contradiction to the experimental observation where a narrow localization bands depending on material exist.
- Volumetric-locking: Ductile damage/fracture is characterized by a high level of plastic strain. Thus, ductile damage models should be formulated at finite strains. Different finite strain formulations (Sidoro and Dogui, 2001; Simo and Miehe, 1992) have been proposed in the last years under the assumption of isotropic hardening, which may results in different numerical efficiency. Due to the quasi-incompressibility constraint enforced at each integration points, the effective dimension of the displacement space is reduced. The reduction is so drastic that the effective displacement space is no more rich enough to ensure spatial convergence. This issue is referred to as "volumetric-locking" which appears in standard displacement-based finite element formulations. In numerical simulations, this issue is illustrated by the oscillations of stress field which may strongly affect the computational convergence and the predicted damage evolution.
- Material failure: highly distorted elements are often observed in the simulations of large crack extensions. This may strongly affect the computational convergence.
- Crack propagation over long distance: the mesh size in crack propagation area is often about 0.1 mm. To advance at least 1 cm in three-dimensional industrial structures, crack should spread over hundreds and thousands of finite elements. In presence of this difficulty, crack propagation over long distance is often performed using explicit algorithm (Xue and Wierzbicki, 2009) and/or linear finite elements (Cao et al., 2013). But these elements are not always suitable for the models requiring different interpolations for displacements or other degrees of freedom. The remeshing technique is sometimes used to reduce the problem size (Cao, 2014; J. Mediavilla et al., 2006).

Aim of PhD thesis

The PhD thesis has been carried out in the laboratory Centre des Matériaux of école des Mines de Paris at Paris-Sciences-et-Lettres (PSL) Research University and in the department of Electrotechnique et Mécanique des Structures (ERMES) of the EDF R&D company. The major goal is to propose and establish a robust (high-quality results in various situations), reliable (the results are not excessively sensitive to the choices of modeling such as spatial/temporal discretization and therefore can be reproduced by different engineers) and efficient (in terms of computing time) modeling, which allows solving the issues mentioned earlier and predicting crack propagation in three-dimensional industrial cases.

Outline of dissertation

The organization of the dissertation and the main information addressed in each chapter are outlined:

- Chapter 1: This chapter is devoted to literature review. Different local approaches for the modeling of ductile damage/fracture are reviewed. The physical problem (lack of material characteristic length) induced by the use of the local approach is emphasized. To solve this problem, different non-local models are presented. Moreover, several numerical problems and the corresponding solutions are shortly shown. The intention of this chapter is not to give an exhaustive review on ductile fracture but rather to explain why we choose the model that is described in chapter 2.
- Chapter 2: In this chapter, a non-local GTN damage model is presented in detail. Finite strains are taken into account so as to describe ductile deformation. To solve the physical problem due to the use of local approach, a non-local formulation is adopted. On a numerical ground, the decomposition-coordination method is put in practice to reduce the non-linearity in the constitutive law and a mixed element formulation is adopted to avoid volumetric locking. Finally a new 5-field finite element is derived from the non-local locking-free variational formulation. At the end of the chapter, some simple simulations are given.
- Chapter 3: This chapter concentrates on several numerical techniques such as the treatment of material failure, the influence of the penalty parameters introduced in the nonlocal locking-free formulations, the convergence criterion, the numerical schemes for the update of the damage variable, adaptive load increment, etc. These studies enable us to know how to well use the proposed GTN model so as to make the modeling and the simulation of ductile fracture robust, reliable and performant.
- Chapter 4: The improved GTN model is applied to simulate large crack propagation under small-scale yielding and plane-strain mode I conditions. The numerical techniques applied to model small-scale yielding and to extract pertinent data from the resulting mechanical fields are described. A parametric study is performed for several values of the material properties in order to estimate their influence on the crack growth resistance.
- Chapter 5: The improved GTN model is applied to simulate different experiments carried out in the framework of the ATLAS+ (Advanced Structural Integrity Assessment Tools for Safety Long Term Operation) project. The experimental results are shortly presented. The model parameters are fitted using parts of the experimental results of small specimens. These parameters are then used to predict the behavior of other small specimens and a full size case study (cracked pipe).
- Chapter 6: In the last chapter, the main results, including the numerical developments and the obtained results, proposed in the dissertation are summarized. The remaining issues (open questions) are listed with some remarks and some recommendations.

1 Literature review

学而不思则罔，思而不学则殆。

L'étude sans raisonnement mène à la confusion ; la pensée sans apprentissage est effort gaspillé.

Learning without thought is labor lost; thought without learning is perilous.

孔子 Confucius

Résumé

Ce chapitre a pour l'objectif de présenter l'état de l'art sur la modélisation et la simulation numérique de la rupture ductile par approches locales. D'abord, la dérivation des modèles classiques de l'endommagement est présentée. Le problème de la localisation pathologique de la déformation, la plasticité et l'endommagement est évoqué. Ensuite, différents remèdes à ce problème sont donnés en détail. Le point commun de ces solutions est d'introduire une longueur caractéristique qui permet de contrôler la largeur de la bande de localisation. Cinq approches de régularisation sont présentées et comparées : méthode de convolution, méthode de gradient implicite, approche micromorphique, approche énergétique enrichie (GEE), approche en phase-field. Leurs avantages, inconvénients et applications à la rupture ductile sont aussi donnés. Puis, des problèmes numériques liés aux simulations par approches locales avec la méthode aux éléments finis sont présentés. Le premier problème est la dépendance aux maillages. Il existe différentes solutions (taille d'élément fixée, modèles de CZM, modèles non locaux, etc.) pour pallier ce problème. Le deuxième problème est le verrouillage numérique qui est lié à l'incapacité des éléments finis standards à trouver une solution de déplacement cohérente avec le changement de volume quasi nul. Une courte recherche bibliographique sur différentes solutions est faite. Le troisième problème est le coût de calcul lié au nombre de degrés de liberté (nombre d'éléments finis et ordre d'interpolation) lors des calculs industriels. Le remaillage adaptative semble un bon choix pour ce problème. Le processus de remaillage est brièvement donné. Le quatrième problème concerne le traitement des éléments cassés. Ces éléments peuvent devenir très distordus et la robustesse du calcul est ainsi fortement perturbée. Quelques solutions de la littérature sont introduites. Enfin, à l'issue de ces études bibliographiques, le modèle qui va être utilisé dans ce travail est proposé.

1.1 Local approach to ductile damage

1.1.1 Homogenization

As we know, heterogeneity is the common point of all real materials, it is mainly due to the existence of defects such as inclusions or micro-voids. It can affect the overall properties of the material. For example, heterogeneities can act as stress concentrators which may lead to void growth and void coalescence in ductile material.

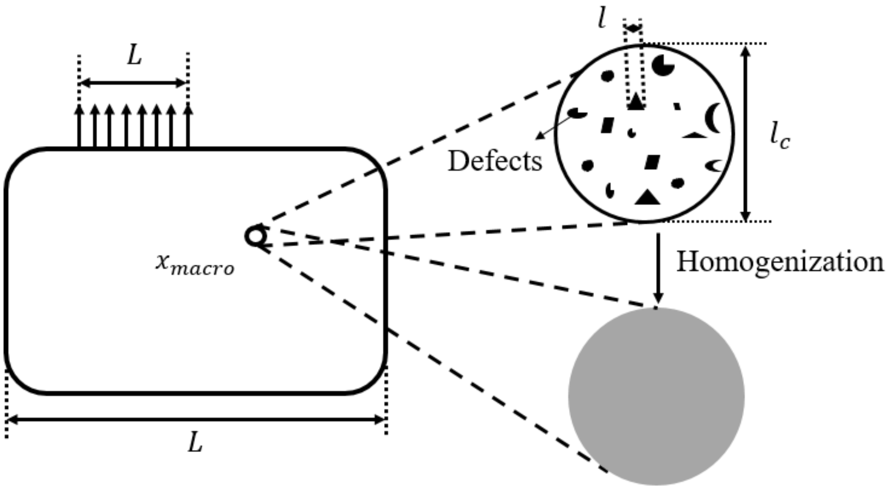

Figure 1.1. Characteristic length scales and homogenization procedure

Different intrinsic length scales can be introduced for a material, as shown in Figure 1.1. In this figure, l stands for the characteristic length of the microstructure and L stands for the characteristic length of the considered geometry, loading or macroscopic fields (stress field, strain field, etc.). In order to treat micromechanical problems in the framework of continuum mechanics, a volume V containing defects over a length scale l_c is considered as a material point. In this case, the microstructure is treated in an averaged way and the material behavior can be interpreted as the behavior of a material point at the macroscopic level. This micro-to-macro process is named "homogenization" (see Figure 1.1). As for the length scale l_c, it should be, on the one hand, small enough so that the volume V can be considered as a point at the macroscopic level, and on the other hand, large enough so that the volume V can be considered as a statistically representative volume (i.e., containing a sufficiently high number of defects):

$$l \ll l_c \ll L \tag{1.1}$$

This relation may not hold in some situations. For example, at crack tip nearby zones, macroscopic stress and strain strongly vary over a very small distance so that the volume element V cannot be considered as a representative volume. A specific homogenization process is required for this kind of situation (Gross and Seelig, 2011).

As will be seen later, numerous constitutive models such as the Gurson damage model (Gurson, 1977) can be derived from micromechanical analyses (homogenization).

1.1.2 Mechanics of ductile damage

As stated in Section 1.1.1, defects exist in any real material. During a deformation process, defects may grow and coalesce while new defects are created at the same time. This leads to a change of material properties, in particular, the decrease of material strength. Such a process is called “damage”. Material damage can be further classified as brittle damage, ductile damage, creep damage, fatigue damage, etc. In our work, only ductile damage will be studied.

Ductile damage is mainly due to void nucleation, growth and coalescence in ductile materials such as steel, aluminum (see for instance (Garrison Jr and Moody, 1987)). In the framework of continuum mechanics, the state of damage at a material point (corresponding to a representative volume V at the microscopic level) may be described by a scalar damage variable in the case of isotropic damage or several damage variables in the case of anisotropic damage (Lemaitre et al., 2000), which obey some adequate evolution laws. In our work, only isotropic damage is considered. Since the real damage process occurs in the representative volume V, the damage evolution law is generally derived from micromechanical models. In the following, several micromechanical models for void growth and void coalescence will be reviewed.

Void growth

Models proposed by (McClintock, 1968) and (Rice and Tracey, 1969) describe the growth of single cylindrical or spherical void in an unbounded region. The material is assumed to be rigid with respect to elasticity and perfectly plastic. In the case of spherical void (Rice and Tracey, 1969), the evolution of the void radius R follows the following rate equation:

$$\frac{\dot{R}}{R} = \alpha \exp\left(\frac{3\sigma_h}{2\sigma_0}\right)\dot{\varepsilon}_{eq} \tag{1.2}$$

where $\alpha = 0.283$ in the original model, σ_0 is the yield stress of the matrix and ε_{eq} is the von-Mises equivalent strain. Several improvements concerning the value of α (Huang, 1991) and the strain hardening effects (Becker et al., 1989; Budiansky et al., 1982) can be found in the literature. Equation (1.2) can be considered as a damage evolution law with R a damage parameter. Failure occurs when $\bar{R} > \bar{R}_c$ where $\bar{R} = R/R_0$ with R_0 the initial void radius and $\bar{R}_c = (R/R_0)_c$ is a material dependent parameter. These micromechanical models can be used in the framework of damage mechanics as long as the interaction among voids is negligible.

The void interaction is not taken into account in (McClintock, 1968; Rice and Tracey, 1969), this problem is first addressed in (Gurson, 1977) in an upper bound analysis of a finite sphere containing a spherical void in the case of a rigid with respect to elasticity (incompressible) perfectly plastic matrix. This analysis yields a plastic yield surface Gr:

$$Gr = \left(\frac{\sigma_{eq}}{\sigma_0}\right)^2 + 2f\cosh\left(\frac{3}{2}\frac{\sigma_h}{\sigma_0}\right) - 1 - f^2 = 0 \tag{1.3}$$

Failure corresponds to a domain where $G_r(\sigma) \leq 0$ reduced to $\sigma = 0$. This condition is met when $f = 1$. This value is obviously too high; this led to the development of the GTN model (see below) to better describe failure. The evolution of the plastic part of the strain tensor can be derived using the normality rule while the evolution law for f derives from incompressibility (see Equations (1.13)(1.14)(1.15) below). In particular, the evolution of f is entirely determined by the plastic yield surface.

Void coalescence

Generally, void coalescence may occur through void sheeting or internal necking. The first micromechanical analysis of void coalescence ($45°$ shear band connecting two voids, i.e., void sheet mechanism) was proposed in (Brown and Embury, 1973). The shear band can be formed when the distance between two voids is approximately the void size. Coalescence by internal necking is analyzed in (Thomason, 1985a, 1985b), this analysis is based on a limit-load analysis of the ligament between voids. Void coalescence occurs when the inter-void ligament reaches its plastic limit load. A simple summary of the Thomason-like model is given below.

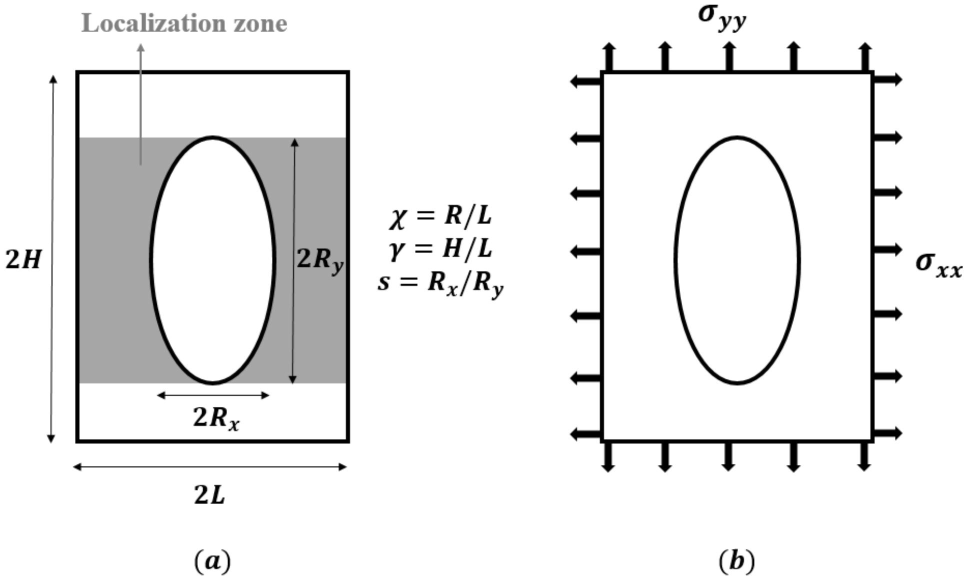

Figure 1.2. Geometry and loading conditions of the Thomason model

We consider a material which can be regarded as a regular array of cylindrical cells (height 2H and diameter 2L) containing spherical voids (see Figure 2 for a cell, $R_x = R_y = R$). It is assumed that the principal directions of the voids correspond to the principal directions of the macroscopic stress tensor. The average stress tensor $\boldsymbol{\sigma}$ acting on the cell is assumed to be axisymmetric with $\sigma_{yy} > \sigma_{rr} = \sigma_{xx}$. The axial equilibrium of the cell is:

$$\pi L^2 \sigma_{yy} = C_f \pi (L^2 - R^2) \bar{\sigma} \tag{1.4}$$

where $\sigma_{yy} = (2/3 + T_r)\sigma_{eq}$ with $T_r = \sigma_h/\sigma_{eq}$ the macroscopic triaxiality and $\bar{\sigma}$ is the flow stress of the matrix material. Note that a perfectly plastic matrix was assumed in the original work of (Thomason, 1985b, 1985a). Equation (1.4) can be interpreted as follows: the external contact force (left hand side) must be equal to the force applied to the ligament region along the loading direction (right hand side). The ligament stress triaxiality increases due to the stress concentration induced by the void. This effect is described by the plastic constraint factor C_f. An empirical expression for C_f is given in (Thomason, 1985b, 1985a):

$$C_f = 0.1\left(\frac{1}{\chi} - 1\right)^2 + 1.2\left(\frac{1}{\chi}\right)^{\frac{1}{2}} \tag{1.5}$$

In the framework of small strains and under the assumption of incompressibility, one have (Zhang et al., 2000):

$$\chi = \left(\frac{3}{2} f\gamma\right)^{\frac{1}{3}} = \left(\frac{3}{2} f\gamma_0 \frac{(1+\varepsilon_y)}{(1+\varepsilon_x)}\right)^{\frac{1}{3}} \approx \left(\frac{3}{2} f\gamma_0 e^{\varepsilon_y - \varepsilon_x}\right)^{\frac{1}{3}} \tag{1.6}$$

In the framework of finite strains and under the assumption of incompressibility, one have (Besson, 2009):

$$\chi = \left(\frac{3}{2} f \gamma_0 e^{\frac{3}{2} k \varepsilon_{D,yy}}\right)^{\frac{1}{3}} \tag{1.7}$$

where the definition of χ, γ can be found in Figure 1.2 , (γ_0, k) are material constants and $\varepsilon_{D,yy}$ is the vertical component of the deviatoric part of $\boldsymbol{\varepsilon}$. The evolution of f can be computed using the Gurson model (Zhang et al., 2000; Zhang and Niemi, 1994a, 1994b). The value of f at the onset of void coalescence is regarded as the critical porosity f_c (Zhang et al., 2000). The suggestion given in (Zhang et al., 2000) does not account for the change of the plastic flow direction during void coalescence. One can refer to (Benzerga, 2002; Pardoen and Hutchinson, 2000; Torki, 2019) for more sophisticated void coalescence and post-coalescence models.

Micromechanics-based constitutive model

Models derived from micromechanical analyses (for example the Gurson model (Gurson, 1977)) have been used to develop semi-empirical extensions relying on phenomenological descriptions of the different damage processes (i.e., nucleation, growth and coalescence). In this part, following (Besson, 2010), we propose to give a typical formulation of theses micromechanics-based models.

It is first assumed that the material has an elastic behavior so that the strain rate tensor can be divided into elastic part $\dot{\boldsymbol{\varepsilon}}^{\boldsymbol{e}}$ and plastic part $\dot{\boldsymbol{\varepsilon}}^{\boldsymbol{p}}$:

$$\dot{\boldsymbol{\varepsilon}} = \dot{\boldsymbol{\varepsilon}}^{\boldsymbol{e}} + \dot{\boldsymbol{\varepsilon}}^{\boldsymbol{p}} \tag{1.8}$$

We recall that micromechanical analyses assume that the material is rigid-plastic. The stresses are then obtained using the Hooke relation:

$$\boldsymbol{\sigma} = \mathbb{E} : \boldsymbol{\varepsilon}^{\boldsymbol{e}} \tag{1.9}$$

where $\mathbb{E}$ is the Hooke stiffness matrix (fourth order tensor).

The plastic strain $\boldsymbol{\varepsilon}^{\boldsymbol{p}}$ is determined from a yield function F and a flow rule:

$$\dot{\boldsymbol{\varepsilon}}^{\boldsymbol{p}} = \lambda \frac{\partial F}{\partial \boldsymbol{\sigma}} \tag{1.10}$$

where λ is the plastic multiplier. This relation is also based on micromechanical analyses.

We assume that isotropic hardening is described by a scalar variable κ which is interpreted as the plastic deformation of the matrix material so that:

$$\dot{\boldsymbol{\varepsilon}}^{\boldsymbol{p}} : \boldsymbol{\sigma} = (1 - f)\dot{\kappa}\bar{\sigma} \tag{1.11}$$

where $\bar{\sigma}$ is the flow stress depending on κ. In our work, the hardening variable κ is used as a strain measure.

For the yield function F, it is assumed that F depends on the hydrostatic and deviatoric part of the stress tensor $\boldsymbol{\sigma}$, the hardening variable κ and the damage parameter f. The consistency condition is:

$$\dot{\kappa} \geq 0, \qquad F(\sigma_h, \sigma_{eq}, f, \kappa) \leq 0, \qquad \dot{\kappa} F = 0 \tag{1.12}$$

Plastic flow occurs when $F = 0$.

The evolution of f is split into the growth part $\dot{f}_g$ and the nucleation part $\dot{f}_n$:

$$\dot{f} = \dot{f}_g + \dot{f}_n \tag{1.13}$$

where f_g can be derived from some micromechanical analyses based on microscopic plastic incompressibility (the microscopic elastic compressibility is neglected):

$$\dot{f}_g = (1 - f)\mathrm{tr}(\dot{\boldsymbol{\varepsilon}}^{\boldsymbol{p}}) \tag{1.14}$$

and f_n can be derived from a purely phenomenological analysis:

$$\dot{f}_n = B_n \dot{\kappa} \tag{1.15}$$

where B_n is the strain rate controlled nucleation rate. Several expressions of B_n are possible among which the expressions proposed in (Chu and Needleman, 1980; Zhang et al., 2000) are widely used in the literature. In (Zhang et al., 2000), a continuous nucleation model is proposed:

$$B_n(\kappa) = b_0 \tag{1.16}$$

where b_0 is a constant number. In (Chu and Needleman, 1980), the strain controlled void nucleation mechanism is assumed to follow a normal distribution:

$$B_n(\kappa) = \frac{f_N}{s_N\sqrt{2\pi}} e^{-\frac{1}{2}\left(\frac{\kappa - \kappa_N}{s_N}\right)^2} \tag{1.17}$$

where κ_N and s_N are the mean value and the standard deviation of the strain tensor, f_N is the void nucleating particles volume fraction. Compared to the model proposed in (Zhang et al., 2000), the model proposed in (Chu and Needleman, 1980) is more sophisticated but less attractive in engineering due to the three parameters to be calibrated.

As for the expression of the yield function F, various models have been proposed. For example, the GTN model, the Rousselier model or their extensions.

Gurson-Tvergaard-Needleman (GTN) model

The yield function proposed in (Gurson, 1977) and improved in (Needleman and Tvergaard, 1984; Tvergaard and Needleman, 1984) is:

$$F = \left(\frac{\sigma_{eq}}{\bar{\sigma}}\right)^2 + 2q_1 f^* \cosh\left(\frac{3q_2\sigma_h}{2\bar{\sigma}}\right) - 1 - (q_1 f^*)^2 \tag{1.18}$$

where (q_1, q_2) are two material constants which allow to more accurately describe void growth kinetics observed in unit cell computations. Based on (Koplik and Needleman, 1988), the values $q_1 = 1.5$ or $q_1 = 1.25$ and $q_2 = 1.0$ are often used. Then it is pointed out in (Faleskog et al., 1998) that (q_1, q_2) depend on the plastic hardening exponent and on the ratio of the yield stress over the Young modulus E. The f^* is the effective porosity which is defined to account for void coalescence:

$$f^* = \begin{cases} f, & f < f_c \\ f_c + \dfrac{\frac{1}{q_1} - f_c}{f_F - f_c}(f - f_c), & f \geq f_c \end{cases} \tag{1.19}$$

where f_c and f_F represent respectively the porosity at the onset of coalescence and at fracture.

Rousselier model

The Rousselier model (Rousselier, 1981) is derived from a thermo-dynamical approach suggested in (Lemaitre and Chaboche, 1978). But it can also be considered as a micromechanics-based model since the void evolution law suggested in (Rice and Tracey, 1969) is used. The yield function of the Rousselier model is:

$$F = \frac{\sigma_{eq}}{1-f} + D\sigma_1 f \exp\left(\frac{\sigma_h}{(1-f)\sigma_1}\right) - \bar{\sigma} \tag{1.20}$$

where (σ_1, D) are two material constants. The recommended values are $D \approx 2$ and $\sigma_1 = (\sigma_0 + \sigma_m)/3$ with σ_m the ultimate engineering stress.

An extension of the Rousselier model can be found in (Tanguy and Besson, 2002):

$$F = \frac{\sigma_{eq}}{(1-f)\bar{\sigma}} + \frac{2}{3} D_R f \exp\left(\frac{3q_R\sigma_h}{2(1-f)\bar{\sigma}}\right) - 1 \tag{1.21}$$

where D_R and q_R are two new parameters. This extended Rousselier model is comparable to the GTN model, as demonstrated in (Tanguy and Besson, 2002). This version of the model is well adapted to rate dependent materials and to situations in which adiabatic heating is present.

1.1.3 Material softening and strain localization

One of the drawbacks to local continuum damage mechanics as presented in the previous part is the problem of the localization of plasticity and damage. This problem is mainly due to the instability in the macroscopic material behavior (softening) induced by the increase of damage. Softening means the drop of the stress carrying capability with increasing deformation. As said in Section 1.1.1, the homogenization process requires an intrinsic length scale which satisfies Equation (1.1). However, the localization problem violates this requirement and in this case, the continuum damage models which are motivated from the micromechanical models lose part of their validity.

This part is devoted to the illustration of the strain/damage localization problem through a simple one-dimensional example and to give a necessary condition in three-dimensional cases for the bifurcation of deformation.

Illustration of strain localization

In the spirit of (Doghri, 2013; Gross and Seelig, 2017; Lorentz, 1999; Zhang, 2016), we consider one bar of length L subjected to a stress-controlled loading and unloading processes with damage model (as shown in Figure 1.3(a)(b)):

$$\sigma = E(1-D)\varepsilon \tag{1.22}$$

where σ denotes the stress, ε denotes the strain, E denotes the Young modulus and D denotes the irreversible damage parameter which is defined as $D = \varepsilon/\varepsilon_F \in [0,1]$ with ε_F the strain at fracture.

At the beginning of loading, one have:

$$\sigma_M = E\left(1 - \frac{\varepsilon_M}{\varepsilon_F}\right)\varepsilon_M, \qquad \frac{d\sigma_M}{d\varepsilon_M} > 0 \tag{1.23}$$

where σ_M is the macroscopic stress and ε_M is the macroscopic strain.

Now we consider a limit case by assuming that the bifurcation occurs when $\varepsilon = \varepsilon_p$ with ε_p the peak strain, as shown in Figure 1.3(a). From certain loading level, one part of the bar of length L_2 (bar 2 in Figure 1.3) remains in plastic loading with increasing damage $D_2 = \varepsilon_2/\varepsilon_F$, while another part of the bar of length L_1 (bar 1 in Figure 1.3) is in elastic unloading with constant damage $D_1 = \varepsilon_p/\varepsilon_F$:

$$\sigma_M = \begin{cases} E(1-D_1)\varepsilon_1, & \text{bar 1} \\ E(1-D_2)\varepsilon_2, & \text{bar 2} \end{cases} \tag{1.24}$$

The macroscopic strain ε_M is:

$$\varepsilon_M = \frac{L_1\varepsilon_1 + L_2\varepsilon_2}{L} \tag{1.25}$$

Combining Equations (1.24)(1.25), one obtain the overall response of the tensile bar:

$$\varepsilon_M = \frac{2L_1}{EL_t}\sigma_M + \frac{\varepsilon_F L_2}{2L_t}\left(1 + \sqrt{1 - \frac{4}{\varepsilon_F E}\sigma_M}\right), \qquad \frac{d\sigma_1}{d\varepsilon_1} \geq 0, \qquad \frac{d\sigma_2}{d\varepsilon_2} \leq 0 \tag{1.26}$$

Equations (1.23)(1.26) describe the overall material responses before and after bifurcation, respectively. Figure 1.3(c) plots this response with different values of L_2/L_t. This figure indicates that infinite possible responses exist. Since the one with $L_2/L_t \to 0$ has least dissipation, this process is energetically preferable. Therefore, strain (and so damage) proceeds in a zero-thickness region.

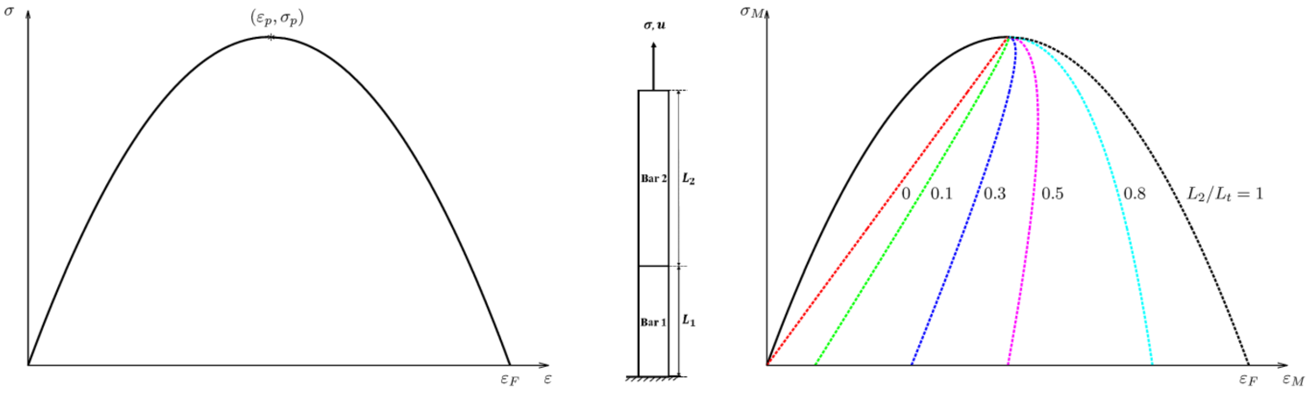

(a) (b) (c)

Figure 1.3. (a) One dimensional material law with damage; (b) Tensile bar; (c) Overall stress-strain response

Condition of bifurcation of deformation

In 3D cases, the bifurcation of deformation leads to the formation of a localization band characterized by its normal $\underline{n}$. Similar to 1D cases, the strain rate tensor is discontinuous across the crack surface ($\Delta\dot{\boldsymbol{\varepsilon}} \neq 0$) while the normal stresses ($\underline{t} = \boldsymbol{\sigma}.\underline{n}$) remains continuous ($\Delta\dot{\underline{t}} = \underline{0}$) due to local equilibrium. In (Hadamard, 1903), it was shown that the strain rate tensor depends on $\underline{n}$ and the direction of the strain rate jump $\underline{g}$:

$$\Delta\dot{\boldsymbol{\varepsilon}} = \frac{1}{2}\left(\underline{n} \otimes \underline{g} + \underline{g} \otimes \underline{n}\right) \tag{1.27}$$

The 1D case given earlier corresponds to the case $\underline{n} \parallel \underline{g}$. As for the case $\underline{n} \perp \underline{g}$, it corresponds to a jump in shear strain rate. In the case of elastic-plastic materials, we assume that the constitutive equation is:

$$\dot{\boldsymbol{\sigma}} = \mathbb{J}_s : \dot{\boldsymbol{\varepsilon}} \tag{1.28}$$

where $\mathbb{J}_s$ is the tangent matrix. So the continuity of the stress $\underline{t}$ can be rewritten as:

$$\Delta\dot{\underline{t}} = (\mathbb{J}_{s1} : \dot{\boldsymbol{\varepsilon}}_1 - \mathbb{J}_{s2} : \dot{\boldsymbol{\varepsilon}}_2).\underline{n} = 0 \tag{1.29}$$

where $\mathbb{J}_{s1}$ and $\mathbb{J}_{s2}$ stand for the tangent matrices of the materials located on the two sides of the discontinuous surface. Linear solid of comparison gives $\mathbb{J}_{s1} = \mathbb{J}_{s2} = \mathbb{J}_s$, so by combining Equations (1.27)(1.29), one can obtain:

$$\mathbb{J}_s : \left(\underline{n} \otimes \underline{g}\right).\underline{n} = \underline{0} \tag{1.30}$$

Equation (1.30) can be rewritten as:

$$\mathbb{A}(\underline{n}).\underline{g} = \underline{0} \tag{1.31}$$

with $\mathbb{A} = \underline{n}.\mathbb{J}_s.\underline{n}$. To have a solution $\underline{g} \neq \underline{0}$ for Equation (1.31), it is necessary that:

$$\exists \underline{n}, \qquad \det\left(\mathbb{A}(\underline{n})\right) = 0 \tag{1.32}$$

The positivity of $\mathbb{J}_s$ leads to the fact that if $\exists \underline{n}', \det(\mathbb{A}(\underline{n}')) < 0$, then $\exists \underline{n}'', \det(\mathbb{A}(\underline{n}'')) = 0$. Equation (1.32) is a prerequisite for a bifurcation of deformation. In this case, a crack ($\underline{n} \parallel \underline{g}$), a shear band ($\underline{n} \perp \underline{g}$) or a mixed band is formed. In other words, the necessary condition to avoid the bifurcation of deformation is:

$$\forall \underline{n}, \qquad \det\left(\mathbb{A}(\underline{n})\right) > 0 \tag{1.33}$$

The condition described in Equation (1.33) corresponds actually to the ellipticity of the (linear) rate problem.

In (Besson et al., 2003, 2001; Billardon and Doghri, 1989), a localization indicator is defined as followed to predict the strain/damage localization:

$$I_b = \min_{\underline{n}, ||\underline{n}||=1} \det\left(\mathbb{A}(\underline{n})\right) \tag{1.34}$$

Localization can occur when $I_b = 0$.

1.2 Nonlocal modification to local approach

As mentioned in the previous section, damage at the continuum level results in strain-softening, i.e. the drop of the stress carrying capability with increasing damage. At the structure scale where constitutive behavior is combined with mechanical equilibrium, strain-softening is responsible for the spatial localization of strain, plastic strain and damage. The scale of the macroscopic field variations becomes comparable to the microstructure scale (micro-void spacing, for instance). This is in contradiction to the length scale separation assumption which underlies the derivation of local constitutive relations, i.e. models that only depend on the point-wise state variables (strain, damage, plasticity, hardening, etc., see Section 1.1 for more details). Besides, such local models would lead to ill-posed boundary value problems resulting from loss of ellipticity of the rate operator (see Section 1.1.3), spurious mesh-sensitivity and unrealistic physical predictions. Therefore the non-local constitutive relations are required as a consequence of overlapping micro and macro length scales. They account for a spatial coupling of neighboring material points: the material state is no more characterized by point-wise state variables and an interaction distance (also named internal length) appears. Different variants of non-local constitutive relations have been proposed in the literature, according to the choice of the effective non-local variables and the non-local operators.

In this section, several ways to introduce the nonlocal effect in the constitutive behavior of materials are summarized. Firstly, the integral nonlocal approach is presented in Section 1.2.1. Secondly, a variant of this approach, named "implicit gradient approach", is given in Section 1.2.2. The major goal of the implicit gradient approach is to avoid the integral form and thus to reduce the numerical implementation burden. Other classes of nonlocal models are based on the introduction of the gradient of some state variables in the constitutive energies of the problem (the micromorphic approach in Section 1.2.3, the gradient enhanced energy (GEE) approach in Sections 1.2.4 and the phase-field approach in Section 1.2.5). Applications of these approaches to ductile failure are also given in each subsection. Finally, a tentative comparison among the different approaches is made in Section 1.2.6 so as to choose an appropriate nonlocal model for our work.

1.2.1 Integral nonlocal approach

The integral nonlocal approach is proposed to describe the microstructure behavior in an averaged sense. The main idea of this approach is to introduce the interaction among material points through a nonlocal quantity (referred to as $\bar{z}$) defined at a material point $\underline{x}$. This quantity is computed from the local quantity z over a finite volume Ω surrounding $\underline{x}$ with a weighted average (Bazant and Pijaudier-Cabot, 1988; Pijaudier-Cabot and Bažant, 1987):

$$\bar{z}(\underline{x}) = \frac{1}{\Psi(\underline{\mathrm{x}})} \int_{\Omega} \psi(\underline{x}, \underline{y}) z(\underline{y})\, d\Omega \tag{1.35}$$

where $\underline{x}$ is the position of the material point, $\underline{y}$ is the position of the volume $d\Omega$ and $\Psi = \int_{\Omega} \psi(\underline{x}, \underline{y})\, d\Omega$ with $\psi(\underline{x}, \underline{y})$ the weight function which is assumed to be homogeneous and isotropic. The frequently used form for ψ in the literature is the Gaussian distribution. For example, in (Peerlings et al., 2001),

$$\psi(\underline{x}, \underline{y}) = \frac{1}{(2\pi)^{\frac{3}{2}} l_c^3} \exp\left(- \frac{\left|\underline{x} - \underline{y}\right|^2}{2 l_c^2} \right) \tag{1.36}$$

where l_c is the intrinsic length scale related to the distance at which spatial interactions among different material points occur and thus to the scale of the microstructure, the factor $(2\pi)^{-3/2} l_c^{-3}$ is given for the normalization of the weight function on $\mathbb{R}^3$: $\int_{\mathbb{R}^3} \psi(\underline{x}, \underline{y}) d\Omega = 1$.

Historically, nonlocal formulation of elasticity with the integral approach was first proposed in (Eringen and Edelen, 1972; Kröner, 1967). Nonlocal formulation of brittle damage of concrete with the integral approach was first developed in (Pijaudier-Cabot and Bažant, 1987). This approach is also applied to ductile damage in (Leblond et al., 1994).

Even if the idea of the integral nonlocal approach is simple, it is numerically complex. Indeed,

- According to Equation (1.35), $\bar{z}(\underline{x})$ depends on $\underline{y}$, so the integration of the constitutive law at point $\underline{x}$ depends on the information at other points. The integration of the constitutive law is no longer autonomic.
- A special procedure or search algorithm is needed to identify the Gauss points $\underline{y}$ over a finite volume Ω surrounding the Gauss point $\underline{x}$. In most cases, this procedure is computationally expensive, especially in 3D cases. This shortcoming may be overcome by introducing a mathematical array in which the numbering of the Gauss points $\underline{y}$ is saved if the intrinsic length scale l_c is introduced in initial configuration (Seidenfuss et al., 2011). However, for some commercial finite element software, it is not always possible to get the information of the desired Gauss points such as the coordinates, the connectivity, etc. Another way is to divide the structure into small cubes and to confine the search area to one cube, as described in (Jirásek, 2007).
- The integral in Equation (1.35) is not quite exact for the points $\underline{x}$ located near the free surface $\partial\Omega$: (1) If the free surface corresponds to the crack lip, then the value of $\bar{z}(\underline{x})$ is affected by the value of $z(\underline{y})$ with $\underline{y}$ the position of the points located on or near the other crack lip, in spite of the gap between the two lips. It is meaningless. One solution can be found in (Desmorat and Gatuingt, 2007). (2) If the free surface corresponds to the boundary, then the weight function ψ should be modified for $\underline{x}$ located near this free surface (Grassl et al., 2014).

Application to ductile failure

The integral approach is first used in the framework of ductile damage in (Leblond et al., 1994). The original Gurson damage model (Gurson, 1977) is used and the regularized variable is the porosity f. This proposal is studied in (Tvergaard and Needleman, 1997, 1995). The main contribution of (Tvergaard and Needleman, 1995) consists in checking and confirming the efficiency of this nonlocal model to eliminate spurious effects arising from unlimited localization of strain and damage. Then the results of some micromechanical simulations (i.e., formation of shear bands and void coalescence) are used in porous plastic solid to calibrate the value of the characteristic length scale l_c (Tvergaard and Needleman, 1997).It is shown that l_c is related to the mean void spacing or the mean void radius, which depends on the failure mechanism (formation of shear band or void coalescence). Then (Enakoutsa et al., 2007) finds that with the nonlocal GTN model proposed in (Leblond et al., 1994) an excessive smoothing of the porosity in the ligament ahead of the crack tip is observed in the simulation of tensile test (axisymmetric modeling), a theoretical analysis of this phenomenon which reveals the origin of the problem is given. To solve this problem, it is proposed to regularize the average of $d(\ln f)/dt$ instead of that of $\dot{f}$. With this proposal, excessive smoothing of the porosity is not observed anymore and the simulation results agree well with the experimental results. The nonlocal GTN model proposed in (Jackiewicz and Kuna, 2003) is based on the regularization of the plastic strain tensor $\boldsymbol{\varepsilon^p}$. The reduction of mesh sensitivity is also emphasized in their work. A summary of the applications of the integral-type nonlocal approach to ductile damage/fracture can be found in Table 1.1.

Table 1.1. Applications of the integral-type nonlocal model to ductile failure

Damage model	Kinematic choice	Configuration[1]	Regularized variable	Reference
Gurson model	Finite strains	-	f	(Leblond et al., 1994)
GTN model	Finite strains	Initial	f	(Tvergaard and Needleman, 1997, 1995)
GTN model	Finite strains	Initial	f or $d\ln f\,/dt$	(Enakoutsa et al., 2007)
GTN model	Finite strains	-	$\boldsymbol{\varepsilon}^{\boldsymbol{p}}$	(Jackiewicz and Kuna, 2003)

1.2.2 Implicit gradient approach

To avoid the integral form shown in Equation (1.35), a Taylor series expansion of z (Bazant et al., 1984) can be used to derive the gradient-enhanced models:

$$z(\underline{y}) = z(\underline{x}) + \frac{\partial z}{\partial x_i}(y_i - x_i) + \frac{1}{2!}\frac{\partial^2 z}{\partial x_i \partial x_j}(y_i - x_i)(y_j - x_j) + \cdots \tag{1.37}$$

where Einstein's summation convention applies to the indices i, j. If ψ is a Gaussian weight function and $\Omega = \mathbb{R}^3$, Equations (1.35)(1.36)(1.37) yield:

$$\bar{z}(\underline{x}) = z(\underline{x}) + c_1\boldsymbol{\nabla}^2\mathrm{z}(\underline{\mathrm{x}}) + c_2\boldsymbol{\nabla}^4 z(\underline{x}) + \cdots \tag{1.38}$$

Otherwise, the odd derivative terms in Equation (1.38) may not vanish. In Equation (1.38), $c_1 \sim l_c^2$ and $c_2 \sim l_c^4$. Even if Equation (1.38) is just a special case, it is still convenient to use it since only an approximation of Equation (1.35) is required.

After disregarding the terms of order four and higher, $\bar{z}$ is approximately equal to:

$$\bar{z}(\underline{x}) = z(\underline{x}) + c_1\boldsymbol{\nabla}^2 z(\underline{x}) \tag{1.39}$$

In addition, special conditions should be postulated for the internal boundary between the process zone and the remaining material and for the external boundary (Peerlings et al., 2001).

With Equation (1.39) and the corresponding boundary conditions, the nonlocal quantity $\bar{z}$ can be explicitly determined from z. This approach is named "explicit gradient approach". It can be seen that $\bar{z} = z$ when $l_c \to 0$ or when $\boldsymbol{\nabla}^2 z = 0$. In the infinitesimal neighborhood of the point $\underline{x}$ (i.e., all points $\underline{w}$ satisfying $|\underline{w} - \underline{x}| \le \epsilon \in \mathbb{R}$ with ϵ can be much smaller than l_c), the gradient term $\boldsymbol{\nabla}^2 z(\underline{x})$ introduces a certain spatial interaction in the constitutive law due to the continuity of z. However, mathematically, the gradient or the second order derivative is just a quasi-local quantity which does not depend on $z(\underline{y})$ for $|\underline{y} - \underline{x}\ | > \epsilon$. Therefore, even if l_c governs the intensity of the spatial interaction, the explicit gradient approximation is only weakly non-local.

An alternative gradient formulation can be derived by applying the Laplacian operator to Equation (1.38) (Peerlings et al., 2001, 1996):

$$\bar{z}(\underline{x}) - c_1\boldsymbol{\nabla}^2\bar{z}(\underline{x}) = z(\underline{x}) + (c_2 - c_1^2)\boldsymbol{\nabla}^4\bar{z}(\underline{x}) + \cdots \tag{1.40}$$

---

[1] The convolution integral form in Equation (1.35) can be performed in the initial or deformed configuration, i.e., the coordinates $\underline{x}$ and $\underline{y}$ are interpreted as initial or current position. In small strains, the initial and deformed configurations are the same.

By disregarding the high terms and by writing $c_1 = l_c^2$, a partial derivative equation in terms of the non-local variable $\bar{z}$ of the Helmholtz type is obtained:

$$\bar{z}(\underline{x}) - l_c^2 \boldsymbol{\nabla}^2 \bar{z}(\underline{x}) = z(\underline{x}) \tag{1.41}$$

Homogeneous natural boundary conditions (De Borst and Mühlhaus, 1992; Mühlhaus and Alfantis, 1991) can be set to complete the definition of $\bar{z}$:

$$\frac{\partial \bar{z}}{\partial \underline{n}} = 0 \text{ on } \partial \Omega \tag{1.42}$$

where $\underline{n}$ is the unit normal to the boundary of Ω, i.e., $\partial\Omega$ so as to have $\int_\Omega \bar{z}\, d\Omega = \int_\Omega z\, d\Omega$. This boundary condition respects the consistency with Equation (1.35). Note that the quasi-local character induced in the explicit formulation is not present in this "implicit gradient" formulation. (See (Peerlings et al., 2001) for the demonstration).

With the implicit gradient approach, the governing equations of the system become:

$$\begin{cases} \boldsymbol{\nabla\sigma} + \underline{f} = \underline{0} \\ \bar{z} - l_c^2 \boldsymbol{\nabla}^2 \bar{z} = z \end{cases} \tag{1.43}$$

where $\underline{f}$ is the body force. The constitutive behavior determines the relationship between the two partial differential equations in (1.43). It should be emphasized that another (set of) degree of liberty $\bar{z}$ is introduced.

Compared to the integral nonlocal approach, the numerical implementation of the implicit gradient approach is easier and the computation cost is less expensive.

Application to ductile failure

Lemaitre-like model

In order to take into account material degradation, (Lemaitre, 1985) introduces a scalar damage variable $D \in [0,1]$ in the context of isotropic damage where the two extremes in the interval represent the sound and fully damaged states respectively. Macro-crack initiates at $D = D_c$ with D_c a critical value depending on the material. An effective stress $\bar{\boldsymbol{\sigma}}$ can be defined as: $\bar{\boldsymbol{\sigma}} = \boldsymbol{\sigma}/(1 - D)$. The Hooke law is written as:

$$\boldsymbol{\sigma} = (1 - D)\, \mathbb{E} : \boldsymbol{\varepsilon}^{\boldsymbol{e}} \tag{1.44}$$

The regularization of the Lemaitre-like model by the implicit gradient approach can be found in (Enakoutsa et al., 2007; Engelen et al., 2003; Feld-Payet et al., 2011; Geers, 2004; Geers et al., 2003; J. Mediavilla et al., 2006a, 2006b, 2006; Seupel et al., 2018; Seupel and Kuna, 2019). In their work, the degradation of the mechanical material properties is indeed represented by a scalar damage variable D, which is coupled to the deformation history of the material through a history variable w:

$$D = D(w) \tag{1.45}$$

The evolution of w is related to a non-local damage driving variable $\bar{z}$ (the energy density release rate, for instance) via the Kuhn-Tucker loading-unloading conditions:

$$\dot{w} \geq 0, \qquad \bar{z} - w \leq 0, \qquad \dot{w}(\bar{z} - w) = 0 \tag{1.46}$$

The ductile damage is introduced through a progressive reduction of the yield stress, one proposal form for the yield function can be:

$$F = \sigma_{eq} - (1 - D)\bar{\sigma}(\kappa) \tag{1.47}$$

In (Engelen et al., 2003), ductile damage is modeled by a gradient extension elastic-plasticity model in the framework of small strains. It is assumed that the Hooke law is not affected by the damage. The hardening variable κ is regularized so that the hardening depends on the nonlocal variable $\bar{\kappa}$ in addition to the local variable κ. The reduction of mesh sensitivity (mesh size and mesh orientation) is confirmed with 1D and 2D finite element simulations. The nonlocal model is improved in (Feld-Payet et al., 2011) to solve the problem of volumetric locking. Compared to (Engelen et al., 2003), the work in (Geers, 2004; Geers et al., 2003) is formulated at finite strains as developed in (Simo and Miehe, 1992). In this case, the Laplacian and the length parameter l_c can be formulated in the undeformed or deformed configurations, leading to either a material (Lagrangian) or a spatial (Eulerian) non-local solution. The differences between these two options are theoretically highlighted and numerically illustrated by tensile and compression tests in (Geers, 2004). Computational examples show that localization takes place in a finite band and never reaches the status of a discrete crack (Geers, 2004). The force-displacement curves demonstrate that the results are mesh size-independent (Geers, 2004). In (J. Mediavilla et al., 2006, 2006a, 2006b; Seupel et al., 2018; Seupel and Kuna, 2019), the elastic-plastic constitutive law is coupled to damage based on the effective stress concept as well as the principle of equivalent strain at finite strains. The remeshing or element-deletion technique is used to eliminate large element distortions. In (J. Mediavilla et al., 2006), the regularized variable is also the hardening variable κ while in (J. Mediavilla et al., 2006a, 2006b), it becomes z satisfying: $\dot{z} = < 1 + B\sigma_h/\sigma_{eq} > \kappa^C\,\dot{\kappa}$ with $<.>$ the Macaulay brackets: $< x > = (x + |x|)/2$ and (B, C) two material constants so as to take into account the dependence on the triaxiality σ_h/σ_{eq}. Both the elastic properties and the plastic yielding are affected by damage evolution. A comparison with a simplified model in which only the strain hardening is decreased with damage yields no significant differences for a special case under monotonic loading conditions and prescribed stress states. This conclusion remains true when elastic strains are small (J. Mediavilla et al., 2006). In (Seupel et al., 2018; Seupel and Kuna, 2019), the difficulties on the use of the element-deletion method in the context of nonlocal damage models are outlined and the efficiency of their nonlocal models are specially studied.

Gurson-like model

The regularization of the Gurson model (Gurson, 1977) by the implicit gradient approach can be found in (Hütter et al., 2014a, 2014b, 2013; Linse et al., 2012). In the work of (Linse et al., 2012), the regularized variable is the dilatational part of the plastic strain $\varepsilon_h = \mathrm{tr}(\boldsymbol{\varepsilon^p})/3$, the GTN model is modified by replacing $\dot{\varepsilon}_h$ by its non-local counterpart $\dot{\varepsilon}_{nl}$ in the evolution equation for void growth. All other equations of the GTN model remain untouched. This formulation is able to eliminate the spurious effects due to the material softening, according to the simulation results of CT in their work. One problem of the model concerns the treatment of the failure zone. In fact, in the broken finite element, the displacement field is not determined anymore while there is still non-local flow through the boundary of the broken element $\partial\Omega_e$. To exclude nonlocal flow to the fracture surface, (Hütter et al., 2013) introduces an additional Dirichlet boundary condition: $\varepsilon_h^F|_{\partial\Omega_e} = \ln((1 - f_0)/(1 - f_F))$ which can be seen as the non-local volumetric plastic strain at fracture. The nonlocal GTN model is then used to simulate large crack growth in the context of plane-strain small-scale yielding conditions. The model captures correctly the states of initial crack tip blunting, crack initiation and crack propagation when the initial porosity is larger than 0.01 (which is high for usual steels) and when the mesh size is small enough. In addition, the experimental results $(J - \Delta a)$ of CT is well captured by simulations. Then this nonlocal GTN model is combined with cohesive zone model (CZM) to model the ductile-brittle transition area in (Hütter et al., 2014a). With the same model, the size-effect due to a secondary void population is investigated in (Hütter et al., 2014b). In this case, the intrinsic length scale l_c is related to the size of the secondary voids.

Rousselier-like model

The regularization of the Rousselier model (Rousselier, 1981) by the implicit gradient approach can be found in (M. K. Samal et al., 2008; Samal et al., 2009; Seidenfuss et al., 2011). In their work, the porosity f is regularized. CT simulations are realized to see the influence of element size and element orientation on the failure behavior. The obtained results are shown to be mesh-independent.

Table 1.2. Application of the implicit gradient model to ductile failure

Ductile model	Kinematic choice	Configuration	Regularized variable	Reference
Lemaitre model	Small strains	-	κ	(Engelen et al., 2003; Feld-Payet et al., 2011)
Lemaitre model	Finite strains	Initial/Deformed	κ	(Geers, 2004; Geers et al., 2003)
Lemaitre model	Finite strains	Deformed	κ	(J. Mediavilla et al., 2006b, 2006a, 2006; Seupel et al., 2018; Seupel and Kuna, 2019)
GTN model	Finite strains	-	ε_v	(Hütter et al., 2014a, 2014b, 2013; Linse et al., 2012)
Rousselier model	-	-	f	(M. K. Samal et al., 2008; Samal et al., 2009; Seidenfuss et al., 2011)

1.2.3 Micromorphic approach

The idea of the micromorphic approach is to model size effects by introducing additional degrees of freedom which describe the kinematic state at the microstructural level. A general framework of this approach is established in (Forest, 2009). The main procedures of this approach will be recalled in this part. We will see that an intrinsic length scale l_c is introduced.

The material behavior is characterized by the classical degree of freedom (displacement $\underline{u}$) and the state variables (the strain tensor $\boldsymbol{\varepsilon}$ and the set of internal variables $\underline{\alpha}$).

Firstly, we introduce the micromorphic variable $\bar{z}$ associated with one state variable z. This $\bar{z}$ is considered as an additional degree of freedom ($\{\underline{u}, \bar{z}\}$). The state space is enlarged to $\{\varepsilon, \underline{\alpha}, \bar{z}, \boldsymbol{\nabla}\bar{z}\}$.

Secondly, we extend the principle of virtual power for any given kinematically admissible fields ($\underline{u}^*, \bar{z}^*$):

$$\mathcal{P}_i(\underline{u}^*, \bar{z}^*) + \mathcal{P}_e(\underline{u}^*, \bar{z}^*) = 0 \tag{1.48}$$

where $\mathcal{P}_i$ is the virtual power of the internal force and $\mathcal{P}_e$ is the virtual power of the external (contact) force:

$$\begin{cases} \mathcal{P}_i = -\int_{\Omega} (\boldsymbol{\sigma} : \boldsymbol{\nabla}\dot{\underline{u}}^* + a\dot{\bar{z}}^* + \underline{b}.\boldsymbol{\nabla}\dot{\bar{z}}^*)\, d\Omega \\ \mathcal{P}_e = \int_{\Omega} \left(\underline{f}.\dot{\underline{u}}^* + d\dot{\bar{z}}^* + \underline{e}.\boldsymbol{\nabla}\dot{\bar{z}}^*\right) d\Omega + \int_{\partial\Omega} (\underline{t}.\dot{\underline{u}}^* + g\dot{\bar{z}}^*)\, dS \end{cases} \tag{1.49}$$

where $\underline{t}$ is the traction, $(a, \underline{b})$ are the generalized stresses associated with $(\bar{z}, \boldsymbol{\nabla}\bar{z})$, $\underline{f}$ is the body force, $(d, \underline{e})$ are the generalized body forces associated with $(\bar{z}, \boldsymbol{\nabla}\bar{z})$ and g is the generalized traction associated with $\bar{z}$.

Thirdly, we derive the governing equations from the above equations for any $\underline{x} \in \Omega$:

$$\begin{cases} \text{div}\,\boldsymbol{\sigma} + \underline{f} = \underline{0} \\ \text{div}\,(\underline{b} - \underline{e}) - (a - d) = 0 \end{cases} \tag{1.50}$$

and the corresponding boundary conditions for any $\underline{x} \in \partial\Omega$:

$$\begin{cases} \underline{t} = \boldsymbol{\sigma}.\underline{n} \\ g = (\underline{b} - \underline{e}).\underline{n} \end{cases} \tag{1.51}$$

Then, the Clausius-Duhem inequality ($D = \int_\Omega \boldsymbol{\sigma}: \dot{\boldsymbol{\varepsilon}} - \dot{F} \geq 0$ with D the dissipation and $F = F(\boldsymbol{\varepsilon}^{\boldsymbol{p}}, \underline{\alpha}, \bar{z}, \boldsymbol{\nabla}\bar{z})$ the Helmholtz free energy) should be used to derive the state laws, i.e., the driving forces $(\boldsymbol{\sigma}, \underline{A}, a, \underline{b})$ associated with the state variables $(\boldsymbol{\varepsilon}^{\boldsymbol{p}}, \underline{\alpha}, \bar{z}, \boldsymbol{\nabla}\bar{z})$:

$$\begin{cases} \boldsymbol{\sigma} = -\dfrac{\partial \mathcal{F}}{\partial \boldsymbol{\varepsilon}^{\boldsymbol{p}}} \\ \underline{A} = \dfrac{\partial \mathcal{F}}{\partial \underline{\alpha}} \\ a = \dfrac{\partial \mathcal{F}}{\partial \bar{z}} \\ \underline{b} = \dfrac{\partial \mathcal{F}}{\partial \nabla \bar{z}} \end{cases} \tag{1.52}$$

Finally, the dissipated energy becomes:

$$\mathcal{D} = \int_\Omega \boldsymbol{\sigma}: \dot{\boldsymbol{\varepsilon}}^{\boldsymbol{p}} + \underline{A}.\dot{\underline{\alpha}}\, d\Omega \tag{1.53}$$

This framework is applied to the elastic-plasticity and brittle damage models, etc in (Forest, 2009). It is stated in his work that the partial Equation (1.41) and the corresponding boundary condition (1.42) of the gradient implicit method (see Section 1.2.2) can be derived from the micromorphic approach. Indeed, in the context of isotropic material behavior and in the absence of body force, if $F = F_l\,(\boldsymbol{\varepsilon}, \boldsymbol{\varepsilon}^{\boldsymbol{p}}, \underline{\alpha}) + \int_\Omega (c(\boldsymbol{\nabla}\bar{z}\,)^2/2 + r_{nl}(\bar{z} - z)^2/2)\, d\Omega$ with F_l the Helmholtz free energy density related to the local formulation of the constitutive law and (r_{nl}, c) two constants, then $a = r_{nl}\,(\bar{z} - z)$, $\underline{b} = c\boldsymbol{\nabla}\bar{z}$ and

$$\begin{cases} \bar{z} - l_c^2 \boldsymbol{\nabla}^2 \bar{z} = z \\ \boldsymbol{\nabla}\bar{z}.\underline{n} = g/c \end{cases} \tag{1.54}$$

where $l_c^2 = c/r_{nl}$ is a characteristic length scale. It can be noticed that when $g = 0$, Equation (1.54) is the same as Equations (1.41)(1.42)(implicit gradient approach).

But unlike the implicit gradient formulation, the micromorphic approach can derive the driving forces involved in the yield function from the expression of F. For example, if $z = \kappa$ and if

$$\mathcal{F} = \int_\Omega \left(\frac{1}{2} \boldsymbol{\varepsilon}^{\boldsymbol{e}}: \mathbb{E}: \boldsymbol{\varepsilon}^{\boldsymbol{e}} + \int_0^\kappa (\bar{\sigma}(s) - \sigma_0) ds + \frac{1}{2} c(\boldsymbol{\nabla}\bar{\kappa})^2 + \frac{1}{2} r_{nl}(\bar{\kappa} - \kappa)^2 \right) d\Omega \tag{1.55}$$

then the driving forces associated with the state variable κ are:

$$A = \sigma_0 - \bar{\sigma}(\kappa) + r_{nl}(\bar{\kappa} - \kappa) \tag{1.56}$$

where $\bar{\kappa}$ can be derived from Equation (1.54) with $z = \kappa$.

The corresponding yield function is:

$$F = \sigma_{eq} - \sigma_0 + A = \sigma_{eq} - \bar{\sigma}(\kappa) - r_{nl}\kappa + r_{nl}\bar{\kappa} \tag{1.57}$$

Note that if $r_{nl}\ (\kappa - \bar{\kappa})^2/2$ is considered as a penalty term to ensure the equality between κ and $\bar{\kappa}$, then the model becomes a constrained micromorphic model. In this case, the value of r_{nl} should be very large, which may cause some numerical problems, in particular, in Newton scheme used to integrate constitutive equations.

Application to ductile failure

The framework proposed in (Forest, 2009) is used in (Brepols et al., 2017; Diamantopoulou et al., 2017) in the field of ductile fracture.

In (Brepols et al., 2017), damage is assumed to exhibit gradient effects. In particular, damage and plasticity are regarded as two independent physical mechanisms. Each mechanism is characterized by its own yield function and loading/unloading condition. Several 1D and 2D simulations are carried out. The results are shown to be mesh-independent. In addition, this model can well capture crack initiation and crack propagation. In (Diamantopoulou et al., 2017), damage is regularized. The comparison between the results obtained by the proposed model and that by classical local damage model validates the model implementation. Mesh-dependency is indeed well reduced.

In addition to the micromorphic approach proposed in (Forest, 2009), there are some other models which are also micromorphic but derived from some special homogenization procedures (Bergheau et al., 2014; Enakoutsa and Leblond, 2009; Gologanu et al., 2007; Hütter, 2017) so as to account for the nonlocal effect. These models are named “second gradient model”.

In (Gologanu et al., 2007), the Gurson’s homogenization approach is extended to the strain-gradient theory in which an additional gradient term appears in the field function. This model is called the GLPD model, it can be classified as a constrained micromorphic theory where microdeformation and macrodeformation are constrained to coincide. Numerical results in (Bergheau et al., 2014; Enakoutsa and Leblond, 2009) shows that the GLPD model can well reduce the spurious effects induced by the strain and damage localization. The problem of the GLPD model is the complex finite element implementation. In addition, the numerical implementation needs the second derivatives of the shape function, so elements of class C^1. Even if this problem can be solved using penalty formulations, numerical implementation is still difficult since the strain tensor is regarded as an additional nodal variable. In order to combine the computational efficiency of the implicit gradient models with the micromechanically sound basis of the GLPD model, in (Hütter, 2017), Gurson’s model is extended to the theory of unconstrained microdilatational media by homogenization. No simulations are introduced in his paper. Further investigation of the efficiency of this model is still expected.

Table 1.3. Application of the micromorphic model to ductile failure

Ductile model	Selected variable	Kinematics	Additional DOF	Reference
GLPD model	$\boldsymbol{\nabla\varepsilon}$	Small strains	$\boldsymbol{\nabla\varepsilon}$	(Bergheau et al., 2014; Enakoutsa and Leblond, 2009; Gologanu et al., 2007)
Gurson-like model	$\boldsymbol{\varepsilon}$	-	$\boldsymbol{\varepsilon}, \boldsymbol{\nabla\varepsilon}$	(Hütter, 2017)
-	Damage variable D	-	$D, \boldsymbol{\nabla} D$	(Diamantopoulou et al., 2017)
-	Damage variable D	-	$D, \boldsymbol{\nabla} D$	(Brepols et al., 2017)

1.2.4 Gradient enhanced energy (GEE) approach

In the micromorphic approach, enforcement of the equality between the micromorphic variable and its local counterpart would lead to the introduction of the gradient of latter in the Helmholtz free energy: This corresponds to gradient enhanced energy (GEE) approach proposed in (Lorentz, 1999; Lorentz and Benallal, 2005; Lorentz and Godard, 2011; Zhang et al., 2018) which consists in introducing the gradient effect in the Helmholtz free energy density:

$$\mathcal{F}(\boldsymbol{\varepsilon},\boldsymbol{\varepsilon^p},\underline{\alpha},z) = \int_\Omega \left(\phi_\ell(\boldsymbol{\varepsilon},\boldsymbol{\varepsilon^p},\underline{\alpha},z) + \frac{1}{2} c\boldsymbol{\nabla} z.\boldsymbol{\nabla} z \right) d\Omega_0 \tag{1.58}$$

where z is one (set of) state variable(s) (internal variable(s) or strain tensor), $\underline{\alpha}$ is the internal variables (in addition to z if z is a (set of) internal variable(s)), c is a nonlocal parameter of unit "Newton", ϕ_l is a point-wise contribution to the Helmholtz free energy. It can be seen that the term $c\boldsymbol{\nabla} z.\boldsymbol{\nabla} z/2$ can control the strain and/or damage localization if z is well chosen and c controls the delocalization intensity. Indeed, if z is an appropriate regularized variable, the term $\int c\boldsymbol{\nabla}\, z.\boldsymbol{\nabla} z/2 \to \infty$ in the case of localization which is impossible since $\mathcal{F}$ is finite.

In the following, for the sake of simplicity, z is taken as a scalar. The Clausius-Duhem inequality ($D = \int_\Omega \boldsymbol{\sigma}: \dot{\boldsymbol{\varepsilon}} - \dot{\mathcal{F}} \geq 0$ with D the dissipation and $F = F(\boldsymbol{\varepsilon^p},\underline{\alpha})$ the free energy) can be used to derive the state laws, i.e., the driving forces $(\boldsymbol{\sigma},\underline{A},Z)$ associated with the states variables $(\boldsymbol{\varepsilon^p},\underline{\alpha},z)$:

$$\begin{cases} \boldsymbol{\sigma} = -\dfrac{\partial \phi_l}{\partial \boldsymbol{\varepsilon^p}} \\ \underline{A} = \dfrac{\partial \phi_l}{\partial \underline{\alpha}} \\ Z = \dfrac{\partial \phi_l}{\partial z} + \operatorname{div}(c\boldsymbol{\nabla} z) \end{cases} \tag{1.59}$$

The dissipated energy is finally written in the following form:

$$\mathcal{D} = \int_\Omega (\boldsymbol{\sigma}: \dot{\boldsymbol{\varepsilon}}^{\boldsymbol{p}} + \underline{A}.\underline{\dot{\alpha}} + Zz)\, d\Omega + \int_{\partial\Omega} (-c\boldsymbol{\nabla} z.\underline{n})\dot{z}\, dS \geq 0 \tag{1.60}$$

It is assumed that no dissipation stems from the boundary, which leads to the boundary condition:

$$\boldsymbol{\nabla} z.\underline{n} = 0 \text{ on } \partial\Omega \tag{1.61}$$

The driving force Z enter in the yield function of the constitutive law so as to account for the nonlocal effect.

The mathematic and numerical properties of the GEE approach are well posed since all equations involved in the GEE approach are derived from the variational analysis. The robusteness is shown in (Lorentz and Godard, 2011; Miehe, 2014) by elastic-plasticity or brittle damage simulations.

Application to ductile failure

Rousselier law

The GEE approach is first applied to ductile damage in (Lorentz and Cano, 2005). The Rousselier damage model is used and the hardening variable κ is regularized. The results show the good independence of the results with respect to the mesh refinement.

GTN law

The GEE approach is recently applied to ductile damage in the framework of finite strains in (Zhang, 2016; Zhang et al., 2018). The GTN damage model is used and the hardening variable κ is regularized. The results show that the width of the localization band can be controlled and the crack path does not depend on mesh orientation. This model will be presented in detail in the next chapter.

Table 1.4. Application of the GEE approach to ductile failure

Ductile model	Kinematic choice	Configuration	Regularized variable	Reference
Rousselier model	Fintie strains	Initial	κ	(Lorentz and Cano, 2005)
GTN model	Finite strains	Initial	κ	(Zhang, 2016; Zhang et al., 2018)

1.2.5 Phase-field approach

As seen in the previous parts, the micromorphic model and the GEE model do not involve the concept of discontinuous crack, which is in contrary to the phase-field approach in which the crack is regularized by a phase-field. Most phase-field models are derived from the variational approaches to "Griffith's theory of brittle fracture" proposed by (Francfort and Marigo, 1998). Various phase-field models are proposed/revisited in the literature such as (Bourdin et al., 2000; Marigo et al., 2016; Tanné, 2017). We emphasize that a well-established phase-field model should tend to the initial cracked problem when the intrinsic length scale(s) introduced in the phase-field model tends to zero.

In this part, we try to establish a general framework in which most of phase-field models can be included. The phase-field models can actually be classified into the class of gradient damage models (coupled with plasticity in the case of ductile damage). The total internal energy density $\mathcal{E}$ of the system can be split into four parts (Alessi et al., 2018):

$$\mathcal{E} = \int_{\Omega_0} \left(\underbrace{A(D)\Phi_e(\boldsymbol{\varepsilon} - \boldsymbol{\varepsilon^p})}_{a} + \underbrace{B(D)\Phi_p(\kappa, \nabla\kappa)}_{b} + \underbrace{\psi_d(D, \nabla D)}_{c} + \underbrace{C(D)\psi_p(\kappa)}_{d} \right) d\Omega_0 \tag{1.62}$$

where D is a scalar phase-field (damage) parameter, (Φ_e, Φ_p) are respectively the elastic and plastic parts of the Helmholtz free energy density, (ψ_d, ψ_p) are respectively the dissipated energy density due to damage and plasticity, $A: [0,1] \to [0,1]$ is a scalar degradation function satisfying $A(0) = 1, A(1) = 0, A'(D) \leq 0$. For instance, $A = (1 - D)^2$. The same properties as A hold for the functions B and C. Equation (1.62) can be seen as a general expression of the phase-field models used in the literature. In this equation, the term a is the elastic potential density, the term b is the plastic hardening contribution, the term c is the dissipated damage work density which is not linked to the plasticity and the term d is the damage-plasticity coupled dissipation density.

Firstly, the elastic part of the Helmholtz free energy density can be written as:

$$\Phi_e(\boldsymbol{\varepsilon} - \boldsymbol{\varepsilon^p}) = \frac{1}{2}(\boldsymbol{\varepsilon} - \boldsymbol{\varepsilon^p}) : \mathbb{E} : (\boldsymbol{\varepsilon} - \boldsymbol{\varepsilon^p}) \tag{1.63}$$

Secondly, the plastic part of the Helmholtz free energy density can be written as:

$$\Phi_p(\kappa, \boldsymbol{\nabla}\kappa) = \int_0^{\kappa} (\bar{\sigma}(s) - \sigma_0)\, ds + \frac{1}{2} c_p (\boldsymbol{\nabla}\kappa)^2 \tag{1.64}$$

where c_p is a constant value linked to the nonlocal length l_p for the plasticity.

Thirdly, the plastic dissipated work ψ_p can be:

$$\psi_p(\kappa) \equiv \sigma_0 \kappa \tag{1.65}$$

Finally, for the dissipated energy density due to damage ψ_d, a widely used form is:

$$\psi_d(D, \nabla D) = \frac{G_c}{c_w}\left(\frac{w(D)}{l_d} + l_d(\underline{\nabla} D)^2\right) \tag{1.66}$$

where G_c is the critical fracture energy per unit area, l_d is the length scale for phase-field and $(w(D), c_w)$ are:

$$w(D) = \begin{cases} D, & AT-1 \\ D^2, & AT-2 \end{cases} \tag{1.67}$$

$$c_w := 4\int_0^1 \sqrt{w(D)}\, dD = \begin{cases} 8/3, & AT-1 \\ 2, & AT-2 \end{cases} \tag{1.68}$$

with AT stands for the Ambrosio-Tortorelli functional (Ambrosio and Tortorelli, 1990).

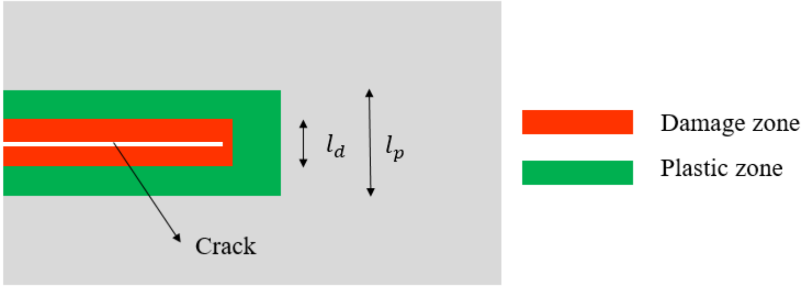

Figure 1.4. Characteristic length sales in phase-field model

It is worth remarking that two length scales are introduced in the current formulation: one for the phase-field, i.e., damage (l_d) in ψ_d and the other for the plasticity (l_p) in Φ_p (see Figure 1.4).

In elastic-plasticity, the damage is not involved and thus $A = B = C = 1$ and $c = 0$ in Equation (1.62).

In brittle damage, the scalar phase-field (damage) field D is sufficient to represent the material degradation since the energy dissipation is mainly due to the creation of new cracked surfaces. Plasticity ($\varepsilon_p = 0$) and hardening effects are not involved in brittle material, so $b = d = 0$ in Equation (1.62). On the contrary, in ductile damage, Plasticity and hardening effects are not negligible and Equation (1.62) holds.

The governing (equilibrium) equation can be derived from energy balance, i.e., $\dot{\mathcal{E}} = \dot{\mathcal{W}}$ with $\mathcal{W}$ external work density. The Clausius-Duhem inequality should be used to derive the state laws, i.e., the driving forces associated with the state variables. These driving forces enter in the yield functions (one yield surface F_p for the plasticity and the other F_d for the damage) in the constitutive law so as to account for the nonlocal effects. In particular, in the absence of damage-plasticity coupling, the plastic yield function does not depend on the damage variable(s) and the damage yield function does not depend on the plastic variable(s).

Application to ductile failure

The applications of the phase-field models to ductile failure can be found in (Aldakheel, 2016; Aldakheel et al., 2018; Alessi, 2018; Ambati, 2016, 2015; Borden et al., 2016; Brach et al., 2019; Kuhn and Noll, 2016; Miehe et al., 2016; Tanné, 2017). All the models can be cast in the same variational framework and differ mainly by the four terms a, b, c, d in Equation (1.62):

- For the term a, the free energy Φ_e remains the same in all models. As for $A(D)$, quadratic or cubic expressions are commonly used.
- For the term b, the gradient plasticity is considered in (Miehe et al., 2016) and so a plastic length scale l_p is introduced in his model.
- For the term c, in all models, a phase-field (damage) length scale l_d is introduced. The expressions used in different models are quite similar.
- For the term d, the difference is mainly found on the expression of $C(D)$, in most cases, the coupling between damage and plasticity is taken into account and $C(D) = A(D)$. The only exception is in (Ambati, 2015) where no coupling is assumed.

von-Mises model with phase-field damage

The model proposed in (Ambati, 2015) uses a characteristic degradation function to realize the coupling between damage and plasticity in a multiplicative format. It is demonstrated in his work that the model can predict crack shape and location in a tensile specimen. This work is then extended at finite strains in (Ambati, 2016).The model suggested in (Borden et al., 2016) introduces a new mechanism to include a measure of stress triaxiality as a driving force for crack initiation and propagation. The incorporation of gradient plasticity into the phase-field model at finite strains are realized in (Miehe et al., 2016). (Brach et al., 2019; Tanné, 2017) study crack initiation and propagation in elastic-perfectly plastic bodies with a variational gradient damage phase-field formulation. Both plane strain and plane stress are addressed. A variational approach to combine brittle, cohesive and ductile fracture is given in (Alessi, 2018).

GTN damage model

The above works assume that there is no plastic dilatation, i.e., the effect of the hydrostatic pressure on plastic flow is not taken into account, which is not in accordance with experimental observations. To this end, in (Aldakheel et al., 2018), the phase field modeling is coupled with the GTN damage model. The sharp crack surface is regularized by a new function depending on the phase-field parameter D and the damage characteristic length l_d, as in Equation (1.62). A phase-field driving force related to the porosity is introduced. Thus the onset of fracture is driven by the critical porosity. The numerical simulations show that this model is able to capture the cup-cone phenomenon.

Table 1.5. Application of the phase-field approach to ductile failure

Constitutive law	Kinematic choice	Configuration	Regularized variable	Reference
von-Mises	Small strains	-	D	(Ambati, 2015)
von-Mises	Finite strains	Initial	D	(Ambati, 2016)
von-Mises	Finite strains	Initial	D	(Borden et al., 2016)
von-Mises	Finite strains	Initial	D, κ	(Miehe et al., 2016)
von-Mises	Finite strains	Initial	D	(Brach et al., 2019; Tanné, 2017)
GTN	Finite strains	Initial	D	(Aldakheel et al., 2018)

1.2.6 Choice of regularization approach and regularized variable

As mentioned in this section, the implicit gradient approach is derived from the integral nonlocal approach, these two approaches are equivalent in some way if the weight function in Equation (1.35) is well chosen. The difficulty to use the integral nonlocal approach lies in its complex numerical implementation, its time-consuming procedures, the special treatment of the points located near/on the free surface. These aforementioned problems can apparently be overcome using the implicit gradient approach. Due to its simplicity and its efficiency, the implicit gradient approach is very often used in the literature. However, this approach leaves many choices for energy regularization and the use of the nonlocal variable $\bar{z}$ in the model (see (Lorentz and Andrieux, 2003)) while many of them are inadequate, in particular under the background of plasticity: the existence of the solution (Polizzotto, 2001) and the regularization of certain constitutive laws (Di Luzio and Bažant, 2005) cannot be ensured.

The micromorphic approach is based on a thermo-mechanical framework. Compared to the implicit gradient approach, the micromorphic approach leaves less choices while the regularization effect can be ensured in most cases. However, in this approach, some additional degrees of freedom related to strain quantities are introduced and controlled, which may be not suitable for the description of crack opening and crack closure. In the literature, some internal variables (such as the hardening variable) are sometimes regularized, in this case, the formulation of the micromorphic approach is similar to that of the GEE approach.

Like the micromorphic approach, the GEE approach and the phase-field approach are derived from a variational analysis, so that sound mathematical and numerical properties are ensured. Compared to the GEE approach, the phase-field approach cannot model the process-zone since this approach consists in regularizing a crack. Besides, stress triaxiality on crack initiation and propagation are not (yet) considered in most phase-field model.

In this work, the GEE will be used since:

- Mathematically, the robustness of the model is demonstrated in (Lorentz, 2017; Lorentz and Godard, 2011) for brittle fracture and in (Zhang, 2016; Zhang et al., 2018) for ductile fracture;
- Numerically, the usual algorithm can be used and thus it is suitable for standard multi-purpose Finite element softwares.

As for the regularized variable, the most used internal variables in the literature for ductile damage model is the damage variable (D for the Lemaitre model and f for the GTN or Rousslier model) and/or the hardening variable κ. Note that even if in the work of (Linse et al., 2012), the volumetric part of the plastic strain tensor ε_v is regularized, it is directly linked to the porosity f in the absence of void nucleation. It is not surprising that unsatisfying results may be obtained when the regularized variable is not well chosen, as pointed out by the assessment of (Andrade et al., 2014; Jirásek and Rolshoven, 2003). Nevertheless, (Andrade et al., 2014) stated that the best regularized variable is the damage variable in the case of the Lemaitre and GTN models. Nevertheless, this conclusion should be further verified by visualizing the equivalent plastic strain field. Moreover, in all simulations given in (Andrade et al., 2014), the mesh size is very coarse and there is only crack initiation (without any propagation) according to their results.

In this work, the hardening variable κ will be used to regularize the constitutive law. This choice is believed to simultaneously control (1) the plastic localization which may result from geometrical considerations (necking) and (2) the damage localization which results from strain softening induced by void growth and void nucleation.

1.3 Problems with the finite element simulation of ductile failure

1.3.1 Mesh sensitivity

As mentioned in Section 1.1.3, strain/damage localization occurs with the use of constitutive law including softening. Numerically, spurious mesh-sensitivity and unrealistic physical predictions may be observed when this kind of constitutive law is used in the finite element analysis. Indeed, as the mesh is refined, the localization zone narrows and finally vanishes. Thus, the dissipated energy also tends to zero. This is in contradiction to the experimental observation where a narrow localization bands depending on material exist. An example of the simulations of Compact Tensile (CT) test has been given in (Besson, 2010). Theses simulations are performed using the GTN damage model with plane-strain modeling. The force versus Crack Mouth Opening Displacement (CMOD) for various mesh sizes has been shown (see Figure 1.5) which clearly illustrates the mesh size effect. As explained in (Besson, 2010), for crack initiation, the decrease of the mesh size leads to the increase of the value of the equivalent strain at crack tip for a given CMOD and thus to an earlier crack initiation. For crack propagation, the energy dissipated per crack extension increment is proportional to the element size under certain assumptions, which can obviously affect the global behavior of the structure.

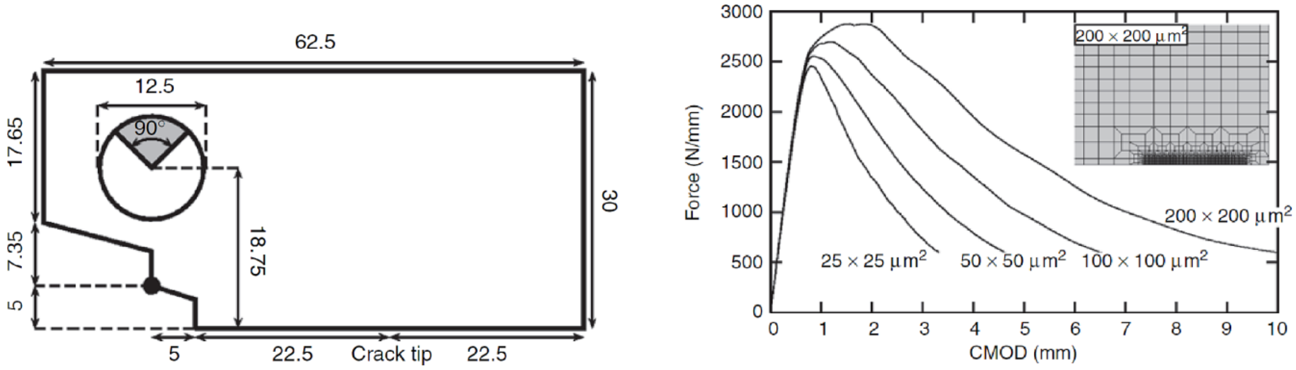

(a) (b)

Figure 1.5. (a) Geometry of CT specimen (mm). The black dot corresponds to the location of CMOD measurement; (b) Force-CMOD curves for different mesh sizes

Possible solutions

Mesh size as a material parameter

An engineering solution to solve the spurious mesh sensitivity is to consider the mesh size as an additional material parameter. In this case, the value of the mesh size is often assumed to represent the mean distance l_c between the inclusions leading to the primary voids (Rousselier, 1981; Sun et al., 1989). The material is seen as an assembly of cells of size l_c containing a single inclusion. Thus, the cell deformation and the role of the secondary voids are not taken into account in this simple description of the material. This interpretation is supported by some experimental observations (Hahn and Rosenfield, 1975; Steglich and Brocks, 1998). This approach is rather simple and many authors show that crack growth and failure behavior can be well predicted with a given mesh size (Nonn and Kalwa, 2010; Pavankumar et al., 2005)

However, it is clear that the simulation results still depend on the mesh orientation and the type of shape functions and quadratic rules, so the model is not predictive (Besson et al., 2006). Besides, mesh size is used to (1) represent the material characteristic length so as to model the energy dissipated during crack extension and (2) discretize structures (notion of spatial convergence). These two roles are to some extent contradictory.

Viscosity

One usual way to reduce the mesh dependency in the literature is to introduce the viscosity in the simulation. The idea of this method is based on the fact that the localization leads to high deformation rates, which can be redistributed in the finite element mesh by viscosity. Generally, viscosity is directly introduced in the constitutive law and thus the material behavior becomes rate dependent. The rate-dependent damage law should not result in ill-posed problems. However, the regularization effect on the mesh dependency is not observed in (Ljustina et al., 2014) even if the damage law is rate-dependent. The explanation that is given in (Ljustina et al., 2014) is that the viscous effect is too low and it disappears with time. Another way to introduce the viscosity is to use an overlay model in which the constitutive law and the viscous law are independent, as done in (Dias da Silva, 2004). In (Dias da Silva, 2004), the regularization effect is observed only in the presence of a very high viscosity. In this case, the material is almost viscoelastic, no matter what the constitutive law is.

The observations in (Dias da Silva, 2004; Ljustina et al., 2014) are not surprising since from a dimensional point of view, for quasi-static analysis, the viscous models only introduce a characteristic time, but not a characteristic length for the localization band. We recall that mesh dependency is a spatial problem, thus the introduction of time scale is not useful.

Besides, according to the results obtained in (Flatten et al., 2006), spurious mesh-sensitivity cannot be prevented by the viscosity even though the model is rate-dependent in the case of a dynamic analysis. In order to solve this problem, the concept of bounded damage rate model is proposed in (Allix, 2013; Allix et al., 2003). The key idea of this method is to determine the internal variables which governs localization and then to bound the rate of these variables. For more details on this model, one can refer to (Allix, 2013; Allix et al., 2003).

Cohesive zone model (CZM)

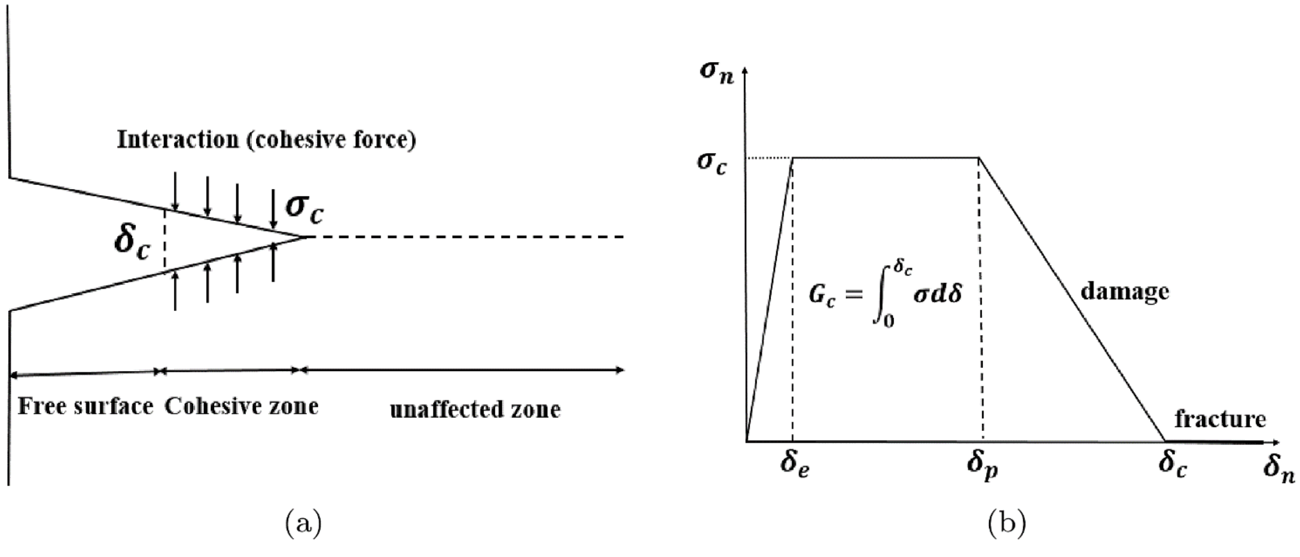

Figure 1.6. (a) Schematic representation of a cohesive zone; (b) stress-displacement jump curves for a ductile material (Tvergaard and Hutchinson, 1992)

An alternative possibility is to bypass the strain localization and introduce a discontinuity as the outcome of the strain localization process. This option can be realized with cohesive zone models (CZM). Note that the crack path must be known when CZM is used, this crack path is considered as the jump of the displacement field. Thus, the relation between the displacement jump and the stress must be given in CZM (see Figure 1.6

for one cohesive law for ductile fracture). Since the aim of this part is just to propose some solutions to the spurious mesh sensitivity problem, we will not describe different CZM here. Compared to ductile damage models, ductile CZM is simpler since only the tensile strength σ_c and the separation work G_c are involved in the constitutive law. In addition, it is possible to account for the shear effect in the cohesive interface. Consequently, CZM are commonly recognized to be an important tool for describing fracture in engineering materials. Nevertheless, some drawbacks should be emphasized: (1) the model is not predictive since the crack path should be known in advance. (2) The physical description of ductile fracture is not accurate as the triaxiality dependence is poorly described. A model, in which the CZM parameters depend on the local triaxiality so as to match the GTN model, is proposed in (Siegmund and Brocks, 1999).

Nonlocal model

As discussed in Section 1.2, during uncontrolled strain localization, the length scale of the macroscopic fields becomes of the same magnitude as that of the microscopic fields, so the scale separation assumption in homogenization process introduced in Section 1.1.1 is no more valid. It is necessary to enhance the homogenization schemes to include this length scale interaction or to introduce a new length scale in a phenomenological way. For more details of these models, one can refer to the Section 1.2. The common point of their works is the introduction of some length scales into the macroscopic equations. These length scales play the role of strain localization limiter.

Comparison of different approaches

In this part, some approaches to solve the problem of mesh sensitivity are presented. The first approach consists in regarding the mesh size as an additional parameter. Even if crack growth and failure behavior of the material can be well predicted in some cases, the model is not predictive in terms of crack path. The second approach is focused on the control of the dissipated energy by introducing either a dissipated energy term in the surface or the viscous phenomenon. The corresponding effect can be observed only when the introduced term is important. Moreover, the strain localization is just postponed with the viscosity. The third approach aims at using CZM to bypass the uncontrolled strain localization problem. Compared to ductile damage models, CZM is simpler but not predictive. The last approach is to introduce a length scale in the constitutive or continuum equations (see Section 1.2). Numerically, the width of the localization band can be controlled by the new length scale. Of course, other approaches may exist in the literature, for example, the damage model can be combined with the discontinuous fields within the elements, and the insertion of the discontinuity occurs when there is loss of ellipticity at the local level (Areias and Belytschko, 2005; Feld-Payet et al., 2015; Oliver et al., 2010).

In this work, the nonlocal model is used to control mesh dependency.

1.3.2 Volumetric-locking

It is well known that the use of the standard displacement-based finite element formulations leads to too stiff solutions and oscillations of the stress field in quasi-incompressible situations. This phenomenon is called “volumetric locking”. The (quasi-)incompressible property is characterized by

$$J = \det(\boldsymbol{F}) \approx 1 \quad \text{or} \quad \mathrm{tr}(\boldsymbol{\varepsilon}) \approx 0 \tag{1.69}$$

where J is the transformation Jacobian and $\boldsymbol{F}$ is the deformation gradient.

Indeed, In the case of linear isotropic elasticity, a material is quasi-incompressible when the Poisson ratio $\nu \approx 0.5$. In this case, the bulk modulus $K \to \infty$ due to the relation $K = E/(3(1-2\nu))$ and thus $\mathrm{tr}(\boldsymbol{\varepsilon}) = \mathrm{tr}(\boldsymbol{\sigma})/K \to 0$ according to the Hooke relation. In the framework of elastic-plasticity (J_2 theory), we have $\mathrm{tr}(\boldsymbol{\varepsilon^p}) = \mathrm{tr}(3\boldsymbol{\sigma_D}/2\sigma_{eq}) = 0$. In most cases, the elastic strain is very small compared to the plastic strain which leads to $\mathrm{tr}(\boldsymbol{\varepsilon}) \approx 0$. In the case of ductile damage, the material is compressible due to the evolution of the porosity. However, when the porosity f is very small, we still have $\mathrm{tr}(\boldsymbol{\varepsilon}) \approx 0$ if the elastic strain is small compared to the plastic strain.

If $\mathrm{tr}(\boldsymbol{\varepsilon}) = \mathrm{div}(\underline{u}) \approx 0$, then the effective degrees of freedom of the displacement are reduced. Some material points are locked, and the spurious oscillation of the stress fields appears. Therefore, the constitutive constraint ($\mathrm{div}(\underline{u}) \approx 0$) should be relaxed.

Over the past years, various methods have been proposed to deal with this problem such as reduced integration, selective integration, B-bar and F-bar methods, enhanced assumed strain (EAS) method, Hybrid High-Order (HHO) method and mixed formulations, etc.. This subsection aims to give a short review of each of the aforementioned methods and to choose a robust and generic one for the current work.

Review on locking-free proposals

Reduced integration

The reduced integration technique is first introduce in (Zienkiewicz et al., 1971). The basic idea is to use lower-order quadrature formula for the estimation of the stiffness matrix. The integration points in one finite element is reduced accordingly. Hence, there are less constraint $\mathrm{div}(\underline{u}) \approx 0$ to be fulfilled and the richness of the degrees of freedom somewhat retrieved. However, this technique sometimes leads to a singular stiffness matrix and introduces zero-energy mode (for instance for Q_4 and T_6 finite elements). With the Q_8 elements, this mode does not exist, but volumetric-locking still exists.

Selective integration

The selective integration technique is first proposed in (Doherty et al., 1969). In selective reduced integration, the shear strain and/or volumetric strains are evaluated in the element midpoint only. This technique gives a better result than the previous technique since the stiffness associated with $\boldsymbol{\varepsilon_D}(\underline{u})$ is not reduced with the selective integration technique. Nevertheless, there are various drawbacks to this technique: (1) It is rather easy to use this technique in the isotropic cases while the extension to the anisotropic or orthotropic cases is complex (Hughes, 2012); (2) The use of quadratic finite elements with this technique leads to some convergence problems since the LBB condition[2] is not fulfilled (Zhang, 2016); (3) In GTN law, the hydrostatic and deviatoric parts of the constitutive relation cannot be separated: the simplicity is somewhat lost.

For instance, the selective integration technique can be used for Q_4 or T_6 elements.

---

[2] LBB (Ladyzenskaia-Babushka-Brezz) condition: Let X and M two Hilbert spaces, let b a continuous bilinear form on $X \times M$. The form b satisfies the LBB condition if and only if:

$$\exists \beta > 0, \qquad \inf_{p \in M} \sup_{v \in X} \frac{b(v,p)}{||v||_X ||p||_M} \geq \beta$$

Discrete LBB condition: Assume that $X_h \subseteq X$ and $M_h \subseteq M$, to obtain a good approximation of the solution by finite element methods, it is necessary to have:

$$\exists \beta_h > 0, \qquad \inf_{p_h \in M_h} \sup_{v_h \in X_h} \frac{b(v_h,p_h)}{||v_h||_X ||p_h||_M} \geq \beta_h \geq \beta_*$$

B-bar and F-bar

In order to overcome some limitations introduced in reduced/selective technique, the B-bar technique is proposed in (Hughes, 2012, 1980) in the framework of small strains. This method consists in, firstly, dividing directly the strain operator $\underline{\boldsymbol{B}}$ (which relates the strains to the displacements) to the hydrostatic part $\underline{\boldsymbol{B}}_h$ and the deviatoric part $\underline{\boldsymbol{B}}_D$, and secondly, modifying $\underline{\boldsymbol{B}}_h$ to $\underline{\boldsymbol{B}}'_h$ so as to reduce its contribution. For instance, the $\underline{\boldsymbol{B}}'_h$ can be the average of all $\underline{\boldsymbol{B}}_h$ in the finite element and thus $\mathrm{tr}(\boldsymbol{\varepsilon})$ is the same everywhere. Since the pressure is related to the volume change, pressure fluctuations are avoided within elements. The new strain operator becomes $\underline{\boldsymbol{B}} = \underline{\boldsymbol{B}}_D + \underline{\boldsymbol{B}}'_h$. There are several advantages with the B-bar technique. Firstly, it does not require to introduce additional degrees of freedom. Secondly, compared to the selective integration method, the B-bar technique is easier to be used in the anisotropic cases.

In the framework of finite strains, the F-bar technique is used. It is based on the multiplicative decomposition of the deformation gradient $\boldsymbol{F}$ into the hydrostatic and deviatoric parts. The stress tensor is then computed from the modified $\boldsymbol{F}$. Different versions of the F-bar method have been proposed in the literature (de Souza Neto et al., 1996, 2011; Elguedj et al., 2008, 2007) . The F-bar method proposed in (de Souza Neto et al., 1996, 2011)is only devoted to linear finite elements. As for the proposal in (Elguedj et al., 2008, 2007), it can be applied to all types of finite elements, but some drawbacks still exist at the level of tangent matrix.

Remark:

- For Q_4 elements, the selective technique and the B-bar technique are the same in the case of rectangular elements.
- For T_6 elements, the selective technique and the B-bar technique are the same if the quadratic nodes are located in the center of each edge of the triangle and if J_2 theory is used. But in this case, we lost the precision given by quadratic finite element.

Enhanced Assumed Strain (EAS) method

The EAS method is initially proposed in (Simo and Rifai, 1990) in the framework of small strains. It is based on the Hu-Washizu three-field variational formulation in which stress, strain and displacement are regarded as three independent variables. The idea of this method is to enhance the strain tensor $\boldsymbol{\varepsilon}$ by an additional term $\boldsymbol{\varepsilon}'$: $\tilde{\boldsymbol{\varepsilon}} = \boldsymbol{\varepsilon} + \boldsymbol{\varepsilon}'$. This new strain tensor is used in the constitutive law and so is involved in the Hu-Washizu mixed variational formulation. An orthogonality between $\boldsymbol{\sigma}$ and $\boldsymbol{\varepsilon}'$ ($\int_\Omega \boldsymbol{\sigma}\colon \boldsymbol{\varepsilon}'\, d\Omega = 0$) is imposed so as to eliminate $\boldsymbol{\sigma}$ from the set of unknowns. Then the enhanced strain tensor is eliminated at element level by some special treatment. This method is first extended to finite strains in (Simo and Armero, 1992) by enhancing the displacement gradient so as to obtain the enhanced deformation gradient: $\widetilde{\boldsymbol{F}} = \boldsymbol{I} + \nabla \underline{u} + \boldsymbol{F}'$. The drawback to this extension is that zero-energy modes can appear in some cases, as shown in (Wriggers, 2008). Some stabilization methods can be introduced to avoid this problem, but may be computationally expensive.

Mixed finite element formulation

The mixed finite element formulation is first introduced in (Herrmann, 1965) for two-field elements and in (Simo et al., 1985) for three-field elements. The basic idea of the mixed finite element formulation is to introduce some additional variables into the global unknowns (Fortin and Brezzi, 1991). For the case where the pressure P and the volume variation θ into the global unknowns: firstly, the strain tensor is enhanced: $\tilde{\boldsymbol{\varepsilon}} = \boldsymbol{\varepsilon} + \boldsymbol{\varepsilon}'$ with $\boldsymbol{\varepsilon}' \sim \big(\theta - \mathrm{tr}(\boldsymbol{\varepsilon})\big)$. This new strain tensor is used in the constitutive law and so is involved in the Hu-Washizu mixed variational formulation. The weak equality between θ and $\mathrm{tr}(\boldsymbol{\varepsilon})$ is ensured by introducing a Lagrange multiplier P, it can be demonstrated that this P correspond to the pressure. More detail will be given in Chapter 2.

The two-field or three-field formulation is often used in the literature, as shown in Table 1.6 in the case of finite strains. This method is generally an efficient way to reduce the volumetric-locking problem. The computational convergence and stability can be ensured when the interpolation order (linear, quadratic, etc.) of the different unknowns satisfies the LBB condition.

Table 1.6. Mixed finite element formulation in finite strains

Reference	Unknowns
(Cervera et al., 2010)	$(\underline{u}, \boldsymbol{\sigma})$
(Brink and Stein, 1996; Sussman and Bathe, 1987)	$(\underline{u}, P)$
(Al Akhrass et al., 2014; Brünig, 1999; Taylor, 2000; Zhang et al., 2018)	$(\underline{u}, P, \theta)$
(Kasper and Taylor, 2000a, 2000b)	$(\underline{u}, \nabla\boldsymbol{\varepsilon}, \boldsymbol{\sigma})$

Hybrid High-Order method

Hybrid High-Order methods are initially introduced in (Di Pietro and Ern, 2015) for linear elasticity problems and in (Di Pietro et al., 2014) for diffusion problems. In these methods, a finite element is split into two parts: faces (element boundary, so line segments in 2D and surfaces in 3D) and cell (element except faces). The concept of the nodal unknowns (i.e., the displacement $\underline{u}$) used in classical finite element formulation disappears, instead, face-based unknowns $\underline{u}_1$ and cell-based unknowns $\underline{u}_2$ are introduced. The displacement field can be discontinuous between the faces and the cell. The idea of this method is to enhance the strain operator $\underline{\boldsymbol{B}}$ by an additional term $\underline{\boldsymbol{B}}'$: $\widetilde{\underline{\boldsymbol{B}}}(\underline{u}_1, \underline{u}_2) = \underline{\boldsymbol{B}}(\underline{u}_1) + \underline{\boldsymbol{B}}'(\underline{u}_1 - \underline{u}_2)$ where $\underline{\boldsymbol{B}}$ is for the cell and $\underline{\boldsymbol{B}}'$ is for the faces. Moreover, the consistency between the local face unknowns and the cell unknowns is weakly enforced by a penalty term. Finally, the cell unknowns can be locally eliminated using a static condensation technique to reduce significantly the computing size since only face unknowns are involved in the formulation. Thanks to the discontinuity of the displacement field between the faces and the cell, the material point is not rigid anymore, volumetric-locking cannot not appear (Abbas et al., 2019a, 2019b, 2018).

There are several attractive points for this method, for example, the construction is dimension-independent and general meshes (including non-conforming meshes) are supported. One of challenge of this method is related to the effort which should be made for the numerical implementation in an existing finite element software since the classical displacement-based finite element formulation is no longer suitable. Besides, even if these methods are already used for elastic-plastic (Abbas et al., 2019a) and hyper-elastic materials (Abbas et al., 2018) in the framework of finite strains, its efficiency and the robustness on the treatment of volumetric-locking should be further investigated in some more complex situations.

Choice of the locking-free model

As seen in the previous part, various methods have been proposed to overcome volumetric-locking problem. All these methods can reduce or solve volumetric-locking. However, the reduced integration method sometimes leads to a singular stiffness matrix and introduces zero-energy modes. The selective integration cannot be used with the GTN law since the hydrostatic and deviatoric parts of the constitutive relation cannot be separated. The EAS method and the mixed element method are all derived from the variational principle, but the former can still lead to zero-energy mode and the latter is efficient only if when the interpolation order for each unknown is well chosen. The hybrid high-order method is attractive on the long term but in fact complex in terms of numerical implementation. Its efficiency and robustness should be further checked in some more complex situations (for example, the coupling with damage laws).

Each method has its own drawbacks. In this work, the mixed element formulation will be used to treat volumetric-locking since the robustness of this method has already been demonstrated in the PhD works of (Zhang, 2016) in ductile damage cases. In the work of (Zhang, 2016), the three-field elements ($\underline{u}, P, \theta$) in which $\underline{u}$ is interpolated in a quadratic manner while (P,θ) are interpolated in a linear manner, have been used. However, it is stated in (Zhang, 2016) that the oscillation of the plasticity occurs for a simple tensile test with axisymmetric modeling when the element P_2 P_1 P_1 (P_2 for quadratic interpolation and P_1 for linear interpolation) is used, as shown in Figure Figure 1.7. A solution of this problem will be given in Chapter 2.

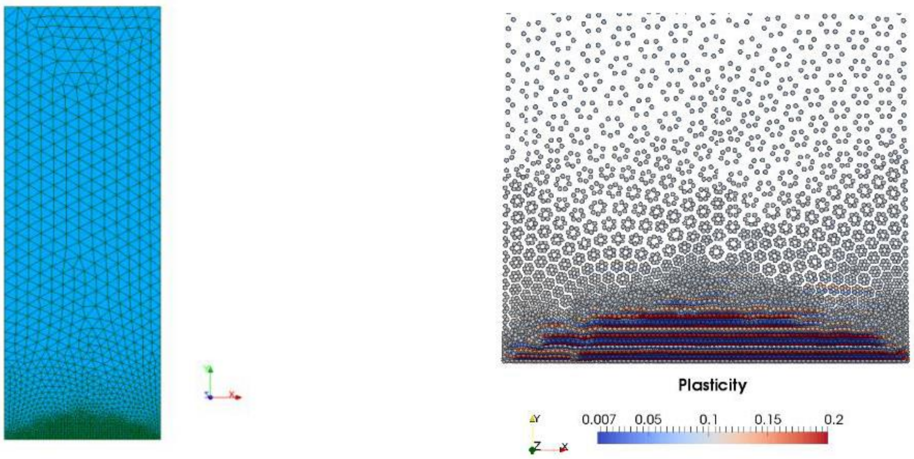

Figure 1.7. (a) Mesh (b) localization band of the plasticity with P_2 P_1 P_1 finite element. (Zhang, 2016)

1.3.3 Adaptive mesh refinement

It is well known that the accuracy of finite element analysis is directly related to the finite element mesh: The discretized solution will approach the continuum solution as the mesh is refined. Early in the analysis process, it makes sense to start with a coarse mesh which can be used as a rough check on applied loads and constraints. After that, the process of mesh refinement begins to get accurate solutions. When it comes to mesh refinement, there is a suite of techniques such as decrease of the element size or increase of the element order. The easiest and commonly used strategy is to globally or locally reduce the element size during mesh generation. Global decrease of the element size is simple to realize but may leads to excessive mesh refinement in regions that are of less interest. Local decrease of the element size is attractive but needs to know in advance the preferential mesh refinement zone, otherwise global refinement is required. This is typically problematic when it comes to industrial three-dimensional simulations where the zone of interest remains unknown. If the entire structure is discretized with fine elements, the required computational complexity[3] (for example time complexity, space complexity) would be very large. To solve this problem, global/local adaptive mesh refinement is often used. The algorithm of adaptive mesh refinement generally includes three main steps: remeshing, field transfer and balance (recovery). In this subsection, these three steps will briefly be reviewed.

---

[3] In computer science, the computational complexity, or simply complexity of an algorithm is the amount of resources required for running it. The computational complexity of a problem is the minimum of the complexities of all possible algorithms for this problem (including the unknown algorithms). The time complexity is the computational complexity that describes the amount of time it takes to run an algorithm.

Remeshing

Adaptive mesh refinement uses an error estimation strategy to determine the point where the local error is largest (see ((Feld-Payet, 2010)) for different options for error indicator). If this error exceeds a given value, the finite element software uses the information to generate a new mesh. This strategy is often regarded as global criterion for the onset of remeshing since the error is computed in the whole structure. Some additional local criteria can be defined, as described for example in (Ladevèze and Pelle, 2001; Oñate and Castro, 1991). Remeshing procedures start once the global and local criteria are met. There are mainly three types of adaptive techniques: *r-method, h-method and p-method*.

The *r-adaptive finite element method* was originally proposed in (Carroll and Barker, 1973; Turcke and McNeice, 1974), which consists in maintaining mesh topology (position and number of nodes, connectivity, etc.) and interpolation types, and relocating the mesh nodes to concentrate them in the zone of interest. The advantage of this method is that the mesh changes continuously. However, it is clear that this method is computationally expensive since the mesh redistribution procedure normally requires to solve a large number of equations in which node coordinates are also unknown variables.

Different from the *r-adaptive finite element method*, the *h-adaptive finite element method* modifies mesh topology. The idea is to subdivide some finite elements into elements of the same type in the zone of interest. One example of the *h-method* is shown in Figure 1.8. In this example, in order to ensure the continuity of the displacement, some special treatment on disconnected nodes (for example the node A in Figure 1.8) or some local mesh modification should be done.

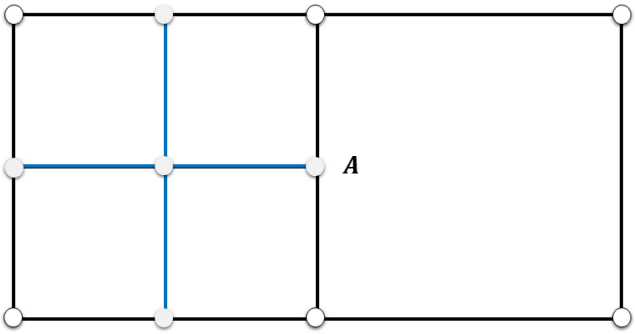

Figure 1.8. Subdivision of a finite element

The *p-adaptive finite element method* is focus on the polynomial order p of the shape functions used in finite element method. It converges exponentially if the exact solution is smooth and converges faster than a uniform refinement with constant polynomial degree (Rank, 1989). This adaptive method is not often used as on the one hand, most commercial finite element software only possesses finite elements with $p \leq 2$, and on the other hand, it is difficult to predict the value of p so as to ensure, at the same time, the accuracy of the solutions and the reasonableness of time complexity.

The combination of the *h-* and *p-adaptive finite element methods* is called the *hp-adaptive finite element method*. It converges exponentially even in the presence of singularities in the exact solution (Rank, 1989). But the drawbacks to the *p-method* still exist.

Field transfer

In this step, the displacement, the strains, the stresses and the internal variables are transferred from the old mesh to the new mesh. The transfer procedure is not easy since a transfer operator should preserve consistency with the constitutive equations, satisfy equilibrium, minimize or avoid numerical diffusion (for example, damage band should not be modified after adaptive refinement) and ensure compatibility with the boundary conditions (J. Mediavilla et al., 2006c; Perić et al., 1996). Generally, it is difficult to respect all constraints in the transfer step. The most important point is to reduce the numerical diffusion (Feld-Payet, 2010). Besides, we can transfer all state variables or just a reduced but fully representative set of state variables from which the remaining variables can be derived using the existent relations among different variables (J. Mediavilla et al., 2006c).

There exist two different transfer operators, one is for variables stored at nodes and the other for variables stored at integration points.

Transfer operator for nodal state variables

For the transfer of state variables at nodes, it is realized by means of interpolation. For each node in new mesh, firstly, we geometrically determine the element of the old mesh in which it locates, then we compute the new variables using the old shape functions (see Figure 1.9).

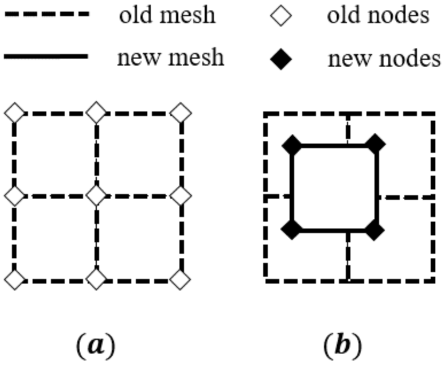

Figure 1.9. (a) Old mesh with nodes; (b) New mesh with new nodes

Transfer operator for state variables at integration points

For the transfer of state variables at integration points, several techniques exist, two of them are presented here.

- Direct transfer: the transfer is realized directly from the old to the new integration points with constant values (for instance the value of the closest old integration point) or by means of interpolation/extrapolation (Espinosa et al., 1998; Ortiz and Quigley Iv, 1991) (see Figure 1.10).

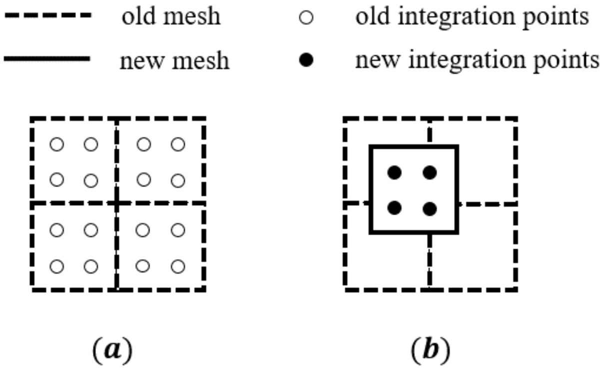

Figure 1.10. (a) Old mesh with old integration points; (b) New mesh with new integration points

- Indirect transfer: Firstly, the state variables are transferred from the old integration points to the old nodes by extrapolation/nodal averaging (see Figure 1.11(a)→(b)). This sub-step is the source of numerical diffusion (see for instance (Hinton and Campbell, 1974; Loubignac et al., 1977) for the improvement). Then, the transfer of variables at nodes should be done (see Figure 1.11(b)→(c)). Finally the state variables at new integration points can be computed using the shape functions of the new mesh (see Figure 1.11(c)→(d)). Compared to the direct transfer, the indirect transfer leads to more numerical diffusion (Lee and Bathe, 1994), but less inconsistencies (PavanaChand and KrishnaKumar, 1998).

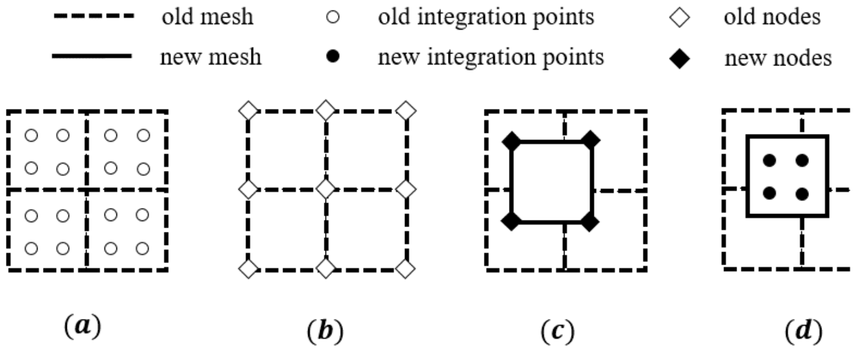

Figure 1.11. (a) Old mesh with old integration points; (b) Old mesh with old nodes; (c) New mesh with new nodes; (d) New mesh with new integration points

Restoration of equilibrium

After the transfer step, the equilibrium equations are generally no more satisfied and the new state variables may be incompatible with the traction boundary conditions. So it is necessary to restore equilibrium before proceeding to a new load increment to preserve numerical stability.

In the work of (J. Mediavilla et al., 2006c), the equilibrium step is realized by doing some iterations under unchanged external loads and boundary conditions. To ensure convergence, it is assumed that all deformation in the balancing-step is elastic since no physical deformation process takes place in this step.

Another way to ensure the equilibrium is to subdivide the next time increment Δt into $\alpha \Delta t$ and $(1-\alpha)\Delta t$ with α being close to 0 and some iterations under normal external loading are made during $\alpha \Delta t$ (Boroomand and Zienkiewicz, 1999). The new state variables at the end of the transfer step are regarded as the initial conditions

1.3.4 Material failure

As shown in (Zhang, 2016), highly distorted elements are observed in the case of simulations of large crack extensions. This may strongly affect the computational convergence. In this subsection, we will focus on the existing literature methods which are used to deal with the distorted elements.

Element deletion

The element deletion method is also called “kill element”. This method consists in removing a finite element when the necessary condition for element deletion is met during the simulation. The necessary condition can be based on the damage value (Li et al., 2011), the stresses value (Phadnis et al., 2013), the strains value (Ko et al., 1997), etc. As shown in Figure 1.12, the numerical algorithm includes the following steps: (1) Element deletion: Elements are removed when the defined criterion is reached. The parameters describing the element connectivity definition, the strains, the stresses and the internal variables such as the damage value are removed. (2) Treatment of the isolated node: after element deletion, some nodes may be isolated and disconnected from the neighboring elements. So it is necessary to also remove such nodes. (3) Rearrangement of the boundary condition: The element deletion can lead to the generation of some new boundary. Therefore, the boundary conditions should be reset accordingly. Otherwise, a re-meshing technique may be applied after removing the broken elements to have a smooth boundary.

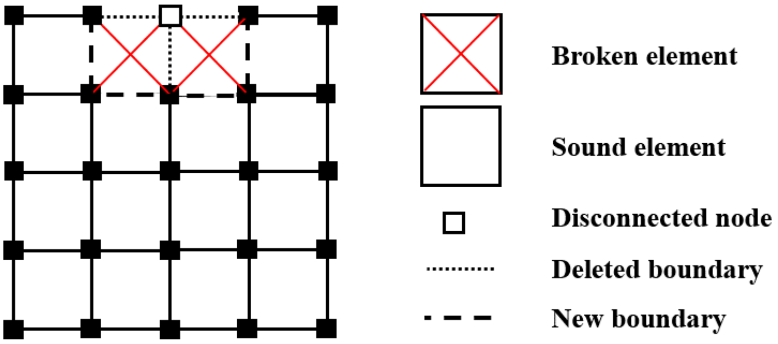

Figure 1.12. Schematic representation of element-deletion method

With this method, the highly distorted element can be eliminated, stress concentration near crack surface (if discretized crack is modeling) can be avoided which prevents over-estimation of stress and strain value (Lee et al., 2009). However, in the context of ductile damage modeling, this method is often used with local damage models such as (Li et al., 2011; Lian et al., 2015, 2013). When it comes to nonlocal models, it is only used in few cases such as (Seupel et al., 2018) in the framework of implicit gradient nonlocal modeling. In (Seupel et al., 2018), the natural boundary conditions for the non-local field equation is directly satisfied on the new element boundary created by element deletion, which may generate a jump-like contribution due to the instantaneous change of the nonlocal flow and thus lead to numerical problems (Hütter et al., 2013). A redistribution of the nonlocal variables are done in spite of some other questionable effects (Seupel et al., 2018). Note that physical inaccuracy may be induced by resetting of the boundary conditions. In addition, it is pointed out in (Seupel et al., 2018) that small increments are needed when element-deletion starts even for a simple crack growth simulations. The same problems may occur in the framework of enhanced energetic nonlocal modeling when “element-deletion” technique is used. Except the special issues concerning the nonlocal variables, the general issue regarding loss of mass during element deletion may also lead to physical inaccuracy in dynamic simulations. Therefore, the modeling and the simulation of fracture with element deletion should be performed and interpreted with caution.

Direct operations on state variables

In the literature, some authors just do some manipulations on state variables of the broken elements, instead of removing these elements. For example, in the work of (Huespe et al., 2012), the damage variable and the plastic strain in broken elements remain unchanged such that no more deformation takes place in these elements. The drawback to this method is that the residual stresses increase. In the work of (Zhang, 2016), the stresses and the rate of the hardening variable are set to be zero in broken points and an artificial tangent stiffness $\lambda\mathbb{E}(\lambda \approx 10^{-5}$ and $\mathbb{E}$ the Hooke matrix) is given to the broken point. However, a very important deformation of the broken element is still observed which may be the source of numerical non-convergence. More integration points in an element can then be added, but it can just postpone the element distortion.

Remeshing technique

A remeshing strategy can be applied to avoid large element distortion, as done in (J. Mediavilla et al., 2006c). For the detail of adaptive mesh refinement, one can refer to the Section 1.3.3. The idea is to replace the distorted element by some new undistorted elements with remeshing. Particularly, the element-deletion method can be used in combination with the remeshing technique so as to obtain a smooth boundary. Remeshing technique can completely avoid element distortion. However, it may become another source of computational convergence issues (see Section 1.3.3 for the numerical problems that can be raised in remeshing procedures). Besides, the physical inaccuracy caused by remeshing, in particular at the transfer step of remeshing, should be properly treated.

1.4 Proposed model

Damage model (Section 1.1)

The micromechanical based constitutive models for ductile fracture are briefly introduced at the beginning of this chapter. For the sake of simplicity, in this work, we focus on the isotropic ductile damage model initially proposed in (Gurson, 1977) and improved by (Needleman and Tvergaard, 1984; Tvergaard and Needleman, 1984), referred to as the GTN model. This model takes into account the coupling between damage and plasticity.

Nonlocal model (Section 1.2)

One drawback to the GTN model is that damage at the continuum level results in strain softening leading to strain localization. In such cases, the macroscopic length scale becomes comparable to the microscopic length scale, which is not in accordance with the homogenization theory. Thus, it is necessary to introduce nonlocal effects in the modeling. The regularized methods can be applied either to the equilibrium equation (Micromorphic approach, plasticity/damage gradient approach) or the constitutive laws (integral nonlocal approach, implicit gradient approach). As discussed in Section 1.2.6, the GEE approach will be used in this work for its sound mathematical and numerical properties. The gradient of hardening variable κ will be introduced to simultaneously control (1) the plastic localization which may result from geometrical considerations (necking) and (2) the damage localization which results from strain softening.

Finite element modeling of ductile failure (Section 1.3)

The problem of mesh-sensitivity that stems from softening disappears with the use of a gradient model provided that the mesh is sufficiently refined.

Another numerical problem is volumetric locking which results in the oscillations of the stress filed. Several methods such as reduced/selective integration, B-bar/F-bar, EAS, HHO, Mixed element methods can be applied to handle this problem. Each method has its own drawbacks, as shown in Section 1.3.2. In this work, the mixed element formulation will be used to treat the volumetric-locking problem since the robustness of this method has already been demonstrated in the PhD works of (Zhang, 2016) in ductile damage case. One problem concerning the localization of plasticity is addressed in (Zhang, 2016), an improvement concerning this problem will be made in this work.

Besides, highly distorted elements can appear during the crack growth simulation with damage model. This problem is typically related to the zero stiffness in the broken elements. The most direct solution is to eliminate these elements with element-deletion method. But in addition to possible physical inaccuracy induced by this method, the difficulties on the treatment of nonlocal variables is another reason for which the element-deletion is not used in this work. Compared to the element-deletion method, the remeshing technique is more attractive but efforts should be made for numerical implementation. In addition, the numerical problems (numerical diffusion, the possible computational non-convergence during the balancing-step, etc) induced by the remeshing technique are not negligible and thus should be properly treated. As for other solutions (artificial stiffness, zero deformation in broken elements), they are rather simple but not really effective. In this work, a viscoelastic regularization is proposed in Chapter 3 to avoid excessively distorted elements. We will see that an additional stiffness and a characteristic time will be introduced in this model: the stiffness should preclude distortion, resulting in a small viscous stress which vanishes with time. The efficiency of this strategy will be illustrated in Chapter 3.

Finally, the adaptive mesh refinement will not be used since in most simulations involved in this work, the zone of interest is known a priori (except for ATLAS pipe as introduced in Chapter 5). An initial local refinement is sufficient. When done correctly, the savings on time and resources can be significant.

Proposed model

In conclusion, in this work, the following model will be used:

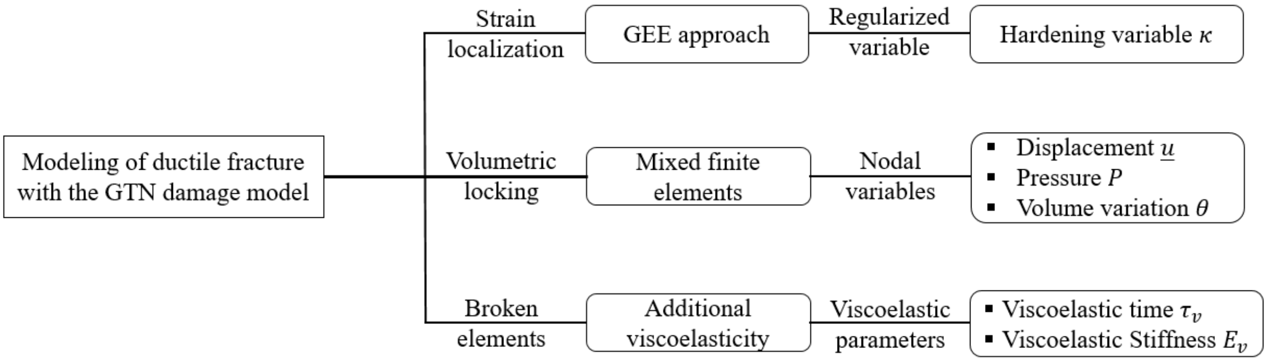

2 A nonlocal GTN model

> *天才是百分之一的天分加百分之九十九的努力。*
>
> *Le génie est fait d'un pourcent d'inspiration et de quatre-vingt-dix-neuf pourcent de transpiration.*
>
> *Genius is one percent inspiration, ninety-nine percent perspiration.*
>
> 托马斯 阿尔瓦 爱迪生 Thomas Alva Edison

Résumé

Dans ce chapitre, le modèle d'endommagement de GTN exprimé en grandes déformations est présenté. Pour résoudre le problème de la localisation de déformation, on adopte un modèle non local qui permet de tenir compte de l'interaction entre des points matériels. Plus précisément, une formulation non-locale basée sur le gradient de la variable d'écrouissage est adoptée. Ce modèle est censé résoudre le problème de la localisation de déformation (un problème physique). On espère qu'il peut améliorer le problème (numérique) de la dépendance au maillage observé dans la simulation des éléments finis. Sur le plan numérique, cette formulation conduit à des gradients spatiaux des variables internes dans la loi de comportement : la méthode de décomposition-coordination est utilisée afin de traiter les termes concernés. Un autre problème numérique à traiter dans ce travail est le verrouillage volumique provenant de la quais-incompressibilité plastique, une formulation variationnelle de type Hu-Washiwu est mise en œuvre. Un terme d'augmentation supplémentaire est introduit dans le Lagrangian correspondant afin d'assurer la coercivité. Finalement, un nouvel élément fini à 5-champ est déduit de la formulation variationnelle régularisée. Des résultats de cas-tests employant le modèle non-local de GTN sont présentés à la fin du chapitre.

In this chapter, the non-local GTN model originally proposed in (Zhang et al., 2018) and improved in our work is recalled. This model brings some answers to the problems of spurious localization. Strain localization is controlled by introducing the gradient of the hardening variable into the Helmholtz free energy (formulation of gradient plasticity). On a numerical ground, this results in spatial gradients of state variables within the constitutive relations: a decomposition-coordination techniques (Fortin and Glowinski, 1983) is used to treat the corresponding term. According to (Zhang et al., 2018), this nonlocal model can effectively reduce spurious mesh-sensitivity in finite element simulations. Another numerical problem to be solved is volumetric locking resulting from plastic quasi-incompressibility (prior to damage), the Hu-Washizu mixed variational principle (Hu, 1955, 1954) is put in practice. An additional augmentation term is introduced into the corresponding Lagrangian in this work in order to ensure coercivity and thus avoid spurious localization of plasticity. Finally, a new 5-field finite element is derived from the non-local locking-free variational formulation. At the end of this chapter, some simple test-cases are provided in order to check the numerical implementation.

2.1 Finite strain modeling

In the work of (Zhang et al., 2018), the GTN model is cast into the logarithmic finite strain formulation proposed by (Miehe et al., 2002; Miehe and Lambrecht, 2001). In this section, this formulation will be described brieftly.

2.1.1 Strain and stress definitions

The logarithmic strain tensor $\boldsymbol{E}$ is defined as:

$$\boldsymbol{E} = \frac{1}{2}\ln(\boldsymbol{F}^T.\boldsymbol{F}) = \frac{1}{2}\ln(\boldsymbol{C}) \tag{2.1}$$

where $\boldsymbol{F}$ is the deformation gradient tensor and $\boldsymbol{C} = \boldsymbol{F}^T.\boldsymbol{F}$ is the Cauchy-Green strain tensor.

The Stress tensor $\boldsymbol{T}$ is defined as the work-conjugated with respect to $\boldsymbol{E}$:

$$\boldsymbol{T}(t):\dot{\boldsymbol{E}}(t) = \boldsymbol{S}(t):\frac{1}{2}\dot{\boldsymbol{C}}(t), \forall\dot{\boldsymbol{F}} \tag{2.2}$$

where $\boldsymbol{S}$ is the second Piola-Kirchhoff stress tensor.

2.1.2 Plasticity

Following (Miehe et al., 2002), the logarithmic strain tensor $\boldsymbol{E}$ is assumed to be addictive:

$$\boldsymbol{E} = \boldsymbol{E}^{\boldsymbol{e}} + \boldsymbol{E}^{\boldsymbol{p}} \tag{2.3}$$

where $\boldsymbol{E}^{\boldsymbol{e}}$ and $\boldsymbol{E}^{\boldsymbol{p}}$ are respectively the elastic and plastic parts of the strain tensor $\boldsymbol{E}$. Under the assumption of pure isotropic hardening, a single scalar variable denoted κ describes the hardening state. The material state is then described by the current strain $\boldsymbol{E}$, the hardening variable κ and the plastic strain $\boldsymbol{E}^{\boldsymbol{p}}$.

As shown in (Miehe et al., 2002; Miehe and Lambrecht, 2001), the additive decomposition of $\boldsymbol{E}$ is particularly attractive since the results obtained by this decomposition are close to those obtained using Lee's multiplicative decomposition of $\boldsymbol{F}$ (Lee, 1981), while leading to the same implementation as in the framework of small strains.

Similar to small strains, we have:

$$\begin{cases} \boldsymbol{T} = \mathbb{E}:\boldsymbol{E^e} \\ \dot{\boldsymbol{E}}^{\boldsymbol{p}} = \dot{\kappa}\dfrac{\partial F}{\partial \boldsymbol{T}}(\boldsymbol{T}, A) \\ F \leq 0,\ \ \dot{\kappa} \geq 0,\ \ \dot{\kappa}F = 0 \end{cases} \tag{2.4}$$

where $\mathbb{E}$ is the Hooke matrix, F is the yield function and $A = A(\kappa)$ the hardening function.

Remark 1:

One can define the tangent operator $\mathbb{J}$ as:

$$\dot{\boldsymbol{T}} = \mathbb{J}:\dot{\boldsymbol{E}} \tag{2.5}$$

Remark 2:

The second Piola-Kirchhoff stress tensor $\boldsymbol{S}$ is obtained from Equation (2.2):

$$\boldsymbol{S} = \boldsymbol{T}:\left(2\frac{\partial \boldsymbol{E}}{\partial \boldsymbol{C}}\right) \tag{2.6}$$

The Cauchy stress can be obtained using:

$$\boldsymbol{\sigma} = \frac{1}{J}\boldsymbol{F}.\boldsymbol{S}.\boldsymbol{F^T} \tag{2.7}$$

where $J = \det \boldsymbol{F}$ that measures the volume variation. Note that both $\boldsymbol{S}$ and $\boldsymbol{\sigma}$ are symmetric.

The standard tangent modulus $\mathbb{J}_s$ which satisfies $\dot{\boldsymbol{S}} = \mathbb{J}_s: \dot{\boldsymbol{C}}/2$ is (Miehe et al., 2002):

$$\mathbb{J}_s = \left(2\frac{\partial \boldsymbol{E}}{\partial \boldsymbol{C}}\right)^{\mathrm{T}}:\mathbb{J}:\left(2\frac{\partial \boldsymbol{E}}{\partial \boldsymbol{C}}\right) + \boldsymbol{T}:\left(4\frac{\partial^2 \boldsymbol{E}}{\partial \boldsymbol{C}^2}\right) \tag{2.8}$$

Here $\partial^2\boldsymbol{E}/\partial^2\boldsymbol{C}$ is a sixth order tensor. The expressions of $\partial\boldsymbol{E}/\partial\boldsymbol{C}$ and $\partial^2\boldsymbol{E}/\partial\boldsymbol{C}^2$ can be found in (Code_Aster Documentation *R5.03.24*, www.code-aster.org).

2.2 Nonlocal modification

Damage usually results in strain-softening, i.e. the drop of the stress carrying capability with increasing damage. At the structure scale where constitutive behavior is combined with mechanical equilibrium, strain-softening is responsible for the spatial localization of the strain field, the plastic strain field and the damage. The scale of the macroscopic field variations becomes comparable to the microstructure scale (micro-void spacing, for instance). This is in contradiction to the length scale separation assumption which underlies the derivation of local constitutive relations, i.e. models that only depend on the point-wise state variables (strain, damage, plasticity, hardening, etc.). Therefore nonlocal constitutive relations are required as a consequence of overlapping micro and macro length scales. They account for a spatial coupling of neighboring material points: the material state is no more characterized by point-wise state variables and an interaction distance (also named internal length) appears.

In the work of (Zhang et al., 2018), in order to take into account the high gradients of the macroscopic fields which result from strain localization, a non-local constitutive relation based on the introduction of the gradient of an internal variable into the global Helmholtz free energy density is proposed. In this work, the gradient of the hardening variable κ is introduced into the global Helmholtz free energy density $\mathcal{F}$. The phenomenological choice of κ is led by the fact that this variable reflects localization of both plasticity and plasticity-induced damage:

$$\mathcal{F}(\boldsymbol{E},\boldsymbol{E^p},\kappa) \;=\; \mathcal{F}_\ell(\boldsymbol{E}(\underline{u}),\boldsymbol{E^p},\kappa) \;+\int_{\Omega_0}\left(\frac{1}{2}c\boldsymbol{\nabla}\kappa.\boldsymbol{\nabla}\kappa\right)d\Omega_0 \tag{2.9}$$

where $\mathcal{F}_l$ is a point-wise contribution to the Helmholtz free energy, $\underline{u}$ is the displacement, Ω_0 is the body domain in the initial configuration and c is a parameter which weights the non-local interactions among neighboring material points. Dimensional considerations show that a non-local length scale can be introduced as:

$$l_{nl} \;=\sqrt{\frac{c}{\sigma_{ref}}} \tag{2.10}$$

where σ_{ref} is a reference stress which can be, for example, the initial yield stress σ_0 or the mean stress $\sigma_m = (\sigma_0+\sigma_{UTS})/2$ with σ_{UTS} the ultimate tensile strength measured in a tensile test.

In Equation (2.9), the free energy contribution $\mathcal{F}_l$ is divided into an elastic part and a plastic (hardening) part:

$$\mathcal{F}_\ell(\boldsymbol{E},\boldsymbol{E^p},\kappa) = \int_{\Omega_0}\big(\phi^e(\boldsymbol{E^e}) + \phi^p(\kappa)\big)d\Omega_0 \tag{2.11}$$

where ϕ^e and ϕ^p are the elastic and plastic parts of the local Helmholtz free energy density:

$$\begin{cases}\phi^e(\boldsymbol{E^e}) \equiv \dfrac{1}{2}\boldsymbol{E^e}\colon\mathbb{E}\colon\boldsymbol{E^e}\\ \phi^p(\kappa) \equiv \displaystyle\int_0^\kappa(\bar{\sigma}(s)-\sigma_0)ds\end{cases} \tag{2.12}$$

and $\bar{\sigma}$ is the flow stress of the matrix material. The latter is a function of κ. In this work, two different form of $\bar{\sigma}$ will be used:

- Unbounded power law:

$$\bar{\sigma}(\kappa) = \sigma_0 \left(1 + \frac{\kappa}{\kappa_0}\right)^n \tag{2.13}$$

- Bounded exponential law:

$$\bar{\sigma}(\kappa) = \sigma_0 + r_1(1 - e^{-g_1\kappa}) + r_2(1 - e^{-g_2\kappa}) \tag{2.14}$$

where $\kappa_0, r_1, r_2, g_1, g_2$ are additional material constants, n is the hardening exponent with $n > 0$. The first form of $\bar{\sigma}$ is often used in the literature and it is unbounded, while the second form bounds the stress when $\kappa \to \infty$.

In the following, we assume that: (1) The evolution is quasi-static and isothermal; (2) There is no viscosity; (3) The strain is involved in a pointwise way only; (4) The forces derive from a potential $W_e(\underline{u})$. Under these assumptions, the variation of $\mathcal{F}$ with respect to $\underline{u}$ provides the equilibrium equations (in a variational form) for any kinematically admissible displacement field:

$$\delta\mathcal{F} = \int_{\Omega_0} (\boldsymbol{T}\colon \delta\mathbf{E}) d\Omega_0 = \delta\mathcal{W}_\mathrm{e}(\underline{u}) \tag{2.15}$$

and the stress definition thanks to Equation (2.11):

$$\boldsymbol{T} = \frac{\partial\phi^\mathrm{e}}{\partial\mathbf{E}} = \mathbb{E}\colon \boldsymbol{E^e} \tag{2.16}$$

Moreover, the dissipation is provided by the variation of $\mathcal{F}$ with respect to $(\dot{\boldsymbol{E}}^{p}, \dot{\kappa})$ and should remain positive:

$$\mathcal{D} =< \delta_{\boldsymbol{E}^p}\mathcal{F} \big| \dot{\boldsymbol{E}}^{\boldsymbol{p}} > + < \delta_\kappa\mathcal{F} \big| \dot{\kappa} > \tag{2.17}$$

Combing Equations (2.9)(2.11)(2.17) yields:

$$\mathcal{D} = \int_{\Omega_0} \left(\boldsymbol{T}\colon \dot{\boldsymbol{E}}^p + A_{nl}\dot{\kappa}\right) d\Omega_0 + \int_{\partial\Omega_0} \left(-c\boldsymbol{\nabla}\kappa.\underline{n}\right)\dot{\kappa} dS \tag{2.18}$$

where the stress tensor $\boldsymbol{T}$ is the driving force associated to $\boldsymbol{E^p}$ and A_{nl} is the driving force associated to κ:

$$\begin{cases} \boldsymbol{T} = -\dfrac{\partial\phi^\mathrm{e}}{\partial\boldsymbol{E^p}} = \mathbb{E}\colon (\boldsymbol{E} - \boldsymbol{E^p}) \\ A_{nl} = -\dfrac{\partial\phi^p}{\partial\kappa}(\kappa) + \mathrm{div}(c\boldsymbol{\nabla}\kappa) = \sigma_0 - \bar{\sigma}(\kappa) + \mathrm{div}(c\boldsymbol{\nabla}\kappa) \end{cases} \tag{2.19}$$

In addition, it is assumed that no dissipation stems from the boundary, which leads to the following boundary condition:

$$c\boldsymbol{\nabla}\kappa.\underline{n} = 0 \quad \text{on } \partial\Omega_0 \tag{2.20}$$

where $\underline{n}$ is the normal vector to the surface $\partial\Omega_0$.

Finally, the positivity of the dissipation is written as:

$$\mathcal{D} = \int_{\Omega_0} \left(\boldsymbol{T}\colon \dot{\boldsymbol{E}}^p + A_{nl}\dot{\kappa}\right) d\Omega_0 \geq 0 \tag{2.21}$$

2.3 Numerical formulation: relaxed variational formulation

On a numerical ground, the former non-local formulation leads to spatial gradients of state variables in the constitutive law. Moreover, in quasi-incompressible situations, volumetric locking may appear. The numerical approach should deal with both difficulties. Following (Lorentz et al., 2008; Taylor, 2000), we introduce a relaxed formulation which is equivalent to the initial problem before spatial discretization by finite elements.

More precisely, a decomposition-coordination technique proposed by (Fortin and Glowinski, 1983) is used to treat the non-locality aspect. The hardening variable κ is duplicated: a first instance (named a) is used at the (global) scale of the structure while a second instance (still named κ) is used at the (local) constitutive law level. As a and κ reflect the same field, they should be equal. A Lagrange multiplier l is introduced to weakly enforce this equality, the corresponding augmented Lagrangian $\mathcal{L}_{nl}$ is:

$$\mathcal{L}_{n\ell}(\boldsymbol{E},\boldsymbol{E^p},\kappa,a,l) \; = \; \mathcal{F}_{\ell}(\boldsymbol{E},\boldsymbol{E^p},\kappa) \; + \int_{\Omega_0}\left(\frac{1}{2}c\boldsymbol{\nabla}a.\boldsymbol{\nabla}a+l(a-\kappa)+\frac{1}{2}r_{nl}(a-\kappa)^2\right)d\Omega_0 \qquad (2.22)$$

The augmentation term $r_{nl}(a-\kappa)^2$ with r_{nl} a penalty parameter is introduced to provide an additional coercivity.

Regarding volumetric locking, the ideas of the Hu-Washizu mixed variational principle (Hu, 1955, 1954) are put in practice. The volumetric strain $\mathrm{tr}(\boldsymbol{E}) = \ln(J)$ with $J = \det\boldsymbol{F}$ is duplicated: a first instance (still name $J(\underline{u})$ is used at the global level while a second instance name θ is used at the constitutive law level. Since $\ln(J)$ and θ reflect the same field, they should be equal. A Lagrange multiplier P is introduced to weakly enforce the equality, the corresponding augmented Lagrangian $\mathcal{L}$ is:

$$\mathcal{L}(\boldsymbol{E},\boldsymbol{E^p},\kappa,a,l,P,\theta) \; = \; \mathcal{L}_{\mathrm{n}\ell}(\overline{\boldsymbol{E}},\boldsymbol{E^p},\kappa,a,l) \; + \int_{\Omega_0}\left(P(\ln(J)-\theta)+\frac{1}{2}r_{inco}(\ln(J)-\theta)^2\right)d\Omega_0 \qquad (2.23)$$

where $\overline{\boldsymbol{E}}$ is the relaxed strain tensor defined as:

$$\overline{\boldsymbol{E}} \; = \; \boldsymbol{E} \; + \frac{1}{3}(\theta-\mathrm{tr}(\boldsymbol{E}))\boldsymbol{I} \qquad (2.24)$$

Compared to the Lagrangian in (Zhang et al., 2018), a new augmentation term $r_{inco}(\ln J-\theta)^2/2$ has been introduced, with r_{inco} a new penalty parameter. It brings an additional coercivity so as to avoid potential appearance of spurious plastic localization (one can refer to chapter 3 for some example of spurious plastic localization) and thus help the convergence of simulation.

As the Lagrangian $\mathcal{L}$ corresponds to a relaxed numerical version of the physical Helmholtz free energy $\mathcal{F}$, its variation is expected to be equal to that of $\mathcal{F}$ for any variation of its variables:

$$\delta\mathcal{L} = \delta\mathcal{F}, \qquad \forall\; \delta\underline{u}, \delta\boldsymbol{E^p}, \delta\kappa, \delta a, \delta l, \delta P, \delta\theta \qquad (2.25)$$

Concerning the variation with respect to $\underline{u}$, it results in the equilibrium variational equation:

$$\delta_{\underline{u}}\mathcal{L} \; = \int_{\Omega_0}\left(\widetilde{\boldsymbol{T}}:\delta\boldsymbol{E}\right)d\Omega_0 \; = \delta_{\underline{u}}\mathcal{F} \; = \; \delta\mathcal{W}_{\mathrm{e}} \qquad (2.26)$$

The expression of $\widetilde{\boldsymbol{T}}$ is

$$\widetilde{\boldsymbol{T}} = (\overline{\boldsymbol{T}})_D + P\boldsymbol{I} + r_{inco}(\mathrm{tr}(\boldsymbol{E})-\theta)\boldsymbol{I} \qquad (2.27)$$

where $\overline{\boldsymbol{T}}$ is the stress tensor used in the constitutive law:

$$\overline{\boldsymbol{T}} = \frac{\partial \phi^e}{\partial \boldsymbol{E}}(\overline{\boldsymbol{E}}, \boldsymbol{E^p}) \tag{2.28}$$

and $(\overline{\boldsymbol{T}})_D$ the deviatoric part of $\overline{\boldsymbol{T}}$.

The variations with respect to (a, l, P, θ) should be equal to zero as $\mathcal{F}$ is not a function of these four variables:

$$\begin{cases} \delta_a \mathcal{L} = \int_{\Omega_0} (c \boldsymbol{\nabla} a \boldsymbol{\nabla} \delta a + (l + r_{nl} a - r_{nl} \kappa) \delta a) d\Omega_0 = 0 \\ \delta_l \mathcal{L} = \int_{\Omega_0} \big((a - \kappa) \delta l\big) d\Omega_0 = 0 \\ \delta_P \mathcal{L} = \int_{\Omega_0} \big((\mathrm{tr}(\boldsymbol{E}) - \theta) \delta P\big) d\Omega_0 = 0 \\ \delta_\theta \mathcal{L} = \int_{\Omega_0} \left(\left(\frac{1}{3} \mathrm{tr}(\overline{\boldsymbol{T}}) - P - r_{inco} (\mathrm{tr}(\boldsymbol{E}) - \theta) \right) \delta\theta \right) d\Omega_0 = 0 \end{cases} \tag{2.29}$$

It can be observed that the initial and the relaxed formulations are equivalent at the continuum level since the variations of $\mathcal{L}$ with respect to (l, P) result in the following relations:$a = \kappa, \theta = \mathrm{tr}(E)$.

Finally, the variations with respect to $\boldsymbol{E^p}$ and to κ lead to the expression of the driving forces:

$$\begin{cases} \overline{\boldsymbol{T}} = \mathbb{E} : (\overline{\boldsymbol{E}} - \boldsymbol{E^p}) \\ \boldsymbol{A_{rlx}} = \sigma_0 - \bar{\sigma}(\kappa) + l + r(a - \kappa) \end{cases} \tag{2.30}$$

We can notice that the relaxed stress $\overline{\boldsymbol{T}}$ is now the driving force associated to the plastic strain. Moreover, compared to Equation (2.19), the divergence term of the driving force associated to κ disappears. As expected, A_{nl} is replaced by A_{rlx} in the constitutive law.

2.4 Finite element formulation

We have seen that the problems presented in Section 2.2 and Section 2.3 are equivalent at continuum level, but no more after spatial discretization. On the one hand, the variables $(\underline{u}, a, l, P, \theta)$ introduced in the relaxed variational formulation are discretized on the basis of Lagrange shape functions. It results in the nodal unknowns of the discretized problem. On the other hand, the stress and the internal variables (including κ) are sampled at the integration points. They are obtained by the integration of the constitutive law at the integration point level.

More precisely, the discretization of $(\underline{u}, a, l, P, \theta) \in (\mathbb{R}^{dim}, \mathbb{R}, \mathbb{R}, \mathbb{R}, \mathbb{R})$ reads:

$$\begin{cases} \underline{u}(\underline{x}) = \boldsymbol{N}^{\underline{u}}(\underline{x}).\underline{U} \\ a(\underline{x}) = N^a(\underline{x})A \\ l(\underline{x}) = N^l(\underline{x})L \\ P(\underline{x}) = N^P(\underline{x})P \\ \theta(\underline{x}) = N^\theta(\underline{x})\Theta \\ \boldsymbol{\nabla}\underline{\mathrm{u}}(\underline{x}) = \underline{\boldsymbol{B}}^{\underline{u}}(\underline{x}).\underline{U} \\ \boldsymbol{\nabla}a(\underline{x}) = \underline{B}^a(\underline{x}).\underline{A} \end{cases} \tag{2.31}$$

where $\boldsymbol{N}^{\underline{u}} \in \mathbb{R}^{dim} \times \mathbb{R}^{n\times dim}$, $N^a \in \mathbb{R}^n$, $N^l \in \mathbb{R}^n$, $N^P \in \mathbb{R}^n$, $N^\theta \in \mathbb{R}^n$, $\underline{\boldsymbol{B}}^{\underline{u}} \in \mathbb{R}^{dim} \times \mathbb{R}^{dim} \times \mathbb{R}^{n\times dim}$, $\underline{B}^a \in \mathbb{R}^{dim} \times \mathbb{R}^n$, $\underline{x} \in \mathbb{R}^{dim}$, $\underline{U} \in \mathbb{R}^{n\times dim}$, $A \in \mathbb{R}^n$, $L \in \mathbb{R}^n$, $P \in \mathbb{R}^n$, $\Theta \in \mathbb{R}^n$ with n the node numbers and dim the space dimension.

Like in the work of (Zhang et al., 2018), $\boldsymbol{N}^{\underline{u}}$ is piecewise quadratic while N^a, N^l, N^P, N^θ are piecewise linear. Consequently, the finite element associated with the five variables $(\underline{U}, A, L, P, \Theta)$ is a $P_2P_1P_1P_1P_1$-type element where P_1 stands for linear interpolation and P_2 stands for quadratic interpolation. Example of non-local locking-free elements with reduced integration (four integration points in each quadrilateral element and three integration points in each triangle element) are shown in Figure 2.1. The formulation for incompressibility treatment is directly based on the Taylor-Hood element, which is known to fulfil the LBB condition (Ern and Guermond, 2013). A linear interpolation for a is chosen to be consistent with the strain field obtained from a P_2 displacement field (Zhang et al., 2018).

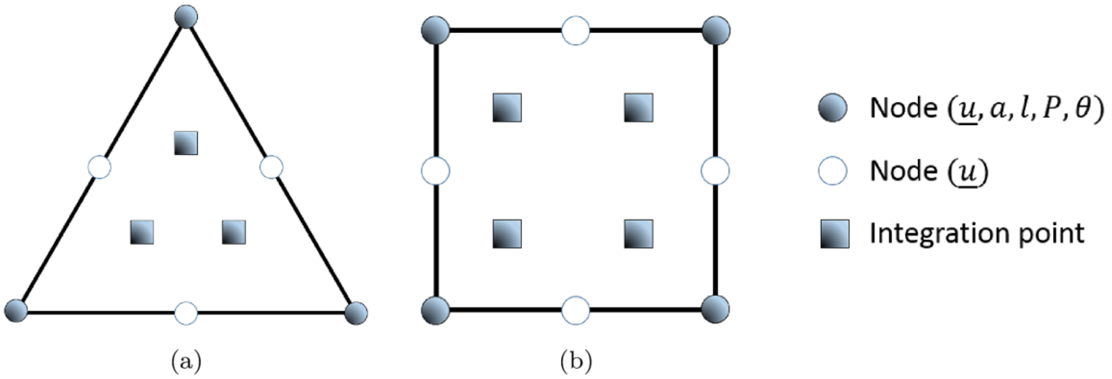

Figure 2.1. Examples of non-local locking-free finite elements with reduced integration: (a) triangle element (b) quadrilateral element

If we differentiate Equation (2.1), we have:

$$\delta\boldsymbol{E} = \frac{\partial \boldsymbol{E}}{\partial \boldsymbol{C}} : \delta\boldsymbol{C} = \mathbb{P} : \left(\boldsymbol{F}^{\mathrm{T}} : \delta\boldsymbol{F}\right) \quad \text{with} \quad \mathbb{P} = 2\frac{\partial \boldsymbol{E}}{\partial \boldsymbol{C}}(\boldsymbol{C}) \tag{2.32}$$

After spatial discretization, the variational equations (2.26)(2.27)(2.28)(2.29)(2.32) result in the following non-linear algebraic system:

$$\begin{cases} \underline{F}^{\underline{u}} = \sum_g w_g \left(\overline{\boldsymbol{T}}_{D,g} + P_g \boldsymbol{I} + r_{inco}\left(\mathrm{tr}\left(\boldsymbol{E_g}\right) - \theta_g\right)\boldsymbol{I}\right) : \mathbb{P}_g : \left(\boldsymbol{F}_{\boldsymbol{g}}^{\mathbf{T}} . \underline{\boldsymbol{B}}_g^{\underline{u}}\right) \\ F^a = \sum_g w_g \left(c\boldsymbol{\nabla} a_g . \underline{B}_g^a + \left(l_g + r_{nl}\left(a_g - \kappa_g\right)\right) N_g^a\right) \\ F^l = \sum_g w_g\left(a_g - \kappa_g\right) N_g^l \\ F^P = \sum_g w_g\left(\mathrm{tr}\left(\boldsymbol{E_g}\right) - \theta_g\right) N_g^P \\ F^\theta = \sum_g w_g \left(\frac{1}{3}\mathrm{tr}\left(\overline{\boldsymbol{T}}_g\right) - P_g - r_{inco}\left(\mathrm{tr}\left(\boldsymbol{E_g}\right) - \theta_g\right)\right) N_g^\theta \end{cases} \tag{2.33}$$

where $\underline{F}^i = (\underline{F}^{\underline{u}}, F^a, F^l, F^P, F^\theta)$ are the internal forces. It should be equal to the external forces $\underline{F}^e = (\underline{F}^{ext}, 0,0,0,0)$.

Equations (2.33) are solved by an iterative Newton-Raphson method with respect to the nodal unknowns $(\underline{U}, A, L, P, \Theta)$. If we note $\underline{X} = (\underline{U}, A, L, P, \Theta)$ and j the j^{th} iteration, then $\underline{X}^{j+1} = \underline{X}^j - \left(\mathbb{K}^j\right)^{-1}\left(\underline{F}^i - \underline{F}^e\right)^j$ with $\mathbb{K}$ the stiffness matrix: $\mathbb{K}^j = \partial(\underline{F}^i - \underline{F}^e)/\partial \underline{X}$. The detailed expression of $\mathbb{K}$ can be found in Appendix A2.

2.5 Porous plasticity material and application to ductile fracture

The formulation proposed to handle isochoric plasticity and gradient hardening has been expressed in the context of a generic plasticity model. Now we focus our attention on the GTN model. It describes porous ductile plasticity with isotropic hardening. The porosity f is considered as an isotropic damage factor. For simplicity, the strain tensor $\overline{\boldsymbol{E}}$ and the stress tensor $\overline{\boldsymbol{T}}$ used in the constitutive law will be denoted $\boldsymbol{E}$ and $\boldsymbol{T}$, respectively.

2.5.1 Definition of a scalar stress measure

In the work of (Besson et al., 2001), an effective scalar stress a_* associated to stress tensor $\boldsymbol{a}$ was introduced. The stress a_* is a representation of the matrix loading when subjected to a macroscopic stress $\boldsymbol{a}$ (stress $\boldsymbol{T}$ in the following) for a given damage level. In the following, the scalar stress measure a_* is defined explicitly or implicitly by the following equation:

$$G(\boldsymbol{a}, a_*, f) = 0 \tag{2.34}$$

One can refer to (Lorentz, 2017) for the mathematical properties of such definition.

In the following, the a_* will be expressed using the porosity f and the first two invariants of the $\boldsymbol{a}$: its hydrostatic part a_h and its von-Mises invariant a_{eq}. The resulting model is therefore isotropic. To reflect the damage effect of porosity, a_* must be an increasing function of f:

$$a_*(\boldsymbol{a}, f_1) < a_*(\boldsymbol{a}, f_2) \quad \text{if} \quad f_1 < f_2 \tag{2.35}$$

It is assumed that a_* is a homogeneous function of $\boldsymbol{a}$ of degree 1 and differentiable. Consequently,

$$\boldsymbol{a}\colon\frac{\partial a_*}{\partial \boldsymbol{a}} = a_* \tag{2.36}$$

As seen in the previous parts, the stress tensor in the logarithmic strain space is denoted $\boldsymbol{T}$, so we can introduce the effective stress tensor $T_* = T_*(\boldsymbol{T}, f)$ associated to $\boldsymbol{T}$.

In the case of the von-Mises model, the effective stress T_* is defined by:

$$G(\boldsymbol{T}, T_*) \equiv \left(\frac{T_{eq}}{T_*}\right)^2 - 1 = 0 \tag{2.37}$$

Now considering the micromechanical-based GTN model proposed by (Gurson, 1977) and improved by(Needleman and Tvergaard, 1984; Tvergaard and Needleman, 1984). This model takes into account a strong coupling between damage and plastic strain. The effective stress T_* is defined by the GTN yield function as:

$$G(\boldsymbol{T}, T_*, f) \equiv \left(\frac{T_{eq}}{T_*}\right)^2 + 2q_1 f^* \cosh(\frac{3}{2} q_2 \frac{T_H}{T^*}) - 1 - (q_1 f^*)^2 = 0 \tag{2.38}$$

In Equation (2.38), T_H and T_{eq} are the hydrostatic stress and the von-Mises equivalent stress respectively. The parameters q_1 and q_2 are two material constants and f^* is the effective porosity which is a function of f so as to account for the rapid drop in the stress carrying capacity during void coalescence:

$$f^* = \begin{cases} f, & f < f_c \\ f_c + \dfrac{\frac{1}{q_1} - f_c}{f_F - f_c}, & f \geq f_c \end{cases} \tag{2.39}$$

where f_c and f_F represent respectively the porosity at the onset of coalescence and the porosity at fracture. Note that Equation (2.37) and Equation (2.38) are obviously equivalent if we set $f^* = 0$ in Equation (2.38).

2.5.2 Yield function and evolution equations

As long as there is no rotation of the eigenbasis of the stress tensor, the scalar stress measure T_* and σ_* are linked by $T_* = J\sigma_*$ with σ_* the scalar effective stress associated to Cauchy stress tensor $\boldsymbol{\sigma}$. Therefore, we propose the following yield function F:

$$F = \frac{T_*}{J} - (\sigma_0 - A) \tag{2.40}$$

where the expressions of the hardening driving force A is provided in Equation (2.30) within the context of the relaxed numerical formulation.

The Kuhn-Tucker consistency conditions is:

$$\lambda \geq 0, F \ \leq 0, \lambda F \ = \ 0 \tag{2.41}$$

where λ denotes the plastic multiplier.

The rate of the plastic strain tensor $\boldsymbol{E^p}$ and the rate of the hardening variable κ are given by application of a normality flow rule:

$$\begin{cases} \dot{\boldsymbol{E}}^{\boldsymbol{p}} \ = \lambda \dfrac{\partial \mathrm{F}}{\partial \boldsymbol{T}} \\ \dot{\kappa} = \lambda \dfrac{\partial F}{\partial A} \end{cases} \tag{2.42}$$

2.5.3 Void nucleation and void growth

The evolution of f is given by the sum of the rate of the void growth $\dot{f}_g$ and the rate of the void nucleation $\dot{f}_n$:

$$\dot{f} = \dot{f}_g + \dot{f}_n \tag{2.43}$$

The void growth rate can be written as:

$$\dot{f}_g \ = \ (1 - \ f)\mathrm{tr}(\dot{\boldsymbol{E}}^{\boldsymbol{p}}) \tag{2.44}$$

where $\dot{\boldsymbol{E}}^{\boldsymbol{p}}$ represents the rate of the plastic strain tensor and $\mathrm{tr}(\dot{\boldsymbol{E}}^{\boldsymbol{p}})$ represents the trace of the rate of the plastic strain tensor which depicts the rate of volume change.

For strain controlled void nucleation mechanism, the rate of void nucleation is defined on the rate of the hardening variable κ by:

$$\dot{f}_n = B_n(\kappa)\dot{\kappa} \quad \Longrightarrow \quad f_n = \int_0^{\kappa} B_n(s)\, ds \tag{2.45}$$

Several expressions of B_n are possible among which the expressions proposed in (Chu and Needleman, 1980) and (Zhang et al., 2000) are widely used in the literature. In (Chu and Needleman, 1980), stress or strain controlled void nucleation mechanism is assumed to follow a normal distribution:

$$B_n(\kappa) = \frac{f_N}{s_N\sqrt{2\pi}} e^{-\frac{1}{2}\left(\frac{\kappa-\kappa_N}{s_N}\right)^2} \tag{2.46}$$

where κ_N and s_N are the mean value and the standard deviation of the strain tensor, f_N is the void nucleating particles fraction. In the work of (Zhang et al., 2000), a continuous nucleation model is proposed:

$$B_n(\kappa) = b_0 \tag{2.47}$$

where b_0 is a constant number. Compared to the model proposed in (Zhang et al., 2000), the model proposed in (Chu and Needleman, 1980) is more sophisticated but less attractive in engineering due to the three parameters to be calibrated.

So far, a complete non-local locking free von-Mises/GTN model for non-porous/porous materials is established. This model is implemented in Code_Aster (software for finite element analysis), developed at EDF (Electricité De France). The integration of the constitutive equations is realized using a semi-implicit scheme (f is updated explicitly) (Zhang et al., 2018). A further discussion about the purely implicit scheme and the semi-implicit scheme will be conducted in Chapter 3. The corresponding numerical implementation can be found in (Zhang et al., 2018) for the semi-implicit scheme and in Appendix A4 for the purely implicit scheme.

2.6 Model validation with some test-cases

In this section, the simulations on an elementary cell, a bar and a notch tensile specimen are performed using the GTN model described above. The major objective of this section consists in validating our numerical implementation and thus providing some reference results. Since these test-cases are just used for the validation of our model implementation, no comment will be given to all results. The validation of the numerical implementation is done through the comparison between the results obtained by Code_Aster (software for finite element analysis developed in EDF) and those obtained by Z-Set (software for finite element analysis developed at Centre des Matériaux, Ecole des Mines de Paris). The percentage difference[4] between the results obtained by the two software is always less than 1%.

Unless otherwise specified in the text, the values of the model parameters used in the simulations are given in Table 2.1. The power law (Equation (2.13)) is used for the flow stress.

Table 2.1. The nominal values of the parameters used in the test-cases

Elasticity	Young modulus E	200000 MPa
	Poisson ratio ν	0.3
Plasticity	Yield stress σ_0	$500\ MPa$
	Hardening variable κ_0	0.0025
	Hardening exponent n	0.1
Damage	Initial porosity f_0	0.01
	Critical porosity f_c	0.05
	Porosity at failure f_F	0.25
	Material constants (q_1, q_2)	(1.5,1.0)
Nonlocality	Nonlocal parameter c	$50\ N$
Numerical parameters	Nonlocal penalty parameter r_{nl}	$5000\ MPa$
	Incompressibility penality parameter r_{inco}	$5000\ MPa$

2.6.1 Simulations of elementary cell

This part aims at presenting the results of the simulations of an elementary cell (referring to as RVE2D) with axisymmetric and plane strain modeling. The initial length and the initial width of RVE2D are the same ($L_{x0} = L_{y0} = L_0 = 1\ mm$). The corresponding mesh is a single quadrilateral element with 4 integration points. Figure 2.2 shows the boundary and loading conditions for each tests. In this figure, the point A corresponds to the origin of the Cartesian (or cylindrical) coordinate system.

For the axisymmetric case, the vertical displacement of all nodes is given: $u_y = \alpha t y$ with $\alpha = 10$. That is to say, the vertical component of $\boldsymbol{F}$ (deformation gradient tensor) is given: $F_{yy} = \alpha t + 1$. Horizontal deformation of AD is restricted. Horizontal deformation of BC remains uniform (see Figure 2.2 (a)). That is to say, the radial component of $\boldsymbol{F}$ is a constant or only depends on x: $F_{rr} = F_{rr}(x)$.

For the plane strain case, four different kinds of boundary conditions are modelled. In particular, the last two types are used to illustrate the fact that damage growth under shear loading cannot be captured by the classical GTN model.

---

[4] Percentage Difference: if we note x_1 and x_2 two different value, then the percentage difference is defined by:

$$\frac{1}{2}\left|\frac{x_1 - x_2}{x_1 + x_2}\right| \times 100\%$$

- Uniaxial tensile case: the vertical displacement of all nodes is given: $u_y = \alpha t y$ with $\alpha = 3$, the horizontal deformation of AD is restricted. Horizontal deformation of BC remains uniform (see Figure 2.2(b1)). That is to say, the following deformation gradient tensor is imposed:

$$\boldsymbol{F} = \begin{pmatrix} F_{xx} & 0 \\ 0 & F_{yy} \end{pmatrix} = \begin{pmatrix} F_{xx} & 0 \\ 0 & \alpha t + 1 \end{pmatrix} \tag{2.48}$$

  Here F_{xx} can be a constant or depends on x.
- Biaxial tensile case: displacement of all nodes are given: $u_x = \alpha t x$,$u_y = \alpha t y$ with $\alpha = 0.2$ (see Figure 2.2(b2)). That is to say, the following deformation gradient tensor is imposed:

$$\boldsymbol{F} = \begin{pmatrix} \alpha t + 1 & 0 \\ 0 & \alpha t + 1 \end{pmatrix} \tag{2.49}$$

- Simple shear case: restriction of vertical displacement of all nodes; Horizontal displacement of all nodes is: $u_x = \alpha t y$ with $\alpha = 40$ (see Figure 2.2(b3)). That is to say, the following deformation gradient tensor is imposed:

$$\boldsymbol{F} = \begin{pmatrix} 1 & \alpha t \\ 0 & 1 \end{pmatrix} \tag{2.50}$$

- Pure shear test: displacement of all nodes are given: $u_x = (\cosh(\alpha t) - 1)x + \sinh(\alpha t)y$, $u_y = \sinh(\alpha t)x + (\cosh(\alpha t) - 1)y$ with $\alpha = 1$ (see Figure 2.2(b4)). That is to say, the following the deformation gradient tensor is imposed:

$$\boldsymbol{F} = \begin{pmatrix} \cosh(\alpha t) & \sinh(\alpha t) \\ \sinh(\alpha t) & \cosh(\alpha t) \end{pmatrix} \tag{2.51}$$

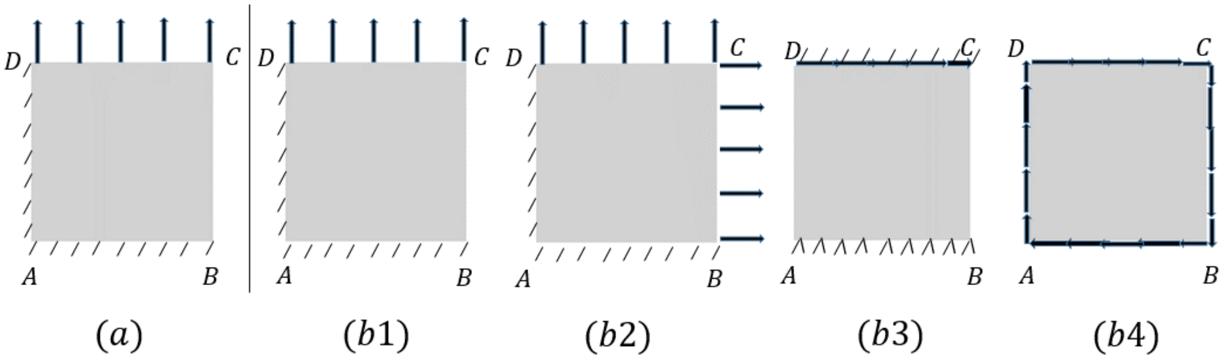

Figure 2.2. Boundary and Loading conditions: (a) axisymmetric and (b) plane-strain modeling ((b1) uniaxial tensile, (b2) biaxial tensile, (b3) simple shear and (b4) pure shear cases)

With the above boundary and loading conditions, it is obvious that the material behavior is purely homogenous. Nonlocal effect does not exist for any values of c. In the following, for each test, we will plot:

- Force – displacement curve
- Evolution of κ and f with increasing load
- Evolution of certain components of $\boldsymbol{\sigma}$ and $\boldsymbol{T}$ with increasing load

Remarks:

- *Uniaxial tensile test with axisymmetric modeling*
  In Figure 2.3, the force F is computed by $F = 2\pi F_y$ with F_y the resultant force on the top edge CD.
- *Uniaxial tensile test with plane-strain modeling*
  In Figure 2.6, the force F is computed by F=2F_y with F_y the resultant force on the top edge CD.
- *Biaxial tensile test with plane-strain modeling*
  In Figure 2.9, the force F is computed by $F = 2F_y$ with F_y the resultant force on the top edge CD.
- *Simple shear test with plane-strain modeling*
  In Figure 2.12, the force F is computed by $F = F_x$ with F_x the resultant force on the top edge CD. The force F, as well as the stress σ_{xy} decrease from a certain value of the deformation gradient F_{xy} even if no damage growth occurs. This observation can be explained by the increase of other components of the stress.

No further comment will be given to the obtained results.

Uniaxial tensile test with axisymmetric modeling

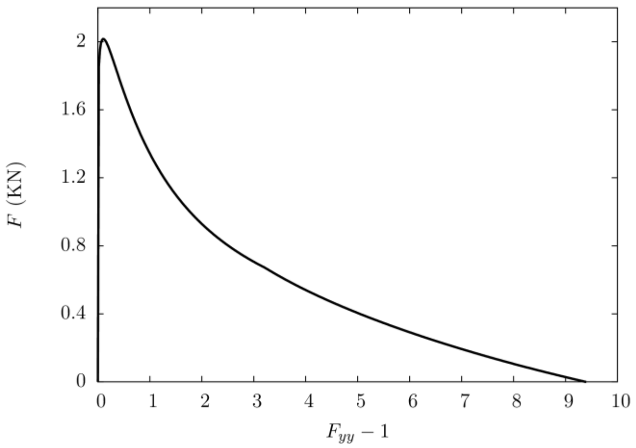

Figure 2.3. Force – displacement (uniaxial tensile test with axisymmetric modeling)

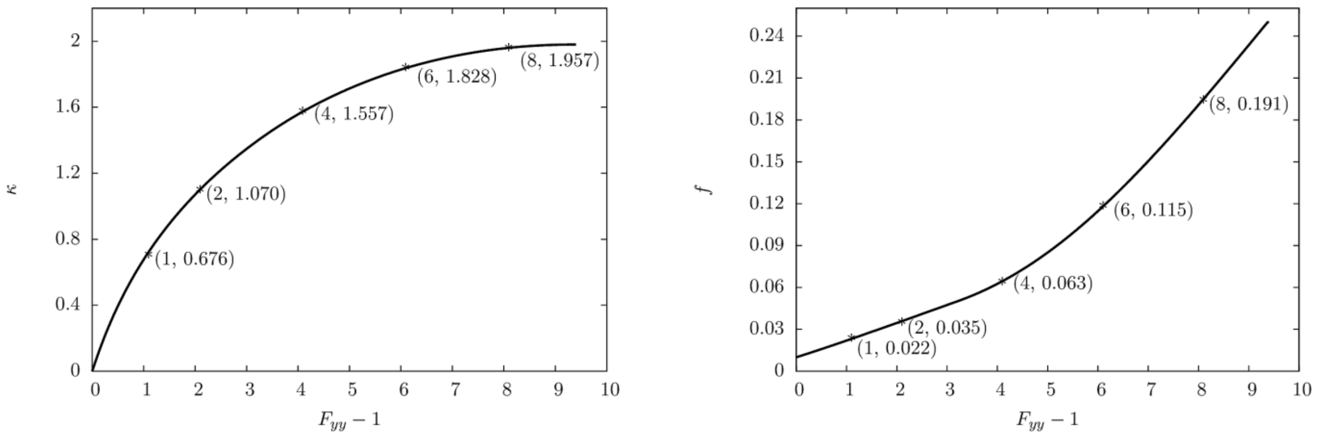

(a) (b)

Figure 2.4. Evolution of the hardening parameter κ and the porosity f with the stretch (uniaxial tensile test with axisymmetric modeling)

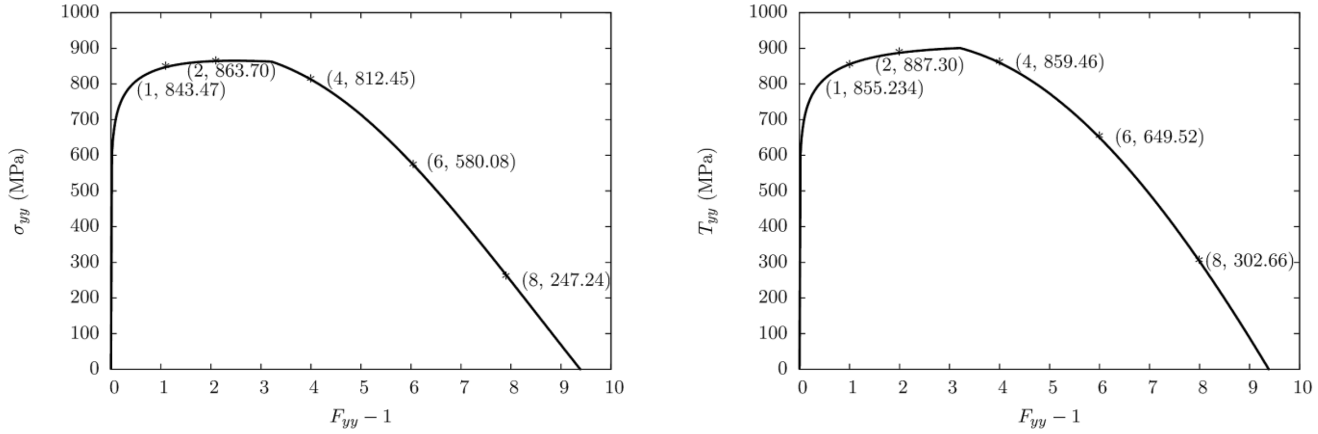

(a) (b)

Figure 2.5. Evolution of the stress σ_{yy} and the stress T_{yy} with the stretch (uniaxial tensile test with axisymmetric modeling)

Uniaxial Tensile test with plane-strain modeling

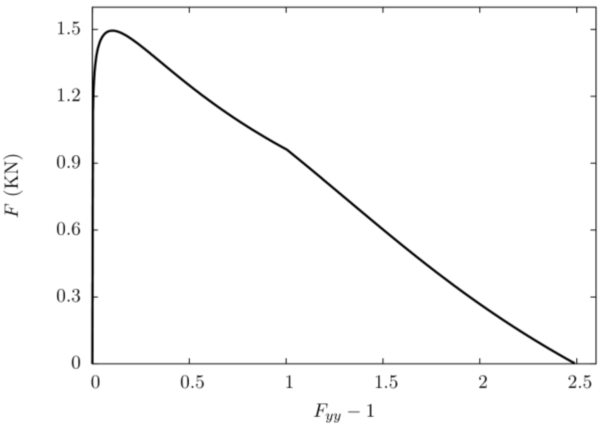

Figure 2.6. Force – displacement (uniaxial tensile test with plane-strain modeling)

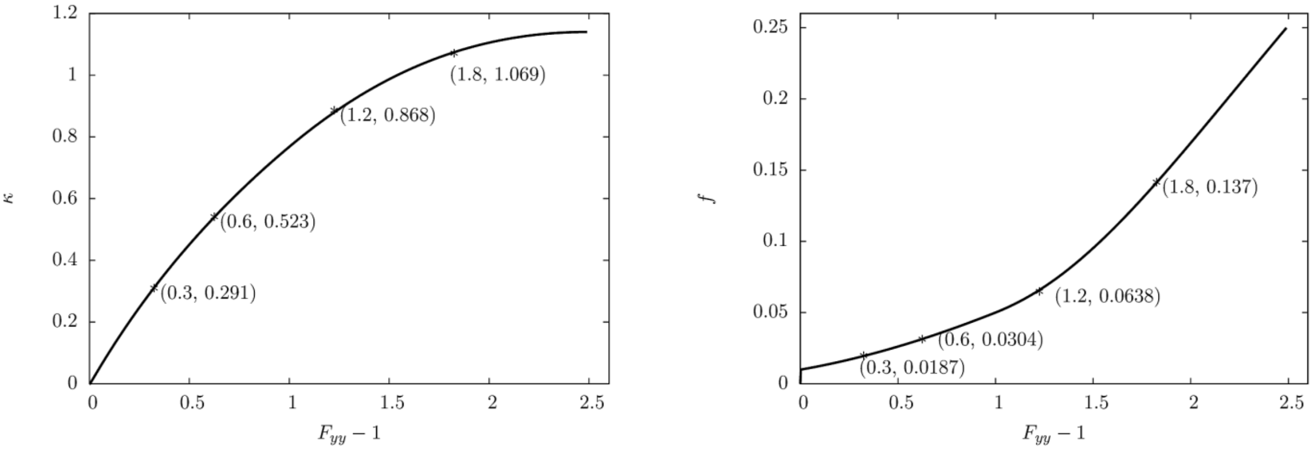

(a) (b)

Figure 2.7. Evolution of the hardening parameter κ and the porosity f with the stretch (uniaxial tensile test with plane-strain modeling)

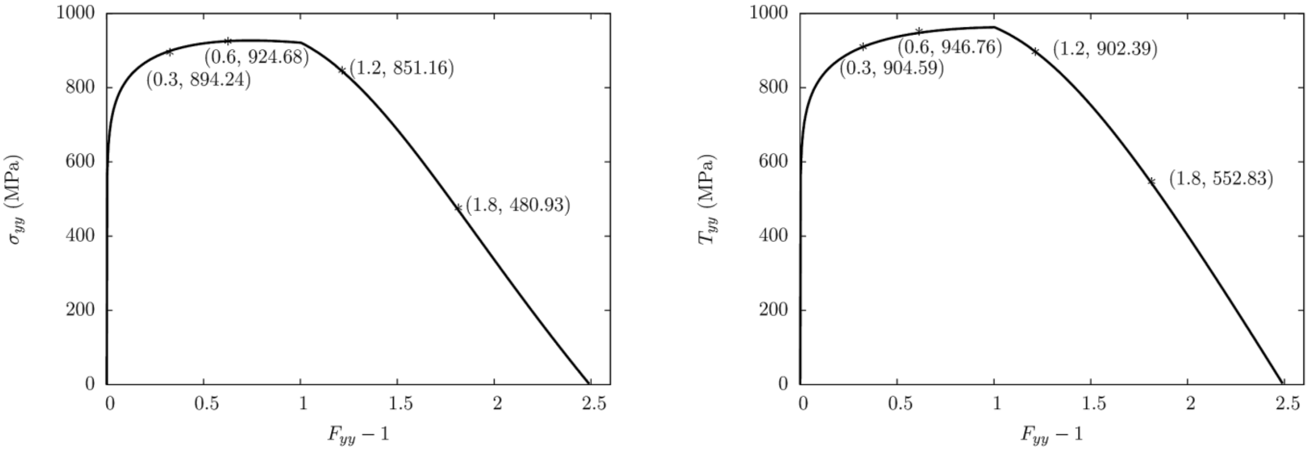

(a) (b)

Figure 2.8. Evolution of the stress σ_{yy} and the stress T_{yy} with the stretch (uniaxial tensile test with plane-strain modeling)

Biaxial tensile test with plane-strain modeling

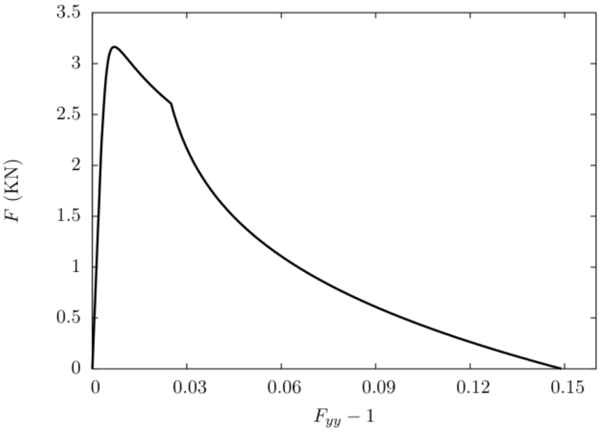

Figure 2.9. Force – displacement (bi-axial test with plane-strain modeling)

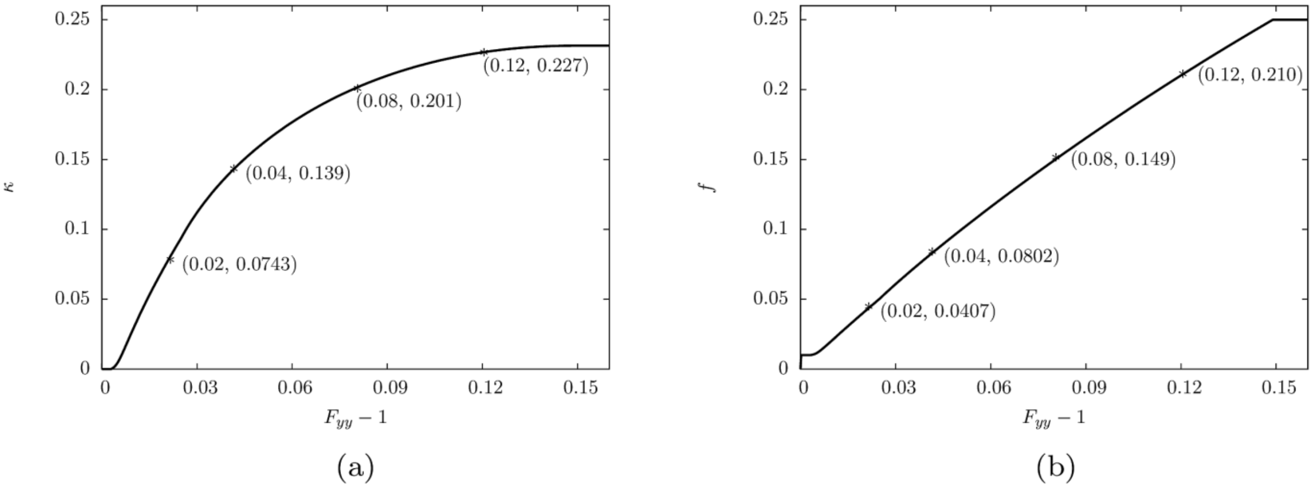

Figure 2.10. Evolution of the hardening parameter κ and the porosity f with the stretch (bi-axial tensile test with plane-strain modeling)

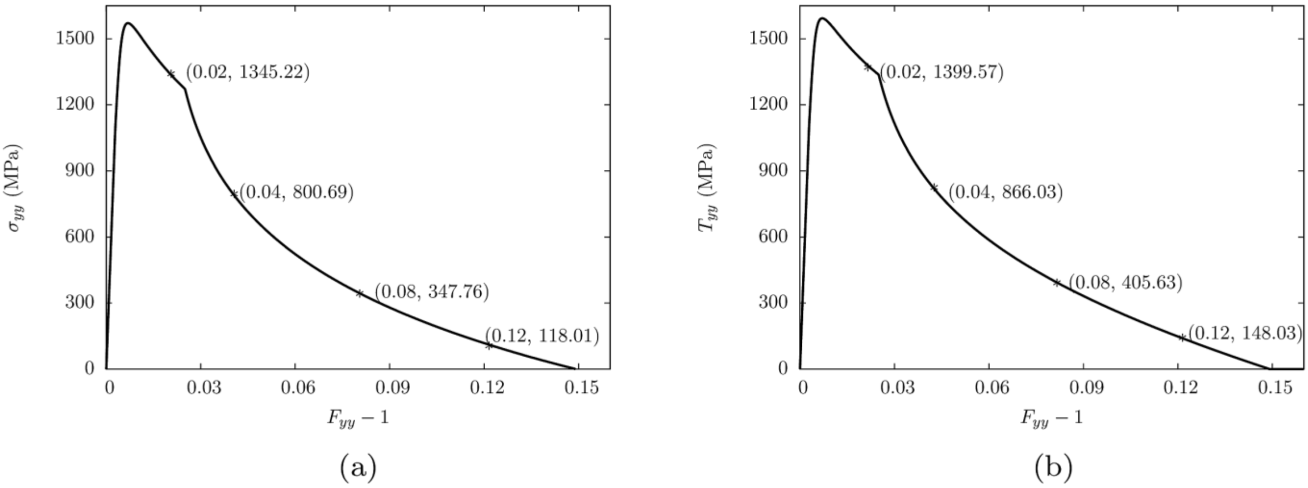

Figure 2.11. Evolution of the stress σ_{yy} and the stress T_{yy} with the stretch (bi-axial tensile test with plane-strain modeling)

Simple shear test with plane-strain modeling

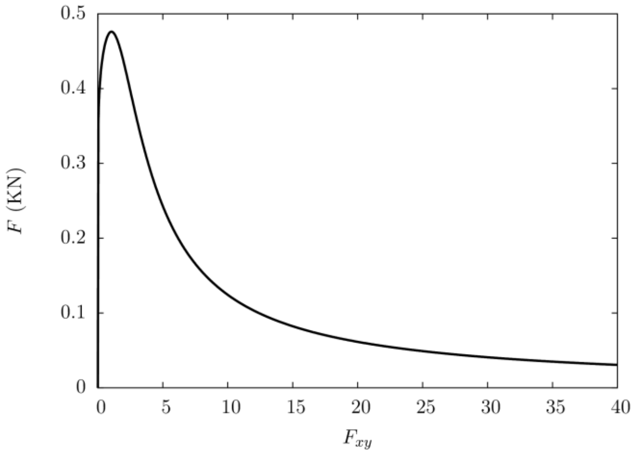

Figure 2.12. Force – displacement (simple shear test with plane-strain modeling)

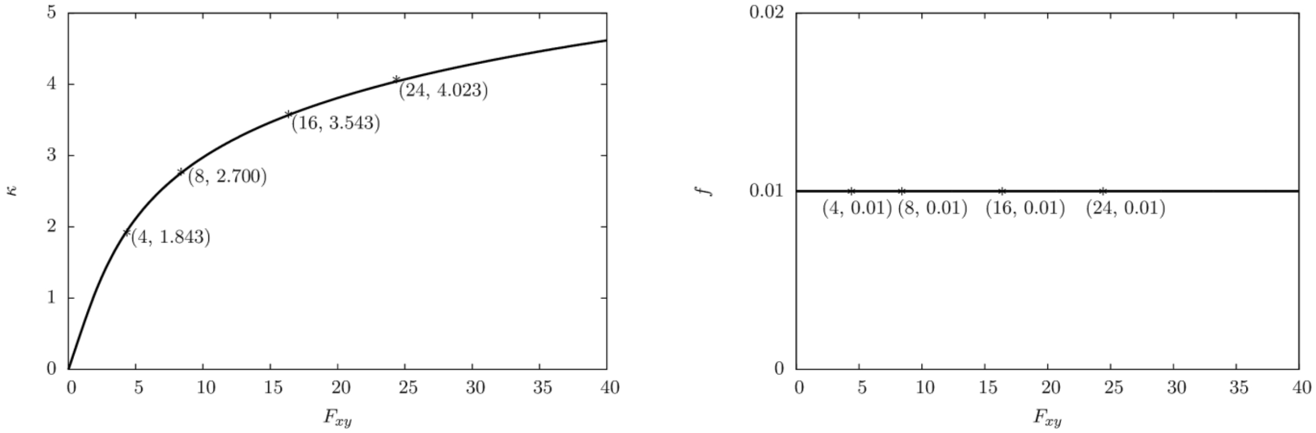

(a) (b)

Figure 2.13. Evolution of the hardening parameter κ and the porosity f with the stretch (simple shear test with plane-strain modeling)

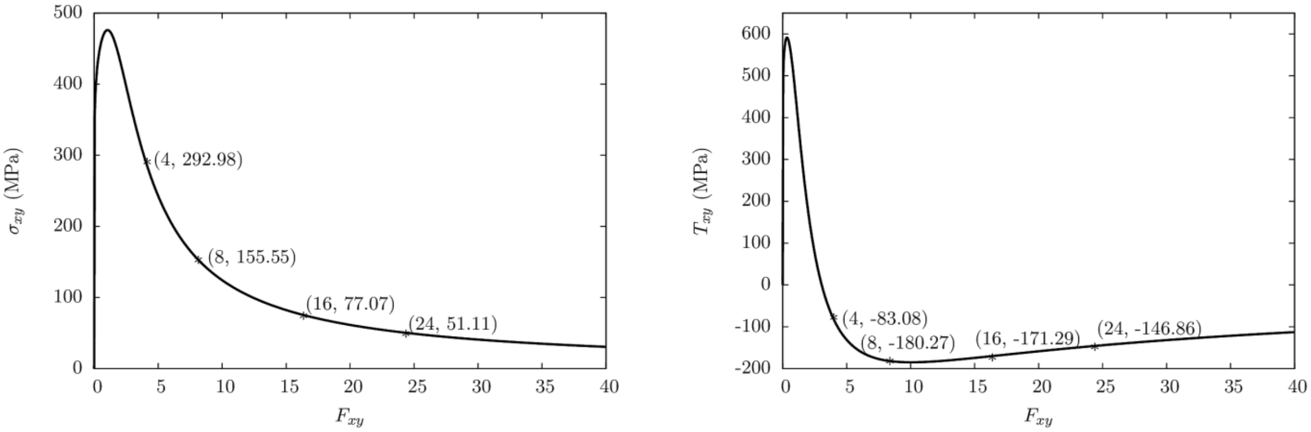

(a) (b)

Figure 2.14. Evolution of the stress σ_{yy} and the stress T_{yy} with the stretch (simple shear test with plane-strain modeling)

<u>Pure shear test with plane-strain modeling</u>

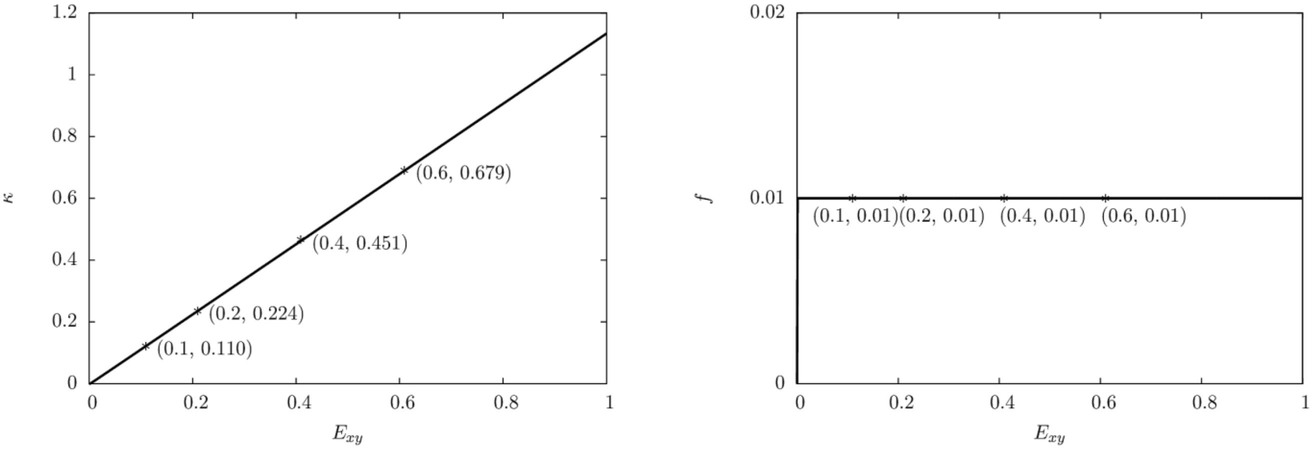

(a) (b)

Figure 2.15. Evolution of the hardening parameter κ and the porosity f with the stretch (pure shear test with plane-strain modeling)

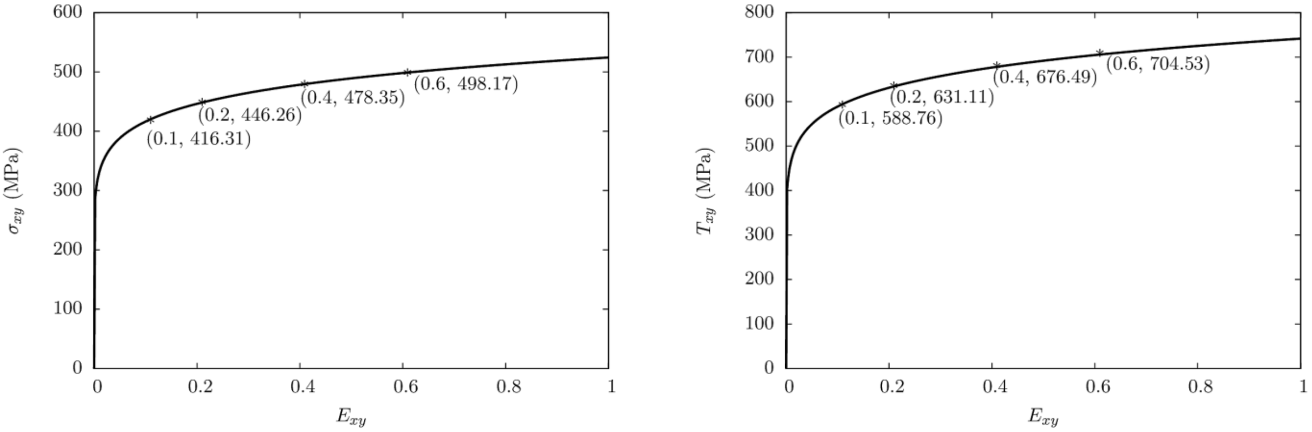

(a) (b)

Figure 2.16. Evolution of the stress σ_{yy} and the stress T_{yy} with the stretch (pure shear test with plane-strain modeling)

2.6.2 Simulation of bar

The simulations of a bar with three-dimensional modeling (referring to as BAR3D) are performed and the corresponding results are presented in this part. The mesh of BAR3D is shown in Figure 2.17. We have $L_{x0} = L_{y0} = 0.1L_{z0} = 1\ mm$. The mesh consists of 128 nodes and 10 hexahedral elements. There are 8 gauss points in each quadratic element.

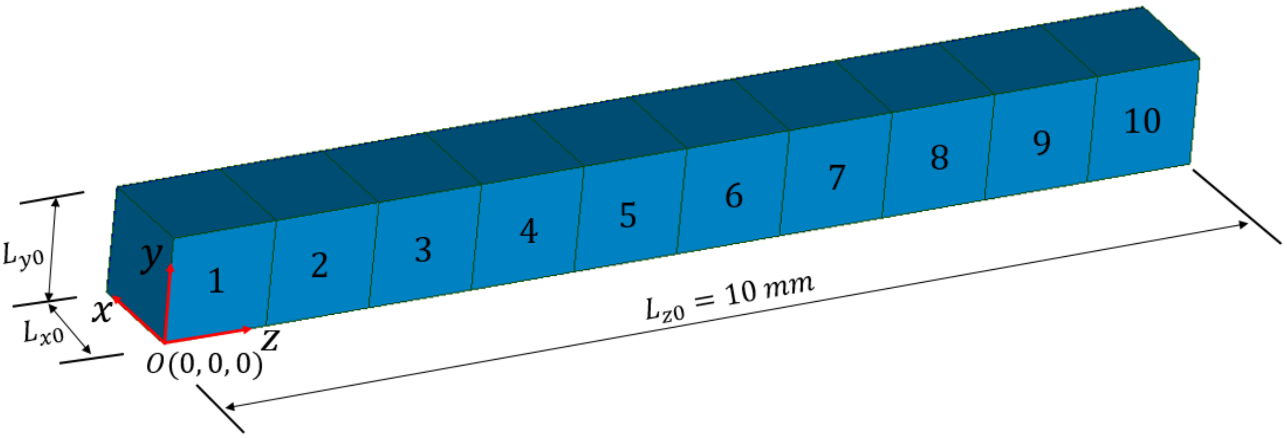

Figure 2.17. Mesh of BAR3D

The value of different model parameters is shown in Table 1 except that the initial porosity f_0 changes with the element number: $f_0 = \{0.0002i, i \in 1, 2, \dots, 10]\}$ where i stands for the i^{er} element layer, the numbering rule is shown in Figure 2.17. Compared to the RVE2D simulations, here the material behavior is not homogeneous since f_0 varies with the position. Thus, the change of c can effectively change the global/local responses. Here, we have $c = 50\ N$ corresponding to a nonlocal length around $l_{nl} = \sqrt{c/\sigma_0} = \sqrt{50/500} \approx 0.3$ mm $<$ 1 mm (1 mm is the mesh size), so the nonlocal effect is low.

The specimen is stretched in the direction of x and y. We note u_x, u_y, u_z the imposed displacement along x, y and z axis respectively. In our study, $u_x = \beta t x$ and $u_y = \alpha\beta t y$ with $\alpha \in \mathbb{R}$ and $\beta \in \mathbb{R}$. For the nodes in the same xy plane, the deformation along z remains uniform. In fact, we are in plane-strain case when $\alpha = 0, \beta \neq 0$ and axisymmetric case when $\alpha = 1, \beta \neq 0$. These two case will be studied later. For axisymmetric case, $\alpha = 1, \beta = 1.7$ and for plane-strain case, $\alpha = 0, \beta = 7$.

The corresponding prescribed deformation gradient tensor $\boldsymbol{F}$ is:

$$\boldsymbol{F} = \begin{pmatrix} \beta t + 1 & 0 & 0 \\ 0 & \alpha\beta t + 1 & 0 \\ 0 & 0 & F_{zz}(z) \end{pmatrix} \tag{2.52}$$

With these boundary and loading conditions, the local response only depends on z. In the following, we plot the following curves for the integration point at which the damage is largest (i.e., the point at which z is the largest):

- Evolution of κ and f with increasing load
- Evolution of certain components of $\boldsymbol{\sigma}$ and $\boldsymbol{T}$ with increasing load
- Evolution of κ and f with the position z

No further comment will be given for the obtained results.

Axisymmetric case

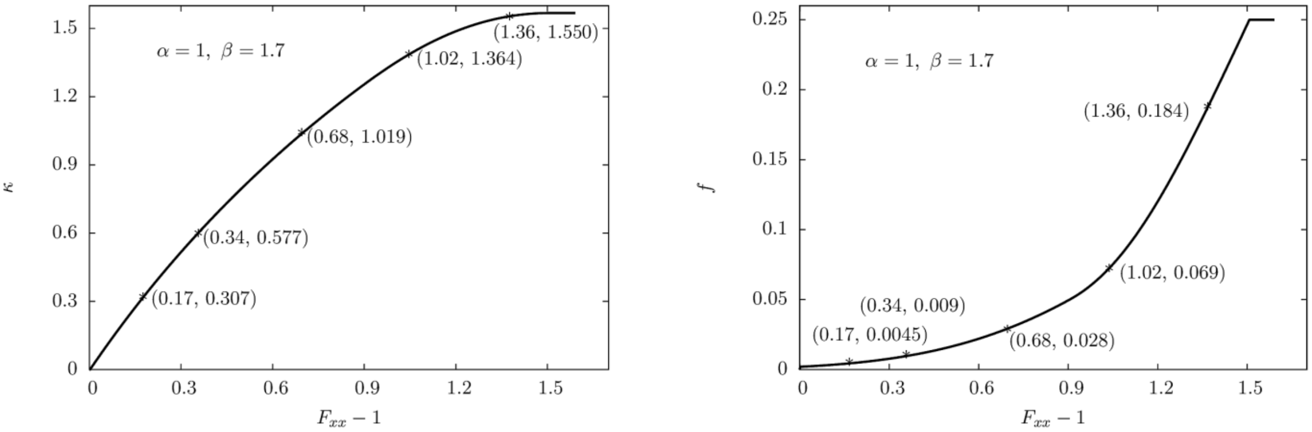

(a) (b)

Figure 2.18. Evolution of the hardening parameter κ and the porosity f with the stretch ($\alpha = 1, \beta = 1.7$)

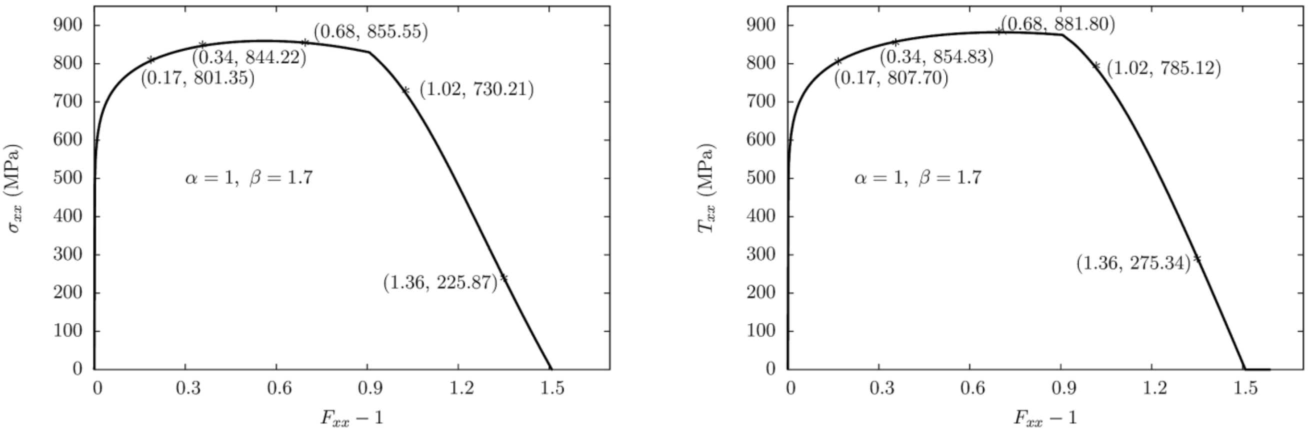

(a) (b)

Figure 2.19. Evolution of the stress σ_{xx} *and the stress* T_{xx} *with the stretch* ($\alpha = 1, \beta = 1.7$)

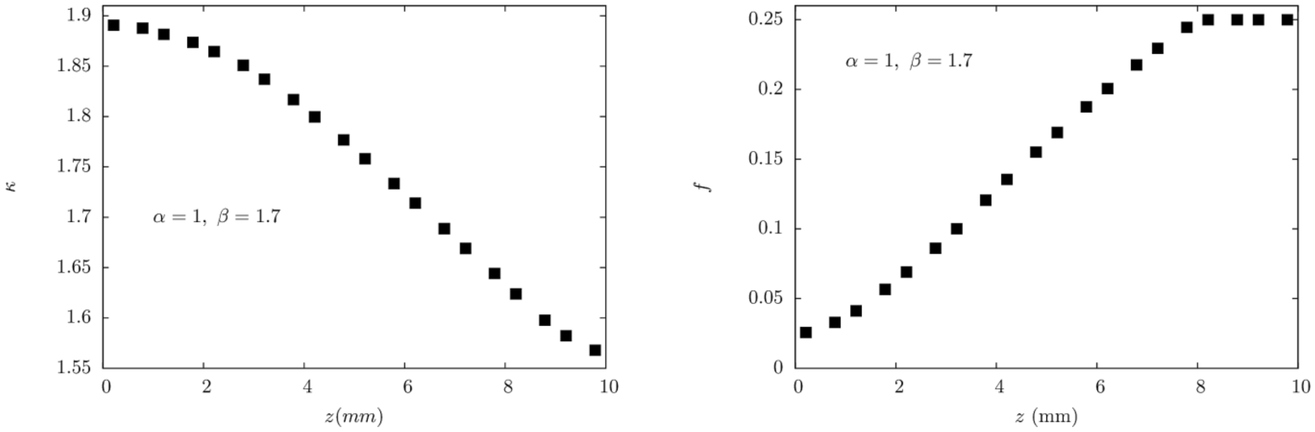

(a) (b)

Figure 2.20. Evolution of the hardening parameter κ and the porosity f *along z-axis* ($\alpha = 1, \beta = 1.7$)

Plane strain case

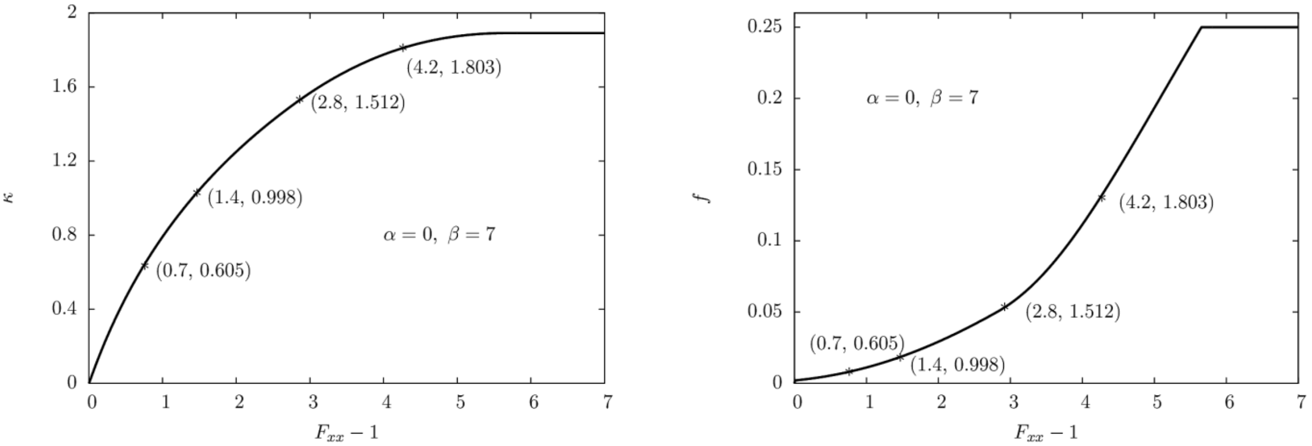

(a) (b)

Figure 2.21. Evolution of the hardening parameter κ and the porosity f with the stretch ($\alpha = 0, \beta = 7$)

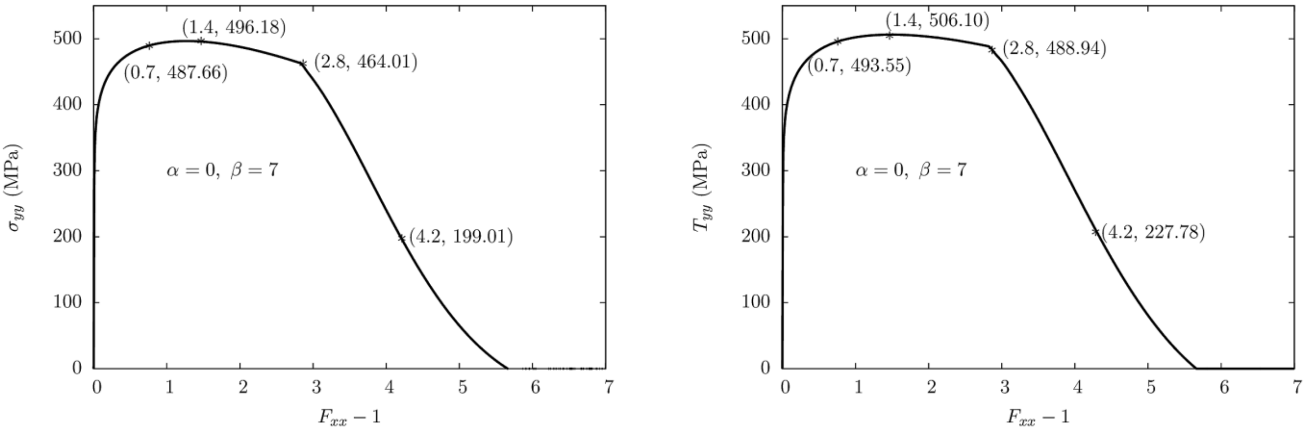

(a) (b)

Figure 2.22. Evolution of the stress σ_{yy} and the stress T_{yy} with the stretch ($\alpha = 0, \beta = 7$)

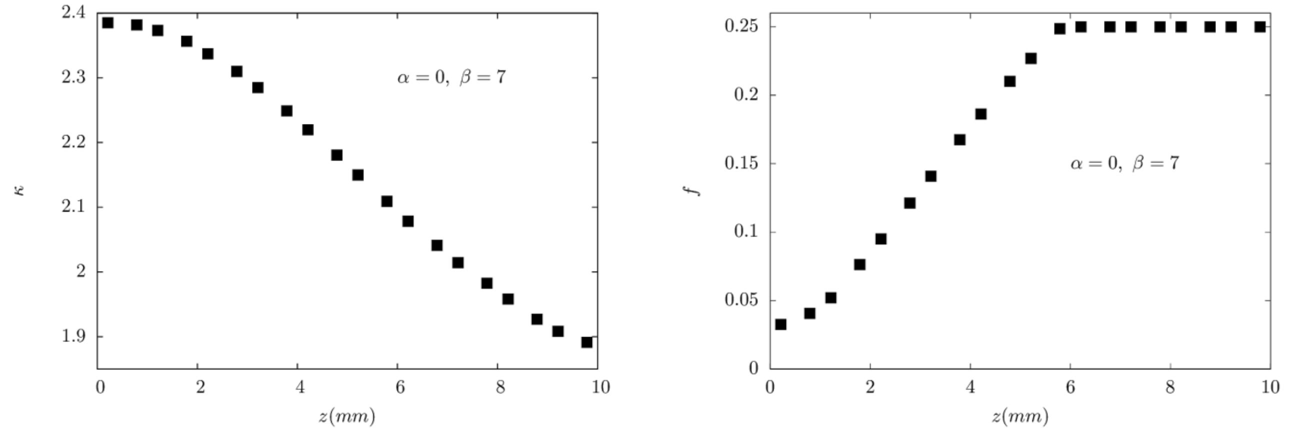

(a) (b)

Figure 2.23. Evolution of the hardening parameter κ and the porosity f along z-axis ($\alpha = 0, \beta = 7$)

2.6.3 Simulation of notch tensile test

Simulations of a notch tensile specimen (referring to as NT) are performed and the corresponding results are presented in this part. A simplified geometry and the corresponding mesh is shown in Figure 2.24. The minimal mesh size is $l_e = 120$ mm. Generally speaking, for the geometry of NT, there are no specific requirements related to the total length H and diameter D outside the notched area. The requirements are only related to the notch geometry and sometimes the length of the material zone of interest h. To ensure that the plastic deformation is limited to the zone of interest, D_n should not exceed h. The notch should be located in the middle of the zone of interest.

The value of different model parameters is shown in Table 2.1 except for the initial porosity $f_0 = 0.001$.

Displacement boundary condition is applied to the top edge, both horizontal deformation of the edge CD and vertical deformation of the bottom edge OA are constrained (see Figure 2.24 (b)).

In the following, we will plot

- Force – displacement curve and Force – diameter reduction curve (Figure 2.25)
- Evolution of the porosity f as a function of the hardening variable κ at two material points ($(X, Y) = (1\text{ mm}, 0\text{ mm}), (X, Y) = (2\text{ mm}, 0\text{ mm})$) in the ligament. Note that the given coordinates are written in initial configuration. (Figure 2.26)
- The evolution of the stress components $\sigma_{rr}, \sigma_{yy}, T_{rr}, T_{xx}$ as a function of the hardening variable κ at ($(X, Y) = (1\text{ mm}, 0\text{ mm})$ and $(X, Y) = (2\text{ mm}, 0\text{ mm})$). (Figure 2.27 and Figure 2.28)

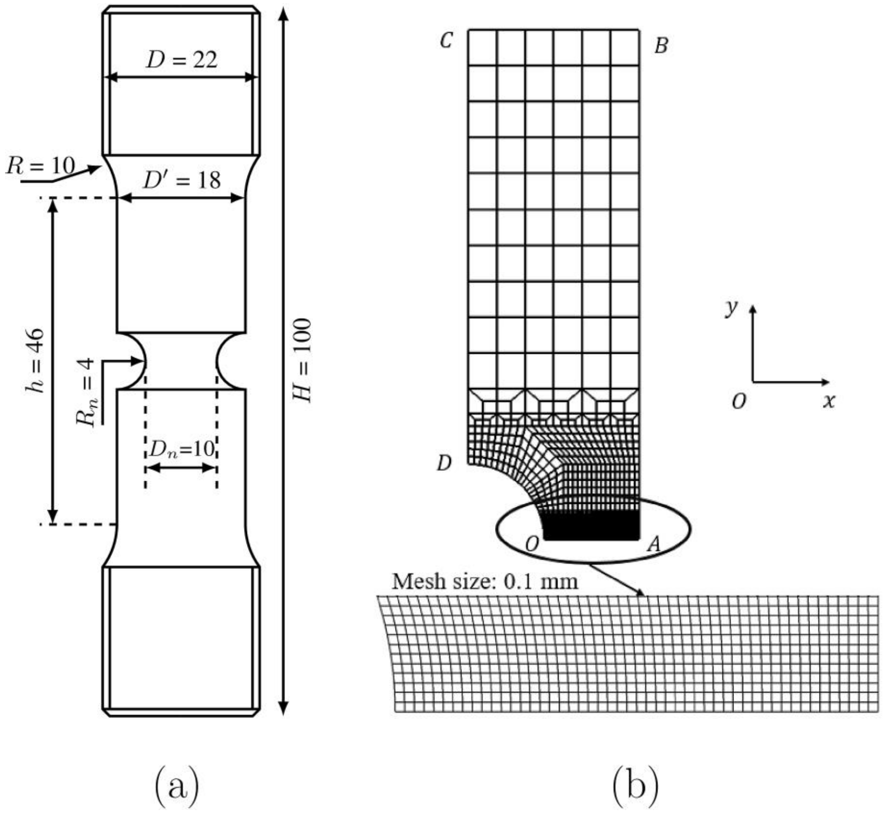

Figure 2.24. (a) Geometry and (b) An example of the mesh of NT

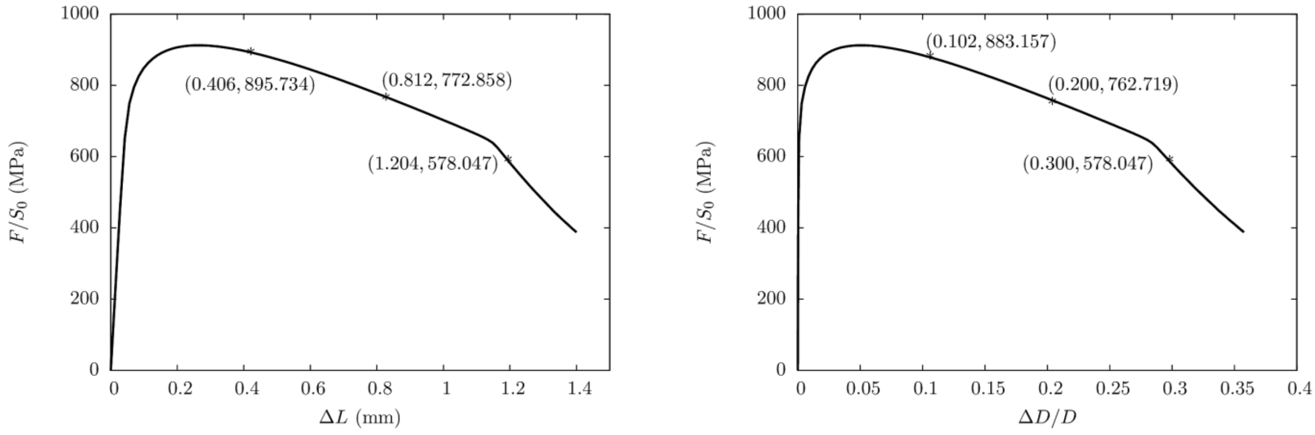

(a) (b)

Figure 2.25. (a) Force - displacement curve (b) Force - Diameter reduction curve

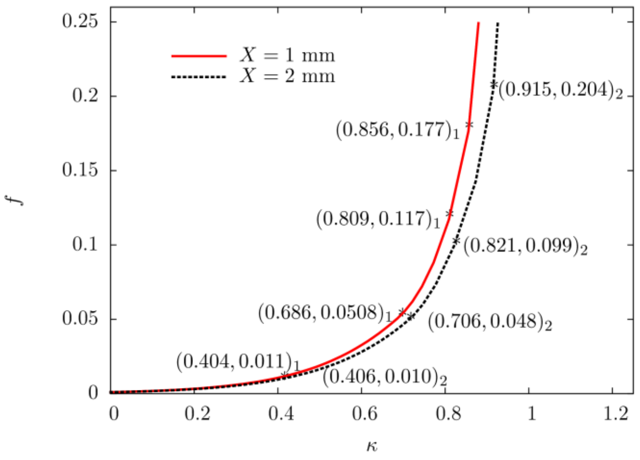

Figure 2.26. f-κ curves

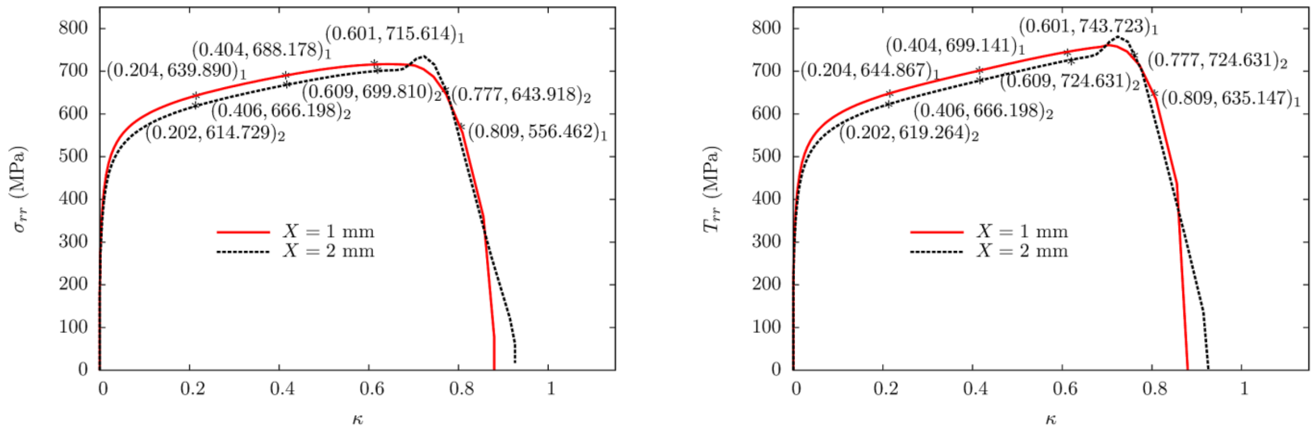

(a) (b)

Figure 2.27. (a) $\sigma_{rr} - \kappa$ curves; (b) $T_{rr} - \kappa$ curves

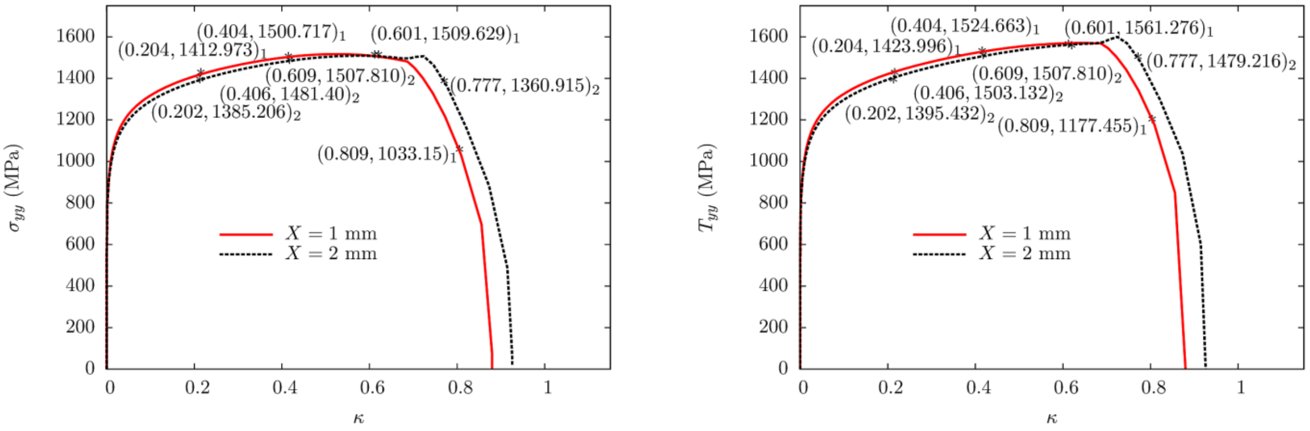

(a)

(b)

Figure 2.28. (a) $\sigma_{yy} - \kappa$ *curves; (b)* $T_{yy} - \kappa$ *curves*

3 Numerical analyses of the nonlocal GTN model

> *我们应该有恒心,尤其要有自信心。我们的天赋是用来做某种事情的, 无论代价多么大, 这种事情必须做到。*
>
> *Nous devons avoir la persévérance, surtout la confiance en nous-mêmes. Notre talent est utilisé pour réaliser quelque chose et on doit la réaliser à n'importe quel prix.*
>
> *We must have perseverance, especially must have self-efficacy. We must believe that our talent is used to do something， no matter how big the cost， we must do these things.*
>
> 玛丽 居里 Marie Curie

Résumé

Ce chapitre est dédié aux différents aspects numériques du modèle GTN non local. L'objectif est d'indiquer à l'utilisateur comment utiliser ce modèle pour faire des simulations robustes.

Dans un premier temps, on se concentre sur le traitement des éléments cassés. En effet, les éléments cassés peuvent devenir très distordus, ce qui fortement perturbe la convergence du calcul. Pour résoudre ce problème, un modèle viscoélastique qui a un effet de stabilisation est proposé. Avec ce modèle, une petite rigidité artificielle est introduite aux points matériels considérés comme rompus, ce qui conduit à des contraintes supplémentaires. Ces contraintes diminuent avec le temps et deviennent zéro à la fin. Des analyses de convergence de ce modèle sont faites. Des simulations sur éprouvette NT sont réalisées afin de déterminer un bon intervalle de valeur pour chaque paramètre du modèle viscoélastique.

Dans un second temps, on se concentre sur le critère de convergence qui est utilisé dans ce travail. Ce critère peut être utilisé même si les différents résidus ont des unités différentes, ce qui rend les simulations numériques plus robustes. Le critère permet également de tenir compte des tailles de mailles très différentes dans le maillage.

Ensuite, on porte notre attention sur les schémas d'intégration pour la mise à jour de la porosité. Deux schémas différents, i.e., schéma semi-implicite et schéma implicite, sont étudiés. La comparaison de ces deux schémas montre que les deux schémas peuvent conduire à des erreurs sur la prédiction de l'endommagement et de la réponse globale quand le pas de temps de calcul n'est pas suffisamment petit. Les deux schémas donnent le même résultat quand le pas de temps tend vers zéro.

Puis, on propose des méthodes de découpage global et local du pas de temps basées sur le contrôle de l'incrément de la porosité afin d'avoir des résultats convergents en temps. Le découpage global permet effectivement de réduire l'écart entre la solution convergée et la solution numérique, mais il peut être très coûteux en temps, notamment en cas de simulations de structures industrielles dont le nombre de degrés de liberté est énorme. En revanche, le découpage local permet non seulement d'obtenir des solutions convergées en temps, mais aussi de réduire le temps de calcul à condition que la matrice de rigidité soit bien évaluée.

Dans la cinquième partie, des simulations avec différentes valeurs de r_{nl} (paramètre de pénalisation non local) sont réalisées afin d'étudier l'effet de r_{nl} sur différents champs mécaniques et sur la réponse globale. Les résultats montrent que dans le cas où la valeur de r_{nl} est trop petite, des oscillations sur la plasticité et l'endommagement peuvent apparaître, ce qui entraine une réponse global fausse.

Enfin, des simulations avec différents valeurs de r_{inco} (paramètre de pénalisation pour l'incompressibilité) sont réalisés afin d'étudier l'effet de r_{inco} sur les différents champs mécaniques et sur la réponse globale. Les résultats montrent que si la valeur de r_{inco} est trop petite, des oscillations sur la plasticité et l'endommagement peuvent apparaître et la réponse globale prédit devient fausse. Par ailleurs, la value de r_{inco} ne peut pas être trop grande, sinon, le problème de verrouillage numérique apparaît de nouveau.

In this chapter, we will study several purely numerical points so as to better understand how to use the nonlocal GTN model which has been presented in the previous chapter. This chapter is organized as follow: firstly, we propose a viscoelastic model to handle the broken finite elements. Secondly, we present the convergence criterion which is used in our work. Thirdly, we compare two different integration schemes for the integration of the constitutive law. Then, we focus on the global and local sub-stepping methods in order to control the error induced by the large load-increment. Finally, we study the two augmentation terms introduced in the model, i.e., $r_{nl}\ (a-\kappa)^2/2$ and $r_{inco}(\mathrm{tr}(\boldsymbol{E})-\theta)/2$. The adequate value ranges for r_{nl} and r_{inco} will be derived from some parametric studies. The results of this chapter will be used in the next two chapters.

3.1 Stabilization with viscoelasticity model

Crack growth simulations with ductile damage models in the framework of finite strains sometimes raise some issues such as highly distorted elements, as shown in (Zhang, 2016) which may strongly affect the computational convergence. One way to reduce this problem is to realize a transition from continuous failure to a discontinuous material separation (with CZM, XFEM, ZCRACK, etc). In this case, the area near the new surfaces should still be properly handled with appropriate techniques (Geers et al., 2003; Seupel et al., 2018). Another way is to use the “element-deletion” technique which consists in eliminating the broken elements according to some predefined criteria. This technique is often applied to the simulations in the context of local damage models (Li et al., 2011; Lian et al., 2015, 2013). When it comes to nonlocal models, this technique is used in few cases such as (Seupel et al., 2018) in the framework of implicit gradient nonlocal modeling. The traitment of the nonlocal variables in new boundaries is particularly difficult which may induce physical inaccuracy and computational non-convergence. Besides, the criteria for element elimination is not quite easy to define. For example, it is necessary to think about the following question: a finite element is deleted when how many integration points are broken? If the criteria are not well defined, then physical inaccuracy may be induced. Finally, the remeshing technique can also be applied to avoid large element distortion, as done in (J. Mediavilla et al., 2006c), but its numerical implementation is rather complex while physical inaccuracy may be induced by the remeshing steps.

This section aims at proposing a simple model to deal with element distortion. We know that when an element fails, the material points inside this element lose their stiffness and so the element becomes distorted. Therefore, we add a small stiffness to the broken elements. It is obvious that the stiffness can induce additional stresses. To limit the additional stiffness and stresses at the end of simulation, we can introduce a time dependence. To this end, we propose to use a simple viscoelastic model which allows for stress/stiffness relaxation. This viscoelastic model is overlapped with the GTN model, it is referred to as “viscoelasticity-GTN overlay model”.

In the following, we consider the case of small-strains. The strain is denoted $\boldsymbol{\varepsilon}$ and the stress is denoted $\boldsymbol{\sigma}$. For the finite strains framework presented in the previous chapter, it is sufficient to replace $\boldsymbol{\varepsilon}$ by $\boldsymbol{E}$ and $\boldsymbol{\sigma}$ by $\boldsymbol{T}$.

3.1.1 Viscoelasticity-GTN overlay model

Before introducing the proposed viscoelastic model, we explain what an overlay model is. For a simple elastic-plastic model, it is rather simple to incorporate the viscous effect into the model. However, when a complex material behavior is modeled, the consideration of the viscous effect in the constitutive law may become complex. So it is appropriated to use an overlay model in which the material constitutive law and the viscoelastic law are in parallel, as shown in Figure 3.1. In the case of the GTN model, we have:

$$\boldsymbol{\sigma}=\boldsymbol{\sigma}_{GTN}+\boldsymbol{\sigma}_{v}, \qquad \boldsymbol{\varepsilon}=\boldsymbol{\varepsilon}_{GTN}=\boldsymbol{\varepsilon}_{v}, \qquad \frac{d\boldsymbol{\sigma}}{d\boldsymbol{\varepsilon}}=\frac{d\boldsymbol{\sigma}_{GTN}}{d\boldsymbol{\varepsilon}_{GTN}}+\frac{d\boldsymbol{\sigma}_{v}}{d\boldsymbol{\varepsilon}_{v}} \tag{3.1}$$

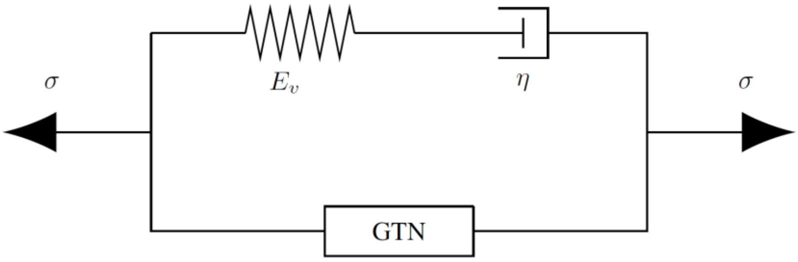

Figure 3.1. Overlay model

The proposed viscoelastic model consists of an assembly of an elastic spring of stiffness matrix $\mathbb{E}_v$and a viscous dashpot of viscosity $\mathbb{D}_v$, as shown in the upper part of Figure 3.1 for the one-dimensional case. In 1D, the stiffness is denoted E_v and the viscosity is denoted η. For the viscoelastic model, it can be demonstrated that:

$$\dot{\boldsymbol{\varepsilon}}_{\boldsymbol{v}} = \mathbb{D}_v^{-1}\colon \boldsymbol{\sigma}_v + \mathbb{E}_v^{-1}\colon \dot{\boldsymbol{\sigma}}_{\boldsymbol{v}} \tag{3.2}$$

In this thesis, we assume that $\mathbb{D}_v = \eta(1/E)\mathbb{E}$ and $\mathbb{E}_v = (E_v/E)\mathbb{E}$ with $\mathbb{E}$ Hooke matrix and E Young modulus of the standard GTN material. Consequently,

$$\dot{\boldsymbol{\sigma}}_{\boldsymbol{v}} + \frac{1}{\tau_v}\boldsymbol{\sigma}_{\boldsymbol{v}} = \mathbb{E}_v\colon \dot{\boldsymbol{\varepsilon}}_{\boldsymbol{v}} \tag{3.3}$$

where $\tau_v = \eta/E_v$ is the viscous characteristic time.

3.1.2 Integration of the viscoelasticity model

It is assumed that the evolution of the viscous strain $\boldsymbol{\varepsilon}_{\boldsymbol{v}}$ is linear in each time step $\Delta t = t_{i+1} - t_i$, i.e.,

$$\forall t \in [t_i, t_{i+1}], \qquad \boldsymbol{\varepsilon}_{\boldsymbol{v}}(t) = \boldsymbol{\varepsilon}_{\boldsymbol{v}}^{\boldsymbol{i}} + \frac{\Delta\boldsymbol{\varepsilon}_{\boldsymbol{v}}}{\Delta t}(t - t_i) + O(t^2) \tag{3.4}$$

where i is the i^{er} time step and the term $O(t^2)$ will be neglected for the integration of the viscoelastic law.

Knowing the initial condition $\boldsymbol{\sigma}_{\boldsymbol{v}}\ (t = t_i) = \boldsymbol{\sigma}_{\boldsymbol{v}}^{\boldsymbol{i}}$, Equation (3.3) with the unknown $\boldsymbol{\sigma}_{\boldsymbol{v}}$ can be directly solved:

$$\forall t \in [t_i, t_{i+1}], \quad \boldsymbol{\sigma}_{\boldsymbol{v}}(t) = e^{-\frac{t-t_i}{\tau_v}}\boldsymbol{\sigma}_{\boldsymbol{v}}^{-} + \left(1 - e^{-\frac{t-t_i}{\tau_v}}\right)\frac{\tau_v}{\Delta t}\mathbb{E}_v\colon \Delta\boldsymbol{\varepsilon}_{\boldsymbol{v}} \quad \text{with} \quad \tau_v = \frac{\eta}{E_v} \tag{3.5}$$

In particular, at $t = t_{i+1}$,

$$\boldsymbol{\sigma}_{\boldsymbol{v}}^{i+1} = e^{-\frac{\Delta t}{\tau_v}}\boldsymbol{\sigma}_{\boldsymbol{v}}^{\boldsymbol{i}} + \left(1 - e^{-\frac{\Delta t}{\tau_v}}\right)\frac{\tau_v}{\Delta t}\mathbb{E}_v\colon \Delta\boldsymbol{\varepsilon}_{\boldsymbol{v}} \quad \text{with} \quad \tau_v = \frac{\eta}{E_v} \tag{3.6}$$

The viscous stress increment is:

$$\Delta\boldsymbol{\sigma}_{\boldsymbol{v}} = -\left(1 - e^{-\frac{\Delta t}{\tau_v}}\right)\boldsymbol{\sigma}_{\boldsymbol{v}}^{\boldsymbol{i}} + \left(1 - e^{-\frac{\Delta t}{\tau_v}}\right)\frac{\tau_v}{\Delta t}\mathbb{E}_v\colon \Delta\boldsymbol{\varepsilon}_{\boldsymbol{v}} \tag{3.7}$$

and the viscous tangent stiffness is

$$\frac{d\Delta\boldsymbol{\sigma_v}}{d\Delta\boldsymbol{\varepsilon_v}} = \left(1 - e^{-\frac{\Delta t}{\tau_v}}\right)\frac{\tau_v}{\Delta t}\mathbb{E}_v \tag{3.8}$$

3.1.3 Convergence analysis

In the previous part, we have demonstrated that the viscoelastic problem consists in solving the following Cauchy problem:

$$\begin{cases} \dot{\boldsymbol{\sigma}}_{\boldsymbol{v}}(t) = -\dfrac{1}{\tau_v}\boldsymbol{\sigma_v} + \mathbb{E}_v\colon \dot{\boldsymbol{\varepsilon}}_{\boldsymbol{v}} = f(t, \boldsymbol{\sigma_v}), \qquad t \in [0, T] \\ \boldsymbol{\sigma_v}(t = 0) = 0 \end{cases} \tag{3.9}$$

where T is the total loading time and $f(t, \boldsymbol{\sigma_v}) = -\boldsymbol{\sigma_v}/\tau_v + \mathbb{E}_v\colon \dot{\boldsymbol{\varepsilon}}_{\boldsymbol{v}}$ is a continuous function which verifies the Lipschitz condition[5] since

$$\forall\left(t, \boldsymbol{\sigma}_{v,1}, \boldsymbol{\sigma}_{v,2}\right), \qquad \left|f\left(t, \boldsymbol{\sigma_{v,1}}\right) - f\left(t, \boldsymbol{\sigma_{v,2}}\right)\right| = \frac{1}{\tau_v}||\boldsymbol{\sigma_{v,1}} - \boldsymbol{\sigma_{v,2}}|| \tag{3.10}$$

We have also demonstrated that this Cauchy problem can be approximatively solved using the iterative method (see Equation (3.6)). Here we rewrite Equation (3.6) in the following form:

$$\boldsymbol{\sigma}_{\boldsymbol{v}}^{i+1} = \boldsymbol{\sigma}_{\boldsymbol{v}}^{\boldsymbol{i}} + \left(\left(e^{-\frac{\Delta \mathrm{t}}{\tau_v}} - 1\right)\boldsymbol{\sigma}_{\boldsymbol{v}}^{\boldsymbol{i}} + \left(1 - e^{-\frac{\Delta \mathrm{t}}{\tau_v}}\right)\frac{\tau_v}{\Delta t_i}\mathbb{E}_v\colon \Delta\boldsymbol{\varepsilon_v}\right) = \boldsymbol{\sigma}_{\boldsymbol{v}}^{\boldsymbol{i}} + \Phi\left(\boldsymbol{\sigma}_{\boldsymbol{v}}^{\boldsymbol{i}}, t_i, \Delta t\right) \tag{3.11}$$

We would like to demonstrate that this iterative method is consistent, stable and convergent. One can refer to (Crouzeix and Mignot, 1984) for the detailed description of consistency, stability and convergence.

Consistency

By definition, the iterative method (Equation (3.11)) is consistent to the Cauchy problem (Equation (3.9)) if for all solution $\boldsymbol{\sigma_v}$ of the Cauchy problem, we have:

$$\lim_{\Delta t \to 0}\sum_{i=0}^{n}|\boldsymbol{\sigma_v}(t_{i+1}) - \boldsymbol{\sigma_v}(t_i) - \Delta t\Phi(t_i, \boldsymbol{\sigma_v}(t_i); \Delta t)| = 0 \tag{3.12}$$

> <u>*Demonstration*</u>
>
> Firstly, we have
>
> $$\boldsymbol{\sigma_v}(t_{i+1}) - \boldsymbol{\sigma_v}(t_i) = \int_{t_i}^{t_{i+1}} \dot{\boldsymbol{\sigma}}_{\boldsymbol{v}}\, dt = \int_{t_i}^{t_{i+1}} \left(-\frac{1}{\tau_v}\boldsymbol{\sigma_v}\right) dt + \mathbb{E}_v\colon \dot{\boldsymbol{\varepsilon}}_{\boldsymbol{v}}\Delta t \tag{3.13}$$
>
> Taylor expansion of $\boldsymbol{\sigma_v}$ gives: $\boldsymbol{\sigma_v} = \boldsymbol{\sigma_v}(t_i) + \dot{\boldsymbol{\sigma}}_{\boldsymbol{v}}^{\boldsymbol{i}}\,(t - t_i) + O(\Delta t^2) = \boldsymbol{\sigma_v}\,(t_i) + O(\Delta t)$, therefore,

---

[5] A function f is called Lipschitz continuous if

$$\exists K > 0, \forall x_1, x_2, \qquad |f(x_1) - f(x_2)| \leq K|x_1 - x_2|$$

$$\boldsymbol{\sigma_v}(t_{i+1}) - \boldsymbol{\sigma_v}(t_i) \sim -\frac{\Delta t}{\tau_v}\boldsymbol{\sigma_v^i} + O(\Delta t)\mathbb{E}_v : \dot{\boldsymbol{\varepsilon}}_{\boldsymbol{v}}\Delta t \tag{3.14}$$

Secondly,

$$\Delta t\Phi(t_i, \boldsymbol{\sigma_v}(t_i); \Delta t) = \left(e^{-\frac{\Delta t}{\tau_v}} - 1\right)\boldsymbol{\sigma_v^i} + \left(1 - e^{-\frac{\Delta t}{\tau_v}}\right)\frac{\tau_v}{\Delta t}\mathbb{E}_v : \Delta\boldsymbol{\varepsilon_v} \tag{3.15}$$

Thirdly,

$$\boldsymbol{\sigma_v}(t_{i+1}) - \boldsymbol{\sigma_v}(t_i) - \Delta t\Phi(t_i, \boldsymbol{\sigma_v}(t_i); \Delta t) \sim \left(-e^{-\frac{\Delta t}{\tau_v}} + 1 - \frac{\Delta t}{\tau_v}\right)\boldsymbol{\sigma_v^i} + \left(1 - \frac{1 - e^{-\frac{\Delta t}{\tau_v}}}{\frac{\Delta t}{\tau_v}}\right)\mathbb{E}_v : \dot{\boldsymbol{\varepsilon}}_{\boldsymbol{v}}\Delta t \sim O(\Delta t^2) \tag{3.16}$$

Finally, we obtain:

$$\lim_{\Delta t \to 0}\sum_{i=0}^{n}|\boldsymbol{\sigma_v}(t_{i+1}) - \boldsymbol{\sigma_v}(t_i) - \Delta t\Phi(t_i, \boldsymbol{\sigma_v}(t_i); \Delta t)| = \lim_{\Delta t \to 0} O(\Delta t^2) = 0 \tag{3.17}$$

Stability

By definition, the iterative method is stable if there exists a constant M independent of Δt such that for all series $\boldsymbol{\sigma}_{v,1}^i$, $\boldsymbol{\sigma}_{v,2}^i$ and ϵ_i with $i = 0,1,\dots,n$ satisfying $\boldsymbol{\sigma_{v,1}^{i+1}} = \boldsymbol{\sigma_{v,1}^i} + \Delta t\phi(t_i, \boldsymbol{\sigma}_{\boldsymbol{v},1}^i; \Delta t)$ and $\boldsymbol{\sigma_{v,2}^{i+1}} = \boldsymbol{\sigma_{v,2}^i} + \Delta t\phi(t_i, \boldsymbol{\sigma_{v,2}^i}; \Delta t) + \epsilon_i$, we have:

$$\max_{0 \le i \le n}\left|\boldsymbol{\sigma}_{v,2}^i - \boldsymbol{\sigma}_{v,1}^i\right| \le M\left(\left|\boldsymbol{\sigma}_{v,2}^0 - \boldsymbol{\sigma}_{v,1}^0\right| + \sum_{i \le n}|\epsilon_i|\right) \tag{3.18}$$

The stability condition tells that a small fluctuation on $\boldsymbol{\sigma_v^i}$ leads to a small fluctuation on the solution due to the existence of the error. The demonstration of Equation (3.18) is not evident. Instead, we can demonstrate the following sufficient condition for the stability:

$$\exists N, \forall t, \forall\, \boldsymbol{\sigma}_{v,1}^i, \boldsymbol{\sigma}_{v,2}^i, \forall \Delta t, \qquad |\Phi\left(t_i, \boldsymbol{\sigma}_{v,1}^i; \Delta t\right) - \Phi\left(t_i, \boldsymbol{\sigma}_{v,2}^i; \Delta t\right)| \le N|\boldsymbol{\sigma}_{v,1}^i - \boldsymbol{\sigma}_{v,2}^i| \tag{3.19}$$

In that case, we have $M = e^{NT}$.

<u>*Demonstration*</u>

We have:

$$\left|\Phi\left(t_i, \boldsymbol{\sigma}_{v,1}^i; \Delta t\right) - \Phi\left(t_i, \boldsymbol{\sigma}_{v,2}^i; \Delta t\right)\right| = \frac{e^{-\frac{\Delta t}{\tau_v}} - 1}{\Delta t}\left|\boldsymbol{\sigma}_{v,1}^i - \boldsymbol{\sigma}_{v,2}^i\right| \le \frac{1}{\tau_v}\left|\boldsymbol{\sigma}_{v,1}^i - \boldsymbol{\sigma}_{v,2}^i\right| \tag{3.20}$$

So the iterative method is stable.

Convergence

The iterative method is consistent and stable, hence, it is convergent (Crouzeix and Mignot, 1984).

3.1.4 Illustrations

In the previous part, we have proposed an analysis of stability, consistency and convergence of the iterative method under the assumption that the strain varies linearly in each time step. In this part, we would like to illustrate it in the presence of elasticity/plasticity in 1D case, i.e., instead of using the GTN model in Figure 3.1, we use here the elastic model or a plastic model, we assume that at $t = 0^-$, the total stress is $\sigma = 0$ while at $t \geq 0^+$, the total stress remains constant: $\Delta\sigma = 0$.

Illustration in the presence of Elasticity

It is assumed that the material is elastic with Young's modulus E. The constitutive law is $\dot{\varepsilon} = (\dot{\sigma} - E\dot{\varepsilon})/E_v + (\sigma - E\varepsilon)/\eta$, i.e.,

$$\dot{\varepsilon} + \frac{EE_v}{\eta(E+E_v)}\varepsilon = \frac{E_v}{\eta(E+E_v)}\sigma + \frac{1}{E+E_v}\dot{\sigma} \tag{3.21}$$

Both analytical and numerical methods can be used to compute the value of ε.

Analytically, knowing the initial condition $\varepsilon(t=0) = \sigma/(E+E_v)$, one obtains:

$$\varepsilon(t) = \frac{\sigma}{E}\left(1 - \frac{E_v}{E+E_v} e^{-\frac{E}{(E+E_v)\tau_v}t}\right) \tag{3.22}$$

Numerically, we have

$$\Delta\sigma = \Delta\sigma_c + \Delta\sigma_v = E\Delta\varepsilon - \left(1 - e^{-\frac{\Delta t}{\tau_v}}\right)\sigma_v^i + \frac{\tau_v E_v}{\Delta \mathrm{t}}\left(1 - e^{-\frac{\Delta t}{\tau_v}}\right)\Delta\varepsilon = 0 \tag{3.23}$$

Therefore,

$$\Delta\varepsilon = \frac{\left(1 - e^{-\frac{\Delta t}{\tau_v}}\right)\sigma_v^i}{E + \frac{\tau_v E_v}{\Delta \mathrm{t}}\left(1 - e^{-\frac{\Delta t}{\tau_v}}\right)} \tag{3.24}$$

Knowing that $\varepsilon(t=0) = \sigma/(E+E_v)$ and $\sigma_v(t=0) = E_v\varepsilon(t=0)$, we can update $\Delta\varepsilon$ using Equation (3.24). With σ_v^i and $\Delta\varepsilon$, we can update σ_v^{i+1} using Equation (3.6).

Figure 3.2(a) plots the evolution of the analytical strain ε_a and the numerical strain ε_n as a function of t/T for different $\Delta t/T$. Here, T corresponds to the total loading time. It shows that for any time steps Δt, the numerical algorithm is free of oscillation. In particular, the maximum value $\varepsilon_M = 0.25\%$ corresponds to the case where the viscoelastic model does not exist since in that case we have directly $\varepsilon_M = \sigma/E = 0.25\%$. This indicates that due to the viscosity, the inviscid solution is slowly attained (stabilization effect). The rate depends on the value of τ_v. Therefore, it is necessary to have $\tau_v \ll T$ so that the viscous effect disappears in the end.

Figure 3.2 (b) plots the error ϵ as a function of t/T for different $\Delta t/T$ where the error is defined as:

$$\epsilon = \left|\frac{\varepsilon_a - \varepsilon_n}{\varepsilon_a}\right| \times 100\% \tag{3.25}$$

From this figure, it can be seen that for a given $\Delta t/T$, the error first increases and then decreases which indicates again that τ_v should be much smaller than T so that the viscous effect disappears in the end. Besides, for a given t/T, the error increases with $\Delta t/T$ which reveals that the time step $\Delta t/T$ should be sufficiently small so as to reduce the oscillation. In conclusion, to obtain a converged solution, we should have:

$$\frac{\Delta t}{T} < \frac{\tau_v}{T} \ll 1 \tag{3.26}$$

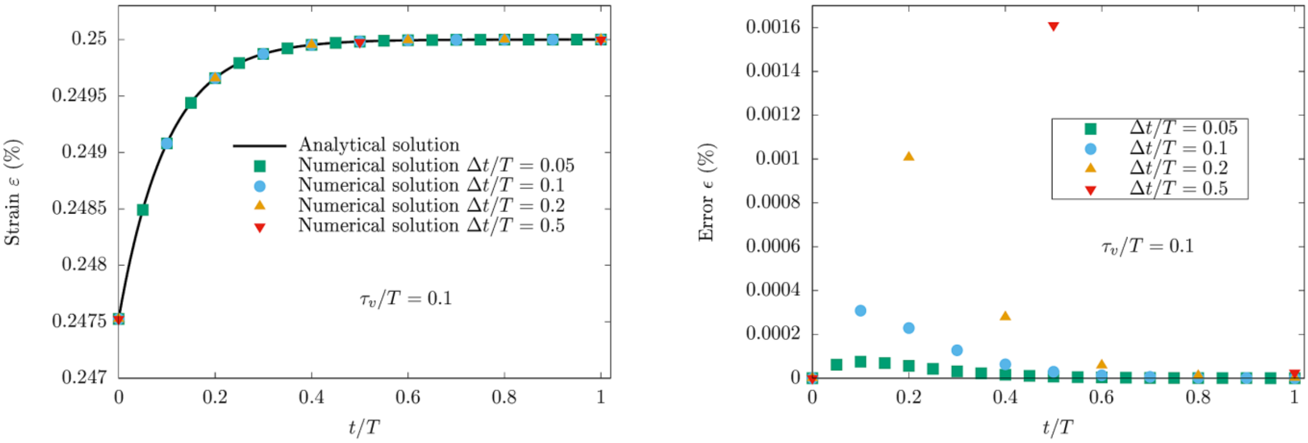

(a)

(b)

Figure 3.2. Evolution of strain and error ($E = 200000\ MPa, E_v = 2000\ MPa, \sigma = 500\ MPa, \tau_v/T = 0.1$)

Illustration in the presence of plasticity

It is assumed that the material behavior is elastic-plastic with linear isotropic hardening $\bar{\sigma}(\kappa) = \sigma_0 + r_h\kappa$ with σ_0 the yield stress, κ the hardening variable and $r_h > 0$ the hardening parameter. Here, the stress and the strain in elastic-plastic part are denoted $(\sigma_c, \varepsilon_c)$.

It is obvious that there exist three cases:

- If $\sigma < \sigma_0$, then we have $\forall t,\ \sigma_c(t) < \sigma < \sigma_0$ since $\sigma = \sigma_c + \sigma_v$ and $\forall t, \sigma_v(t) \geq 0$. In this case, the material is always elastic (see the previous part)
- If $\sigma \geq \sigma_0$ and $\sigma_c(t=0) \leq \sigma_0$, then the material is first elastic and then plastic. In this case, $\sigma_c(t=0) = E\sigma/(E+E_v) < \sigma_0$, i.e., $\sigma_0 \leq \sigma \leq (E_v/E + 1)\sigma_0$
- If $\sigma > \sigma_0$ and $\sigma_c(t=0) > \sigma_0$, i.e., $\sigma > (E_v/E + 1)\sigma_0$, then the material is always plastic

It is obvious that in the absence of the viscosity, the second case does not exist. Therefore, it is necessary to have $E_v/E \ll 1$ such that the viscosity can be neglected. In the following, we assume that $\sigma = 500\ MPa, E =$ 200000 MPa, $E_v = 2000$ MPa, $r_h = 2000$ MPa and $\sigma_0 = 450$ MPa. In that case, we have $\sigma > (E_v/E + 1)\sigma_0$ and the material is always plastic.

The set of equations to be solved is:

$$\begin{cases} \sigma_c = \sigma_0 + r_h\varepsilon_c^p \\ \sigma_c = E(\varepsilon - \varepsilon_c^p) \\ \sigma = \sigma_c + \sigma_v \\ \dfrac{\dot{\sigma}_v}{E_v} + \dfrac{\sigma_v}{\eta} = \dot{\varepsilon}_c^p + \dfrac{\dot{\sigma}_c}{E} \end{cases} \tag{3.27}$$

Both analytical and numerical method can be used to solve this equation.

Analytically, Equation (3.27) leads to a differential equation on σ_c with $\sigma_c(t=0) = E\sigma/(E+E_v)$:

$$\dot{\sigma_c} + \frac{1}{\tau_c}\sigma_c = \frac{\sigma}{\tau_c}\ , \qquad \text{with } \tau_c = \eta\left(\frac{1}{E} + \frac{1}{r_h} + \frac{1}{E_v}\right) \tag{3.28}$$

It yields:

$$\sigma_c = \sigma\left(1 - \frac{E_v}{E+E_v}e^{-\frac{t}{\tau_c}}\right) \tag{3.29}$$

Therefore,

$$\varepsilon = \varepsilon_c = \frac{\sigma_c - \sigma_0}{r_h} + \frac{\sigma_c}{E} = \left(\frac{1}{r_h} + \frac{1}{E}\right)\left(1 - \frac{E_v}{E+E_v}e^{-\frac{t}{\tau_c}}\right)\sigma - \frac{\sigma_0}{r_h} \tag{3.30}$$

It can be noticed that $\varepsilon(t \gg \tau_c) = \sigma/E\ + (\sigma - \sigma_0)/r_h$. Apparently, if there is no viscosity, we have directly $\forall t,\ \varepsilon(t) = \sigma/E\ + (\sigma - \sigma_0)/r_h$.

Numerically, since $\dot{\varepsilon} = \dot{\sigma_c}/E + (\dot{\sigma_c} - \dot{\sigma_0})/r_h$, the increment of σ_c is

$$\Delta\sigma_c = \frac{Er_h}{E+r_h}\Delta\varepsilon \tag{3.31}$$

So the increment of σ is:

$$\begin{aligned}\Delta\sigma &= \Delta\sigma_c + \Delta\sigma_v \\ &= \frac{Er_h}{E+r_h}\Delta\varepsilon - \left(1 - e^{-\frac{\Delta t}{\tau_v}}\right)\sigma_v^i + \frac{\tau_v E_v}{\Delta \mathrm{t}}\left(1 - e^{-\frac{\Delta t}{\tau_v}}\right)\Delta\varepsilon \\ &= \left(\frac{Er_h}{E+r_h} + \frac{\tau_v E_v}{\Delta \mathrm{t}}\left(1 - e^{-\frac{\Delta t}{\tau_v}}\right)\right)\Delta\varepsilon - \left(1 - e^{-\frac{\Delta t}{\tau_v}}\right)\sigma_v^i\end{aligned} \tag{3.32}$$

Since $\Delta\sigma = 0$, we have

$$\Delta\varepsilon = \frac{\sigma_v^i\left(1 - e^{-\frac{\Delta t}{\tau_v}}\right)}{\frac{Er_h}{E+r_h} + \frac{\tau_v E_v}{\Delta t}\left(1 - e^{-\frac{\Delta t}{\tau_v}}\right)} \tag{3.33}$$

Knowing that $\sigma_v(t=0) = E_v\sigma/(E+E_v)$, $\sigma_c(t=0) = E\sigma/(E+E_v)$ and $\varepsilon(t=0) = \sigma_c(t=0)/E + (\sigma_c(t=0) - \sigma_0)/r_h)$, we update $\Delta\varepsilon$ using Equation (3.33). With σ_v^{i+1} and $\Delta\varepsilon$, we update σ_v^+ using Equation (3.6).

Figure 3.3 (a) plots the evolution of the analytical strain ε_a and the numerical strain ε_n as a function of t/T for different $\Delta t/T$. It shows that for sufficiently small Δt (in our case, $\Delta t/T \leq 0.1 \sim \tau_v/T$), the numerical algorithm is free of oscillation. The maximum value $\varepsilon_{max} = 0.0275$ corresponds to the case where the viscoelastic model does not exist. This indicates that due to the viscosity, the inviscid solution is slowly attained (stabilization effect). The velocity depends on the value of τ_v. Therefore, it is necessary to have $\tau_v \ll T$ so that the viscous effect disappears in the end.

Figure 3.3 (b) plots the error ϵ as a function of t/T for different $\Delta t/T$. From this figure, it can be seen that for a given $\Delta t/T$, the error first increases and then decreases which indicates again that τ_v should be much smaller than T so that the viscous effect disappears in the end. Besides, for a given t/T, the error increases with $\Delta t/T$ which reveals that the time step $\Delta t/T$ should be sufficiently small so as to reduce the numerical oscillation.

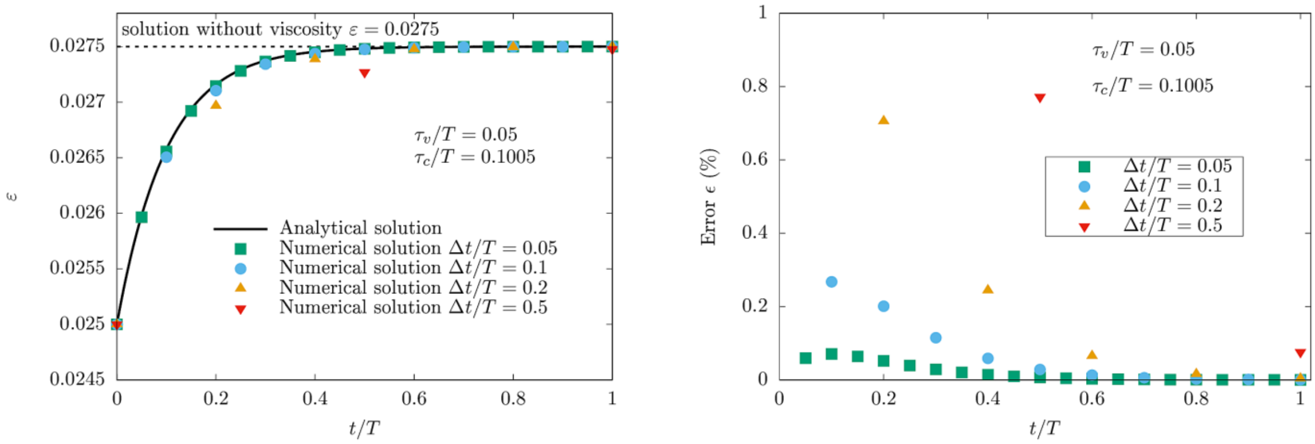

(a) (b)

Figure 3.3. Evolution of strain ($E = 200000\ MPa, E_v = 2000\ MPa, \tau_v/T = 0.05, \sigma = 500\ MPa, \sigma_0 = 450\ MPa, r_h = 2000\ MPa$)

3.1.5 Effects of the viscoelastic parameters

In the previous part, we have illustrated the effect of the viscosity in two simple cases. However, these two cases are not quite realistic due to $\sigma =$ constant. In this part, we would like to illustrate the effect of the viscosity in two real cases: simulations of NT and CT. The nonlocal GTN law is used for the damage part of the law. Without otherwise specified, the parameters used in this simulation are shown in Table 3.1. In particular, T in Table 3.1 is the total load level.

Table 3.1. The nominal values of the parameters used in the simulations

Elasticity	Young modulus E	200000 MPa
	Poisson ratio ν	0.3
Plasticity	Yield stress σ_0	500 MPa
	Hardening variable κ_0	0.0025
	Hardening exponent n	0.1
Damage	Initial porosity f_0	0.001
	Critical porosity f_c	0.05
	Porosity at failure f_F	0.25
	Material constants (q_1, q_2)	(1.5,1.0)
Nonlocality	Nonlocal length l_{nl}	0.3 mm
Numerical parameters	Nonlocal penalty parameter r_{nl}	$10\sigma_0$
	Incompressibility penalty parameter r_{inco}	$10\sigma_0$
	Viscoelastic modulus E_v	$0.001E$
	Viscoelastic time τ_v	$0.01T$

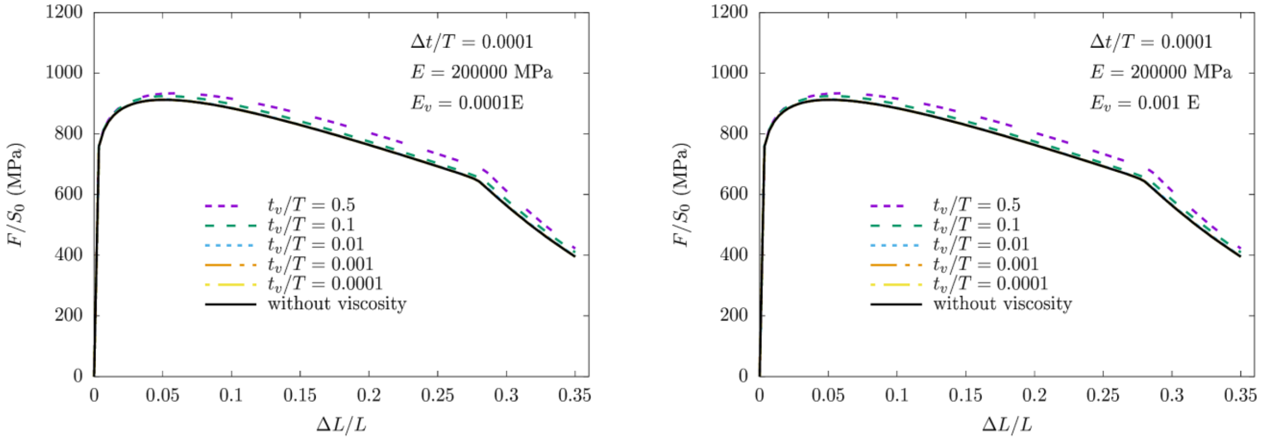

(a) $E_v = 0.0001E$ (b) $E_v = 0.001E$

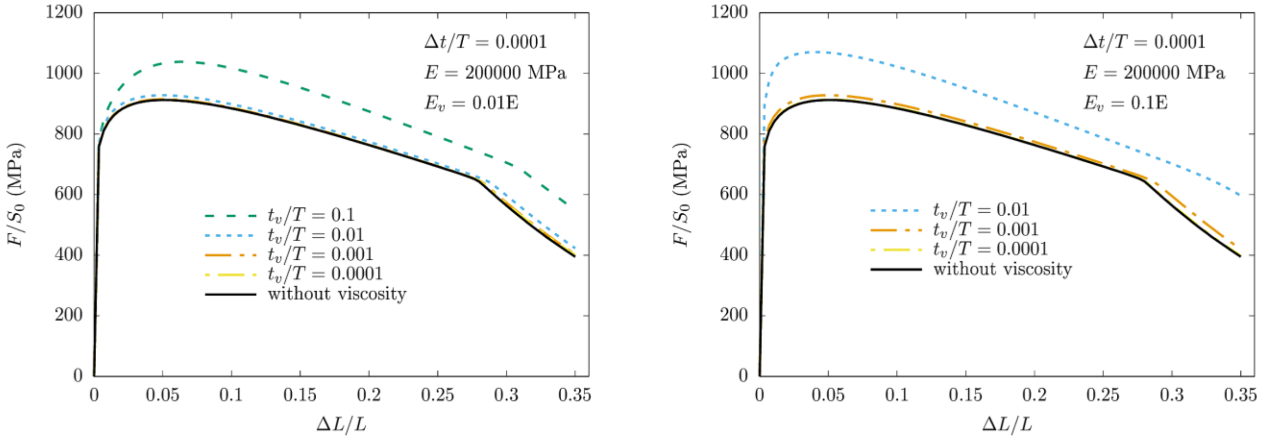

(c) $E_v = 0.01E$ (d) $E_v = 0.1E$

Figure 3.4. Force-displacement curves for different E_v and τ_v

NT simulations

By performing NT simulations, we would like to evaluate the influence of the viscous parameters on the global material response.

The mesh for the NT specimens can be found in Figure 2.24. Simulations of NT are carried out for $\tau_v/T = 0.0001, 0.001, 0.01, 0.1, 0.5$ and $E_v/E = 0.0001, 0.001, 0.01, 0.1$. The predefined time step $\Delta t/T$ is set to 10^{-4} to have a time-converged solution.

Figure 3.4 plots the force-displacement curves obtained from the simulations of NT for different E_v and τ_v. The curve obtained from the simulation without viscoelasticity is also shown in this figure. We recall that the viscous effect decreases with the value of τ_v and/or E_v. The results show that firstly, a too large value for τ_v or E_v may lead to an overestimation on the force and postpone crack initiation, and secondly, the influence of the viscosity on global response is negligible when $E_v\tau_v \leq 10^{-5}ET$. In practice, it is suggested that $E_v/E \leq 0.01$ such that the viscous stiffness is negligible to the material stiffness. Besides, the result also indicates that as long as $E_v\tau_v/ET \leq 10^{-5}$, the viscous solution converges to the inviscid solution even if $\tau_v/T \sim \Delta t/T$. We recall here that in the case of a purely viscoelastic material, we should have $\Delta t/T < \tau_v/T$ to have a converged solution.

In our work, we use $E_v/E = 0.001$ and $\tau_v/T = 0.01$. In this case, the predefined load increment $\Delta t/T$ is suggested to be smaller than τ_v/T.

CT simulations

Different from NT simulations, ductile tearing (lots of broken elements) can be observed in CT simulations. These broken elements can become distorted and thus affect the computational convergence. So here we would like to assess the robustness of the adopted numerical viscoelastic scheme for the treatment of element distortion.

The geometry and the mesh (with reduced integration, i.e., 4 integration points in each quadrilateral element) for the CT specimens can be found in Figure 3.5. Usual symmetry and boundary/loading conditions are accounted for. The damage parameter q_2 is set to $q_2 = 1.2$. Two Simulations of CT are carried out: one without viscoelasticity and another with viscoelasticity ($\tau_v/T = 0.01$, $E_v = 0.001E$). Here, the final load level corresponds to an $COD = 8$ mm.

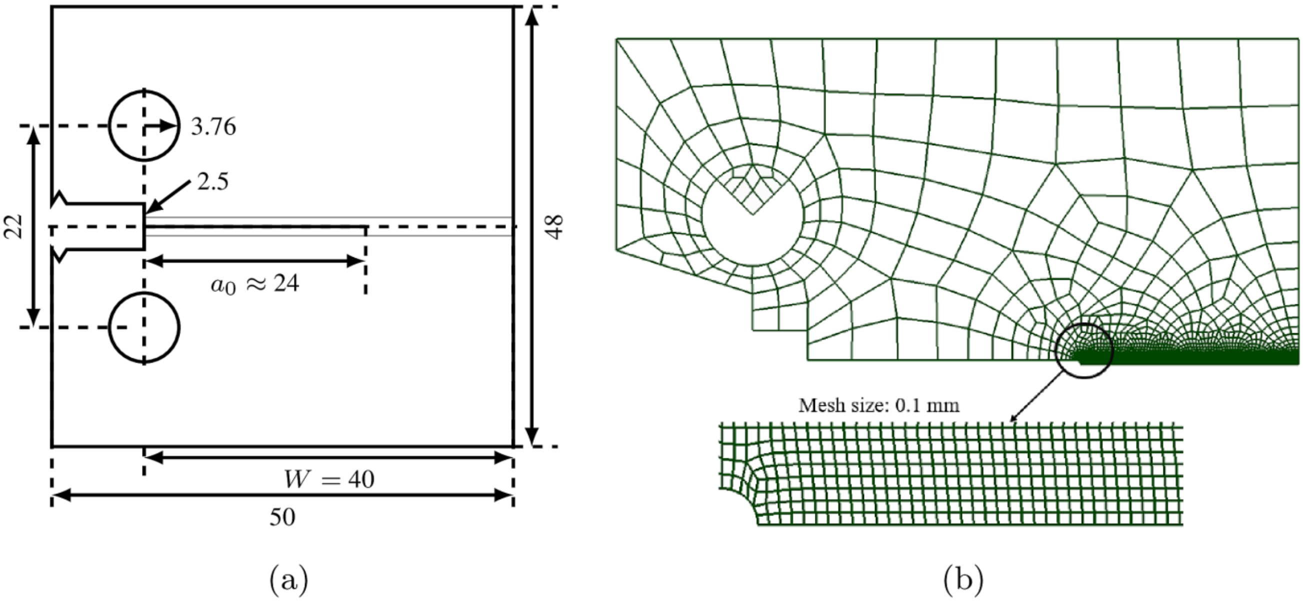

(a) (b)

Figure 3.5. (a) Geometry and (b) Mesh of CT

Figure 3.6 plots the force-COD curves with and without viscosity. It is observed that the results without and with viscosity almost overlap, which indicate that the chosen values of E_v and τ_v do not affect the global reponse. Besides, a convergence problem appears when $COD \approx 3$ mm for the simulation without viscoelasticity, while for the simulation with viscoelasticity, there is not convergence problem.

Figure 3.7 plots the distribution of the porosity in deformed configuration for $COD = 3$ mm and $COD = 8$ mm. Note that here each quadrangle corresponds to an integration point. For $COD = 3$ mm, the comparison between Figure 3.7(a) (without viscoelasticity) and Figure 3.7(b) (with viscosity) tells that the viscosity can reduce the element distortion and stabilize the solution. Note that due to the low triaxiality, one or several integration points in the crack-tip nearby zone are never broken. This problem will be discussed later in Chapter 4 and one solution will be given in Appendix A5.6. Thanks to the viscoelasticity, the simulation is performed up to the final load ($COD = 8$ mm). No distorted element is observed during crack propagation.

In conclusion, the viscoelasticity is capable of reducing, even avoiding element distortion and thus helps the convergence of the simulation.

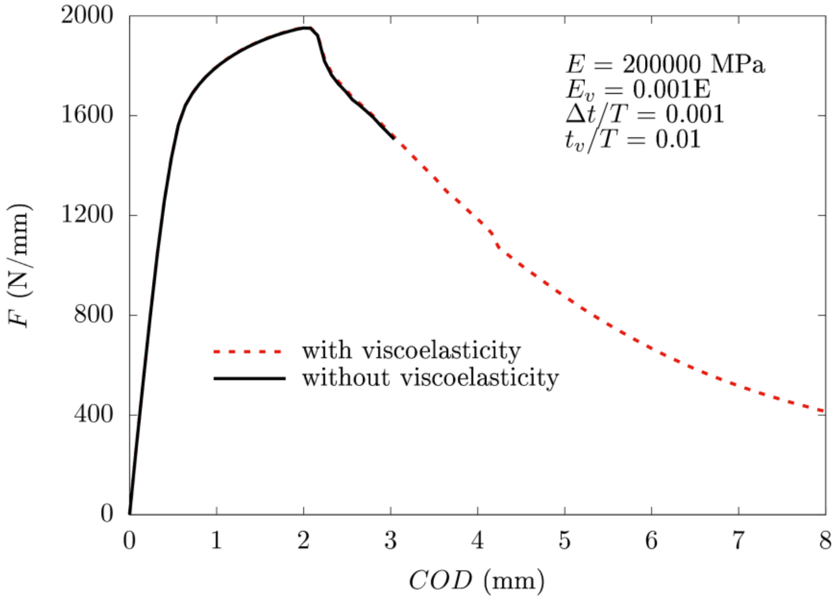

Figure 3.6. Force-COD curves for the cases without and with viscoelasticity

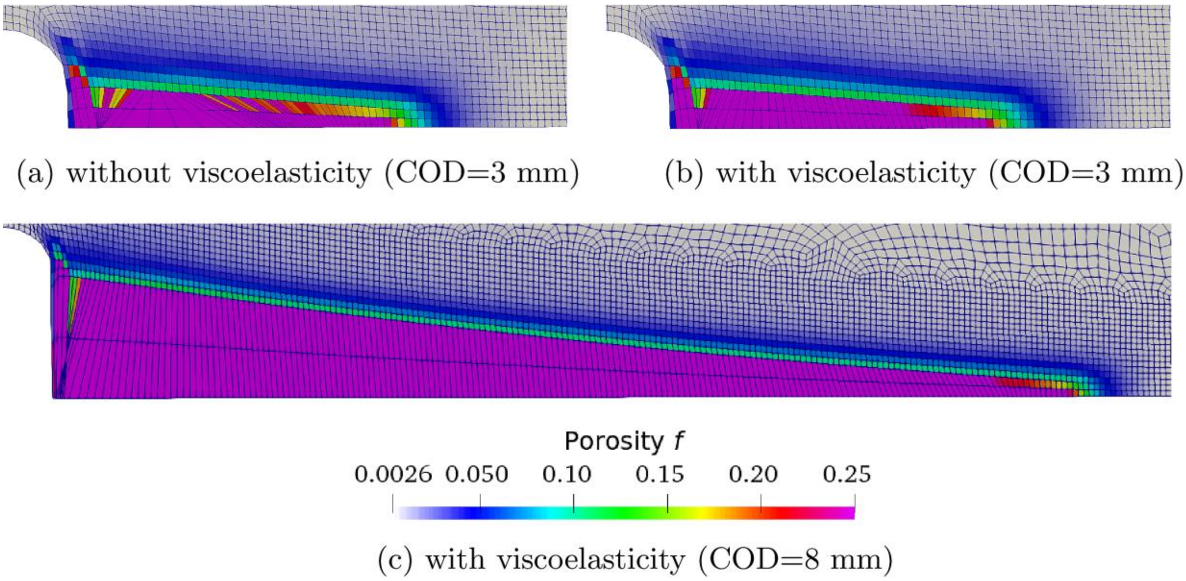

(a) without viscoelasticity (COD=3 mm)

(b) with viscoelasticity (COD=3 mm)

(c) with viscoelasticity (COD=8 mm)

Figure 3.7. Distribution of porosity field in deformed configuration without or with viscoelasticity for different COD

3.2 Convergence criterion for Newton-Raphson method at global level

A system of nonlinear algebraic equations is often solved by means of a Newton-Raphson method. This method is iterative and is repeated until the residual vector is “close” to zero. In our work, the residual vector $\underline{R}$ is $\underline{R} = \underline{F}^i - \underline{F}^e$ with $\underline{F}^e = (\underline{F}^{ext}, 0, 0, 0, 0)$ the external force and $\underline{F}^i = \left(\underline{F}^{\underline{u}}, F^a, F^l, F^P, F^\theta\right)$ the internal force which is:

$$\begin{cases} \underline{F}^{\underline{u}} = \sum_g w_g\left(\overline{\boldsymbol{T}}_{D,g} + P_g \boldsymbol{I} + r_{inco}\left(\mathrm{tr}\left(\boldsymbol{E_g}\right) - \theta_g\right)\boldsymbol{I}\right) : \mathbb{P}_g : \left(\boldsymbol{F}_{\boldsymbol{g}}^{\mathbf{T}} . \underline{\boldsymbol{B}}_g^{\underline{u}}\right) \\ F^a = \sum_g w_g \left(c\boldsymbol{\nabla} a_g . \underline{B}_g^a + \left(l_g + r_{nl}\left(a_g - \kappa_g\right)\right) N_g^a\right) \\ F^l = \sum_g w_g\left(a_g - \kappa_g\right) N_g^l \\ F^P = \sum_g w_g\left(\mathrm{tr}\left(\boldsymbol{E_g}\right) - \theta_g\right) N_g^P \\ F^\theta = \sum_g w_g \left(\frac{1}{3}\mathrm{tr}\left(\overline{\boldsymbol{T}}_g\right) - P_g - r_{inco}\left(\mathrm{tr}\left(\boldsymbol{E_g}\right) - \theta_g\right)\right) N_g^\theta \end{cases} \tag{3.34}$$

In order to check whether $\underline{R}$ is close to zero, a classical criterion consists in checking whether the L-infinity[6] norm of $\underline{R}$ is smaller than a predefined small value ϵ:

$$\left\|\underline{R}\right\|_\infty \leq \epsilon \tag{3.35}$$

This criterion is often not satisfactory since the units of the different components of $\underline{R}$ can be different. Indeed, in this work, $\underline{R}^{\underline{u}}, R^a$ and R^θ have the same unit as stress, while R^P and R^l have the same unit as strain. In this case, the value of ϵ may be too large for certain residuals and/or too small for others. Moreover, the value of each components of $\underline{F}^i$ depends on local element size, the criterion in Equation (3.35) is easier to be fulfilled with smaller element size (Badel and Lorentz, 2011).

Therefore, it is necessary to use a criterion which is able to overcome these disadvantages. In this work, an extension of the criterion proposed in (Badel and Lorentz, 2011) is used. In this criterion, the following properties hold:

- A reference force $\underline{F}_{ref} \in \mathbb{R}^n$ (with n the number of degrees of freedom) is set up from some user-defined values;
- The criterion is controlled by a small dimensionless value ϵ;
- The criterion is independent of mesh size.

The key point of this criterion is to define the reference force $\underline{F}_{ref}$. Each component of $\underline{F}_{ref}$ reflects the magnitude of each component of $\underline{R}$. Then we compare $\underline{R}$ and $\underline{F}_{ref}$ component by component:

$$\forall j \in DOF, \qquad \left|R_j\right| \leq \epsilon\left(\underline{F}_{ref}\right)_j \tag{3.36}$$

---

[6] L-infinity norm: the largest magnitude among each element of a vector.

In view of the units of each component of $\underline{R}$, the reference force is computed from a user-defined scalar stress σ_{ref}, a user-defined scalar strain ε_{ref} and a user-defined hardening variable κ_{ref}. The expression of $\underline{F}_{ref}$ is defined on the basic of the expression of $\underline{R}$:

$$\begin{cases} \underline{F}_{ref}^{u} = \sum\limits_{g} \left(w_g \left(\sigma_{ref} \underline{I} \otimes \underline{I} + \min\left(\sigma_{ref}, r_{inco} \varepsilon_{ref}\right) \underline{I} \otimes \underline{I} \right) : \left| \mathbb{P}_g : \left(\boldsymbol{F}_{\boldsymbol{g}}^{\mathbf{T}} . \underline{\boldsymbol{B}}_g^{u} \right) \right| \right) - \underline{F}^{\boldsymbol{e}} \\ F_{ref}^{a} = \sum\limits_{g} w_g \left(\min(\sigma_{ref}, r_{nl} \kappa_{ref}) N_g^{a} \right) \\ F_{ref}^{l} = \sum\limits_{g} w_g \kappa_{ref} N_g^{l} \\ F_{ref}^{P} = \sum\limits_{g} w_g \varepsilon_{ref} N_g^{P} \\ F_{ref}^{\theta} = \sum\limits_{g} w_g (\min(\sigma^{ref}, r_{inco} \varepsilon_{ref})) N_g^{\theta} \end{cases} \tag{3.37}$$

where $\underline{I} = (1 \quad 1 \quad 1)^T$. Note that the value of $\underline{F}_{ref}^{u}$ depends on the chosen basis since $\left| \mathbb{P}_g : \left(\boldsymbol{F}_{\boldsymbol{g}}^{\mathbf{T}} . \underline{\boldsymbol{B}}_g^{u} \right) \right|$ is not a tensor but a matrix[7], but the order of the magnitude is preserved for any change of basis.

With the definition of $\underline{F}_{ref}$ given in Equation (3.37), each component of $\underline{F}_{ref}$ has its correct unit. As for the value of $(\sigma_{ref}, \varepsilon_{ref}, \kappa_{ref})$, one can take for example $(\sigma_{ref}, \varepsilon_{ref}, \kappa_{ref}) = (\sigma_0, 0.01, 0.01)$. In this work, the value of ϵ is set to 10^{-3}.

---

[7] In 2D, a tensor is commonly represented by a matrix that results from applying it to different basis. Do not forget that any such matrix is just a representation of the tensor, but not the tensor itself. Here, assume that a tensor A is represented by $\left(A_{ij}\right)_{0 \le i \le m, 0 \le j \le n}$ in a given basis, we define the matrix |A| as $|A| = \left(|A_{ij}|\right)_{0 \le i \le m, 0 \le j \le n}$.

3.3 Staggered and implicit schemes at local level

3.3.1 Set of equations

In this work, the displacement $\underline{u}$, the nonlocal variable a, the Lagrange multiplier l are discretized on the basis of Lagrange shape functions. They correspond to the nodal unknowns of the discretized problem. The strain $\boldsymbol{E}$, the stress $\boldsymbol{T}$, the plastic strain $\boldsymbol{E^p}$, the hardening variable κ, the porosity f are sampled at the integration points. The stress $\boldsymbol{T}$, the internal variables $(\boldsymbol{E^p}, \kappa, f)$ are thus obtained through the integration of the constitutive equations at the integration point level. We recall the nonlocal GTN constitutive relations:

$$\begin{cases} \boldsymbol{T} = \mathbb{E}:(\boldsymbol{E} - \boldsymbol{E^p}) \\ G = \left(\dfrac{T_{eq}}{T_*}\right)^2 + 2q_1 f^* \cosh\left(\dfrac{3}{2} q_2 \dfrac{T_H}{T^*}\right) - 1 - (q_1 f^*)^2 \equiv 0 \\ F = \dfrac{T^*}{J} - \bar{\sigma}(\kappa) + l + r_{nl}(a - \kappa) \\ \dot{\kappa} = \lambda \dfrac{\partial F}{\partial A}, \\ \dot{\boldsymbol{E}}^{\boldsymbol{p}} = \lambda \dfrac{\partial F}{\partial \boldsymbol{\sigma}} \\ \lambda \geq 0,\ F \leq 0,\ \lambda F = 0 \\ f = f_g + f_n = (1 - f)\mathrm{tr}\big(\dot{\boldsymbol{E}}^{\boldsymbol{p}}\big) + B_n(\kappa)\dot{\kappa} \\ f^* = \begin{cases} f, & f < f_c \\ f_c + \dfrac{\dfrac{1}{q_1} - f_c}{f_F - f_c}, & f \geq f_c \end{cases} \end{cases} \tag{3.38}$$

In order to ensure the existence and the uniqueness of the solution of the above set of equations, (Enakoutsa et al., 2007) proposed to use an implicit time-discretization with respect to $(\boldsymbol{E^p}, \kappa)$ for a given value of the porosity f and then to update the porosity. This proposal corresponds to a staggered scheme. Compared to the fully implicit scheme, the staggered scheme allows for easier convergence of the elastoplastic iterations. Besides, according to our numerical experience, without any “special” numerical techniques, it is almost impossible to carry on the simulation up to complete failure of the structure when the fully implicit scheme is used. However, it should be noticed that the staggered scheme leads to a state which does not respect the constitutive law at the end of a time step and thus a non-equilibrium is generated in the next time step.

For the staggered scheme, (Zhang et al., 2018) showed that Equation (3.38) can be simplified as:

$$\begin{cases} \bar{G}(p, T_*) = \left(\dfrac{T_{eq}^e \bar{q}(p, T_*)}{T_*}\right)^2 + 2q_1 f^* \cosh\left(\dfrac{3}{2} q_2 \dfrac{T_H^e p}{T^*}\right) - 1 - (q_1 f^*)^2 = 0 \\ \bar{M}(p, T_*) = -\bar{T}_*\left(\bar{\lambda}(p, T_*)\right) + T^* = 0 \end{cases} \tag{3.39}$$

where p and q are defined by $T_h^e = pT_h, T_{eq}^e = qT_{eq}$ and

$$\begin{cases} \bar{q}(p,T_*) = \dfrac{T_*\bar{\Lambda}\left(\dfrac{T_h^e p}{T_*}\right)}{T_*\bar{\Lambda}\left(\dfrac{T_h^e p}{T_*}\right) + \dfrac{\mu}{\kappa}T_h^e(1-p)} \\ \bar{\lambda}(p,T_*) = \dfrac{JT_h^e(1-p)}{3K\bar{\Lambda}\left(\dfrac{T_h^e p}{T_*}\right)\bar{\Theta}\left(\dfrac{T_h^e p}{T_*}, \dfrac{T_{eq}^e\bar{q}(p,T_*)}{T_*}\right)} \end{cases} \tag{3.40}$$

with

$$\begin{cases} \bar{\Lambda}(x) = \dfrac{1}{2}q_1 q_2 f_* \sinh\left(\dfrac{3}{2}q_2 x\right) \\ \bar{\Theta}(x,y) = \left(y^2 + 3x\bar{\Lambda}(x)\right)^{-1} \end{cases} \tag{3.41}$$

The existence and the uniqueness of the solutions (p, T_*) has been demonstrated in (Zhang et al., 2018).

For the fully implicit scheme, it can be demonstrated that Equation (3.38) can be reduced to:

$$\begin{cases} \bar{G}(p,T_*,f) = \left(\dfrac{T_{eq}^e\bar{q}(p,T_*,f)}{T_*}\right)^2 + 2q_1 f^* \cosh\left(\dfrac{3}{2}q_2\dfrac{T_H^e p}{T^*}\right) - 1 - (q_1 f^*)^2 = 0 \\ \bar{M}(p,T_*,f) = -\bar{T}_*\left(\bar{\lambda}(p,T_*,f)\right) + T^* = 0 \\ \bar{N}(p,T_*,f) = \Delta f - \dfrac{1-f}{J}\bar{\lambda}(p,T_*,f)\mathrm{tr}\left(\dfrac{\partial T_*}{\partial \boldsymbol{T}}\right) - \bar{B}_n\left(\bar{\lambda}(p,T_*,f)\right)\bar{\lambda}(p,T_*,f) = 0 \end{cases} \tag{3.42}$$

where

$$\begin{cases} \bar{q}(p,T_*,f) = \dfrac{T_*\bar{\Lambda}\left(\dfrac{T_h^e p}{T_*},f\right)}{T_*\bar{\Lambda}\left(\dfrac{T_h^e p}{T_*},f\right) + \dfrac{\mu}{\kappa}T_h^e(1-p)} \\ \bar{\lambda}(p,T_*,f) = \dfrac{JT_h^e(1-p)}{3K\bar{\Lambda}\left(\dfrac{T_h^e p}{T_*},f\right)\bar{\Theta}\left(\dfrac{T_h^e p}{T_*}, \dfrac{T_{eq}^e\bar{q}(p,T_*,f)}{T_*},f\right)} \\ \dfrac{\partial T_*}{\partial \boldsymbol{T}}(p,T_*,f) = \bar{\Theta}\left(\dfrac{T_h^e p}{T_*}, \dfrac{T_{eq}^e\bar{q}(p,T_*,f)}{T_*},f\right)\left[\dfrac{3}{2}\dfrac{\boldsymbol{T_D}}{T_*} + \bar{\Lambda}\left(\dfrac{T_h^e p}{T_*},f\right)\boldsymbol{I}\right] \end{cases} \tag{3.43}$$

with

$$\begin{cases} \bar{\Lambda}(x,f) = \dfrac{1}{2}q_1 q_2 f_* \sinh\left(\dfrac{3}{2}q_2 x\right) \\ \bar{\Theta}(x,y,f) = \left(y^2 + 3x\bar{\Lambda}(x,f)\right)^{-1} \end{cases} \tag{3.44}$$

We did not succeed in demonstrating the existence nor the uniqueness of the solution for the implicit scheme.

The solution algorithm of the staggered scheme can be found in (Zhang et al., 2018) and the solution algorithm of the fully implicit scheme can be found in Appendix A4. These two schemes have been implemented in Code_Aster, an open-source finite element software developed at EDF (www.code-aster.org).

3.3.2 Comparison

In order to compare these two schemes, several simulations of simple tensile test on Representative Volume Element (RVE) assuming plane strain conditions are performed. The advantage to perform RVE simulations, but not NT or CT simulations is that the predefined load-step will not be refined during the simulation in most cases. The initial length and the initial width of RVE2D are the same ($L_{x0} = L_{y0} = L_0 = 1\ \mathrm{mm}$). The corresponding mesh is a single quadrilateral element with 4 integration points. The prescribed deformation gradient tensor is:

$$\boldsymbol{F} = \begin{pmatrix} F_{xx} & 0 \\ 0 & F_{yy} \end{pmatrix} = \begin{pmatrix} F_{xx} & 0 \\ 0 & \alpha t + 1 \end{pmatrix} \tag{3.45}$$

where α is a constant, $t \in [0,1]$ is the load level.

The initial porosity is set to $f_0 = 0.01$, other material parameters are listed in Table 3.1.

Figure 3.8 plots the evolution of the porosity f and the force F as a function of the stretch defined by $\Delta L_y / L_0 = \alpha t = F_{yy} - 1$. It is observed that when the load increment is not small enough, the staggered scheme underestimates the porosity and thus overestimates the global force. The opposite trend is observed for the implicit scheme. Fortunately, when the load increment is sufficiently small, the two schemes converge to the same result. Therefore, both schemes need small load increments to obtain converged solutions.

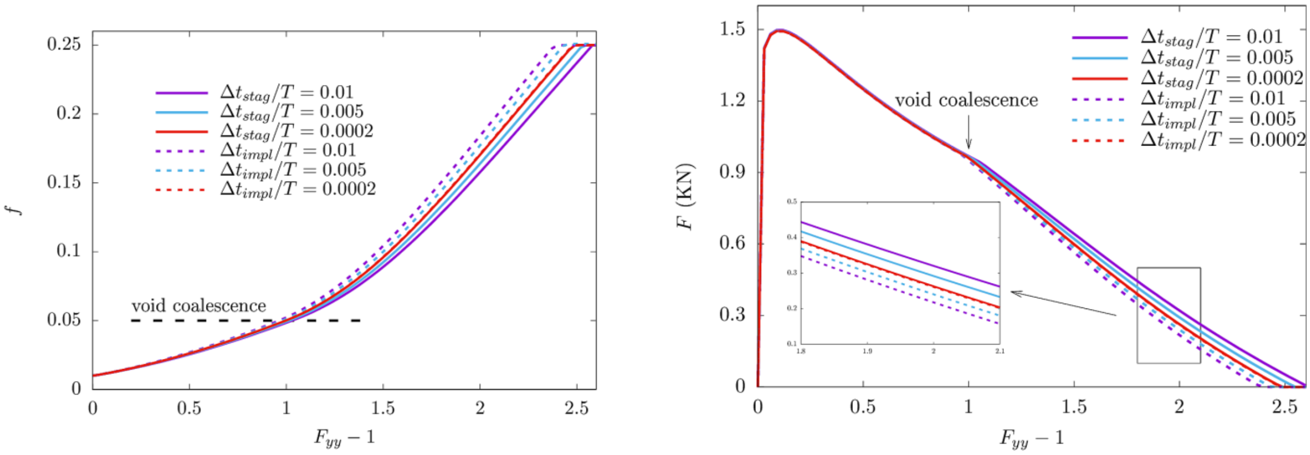

(a) (b)

Figure 3.8. (a) Evolution of the porosity with stretch; (b) Force-displacement curves

3.4 Adaptive load increment

3.4.1 Error estimation

To see the importance of small load increments, we define the following error estimator:

$$\epsilon\left(\frac{\Delta L}{L}\right) = \left|\frac{f - f_{conv}}{f_F}\right|_{\Delta L/L} \tag{3.46}$$

where f_{conv} is the convergent solution for the porosity.

We still focus on the simulations presented in Section 3.3.2. Figure 3.9(a) plots the evolution of the error ϵ with the stretch. It is observed that on the one hand, both schemes induce some error on f from the very beginning of the simulation and this error strongly depends on the predefined load increment $\Delta t/T$ and thus on the damage increment Δf; on the other hand, the error increases very rapidly at void coalescence stage (i.e., the deformation gradient $F_{yy} - 1 \geq 1$). These two observations indicate that the error is directly linked to the damage increment Δf.

Figure 3.9(b) compares the error induced by different predefined load increment ($\Delta t/T = 0.005, 0.01$). It shows that the ratio of $\epsilon_{0.01}/\epsilon_{0.005}$ remains almost constant (around 2). That indicates that the error may be proportional to Δt ($\epsilon \propto \Delta t$).

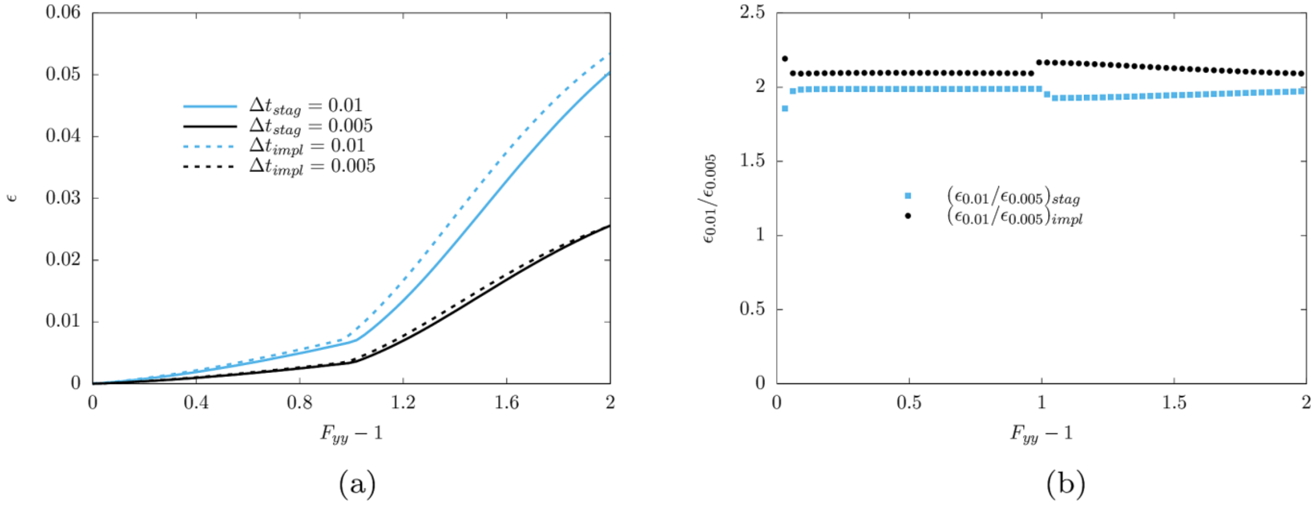

Figure 3.9. (a) Evolution of the error on the porosity with the stretch; (b) Comparison of the errors induced by two different load increments

3.4.2 Global sub-stepping method

According to the previous part, the accumulated error on the porosity f strongly depends on the load increment. So it is necessary to use a sufficiently small load increment to ensure the accuracy of the solutions. However, it is difficult to get the value of this small load increment. Thus, it may be preferable to control the increment of one variable. In our work, the porosity f is controlled: $\Delta f = f_{i+1} - f_i \ll 1$ with i the i^{er} time step. In most cases, the porosity varies from $f_0(\sim 10^{-4})$ to $f_F(\sim 10^{-1})$, hence it is sufficient to only control the increment of $\ln(f)$ such that $\Delta \ln(f) = \ln(f_{i+1}) - \ln(f_i) \leq \epsilon \ll 1$. Indeed, we have $\Delta \ln f = \Delta f/f \Longrightarrow \Delta f \leq 0.1 \Delta \ln f$ since $f \sim [10^{-4}, 0.1]$. This analysis is in agreement with the previous works done in (Zhang, 2016). In the work of (Zhang, 2016), an error analysis in purely hydrostatic situation was carried out and it was demonstrated that the variable to be controlled is $\ln(f)$. Consequently, the control on $\Delta \ln f$ leads to the control on Δf. As soon as the criterion on $\ln f$ is not fulfilled, the load step at global level is divided. Here the global level refers to the structure scale (mechanical equilibrium). We call this method “global sub-stepping method” in the following.

To evaluate the influence of the values of ϵ on the global response, several simulations of CT for $\epsilon = 0.005, 0.01, 0.03, 0.05, 0.1$ are performed. The corresponding geometry and mesh can be found in Figure 3.5. The model parameters which are used in these simulations can be found in Table 3.1 except for $q_2 = 1.2$. Usual symmetry and boundary/loading conditions are accounted for. The final load level correspond to an $COD = 4$ mm. The predefined load increment $\Delta t/T = 0.001$ with T the final load level.

Figure 3.10(a) plots the curves of force-COD for different ϵ with global sub-stepping method. The case without any stepping method is also shown in this figure. The converged solution is obtained by doing a simulation with $\Delta t/T = 0.0001$. It is observed that the difference between the result without sub-stepping method and the converged solution cannot be neglected. With the global-stepping method, the solution approach little by little the converged solution with the decrease of ϵ. They are almost overlapped when $\epsilon \leq 0.01$.

However, when it comes to large size computations, the global sub-stepping method may be computationally expensive. Indeed, as long as the criterion is not fulfilled at one integration point, then the load step would be divided at global level and at all integration points.

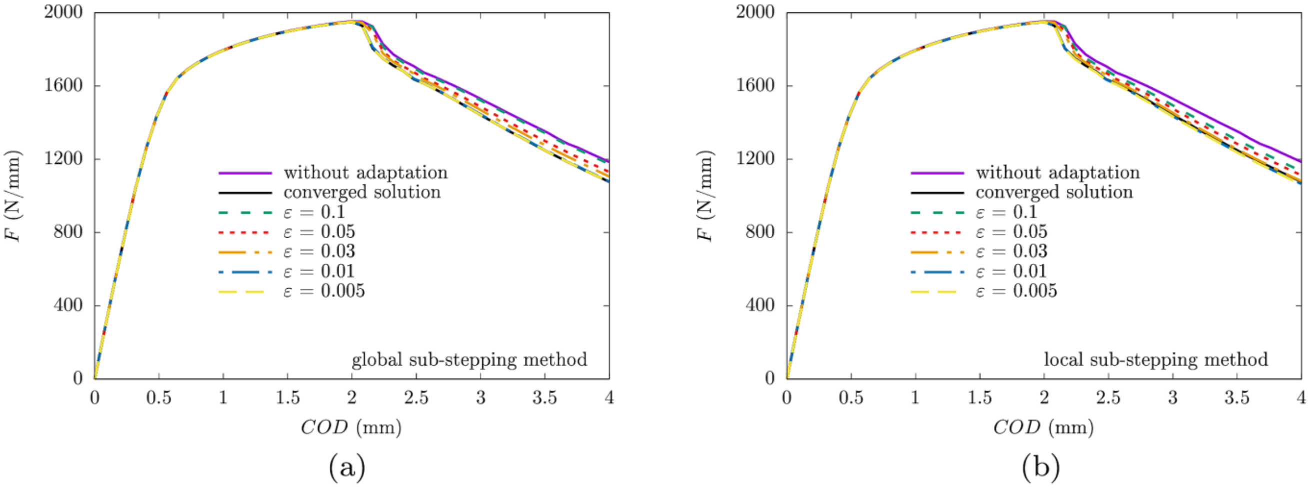

Figure 3.10. Force-COD curves for different ϵ (a) with global sub-stepping method); (b) with local sub-stepping method

3.4.3 Local sub-stepping method

The global sub-stepping method may be computationally expensive in some cases. In this part, we would like to test a less expensive method, i.e., local sub-stepping method. The idea of this method is to divide the load step in several sub-steps only for the integration of the constitutive law where the criterion given on $\Delta\ln(f)$ is violated. In that case, the strain increment and the nonlocal variables are directly sub-divided (see Figure 3.11) and the equilibrium equations are fulfilled only at the end of the time step. This approach is thought to be less time-consuming than the global one since the global Newton method at equilibrium level with the solution of the large linear system is not applied at each sub-increment, that is to say, the intermediate histories of strain and nonlocal variables are not linear in each time step with global sub-stepping method. However, with the local sub-stepping method, the tangent operator is no more consistent which can postpone or even preclude convergence of the global algorithm. Note that a consistent tangent operator can be retrieved with some effort but it was not done in this work.

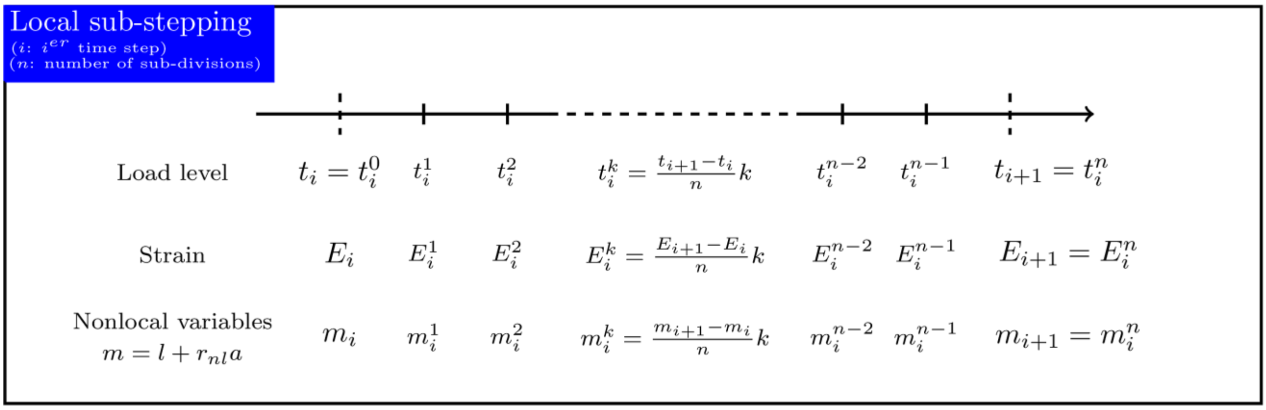

Figure 3.11. Schematic local sub-stepping method

In order to compare the accuracy of both methods, the same simulations as in the previous part are performed except that the local sub-stepping method is used.

Figure 3.10(b) plots the curves of force-COD for different ϵ with local sub-stepping method. It is observed that with the local-stepping method, the solution approach little by little the converged solution with the decrease of ϵ. They are almost overlapped when $\epsilon \leq 0.01$.

Figure 3.12 compares the results obtained with the global and the local sub-stepping methods for $\epsilon = 0.03$ (no converged solution) and for $\epsilon = 0.01$ (converged solution). It is shown that the results obtained with the global and local sub-stepping methods almost overlap in both cases, which indicates that the local sub-stepping method almost gives the same accuracy as the global one.

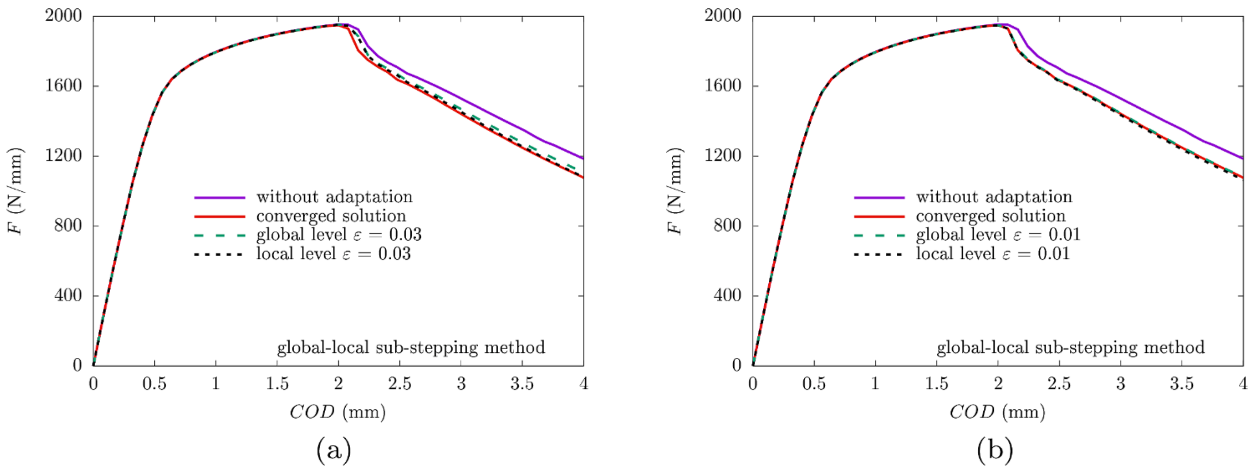

(a) (b)

Figure 3.12. Comparison between the results obtained with the global and the local sub-stepping methods for (a) $\epsilon = 0.03$ and (b) $\epsilon = 0.01$

In conclusion, no loss of accuracy is observed with the local sub-stepping method, which indicates that the assumption of linear history of strain and nonlocal variables is reasonable provided that the initial load step is not too large. In practice, if the initial load step is too large, convergence will be not ensured with the local sub-stepping method.

As for the value of ϵ, it should be chosen so as to ensure the trade-off between accuracy and performance: on the one hand, this value cannot be too large as its effect on error control would become negligible; on the other hand, it cannot be too small, otherwise, too many material points would suffer local division of load steps. In view of the previous results, it is suggested that $\epsilon = 0.01$.

Besides, the local and global stepping methods can be used at the same time: if $\Delta \ln f > \epsilon$, then the local stepping is activated. If the global Newton scheme is not convergent due to the non-consistent tangent operator, then the global sub-stepping is activated.

3.5 Penalty with respect to the plasticity

We recall here the expression of Lagrangian $\mathcal{L}_{nl}$, mentioned earlier in Chapter 2:

$$\mathcal{L}_{n\ell}(\boldsymbol{E},\boldsymbol{E^p},\kappa,a,l) \ = \ \mathcal{F}_{\ell}(\boldsymbol{E},\boldsymbol{E^p},\kappa) \ + \int_{\Omega_0} \left(\frac{1}{2}c\boldsymbol{\nabla}a.\boldsymbol{\nabla}a + l(a-\kappa) + \frac{1}{2}r_{nl}(a-\kappa)^2\right) d\Omega_0 \tag{3.47}$$

An augmentation term $r_{nl}(a-\kappa)^2/2$ with r_{nl} a penalty parameter is added in the Lagrangian. This term provides an additional coercivity so as to avoid potential oscillation of the accumulated plasticity κ. In the following, we will explain the origin of such oscillation.

The Lagrange multiplier l in the vector space $\mathbb{L}$ ensures that:

$$\forall l \in \mathbb{L}, < a-\kappa, l >= 0 \tag{3.48}$$

Thus, the oscillation of κ (i.e., $\kappa^{\perp} = \kappa - a$) belongs to the orthogonal space of $\mathbb{L}$ (i.e., $\mathbb{L}^{\perp}$): $\kappa^{\perp} \in \mathbb{L}^{\perp}$. Some degrees of freedom hence exist for κ and they are not controlled by the gradient term $\boldsymbol{\nabla}a$ since this term is only applied to the variable a. Therefore, it is possible that the space $\mathbb{L}^{\perp}$ is so "large" that the loss of ellipticity related to the strain softening character of the constitutive law is triggered. In that case, the oscillation of $\kappa^{\perp}$ and thus the oscillation of κ occur. However, at the continuum level, the value of $\kappa^{\perp} = a - \kappa$ should be equal to zero. Therefore, a quadratic term $r_{nl}(\kappa^{\perp})^2$, which does not have any effect at the continuum level, can bring additional definite positivity with respect to $\kappa^{\perp}$ so as to counter balance the loss of ellipticity mentioned above. Indeed, this quadratic term can be interpreted as an additional strain hardening of modulus r_{nl}. In conclusion, the value of r_{nl} should be large enough so that the constitutive law remains hardening with respect to κ for any value of a and l. Of course, the value r_{nl} should not be too large since the global Newton algorithm can fail in the case of too large r_{nl}.

In this section, we would like to illustrate the effects of this term with the simulations of Notched Tensile (NT) specimens. For that, several simulations (axisymmetric modeling) for $r_{nl} = 10$, 100, 1000, 5000, 10000, 100000 MPa are performed. The geometry and the mesh of NT, as well as the boundary and loading conditions are shown in Figure 2.24. The model parameters used in the simulations are listed in Table 3.1 except that the mixed element for the treatment of incompressibility is not used.

The fields of the hardening variable κ and the porosity f for different r_{nl} are shown in Figure 3.13. It is shown that the oscillation of κ exists when r_{nl} is not large enough ($r_{nl} \leq 5000$ MPa $= 10\sigma_0$). The same oscillation is observed in the field of f (see Figure 3.14) which is obvious as κ is linked to the plastic strain $\boldsymbol{E^p}$ through the flow rules and f is linked to $\boldsymbol{E^p}$ through the evolution law for the porosity in the GTN model. Due to the oscillation of f, the crack length is not well evaluated. In view of the obtained results, it is suggested that $r_{nl} \geq 10000$ MPa $\approx 20\sigma_0$ with σ_0 the yield stress when the 3-field $(\underline{u}, a, l)$ GTN model is used. We will see in the next section and in Appendix 5 that when the 5-field GTN model is used, it is sufficient to take $r_{nl} \geq 10\sigma_0$.

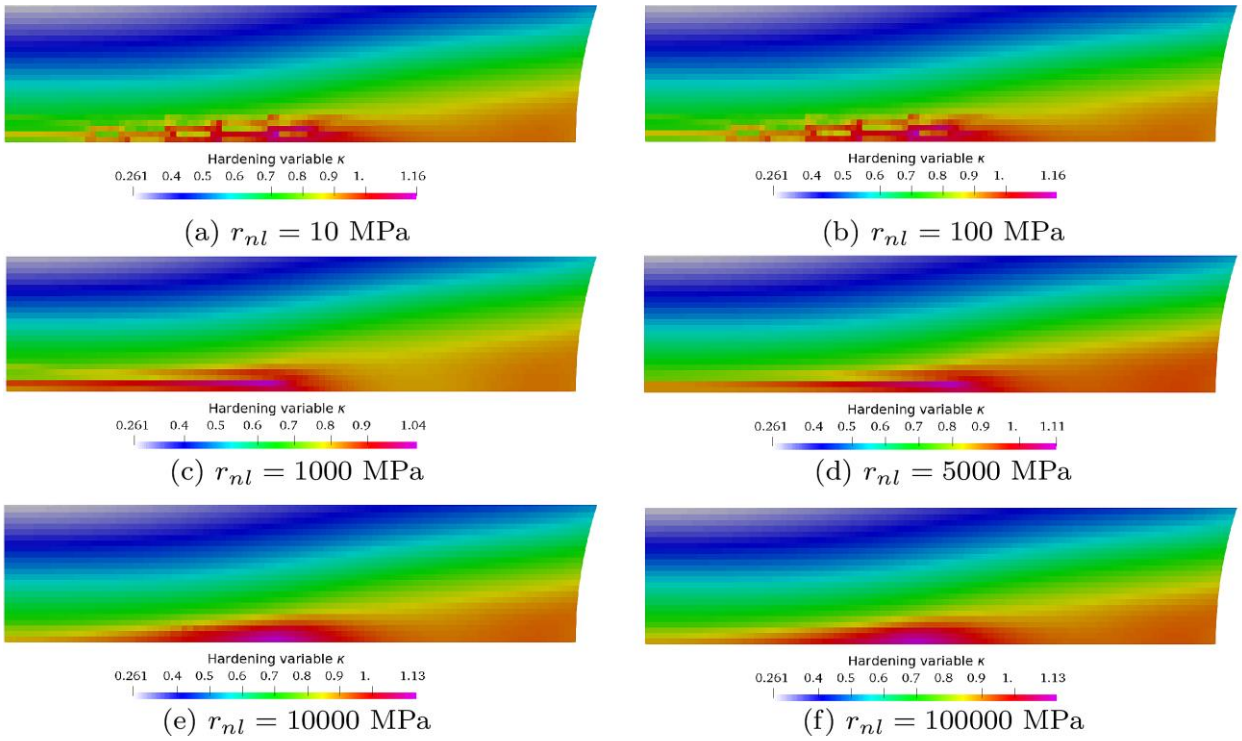

(a) $r_{nl} = 10$ MPa (b) $r_{nl} = 100$ MPa

(c) $r_{nl} = 1000$ MPa (d) $r_{nl} = 5000$ MPa

(e) $r_{nl} = 10000$ MPa (f) $r_{nl} = 100000$ MPa

Figure 3.13. The fields of the hardening variable κ for different r_{nl} (Mean stretch =9.5%)

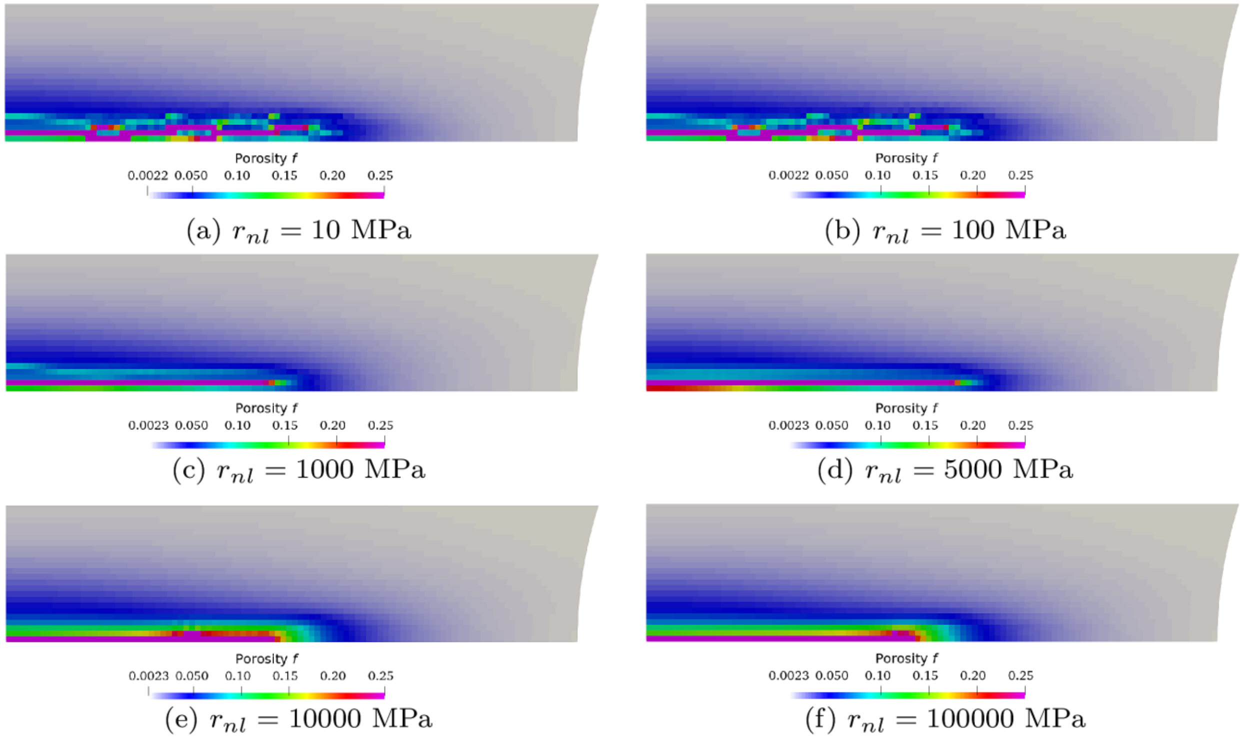

(a) $r_{nl} = 10$ MPa (b) $r_{nl} = 100$ MPa

(c) $r_{nl} = 1000$ MPa (d) $r_{nl} = 5000$ MPa

(e) $r_{nl} = 10000$ MPa (f) $r_{nl} = 100000$ MPa

Figure 3.14. The fields of the porosity for different r_{nl} (Mean stretch =9.5%)

3.6 Penalty with respect to the volumetric strain

We recall here the expression of Lagrangian $\mathcal{L}$, mentioned earlier in Chapter 2:

$$\mathcal{L}(\boldsymbol{E}, \boldsymbol{E^p}, \kappa, a, l, P, \theta) \; = \; \mathcal{L}_{\mathrm{n}\ell}(\overline{\boldsymbol{E}}, \boldsymbol{E^p}, \kappa, a, l) \; + \int_{\Omega_0} \left(P(\ln(J) - \theta) + \frac{1}{2} r_{inco} (\ln(J) - \theta)^2 \right) d\Omega_0 \qquad (3.49)$$

This mixed element formulation is used to solve volumetric locking. A new augmentation term $\frac{1}{2} r_{inco}(\ln(J) - \theta)^2$ has been introduced in our work, with r_{inco} a new penalty parameter. It brings an additional coercivity so as to avoid potential appearance of spurious plastic localization. In the following, we will explain the origin of the plastic localization.

Initially, volumetric locking results from the fact that the quasi-incompressibility constraint enforced at each integration points reduces the effective dimension of the displacement space. The reduction is so drastic that the effective displacement space is no more rich enough to ensure spatial convergence. Therefore, a new kinematic degree of freedom θ is introduced in order to relax this constraint on the displacement: θ should be approximately equal to zero due to the quasi-incompressibility assumption, but not $\ln J(\underline{u})$. As θ should nevertheless reflect $\ln J(\underline{u})$, a Lagrange multiplier $P \in \mathbb{P}$ ensures the correspondence:

$$\forall P \in \mathbb{P}, < \ln J(\underline{u}) - \theta, P >= 0 \qquad \Longrightarrow \qquad \theta = \ln J(\underline{u}) + \theta^{\perp}, \theta^{\perp} \in \mathbb{P}^{\perp} \qquad (3.50)$$

Compared to the initial situation, an additional degree of freedom is introduced through $\theta^{\perp}$ which is expected to avoid volumetric locking. The choice of $\mathbb{P}$ affects the efficiency of the approach: $\mathbb{P}$ should not be too large to fulfill the LBB condition and thus to have a well-posed dual problem. The choice of the Taylor-Hood element (i.e., quadratic interpolation for $\underline{u}$ and linear interpolation for P) fulfills the LBB condition. In addition, $\mathbb{P}$ should not be too small, i.e., $\mathbb{P}^{\perp}$ should not be too large so that the primal problem remains well-posed with respect to the enhance kinematics. This can be achieved by the use of the Taylor-Hood finite element in the framework of small strains. However, it is not true anymore in the framework of finite strains, as shown in (Auricchio et al., 2013; Lorentz et al., 2008). In finite strains, the primal problem may become ill-posed, leading to the oscillation of $\theta^{\perp}$ and thus the plastic oscillations through the constitutive relation. Therefore, the quadratic term $r_{inco}(\theta^{\perp})^2/2$ brings an additional coercivity so that the primal problem becomes well-posed again. However, the higher the penalty parameter is, the less efficient the additional kinematic freedom provided by $\theta^{\perp}$ is: volumetric-locking could be retrieved. In conclusion, r_{inco} should be large enough to ensure the well-posed primal problem and sufficiently small to avoid volumetric locking.

In some cases, the control on $\boldsymbol{\nabla} a$ proves sufficient to avoid plastic oscillations, providing an indirect control on $\theta^{\perp}$, as shown in (Zhang, 2016). Indeed, it is stated in (Zhang, 2016) that the introduction of the nonlocal penalty term $r_{nl}(a - \kappa)/2$ can avoid the oscillation of the plasticity in the absence of the quadratic term $r_{inco}(\theta^{\perp})^2/2$ in his case. We will see that this conclusion is not always true. Besides, we have stated in the previous section that r_{nl} should be large than $20\sigma_0$ to avoid plastic oscillation when $r_{inco} = 0$, we will see that when $r_{inco} > 0$, we can simply take $r_{nl} \geq 10\sigma_0$ to preclude plastic oscillation.

In the following, we would like to illustrate the effects of the quadratic term $r_{inco}(\theta^{\perp})^2/2$ in two scenarios: (1) pure von-Mises without nonlocal (gradient controlled) effects; (2) GTN with nonlocal effects. The first scenario has been studied in (Lorentz et al., 2008) for $r_{inco} = 0$ and the oscillation of plasticity was observed. So here it is expected that the quadratic term can avoid this oscillation. The second scenario is studied to demonstrate that in the absence of $r_{inco}(\theta^{\perp})^2/2$, the nonlocal term $r_{nl}(a - \kappa)/2$ may not sufficient to avoid or postpone the oscillation of the plasticity and the damage.

The simulations of NT for different r_{inco} (r_{inco} = 0, 100, 1000, 5000, 10000, 100000 MPa) are performed. The geometry and the mesh of NT, as well as the boundary and loading conditions are shown in Figure 2.24. Unless otherwise stated, the material parameters used in the simulations are listed in Table 3.1.

Scenario 1

For the first case, we set $c = 0$ N and $r_{nl} \approx 0$ MPa to exclude the nonlocal effect. The von-Mises law is used. Figure 3.15 shows the field of the hardening variable κ. It is shown that the oscillation of the plasticity exists in the case of small values for r_{inco}, as observed in (Lorentz et al., 2008), and disappears when r_{inco} is large enough (r_{inco}~$5000\ MPa$). Similar to r_{nl}, a too small value of r_{inco} leads to an incorrect global response, as shown in Figure 3.16.

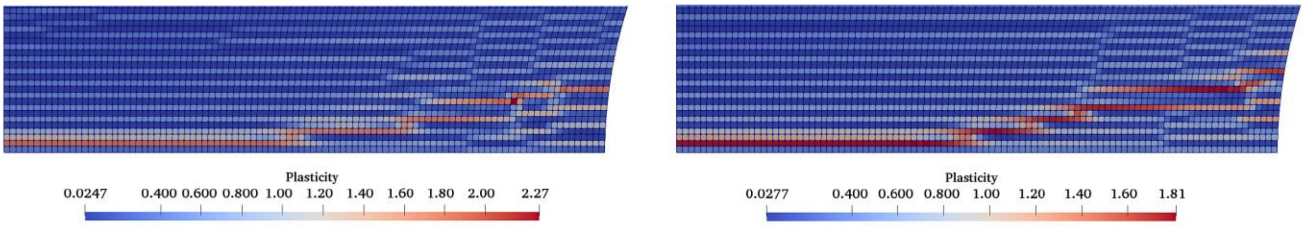

(a) $r_{inco} = 0$ MPa (b) $r_{inco} = 100$ MPa

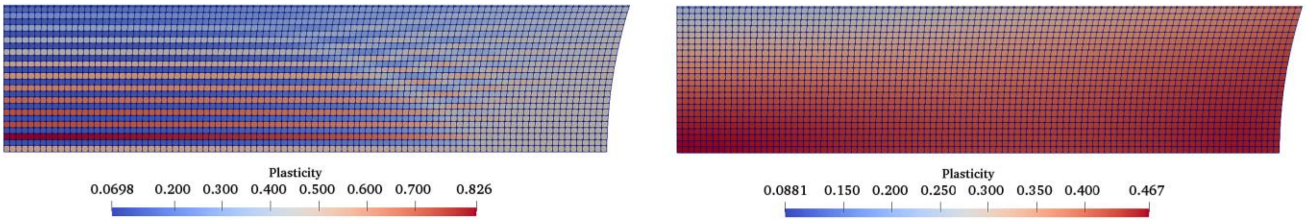

(c) $r_{inco} = 1000$ MPa (d) $r_{inco} = 5000$ MPa

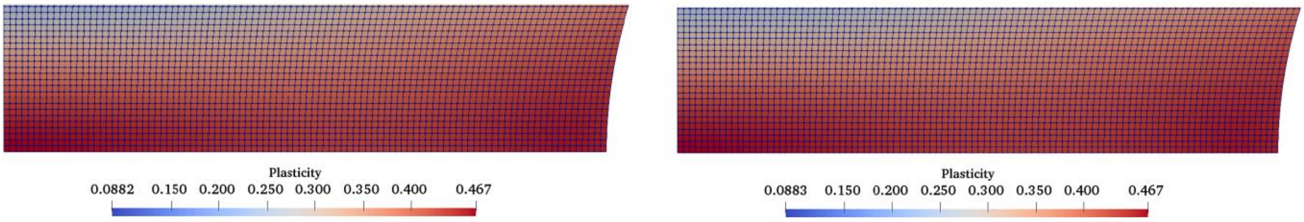

(e) $r_{inco} = 10000$ MPa (f) $r_{inco} = 100000$ MPa

Figure 3.15. Hardening parameter with different r_{inco} *(mean stretch 6%)*

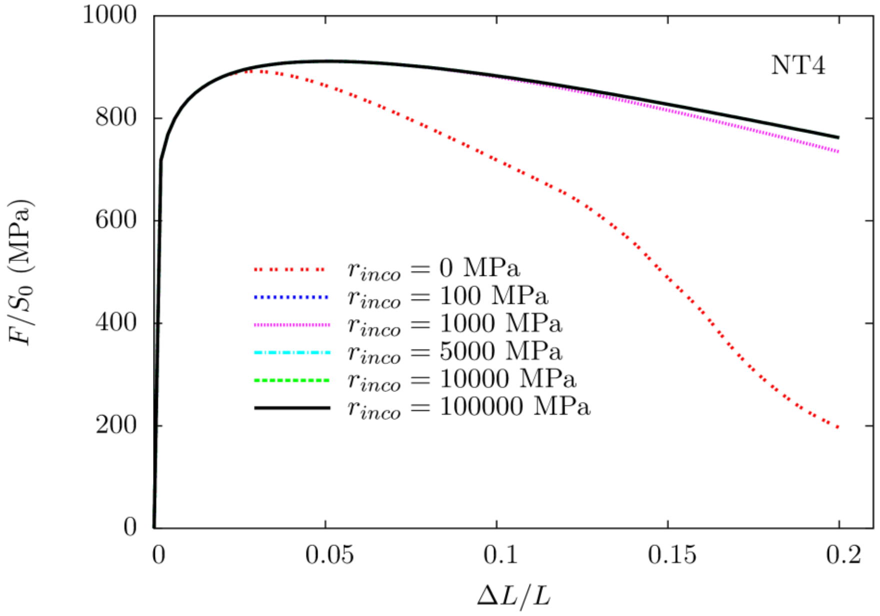

Figure 3.16. Force-Diameter reduction curves for different r_{inco} (mean stretch 6%)

Scenario 2

For the second case, we set $c = 50$ N, $r_{nl} = 5000$ MPa. The GTN damage model is used. Figure 3.17 plots the profile of the porosity in the ligament for $r_{inco} = 0$ and 5000 MPa. The oscillation of the porosity f are observed for $r_{inco} = 0$ MPa and it disappears for $r_{inco} = 5000$ MPa. Macroscopically, this oscillation is interpreted as a discontinuous crack (some material points never fail), as shown in the same figure. This is problematic since the finite elements containing these no-broken points never stop deforming which leads to element distortion and thus computational non-convergence.

Figure 3.18 plots the field of the hydrostatic stress for different r_{inco}. It can be observed that stress oscillation inside the localization band becomes non-negligible when $r_{inco} \geq 10000$ MPa, i.e., volumetric-locking appears again for large values of r_{inco}. Therefore, the value of r_{inco} should not be too large. In view of the local and the global responses, it is suggested that $r_{inco} \sim 5000$ MPa $\approx 10\sigma_0$ with σ_0 the yield stress.

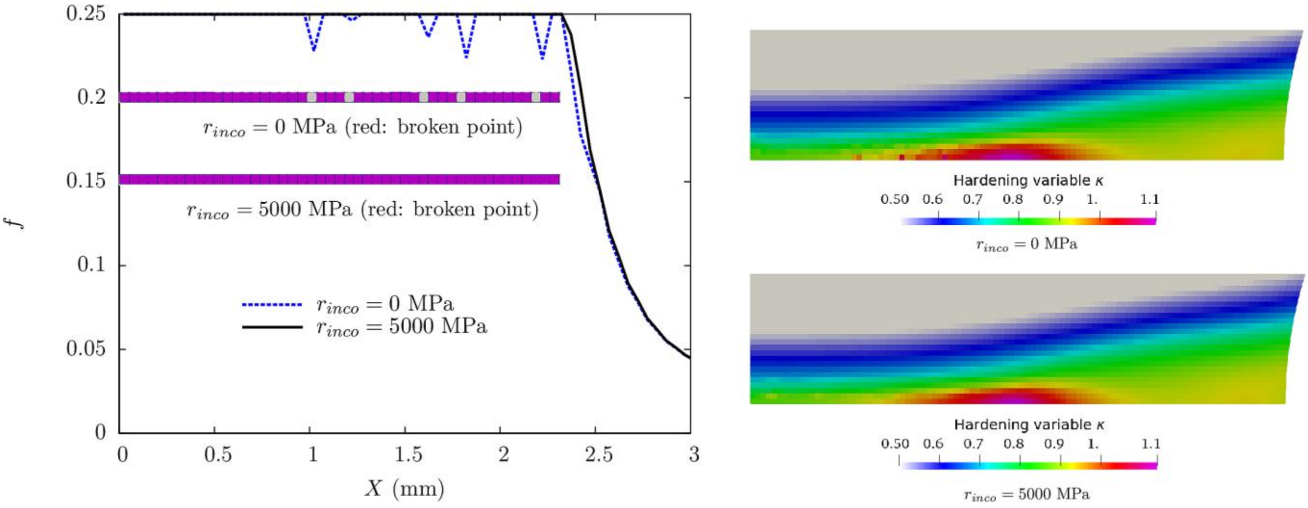

Figure 3.17. Evolution of porosity f in the ligament for different r_{inco} (mean stretch 10%)

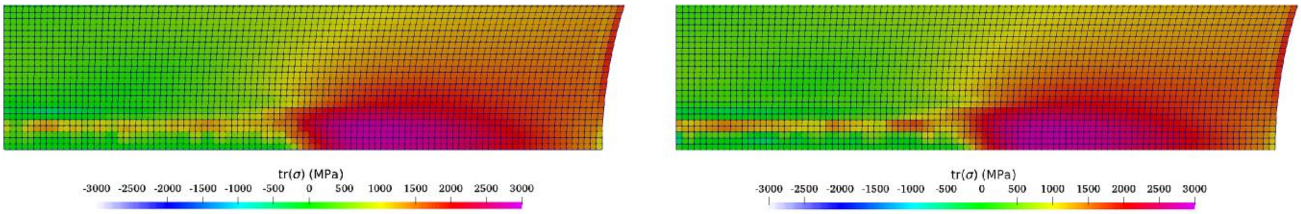

(a) $r_{inco} = 0$ MPa (b) $r_{inco} = 100$ MPa

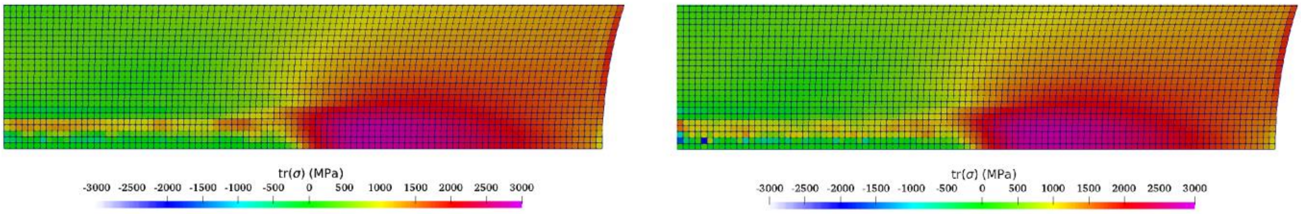

(c) $r_{inco} = 1000$ MPa (d) $r_{inco} = 5000$ MPa

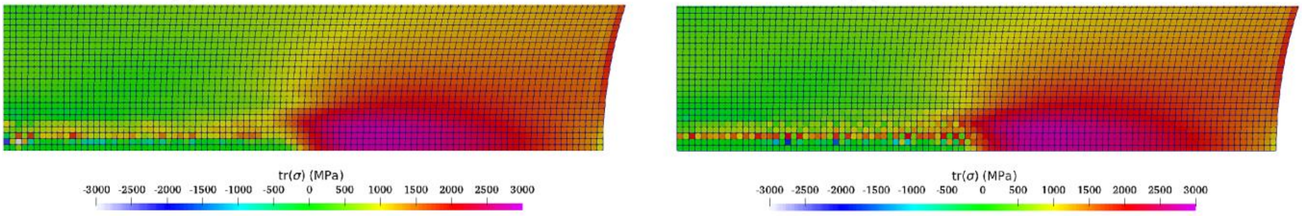

(e) $r_{inco} = 10000$ MPa (f) $r_{inco} = 100000$ MPa

Figure 3.18. The hydrostatic stress for different r_{inco} (mean stretch 10%)

3.7 Summary

This chapter consists in discussing different numerical aspects of the nonlocal locking-free GTN model. The study of these numerical aspects allows knowing how to correctly use the model so as to perform reliable simulations.

First of all, we focus on the treatment of the broken finite elements. As mentioned in Chapter 1, there exist several ways to handle these elements, but each way has its own drawbacks. In this work, it is proposed to use a simple viscoelastic model which has a stabilization effect on global problem. With this model, a small and time-vanishing stiffness is introduced. This stiffness leads to some additional stresses which vanish with increasing time. Two parameters are involved in this model: a viscoelastic stiffness E_v and a viscoelastic characteristic time τ_v. The simulations of NT and CT are performed. According to the results, it is suggested that $E_v = 0.001E$ and $t_v = 0.01T$ with E Young's modulus and T the total loading time. With these values, the element distortion in CT is well reduced.

Secondly, the convergence criterion which is used in this work is shown. It is based on the derivation of a reference nodal vector on the basis of physical engineering quantities. This criterion can be used even when the different residuals have different units. By using this criterion, the simulation result should be reliable.

Thirdly, we compare two different integration schemes for the constitutive law. The first one is called "staggered scheme" which consists in doing an implicit time-discretization with respect to $(\boldsymbol{E^p}, \kappa)$ and an explicit update of f. The second one is called "implicit scheme" which consists in doing an implicit time-discretization with respect to $(\boldsymbol{E^p}, \kappa, f)$. Simulations of RVE are performed with both schemes. The results show that the accuracy of both schemes is the same and that they are convergent.

Then, in order to control the error introduced by the large load increment, a global sub-stepping method and a local sub-stepping method are proposed. The sub-stepping is based on the control on the increment of $\ln f$. Both methods give a time-convergent results if the criterion defined on $\Delta \ln f$ is correctly chosen. The global sub-stepping method can be computationally expensive, especially when it comes to three-dimensional simulations with many degrees of freedom. The local sub-stepping method can efficiently solve this issue. But it is necessary to well evaluate the tangent matrix for the points at which the local adaptation is activated so as to avoid the global non-convergence of Newton-Raphson algorithm due to inconsistent tangent operator.

Finally, the two augmentation terms introduced in the Lagrangian, i.e., $r_{nl}(a-\kappa)^2/2$ and $r_{inco}(\mathrm{tr}(\boldsymbol{E})-\theta)/2$ are studied. Simulations of simple tensile test on NT with different r_{nl} or r_{inco} are performed to see the effects of these two terms on the mechanical fields or on the global response. The results indicate that both terms helps avoid the oscillations of the plasticity and the damage. For the value of r_{nl}, it cannot be too small, otherwise the penalty effect becomes negligible. But we can take large values for r_{nl} as long as the problem remains well conditioned. For the value of r_{inco}, it cannot be too small, otherwise the oscillations of the plasticity and/or the damage cannot be reduced. It cannot be too large, otherwise the issue of volumetric-locking appears again. It is suggested that $r_{nl} \geq 10\sigma_0$ and $r_{inco} \approx 10\sigma_0$.

4 Model properties in the context of small-scale yielding

所谓老练就是既能声明自己的看法,又不得罪人的艺术。

Le tact c'est l'art de proposer un argument sans se faire un ennemi.

Tact is the art of making a point without making an enemy

艾萨克 牛顿 Isaac Newton

Résumé

Ce chapitre porte sur les propriétés physiques du modèle GTN non-local.

Le but de ce chapitre est de voir comment le modèle GTN non-local est capable de construire une courbe de résistance à la déchirure ductile J-Δa sous les hypothèses de plasticité confinée (« small-scale yielding » en anglais), Mode I et déformations planes. En quelque sorte, on cherche à établir une relation entre l'approche globale (J) et l'approche locale (GTN).

Des simulations de la grande propagation de fissure sont réalisées avec le modèle GTN non-local. Une nouvelle méthode basée sur le champ de la porosité pour post-traiter la longueur de fissure est introduite. Des études paramétriques sur les différents paramètres numériques du modèle sont faites afin d'estimer leur influence sur la courbe $J - \Delta a$.

Une relation linéaire entre la largeur de la bande de localisation et la longueur intrinsèque non-locale est établie. Ensuite, l'émoussement, l'amorçage et la grande propagation (~200 éléments finis cassés) de fissure peuvent être prédits par le modèle GTN non-local. En particulier, un état quasi-stationnaire local est constaté pour les champs de contraintes, de porosité et de variable d'écrouissage. Par ailleurs, on a constaté que la ténacité (J à l'amorçage) et le comportement à la déchirure peuvent fortement être impactés par les propriétés du matériau (porosité initiale, porosité de coalescence, paramètres d'écrouissage, etc.). Enfin, Les résultats montrent la robustesse et la fiabilité de la formulation numérique du modèle GTN.

The main purpose of this chapter is to investigate how the non-local GTN model is able to construct a $J-\Delta a$ resistance curve in the context of plane strain and mode I small-scale yielding and so establish a link between the J approach and the GTN-based approach. In particular, the effects of the GTN material parameters and the internal length of the model on the $J-\Delta a$ resistance curve are thoroughly studied. The small-scale yielding conditions are fulfilled through the boundary-layer model where the far-field is only characterized by the elastic stress intensity factor K related to J by Irwin's formula. The small-scale yielding framework hence reflects the vicinity of a crack tip without including any geometrical or constraint effect. This is the best adapted configuration to apply the global approach to ductile fracture. A second objective of the study consists in evaluating the robustness and the reliability of the non-local GTN formulation by performing simulations of large crack propagation in small-scale yielding.

This chapter is organized as follows. Some basic knowledge about Linear Elastic Fracture Mechanics (LEFM) and Elastic-Plastic Fracture Mechanics (EPFM) are summarized in Section 4.1. The simulation techniques, which will be used in Section 4.3, are described in Section 4.2. Crack initiation and crack propagation under small-scale yielding Mode I plane-strain conditions is simulated using the nonlocal locking-free GTN model (see Chapter 2 for model description) and the results are presented in Section 4.3. A short conclusion and perspective are given in Section 4.4.

4.1 Crack propagation in small-scale yielding

4.1.1 Stress analysis of cracks in elasticity

Under the assumption of isotropic linear elastic material behavior, it is possible to derive closed form expressions of the stress tensor for some cracked configurations subjected to external forces, as described in (Irwin, 1957; Sneddon, 1946; Westergaard, 1939). If we define a polar coordinate axis with the origin at the crack tip, then the stress filed in any linear elastic cracked body is given by:

$$\boldsymbol{\sigma} = \frac{K}{\sqrt{2\pi r}}\boldsymbol{f}(\theta) + \sum_{m=0}^{\infty} A_m r^{\frac{m}{2}} \boldsymbol{g_m}(\theta) \tag{4.1}$$

where $\boldsymbol{\sigma}$ denotes the stress tensor, (r,θ) denotes the polar coordinates (see Figure 4.1), K denotes the stress intensity factor, $\boldsymbol{f}$ and $\boldsymbol{g_m}$ denote two dimensionless functions of θ, A_m denotes the amplitude for the m^{th} term.

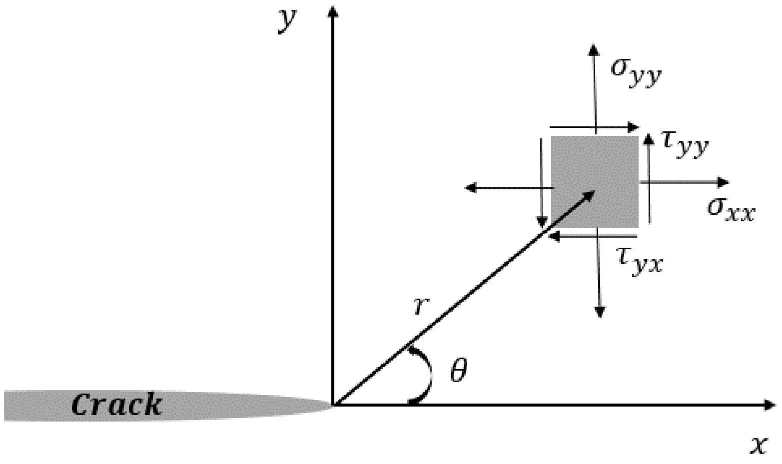

Figure 4.1. Definition of polar coordinate axis ahead of a crack tip

Equation (4.1) describes a stress singularity. Indeed, for any given configuration, there exists a leading term which is proportional to $1/\sqrt{r}$. As $r \rightarrow 0$, the leading term tends to infinity, while the other terms remains finite. In particular, the value of K depends on the geometry.

Generally speaking, a crack can experience three types of loading, i.e., mode I, mode II and mode III. In this work, we only focus on mode I loading, where the principal load is applied normal to the crack plane. Mode I loading tends to open the crack. The singular stress fields and displacement fields in the case of plane strain for Mode I are given in Table 4.1 and Table 4.2. In Table 4.2, the parameter μ is the shear modulus.

According to Table 4.1, the stresses on the crack plane ($\theta = 0°$) near and ahead of the crack tip are:

$$\sigma_{xx} = \sigma_{yy} = \frac{K}{\sqrt{2\pi r}} \tag{4.2}$$

while stresses far away from the crack tip are governed by the remote boundary conditions. If the stress intensity factor K is known, the stress tensor, the strain tensor and the displacement can be solved using Table 4.1 and Table 4.2. For simple configurations, closed-form solution of K can be derived analytically, one can refer to (Anderson, 2017) for closed-form solutions of K for common test specimens. Otherwise, K should be estimated by some experiment techniques (for example strain gage based method (Dally and Sanford, 1987)) or numerical analysis (such as finite element method). It should be noticed that it is difficult, even impossible to measure K completely by experiments. One should keep in mind that the stress intensity factor K is a coefficient in William solution (Equation (4.1)) but not a physical parameter, hence, it cannot be measured but only calibrated on the basis of a stress, strain or displacement measure. For instance, in strain gage method presented in (Dally and Sanford, 1987), the William solution (Equation (4.1)) is used to link the strain to the stress intensity factor K.

Table 4.1. Stress fields ahead of a crack tip for Mode I in a linear elastic isotropic material (plane strain case)

$\boldsymbol{\sigma_{xx}}$	$\frac{K}{\sqrt{2\pi r}}\cos\left(\frac{\theta}{2}\right)\left(1-\sin\left(\frac{\theta}{2}\right)\sin\left(\frac{3\theta}{2}\right)\right)$
$\boldsymbol{\sigma_{yy}}$	$\frac{K}{\sqrt{2\pi r}}\cos\left(\frac{\theta}{2}\right)\left(1+\sin\left(\frac{\theta}{2}\right)\sin\left(\frac{3\theta}{2}\right)\right)$
$\boldsymbol{\sigma_{zz}}$	$\nu(\sigma_{xx}+\sigma_{yy})$
$\boldsymbol{\tau_{xy}}$	$\frac{K}{\sqrt{2\pi r}}\cos\left(\frac{\theta}{2}\right)\sin\left(\frac{\theta}{2}\right)\cos\left(\frac{3\theta}{2}\right)$
$\boldsymbol{\tau_{xz}}$	0
$\boldsymbol{\tau_{yz}}$	0

Table 4.2. Displacement fields ahead of a crack tip for Mode I in a linear elastic isotropic material (plane strain case)

$\boldsymbol{u_x}$	$\frac{K}{2\mu}\sqrt{\frac{r}{2\pi}}\cos\left(\frac{\theta}{2}\right)\left(2-4\nu+2\sin^2\left(\frac{\theta}{2}\right)\right)$
$\boldsymbol{u_y}$	$\frac{K}{2\mu}\sqrt{\frac{r}{2\pi}}\sin\left(\frac{\theta}{2}\right)\left(4-4\nu-2\cos^2\left(\frac{\theta}{2}\right)\right)$

4.1.2 Energy release rate and path-independent contour integral

Energy release rate

By applying the first law of thermodynamics to crack extension, (Griffith, 1921) deduced that a crack can form or grow only if such a process does not increase the total energy of the system. An energy release rate J is defined as the instantaneous loss of total potential energy Π per unit crack growth area A:

$$J = -\frac{d\Pi}{dA} \tag{4.3}$$

The definition given in Equation (4.3) holds for linear or nonlinear elastic materials.

Under the assumption of isotropic linear elastic material behavior, Mode I and plane-strain condition, the relationship between the stress intensity factor K and the energy release rate J is (Irwin, 1957):

$$J = \frac{K^2(1-\nu^2)}{E} \tag{4.4}$$

Path-independent contour integral

The path-independent contour integral J_{Rice} was proposed in (Rice, 1968) for the analysis of cracks:

$$J_{\mathrm{Rice}} = \int_\Gamma \left(w dy - \tau_i \frac{\partial u_i}{\partial x} \right) ds \tag{4.5}$$

where w is the strain energy density, τ_i are the components of the traction vector, u_i are the displacement vector components and ds is the length increment along the arbitrary contour Γ around the crack tip. This J_{Rice} was shown to be equal to the energy release rate J in a linear or nonlinear elastic body containing a crack.

In small-scale yielding conditions, the definition of path integral still holds as long as the chosen contour remains in the elastic zone, while the definition of energy release rate J does not hold anymore since part of the strain energy absorbed by the material is not recovered due to the plasticity when the crack grows. So Equation (4.4) does not have too much meaning. Despite all that, the plastic zone is negligible compared to the entire structure in small-scale yielding, so later in this thesis, we will see that the contour integral J_{Rice} is (almost) equal to $K^2(1-\nu^2)/E$.

4.1.3 Crack tip plasticity in small-scale yielding

Stresses predicted by Linear Elastic Stress Analysis is infinite at the crack tip, according to Equation (4.1). However, due to the finite crack-tip radius and inelastic deformation in real material, stresses should remain finite at crack tip. Therefore, the concept of Linear Elastic Fracture Mechanics becomes inaccurate as the inelastic region at the crack tip grows. Crack length corrections are available in the case of small-scale yielding. In this part, we will give an order of magnitude of the plastic size r_p in plane strain case.

On elastic-plastic interface on the cracked plane, we have $\sigma_{eq} \sim \sigma(r = r_p) \sim \sigma_0$ with σ_0 the yield stress. According to Equation (4.1)), we have $\sigma(r = r_p) \sim K/\sqrt{r_p}$. Thus, we obtain $\sigma_0 \sim K/\sqrt{r_p}$, that is to say,

$$r_p \sim \left(\frac{K}{\sigma_0}\right)^2 \tag{4.6}$$

The detailed expression of Equation (4.6) is given in (Anderson, 2017) as:

$$r_p = \frac{1}{3\pi}\left(\frac{K}{\sigma_0}\right)^2 \tag{4.7}$$

For the general cases in which $\theta \neq 0$, it is shown in (Anderson, 2017) that:

$$r_p(\theta) = \frac{1}{4\pi}\left(\frac{K}{\sigma_{eq}}\right)^2 \left((1-2\nu)^2(1+\cos\theta) + \frac{3}{2}\sin^2\theta\right) \tag{4.8}$$

4.1.4 Small-scale yielding: J-controlled fracture

The so-called J-controlled fracture means that J completely characterizes the crack-tip conditions when there is not excessive plasticity or significant crack growth. In the context of small-scale yielding, where the plastic and cracked zone are assumed to be negligible compared to elastic zone, both K and J characterize crack-tip conditions. Figure 4.2 schematically illustrates the effect of plasticity on the stresses at the crack tip nearby zone in small-scale yielding. In this figure, l_c means the characteristic length scale. A K-dominated zone where the stress is proportional to $1/\sqrt{r}$ exists at a short distance from the crack tip. Under the assumption of monotonic and quasi-static loading, a J-dominated zone occurs in the plastic zone where the elastic singularity does not exist anymore. In particular, if hardening obeys the Rambert-Osgood law ($\varepsilon/\varepsilon_0 = \alpha(\sigma/\sigma_0)^{1/n}$ with α a dimensionless constant, $\varepsilon_0 = \sigma_0/E$ and n the strain-hardening exponent), the HRR solution[8] would be valid in this plastic zone (Hutchinson, 1968; Rice and Rosengren, 1968). Well inside of the J-dominated region, a finite strain region occurs within around 2δ from the crack tip with δ the Crack Tip Opening Displacement. The HRR solution is not valid anymore (see for example (Hutchinson, 1968) for the explanation). In this region, the general solution of the displacement $\underline{u}$ is known as Williams-series. Only the first term of the series will be considered in this work:

$$\begin{cases} \mathrm{u_x(r,\theta)} = \dfrac{\mathrm{K(1+\nu)}}{\mathrm{E}}\sqrt{\dfrac{r}{2\pi}}\cos\left(\dfrac{\theta}{2}\right)(3-4\nu-\cos\theta) \\ \mathrm{u_y(r,\theta)} = \dfrac{\mathrm{K(1+\nu)}}{\mathrm{E}}\sqrt{\dfrac{r}{2\pi}}\sin\left(\dfrac{\theta}{2}\right)(3-4\nu-\cos\theta) \end{cases} \tag{4.9}$$

It is worth noticing that in the case of elastic-plastic conditions, there is no longer a K field; in the case of large-scale yielding, finite strain zone is dominated and K or J-dominated region does not exist anymore. However, in small-scale yielding, the K-dominated and J-dominated zones always exist.

Generally speaking, there are three distinct stages of crack growth resistance behavior in small-scale yielding, as shown in Figure 4.3. During crack blunting, the plasticity and the damage grow at the crack-tip nearby zone without any crack extension, the slope of J resistance curve is constant. Then crack starts to grow at crack initiation stage, the crack-tip stresses and strains may be affected by the original blunted crack tip. According to (Anderson, 2017), a steady-state can be reached when crack grows well beyond the initial blunted crack tip, in this case, the history of local variables (e.g., stresses, strains, state variables) are independent of crack growth. A plastic wake can be observed at this stage and the J resistance curve becomes flat provided that the material

---

[8] The HRR singularity is :

$$\sigma_{ij} = \sigma_0\left(\frac{EJ}{\alpha\sigma_0^2 I_n r}\right)^{\frac{1}{n+1}}\tilde{\sigma}_{ij}(n,\theta)$$

where I_n is an integration constant

properties remains the same with position. At this point, the local state of different variables is not uniquely characterized by K or J.

Initially, the curve $J(\Delta a)$ has been thought as an intrinsic property of the material. Further investigations have shown that it may depend on the structure geometry and the loading conditions, in particular through the triaxiality (T-stress).

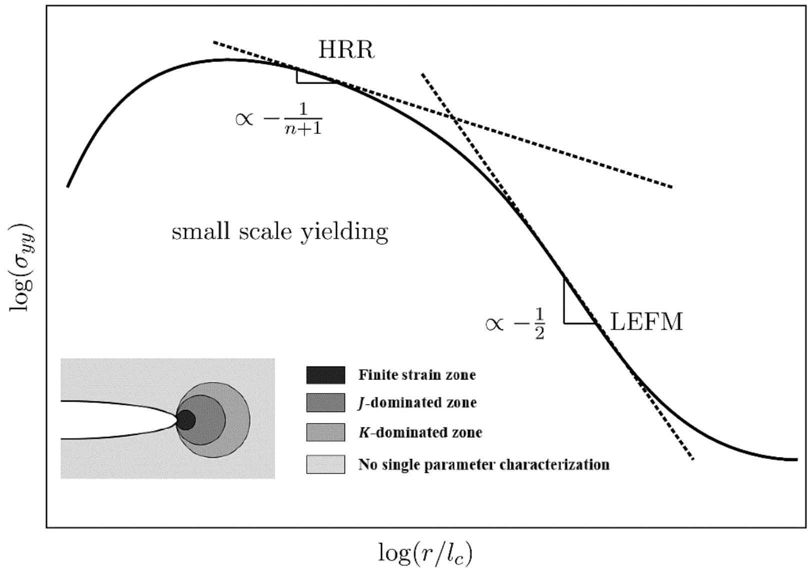

Figure 4.2. Effect of plasticity on the crack-tip stress fields in the context of small-scale yielding

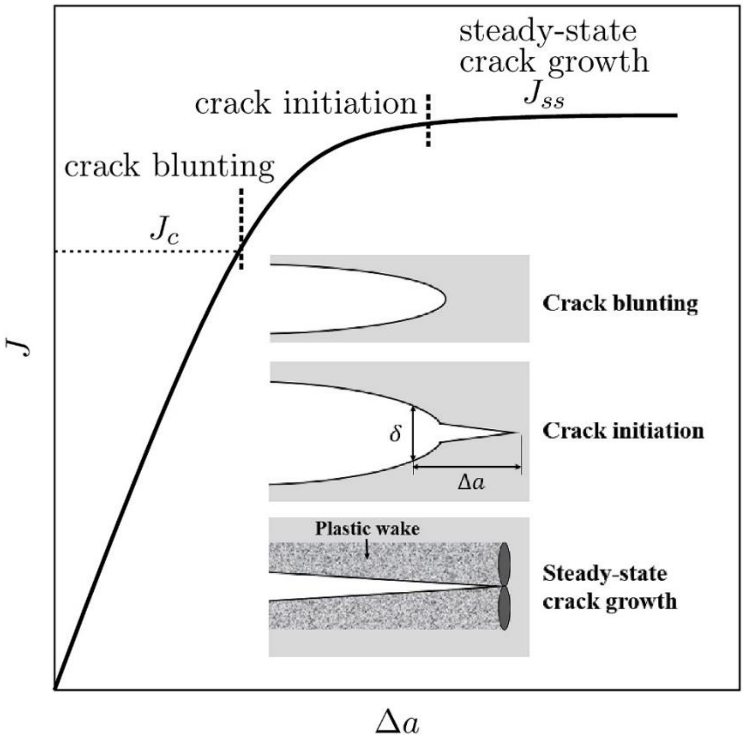

Figure 4.3. Three distinct stages of crack growth resistance behavior in small-scale yielding

4.1.5 Ductile tearing

For ductile material, J increases with crack growth, this increase is normally associated with void growth and void coalescence. As shown in Figure 4.4, at crack blunting stage, J is linear with crack length Δa. Here $\Delta a = \Delta a_{bl} + \Delta a_{tear}$ with Δa_{bl} crack growth due to blunting and Δa_{tear} crack extension corresponding to the actual ductile tearing. As load increases, local failure at crack tip occurs. An instability can be encountered during crack initiation, especially in the case of load control. Fracture toughness J_c is generally defined at the beginning of crack extension. This critical point gives some information about the fracture behavior of a ductile material. However, sometimes, it is difficult to define this critical point. In that case, J_c is generally defined as $J_c = J_{0.2}$ with $\Delta a = 0.2$ mm. The slope of the J resistance curve can be quantified by a dimensionless tearing modulus T_{ear} which is defined as (Paris et al., 1979):

$$T_{ear} = \frac{E}{\sigma_0^2}\frac{\partial J}{\partial \Delta a} = \frac{E}{\sigma_0}\frac{\partial\left(\frac{J}{\sigma_0 l_c}\right)}{\partial\left(\frac{\Delta a}{l_c}\right)} \tag{4.10}$$

where l_c denotes a characteristic length scale for dimensional analysis even though the value of T_{ear} is independent of l_c.

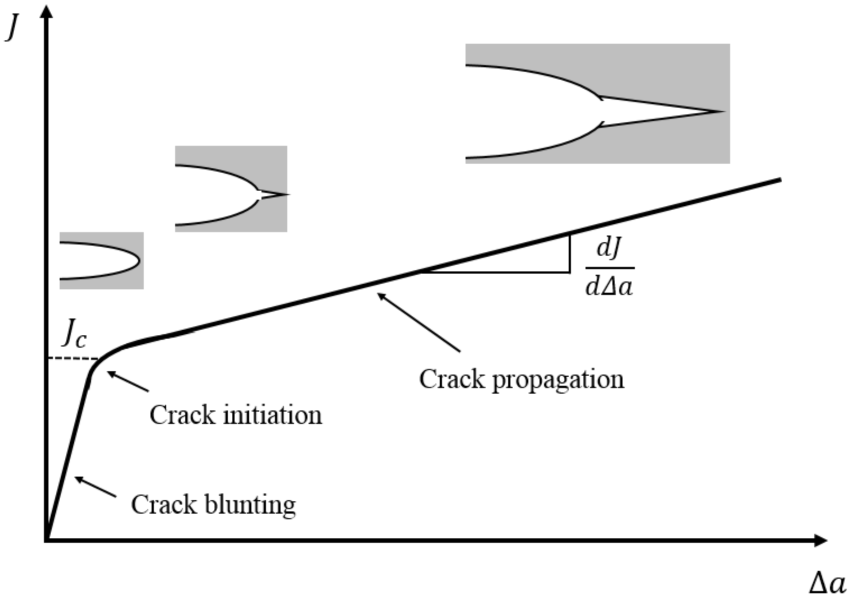

Figure 4.4. Schematic J resistance curve for a ductile material

4.2 Numerical methodology for small-scale yielding problem

Crack initiation and crack propagation under small-scale yielding and Mode I plane-strain conditions using the non-local GTN model (see chapter 2) are investigated in Section 4.3. The main objectives of this numerical study are:

- To prove the reliability of the model to predict crack initiation and to achieve large amounts of crack extension
- to establish a simple formula allowing to link the width of the localization band to the non-local length scale
- to introduce a reliable way to compute the crack length
- to investigate the influence of some parameters of the model on the crack resistance curve

In this section, the framework of the small scale yielding problem and the details of pre-/post-processing are introduced.

4.2.1 Framework of the small-scale yielding problem

The small-scale yielding model consists of a circular region of radius $R_{ext} \to \infty$ containing a crack and subjected to increasing displacement of the elastic mode I singular field applied on the far outer boundary, as shown in Equation (4.9). The conditions of small-scale yielding is fulfilled using the boundary-layer model developed by (McMeeking, 1977; McMeeking and Rice, 1975; Rice and Tracey, 1973). A schematic boundary-layer geometry is shown in Figure 4.5. This model is generally used to investigate the role of micromechanical parameters in relation to ductile crack initiation and growth.

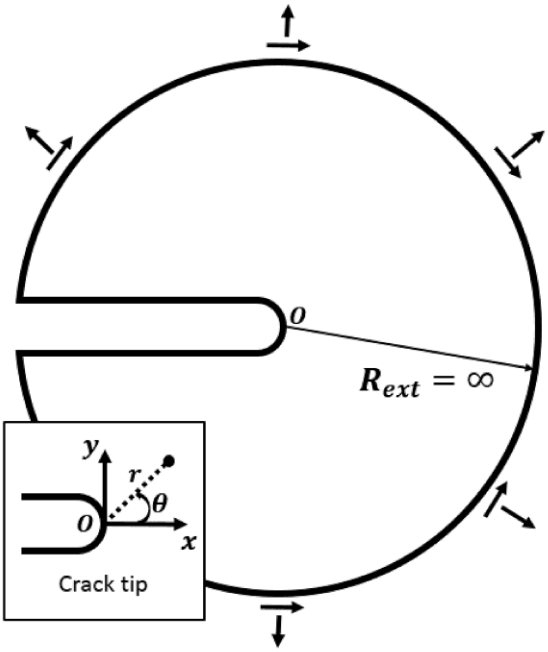

Figure 4.5. Schematic small-scale yielding problem geometry and conventions

For dimensional analysis, the path integral J can be normalized as $J/(\sigma_0 h)$ with h being a length scale to be defined. We start by giving a short summary of different length scales which are involved in the current problem:

- The external radius R_{ext} of the boundary-layer model: this quantity is considered as infinity.

- The size of the plastic zone R_p (see Equation (4.7)). Small-scale yielding condition requires $R_p \ll R_{ext}$. In practice, it is suggested $R_p \leq 0.05R_{ext}$. Note that R_p depends on the load level.
- The size of the process zone $R_{pz} = J/\sigma_0$. A finite deformation zone exists ahead of the crack tip within approximately $2R_{pz}$. Note that R_{pz} also depends on the load level.
- The non-local length scale $l_{nl} = \sqrt{c/\sigma_0}$ or $l_{nl} = \sqrt{c/\sigma_Y}$ where $\sigma_Y = (\sigma_0 + \sigma_{UTS})/2$ with σ_{UTS} is the ultimate tensile stress which is defined by $\sigma_{UTS} = \bar{\sigma}(\kappa')e^{-\kappa'}$ where κ' fulfills the condition $\bar{\sigma}(\kappa') = \bar{\sigma}'(\kappa')$.

For the normalization of J, it is necessary to use a length scale which remains constant during the simulation. For example, in the (Xia and Shih, 1995) in which a purely local model is used, the mesh size D is considered for the normalization. In this paper, the non-local length scale l_{nl} is used.

In this chapter, the unbounded power hardening law is used. We recall its form:

$$\bar{\sigma}(\kappa) = \sigma_0 \left(1 + \frac{\kappa}{\kappa_0}\right)^n \tag{4.11}$$

where (κ_0, n) are two hardening parameters.

A dimensional analysis shows that the crack-resistance curve $J(\Delta a)$ can be expressed as follows:

$$J(\Delta a) = \sigma_0 l_{nl} Function(\frac{\Delta a}{l_{nl}}, \frac{E}{\sigma_0}, \nu, \kappa_0, n, f_0, f_c, f_F, q_1, q_2) \tag{4.12}$$

where Δa is the crack length. In Equation (4.12), the parameters $\left(\frac{E}{\sigma_0}, \nu, \kappa_0, n\right)$ characterize the elastic-plastic properties of the matrix material and the parameters $(f_0, f_c, f_F, q_1, q_2)$ characterize the GTN damage model.

4.2.2 Pre-processing: material properties and finite element discretization

The boundary model is spatially discretized. Only half of geometry needs to be modeled due to symmetry of the geometry and the loading condition (except in the case of crack bifurcation). A typical mesh is depicted in Figure 4.6. In this mesh, 22962 elements are used to discretize the circular domain with about 10000 quadrilateral elements refined in the process zone of width B (as shown in Figure 4.6(b)). In particular, a small initial notch radius R_n is added in the process zone to improve the computational convergence and to avoid excessive element distortion before crack initiation.

Unless otherwise specified in the text, the normalized model parameters used in the simulations are listed in Table 4.3. In particular, the influence of different numerical parameters (mesh size l_e, nonlocal penalty parameter r_{nl}, incompressibility penalty parameter r_{inco}, two nucleation parameters, the external radius of the boundary layer model R_{ext} and the initial notch radius R_n) on the global response (J resistance curve) is investigated so as to choose an appropriate (range of) values for each numerical parameter. To avoid repeating results already given in Chapter 3, these studies and the corresponding results are put in Appendix A5. Note that the yield stress σ_0, the total loading time T and the non-local length l_{nl} are used for the normalization in dimensional analysis, so it is meaningless to modify them. Finite element simulations are performed using Code_Aster, a software suite for finite element analyses.

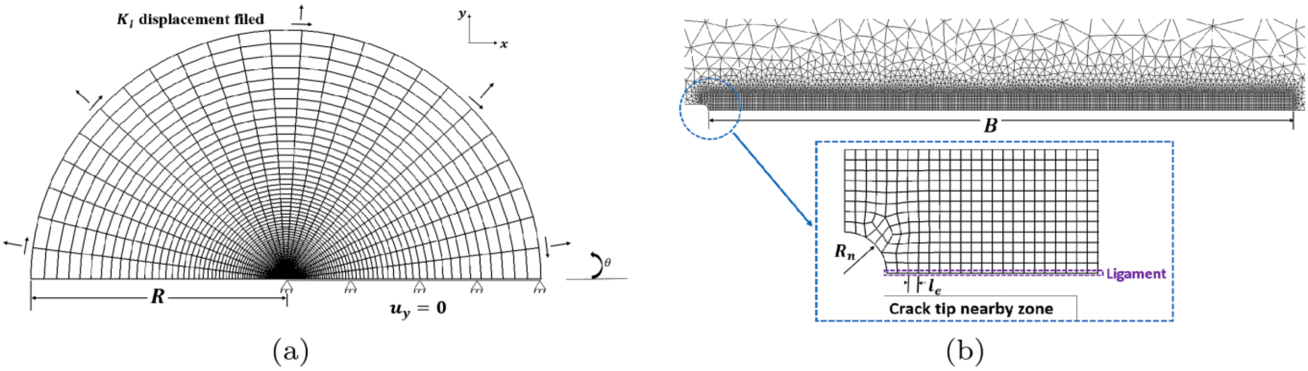

(a) (b)

Figure 4.6. Small-scale yielding mesh (a) in the outer area; (b) in the process-zone

Table 4.3. The normalized nominal values of the parameters used in the simulations

Elasticity	Young modulus E/σ_0	400
	Poisson ratio ν	0.3
Plasticity	Hardening variable κ_0	0.0025
	Hardening exponent n	0.1
Damage	Initial porosity f_0	0.001
	Critical porosity f_c	0.05
	Porosity at failure f_F	0.25
	Material constants (q_1, q_2)	(1.5,1.0)
Numerical parameters	Penalty parameter r_{nl}/σ_0	10
	Penalty parameter r_{inco}/σ_0	10
	Viscoelastic modulus E_v/σ_0	0.4
	Viscoelastic time τ_v/T	0.01
	Initial notch radius R_n/l_{nl}	1.4
	Mesh size l_e/l_{nl}	0.35

4.2.3 Post-processing: definition of crack length

Two types of definitions of the crack length Δa will be discussed. The initial crack tip is considered as the origin of the axes, as shown in Figure 4.5. We use, in this chapter, the uppercase letters (*X*, *Y*) for the coordinates in the initial configuration and the lowercase letters (*x*, *y*) for the coordinates in the deformed configuration. It is important to notice that both definitions of Δa are based on the deformed configuration, which is different from other studies such as (Hütter et al., 2013; Linse et al., 2012).

Literature method

The crack length Δa is often defined as:

$$\Delta a \equiv x_{tip} - x_{ref} \tag{4.13}$$

where x_{ref} is the x-coordinates of a defined reference point in the deformed configuration, x_{tip} is the x-coordinate of the farthest failure point in the ligament in the deformed configuration: $x_{tip} = \max(x, f(x) = f_F)$ with f the porosity and f_F the porosity at fracture (see Figure 4.6(b) for the position of ligament). Intuitively, for the reference point, it is possible to take the initial crack tip or some other points closed to the initial crack tip in the deformed configuration, for example the point just above the initial crack tip. Generally speaking, the position of the initial crack tip in the deformed configuration should not be used as the displacement of this point does not have too much meaning any more when the element containing this point fails or distorts.

In our work, the position of the farthest point satisfying $f = f_F$ in the ligament is used as an indication of the current crack tip. In the literature, instead of using the position of the farthest failure point, some authors used for example the position of the farthest point satisfying $f = f_c$ (Seidenfuss et al., 2011; Xia and Shih, 1995) or the position of the current maximum stress in the ligament (Hütter et al., 2013).

Proposed new method

This method is based on the assumption that during deformation, the (upper part of the) notch remains almost a circle. This allows defining the center (x_n, y_n) and the radius r_n of the current notch. At the beginning, we have $(x_n, y_n) = (-R_n, 0)$ and $r_n = R_n$. We distinguish two stages: crack tip blunting stage if $\max\big(f(x)\big) < f_F$ and crack propagation stage if $\max\big(f(x)\big) \geq f_F$ in the ligament. During crack tip blunting stage, the notch radius increases with increasing loading and we note r_{blunt} the radius at the end of the blunting stage. During crack propagation, we assume that the notch radius remains constant: $r_n \approx r_{blunt}$ (translation of the notch).

These assumptions are illustrated in Figure 4.7. They will be numerically validated in Section 4.3. They enable two geometrical definitions of the crack extension, whether the blunting should be incorporated or not:

$$\Delta a := \begin{cases} x_{\text{tip}} - (x_n + R_n), & \text{incorporation of blunting stage} \\ x_{\text{tip}} - (x_n + r_n), & \text{otherwise} \end{cases} \tag{4.14}$$

Note that the crack tip blunting length δ is shown in Figure 4.7, this length corresponds to the displacement of the initial crack tip. During crack tip blunting, the crack tip opening displacement CTOD is around 2δ.

A further discussion on these two methods can be found in the next section.

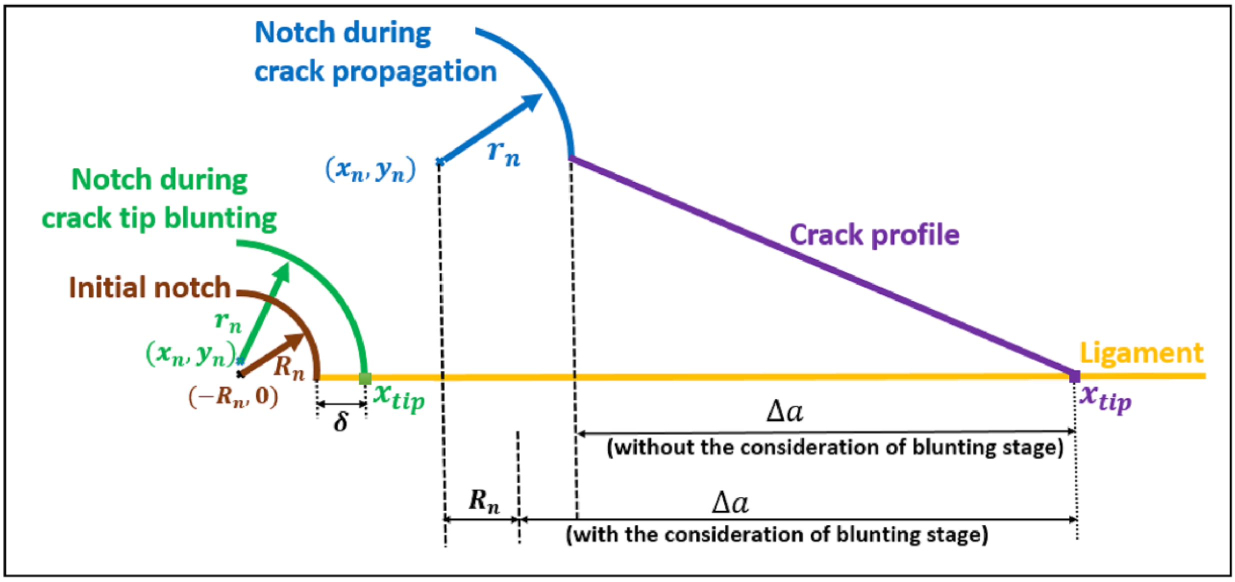

Figure 4.7. Definition of crack propagation length Δa

4.3 Results and discussion

4.3.1 Relation between the width of the localization band and the nonlocal length

This part aims at establishing the relationship between the width of the localization band l_b and the non-local characteristic length l_{nl}. The former is defined as the width of the stable crack propagation zone where $f \geq 2f_c$ (see Figure 4.8) while we recall that l_{nl} is derived from the non-local parameter c and the initial yield stress σ_0 as: $l_{nl} = \sqrt{c/\sigma_0}$ or $l_{nl} = \sqrt{c/\sigma_Y} = \sqrt{2c/(\sigma_{UTS} + \sigma_0)} = \sqrt{2c/(\sigma_0(n/\kappa_0)^n e^{-n+\kappa_0} + \sigma_0)}$.

Simulations are performed for $n = 0.15$ and for different value of κ_0: $\kappa_0 = 0.001, 0.002, \ldots, 0.01$. For each simulation, the evolution of l_b/l_{nl} against the position in the ligament is plotted (see Figure 4.8(a) for an example), then the maximal value of l_b/l_{nl} is considered as the width of the localization band for the corresponding κ_0. We recall that the yield stress σ_0 is used for normalization in the dimensional analysis, so it is meaningless to modify it. One can observe that during crack growth, the width of the localization band remains almost unchanged (see Figure 4.8 (a)). Figure 4.8(b) plots the evolution of l_b/l_{nl} as a function of κ_0, it is shown that the relationship between l_b and l_{nl} is rather linear, regardless of the definitions of l_{nl}. The value of l_b/l_{nl} is slightly more stable when $l_{nl} = \sqrt{c/\sigma_Y}$ than that when $l_{nl} = \sqrt{c/\sigma_0}$, which indicates that using σ_Y may be slightly better than σ_0 for the definition of l_{nl}.

$$l_b = \begin{cases} (1.3 \pm 0.2) l_{nl}, & l_{nl} = \sqrt{c/\sigma_0} \\ (1.5 \pm 0.1) l_{nl}, & l_{nl} = \sqrt{c/\sigma_Y} \end{cases} \tag{4.15}$$

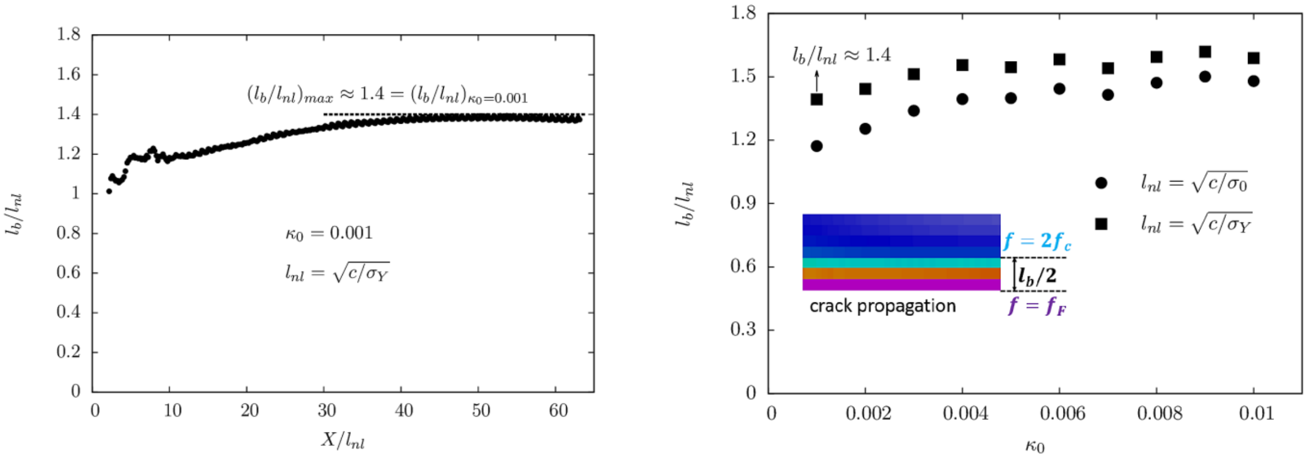

(a) (b)

Figure 4.8. The evolution of l_b/l_{nl} in the ligament when $\kappa_0 = 0.001$; (b) the evolution of l_b/l_{nl} as a function of κ_0

In addition, the definition of l_b depends on the value of f_c, so it is interesting to see the influence of f_c on l_b. Simulations are performed with $f_c = 0.01, 0.05, 0.1$. The definition of l_b remains unchanged, i.e., the width of the zone where $f \geq 2f_c$. The results are given in Table 4.4. It is seen that the value of l_b/l_{nl} decreases with increasing f_c. This result is not surprising since the definition of the localization band depends on f_c. Consequently, the relation between l_b and l_{nl} should be recalibrated when the value of f_c changes. Besides, with such definition of l_b, the porosity at fracture f_F should be at least $2f_c$.

Table 4.4. Value of l_b/l_{nl} for different f_c ($f_F = 0.25$)

$\boldsymbol{f_c}$	0.01	0.05	0.10
$\boldsymbol{l_b/l_{nl}}$	2.66	1.30	0.73

4.3.2 Comparison between Irwin formula and path contour integral

We have seen that in the case of elasticity, the path-independent contour integral J_{Rice} is equal to energy release rate J. Therefore, $J_{Rice} = J$ in elasticity. In this part, we would like to demonstrate that in small scale yielding, we also have $J_{Rice} \approx J$.

Figure 4.9 plots the J resistance curves for $J = K^2(1-\nu^2)/E$ and J_{Rice}. In particular, the contour that we choose to compute J_{Rice} is well in the elastic zone of the small-scale yielding model. The results show that the two methods give almost the same result, which indicates that in small scale yielding conditions, we have $J_{Rice} \approx K^2(1-\nu^2)/E$. In the following, the Irwin formula will be used for the computation of J_{Rice}. Instead of using J_{Rice}, we will note J for the sake of simplicity.

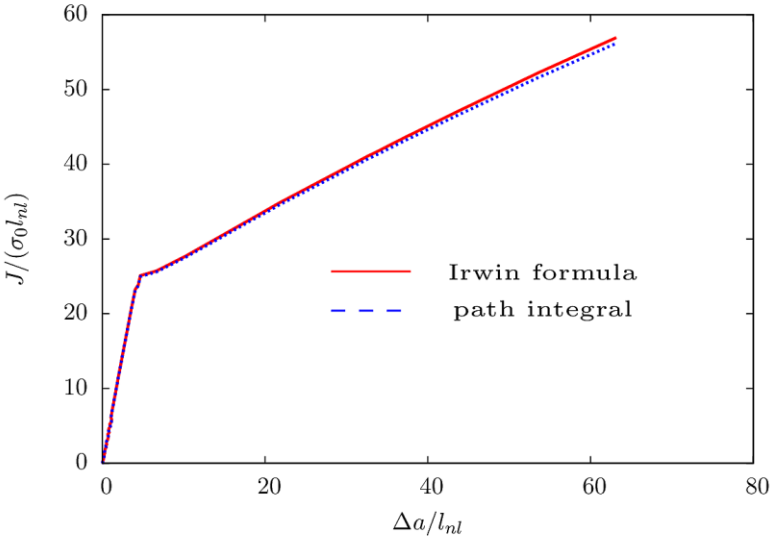

Figure 4.9. J resistance curves with Irwin formula and path integral

4.3.3 Validation of post-processing technique for blunting assessment

The objective of this part is to verify whether *the proposed new method* is satisfactory for extracting Δa. For the detail of *the literature method* and *the proposed new method*, one can refer to Section 4.2.3. Firstly, the assumption stated in Section 4.2.3, i.e., the notch remains almost circular during crack propagation, can be simply validated by visualizing the notch shape at different load levels (see for example Figure 4.14). In addition, Figure 4.10(a) plots the evolution of the notch radius r_n with increasing loading. It is shown that there is linear growth of r_n during crack tip blunting while during crack propagation, r_n increases very slowly. This is in accordance with our assumption.

Secondly, two scenarios will be studied: with and without the consideration of crack tip blunting for the computation of Δa. The former corresponds to $\Delta a = \Delta a_{bl} + \Delta a_{tear}$ and the latter corresponds to $\Delta a = \Delta a_{tear}$ with Δa_{bl} crack growth due to blunting and Δa_{tear} crack extension corresponding to the actual ductile tearing. For the first scenario, only the *proposed new method* is used while for the second scenario, both *the literature method* and *the proposed new method* are used. For the second scenario, it is necessary to choose a reference point (i.e. x_{ref} in Equation (4.13)) for the *literature method*. As said in Section 4.2.3, the initial crack tip cannot be considered as a reference point as the element containing this point fails during loading and the displacement of this point is not reliable any more. Instead of using the initial crack tip, we use the point located above the initial crack tip, as shown in Figure 4.10(b). Figure 4.10(b) plots the evolution of the crack length Δa as a function of increasing load. It shows that:

- For the second scenario (without the consideration of crack tip blunting), both methods give almost the same results. It reveals that both *the literature method* and *the proposed new method* can be used to extract the physical crack extension.
- If we compare the two scenarios, the curve slopes during crack propagation are the same in the three cases.

The literature method is rather simple but it cannot take into account the blunting. Therefore, in the following, the *proposed new method* is used and the crack tip blunting stage is taken into account for the computation of Δa in agreement with experimental practice (Pardoen and Delannay, 2000).

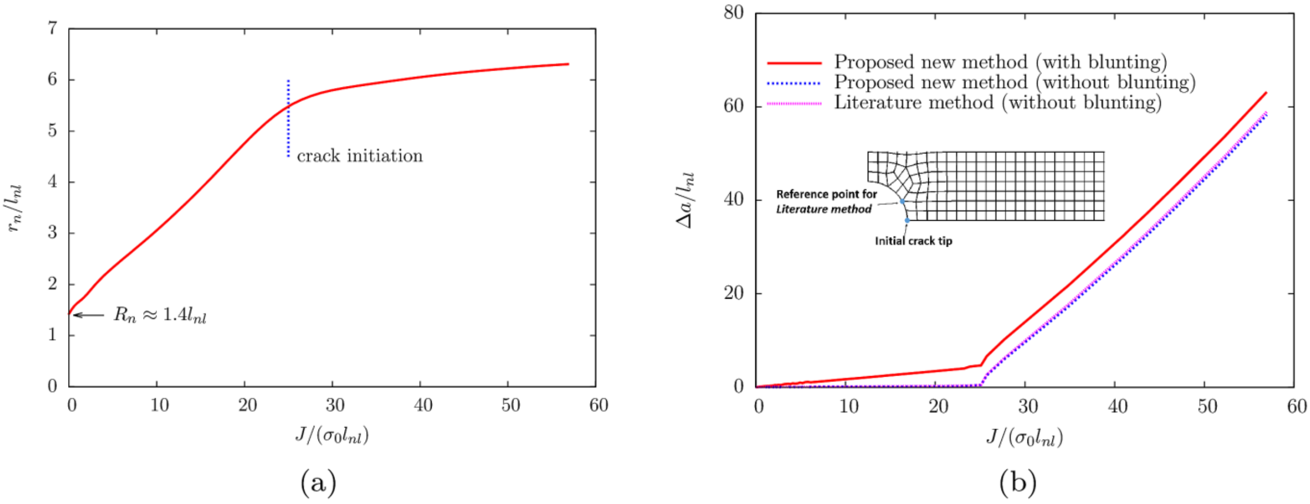

Figure 4.10. Evolution of (a) the notch radius r_n; (b) the crack length Δa with increasing loading

4.3.4 Crack-tip blunting, crack initiation and crack propagation

In this part, several simulations are performed using the parameters introduced in Table 4.3. Figure 4.11(a) shows the evolution of the porosity f ahead of the notch with increasing loading. From this figure, it is observed that the porosity at the crack tip grows slowly when compared to that at other nearby points, which results in the fact that the first failure ($f = f_F$) does not occur at the crack tip (see the enlargement in Figure 4.11 (a) for $J/(\sigma_0 l_{nl}) \approx 26$).

Figure 4.11(b) plots the corresponding crack opening stress σ_{yy}. It shows that during crack tip blunting, there is a single stress peak and it is far away from the crack tip. After crack initiation, another stress peak appears near the current crack tip and the crack propagates slowly at this stage. As loading increases, the initial stress peak finally disappears and the crack propagates quickly. After the disappearance of the initial stress peak, the stress profile shifts along the ligament with increasing loading. In particular, the maximum crack opening stress remains the same. At this stage, the stress profile ahead of the running crack is much steeper than that at crack initiation.

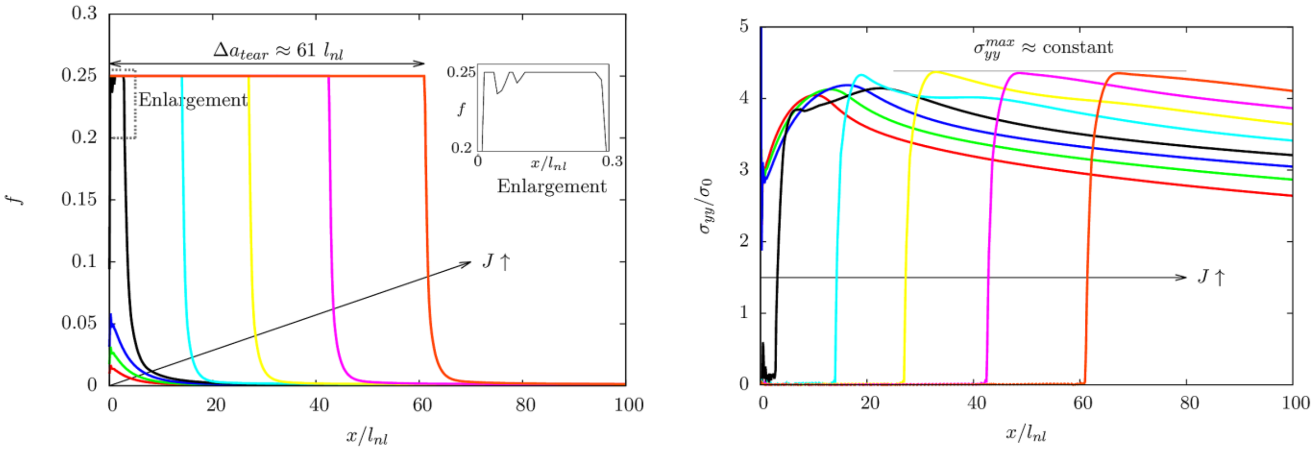

(a) (b)

Figure 4.11. Evolution of (a) the porosity f; (b) the crack opening stress σ_{yy} *in the ligament when* $J/(\sigma_0 l_{nl}) \approx$ 10,14,20,26,33,40,49,58)

Figure 4.12(a) plots the distribution of the hardening variable κ in the ligament at different load levels. The κ profile moves along the ligament with increasing loading, which is similar to that of σ_{yy}. One can observe that there exists a critical position x_c such that κ at the failure points remain almost constant for $x > x_c$. In the current case, this constant value is around $\kappa = 0.4$. To further investigate this failure zone, we can, for example, plot the history curves at different points in the ligament. For instance, the f - κ curves at some points in the ligament are given in Figure 4.12 (b), their location is given in the initial configuration. One can see that the $f - \kappa$ curves at the Gauss points located ahead of $X \approx 18l_{nl}$ almost overlap, i.e., all material points located at $X \geq 18l_{nl}$ have the same history which may correspond to a steady-state evolution.

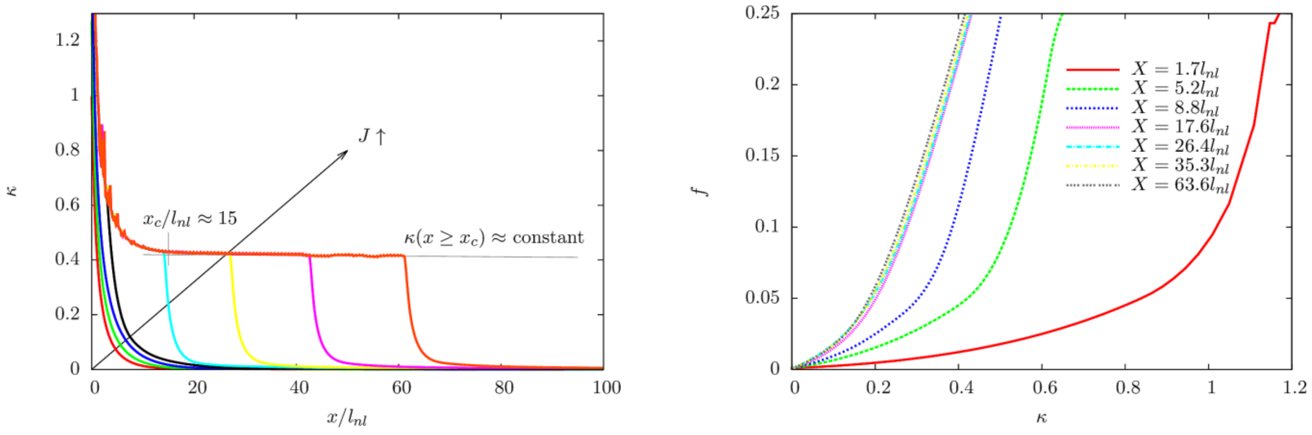

(a) (b)

Figure 4.12. (a) Distribution of the hardening variable κ when $J/(\sigma_0 l_{nl}) = 10,14,20,26,33,40,49,58$ *in the ligament; (b)* $f - \kappa$ *history curves at different positions in the ligament*

Figure 4.14 illustrates crack tip blunting, crack initiation and crack propagation with increasing loading in the initial and deformed configurations. During crack tip blunting, the notch remains almost circular. As load increases, the crack appears near the initial crack tip and then propagates. Note that the notch still retains a circle shape during crack propagation; it is actually the prerequisite to the definition of the crack length Δa with the *proposed new method*. In addition, one can observe that damage forms in front of the current crack tip and moves along the ligament. A linear crack opening profile is obtained, as predicted by (Rice et al., 1980), observed by (Hütter et al., 2013) in the simulations and measured by (Heerens and Schödel, 2003) in the experiments. This implies that a crack tip opening angle CTOA can be defined. In the present case, CTOA is around 16° at the end of loading, as shown in Figure 4.13.

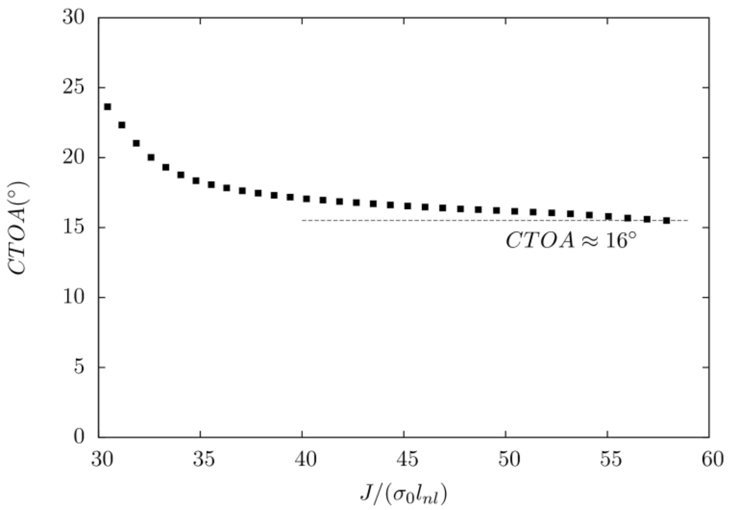

Figure 4.13. CTOA at different load levels

At the final stage of loading, more than 800 finite elements along the ligament have fully failed (violet part in Figure 4.14). Most results in this part correspond to a loading stage at which 180 finite elements along the ligament are broken. Note that no element-deletion method is applied in our case. Some authors also succeeded in simulating large crack growth by means of local GTN model (Xia and Shih, 1995), or non-local GTN model (Hütter et al., 2013). In both cases, the issue of volumetric locking was not dealt with. In the work of (Xia and Shih, 1995), the mesh size is considered as a material parameter so that the mesh-dependency problem still exists. In the work of (Hütter et al., 2013), the large crack growth was performed with $f_0 = 0.1$ or $f_0 = 0.01$, values which are not adapted to most materials - modern steels and aluminum alloys are processed so that f_0 is below 10^{-3}.

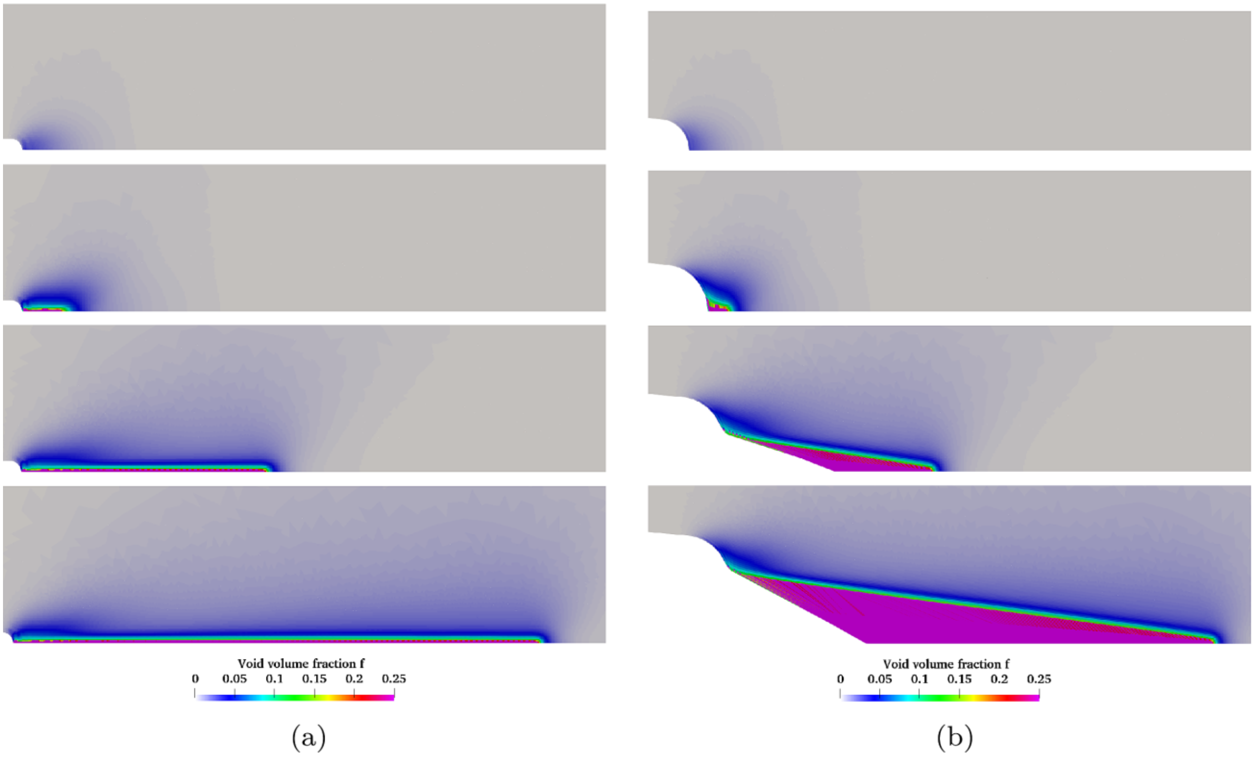

(a) (b)

Figure 4.14. Distribution of the porosity f under (a) undeformed and (b) deformed shapes when $J/(\sigma_0 l_{nl}) = 14,26,40,58$

Figure 4.15 compares the energies dissipated during crack propagation in the localization band ($\mathcal{W}_{lb}^{p}$, the localization band is defined as the zone where $f \geq 2f_c$) and in the entire volume ($\mathcal{W}^{p}$). These two quantities are defined and computed as:

$$\begin{cases} \mathcal{W}^{p} = \displaystyle\int_0^t \int_{\Omega_0} \left(\boldsymbol{T} : \dot{\boldsymbol{E}}^{\boldsymbol{p}}\right) d\Omega_0 dt \\ \mathcal{W}_{lb}^{p} = \displaystyle\int_0^t \int_{\Omega_{lb}} \left(\boldsymbol{T} : \dot{\boldsymbol{E}}^{\boldsymbol{p}}\right) d\Omega_{lb} dt \end{cases} \tag{4.16}$$

where t stands for the current load level and Ω_{lb} stands for the region in which $f \geq 2f_c$. Note that Ω_{lb} can change at each time step and $\mathcal{W}_{lb}^{p} = 0$ if $f < 2f_c$ for all material points.

Figure 4.15 (a) plots the evolution of $\mathcal{W}_p$ and $\mathcal{W}_{lb}^{p}$. $\mathcal{W}_{lb}^{p}$ varies linearly with crack advance which indicates that the energy dissipated in the localization band per unit crack advance is constant. The evolution of $\mathcal{W}^{p}$ is first rather quadratic and then becomes almost linear. To compare these two energies, Figure 4.15 (b) plots the evolution of $\mathcal{W}_{\mathrm{lb}}^{p}/\mathcal{W}^{\mathrm{p}}$ and $\partial\mathcal{W}_{lb}^{p}/\partial\mathcal{W}^{p}$. One can observe that $\mathcal{W}_{lb}^{p}$ is very small when compared to $\mathcal{W}^{p}$ and $\mathcal{W}_{\mathrm{lb}}^{p}/\mathcal{W}^{\mathrm{p}}$ increases at the beginning and tends to a constant (around 0.001) as crack extends. On the contrary, the value of $\partial\mathcal{W}_{lb}^{p}/\partial\mathcal{W}^{p}$ decreases at first and reaches to the same constant at $\Delta a_{tear}/l_{nl} \approx 10$. This observation shows that the energy consumed for crack propagation tends to be proportional to the total dissipated energy for long cracks. In some ways, it indicates that the steady state may be reached which is consistent with the observed evolutions of opening stress, damage and plastic strain along the crack path (Figure 4.11and Figure 4.12).

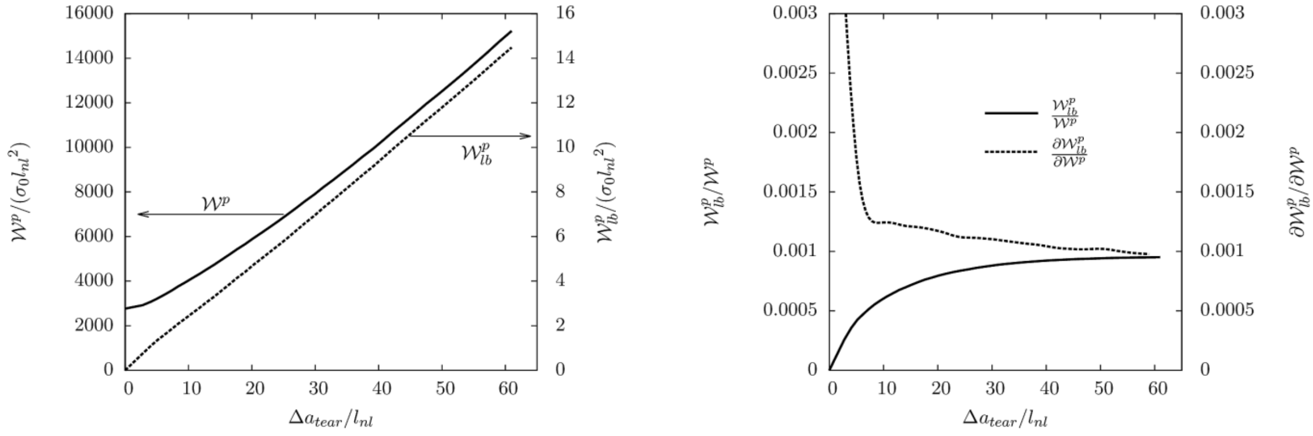

(a) (b)

Figure 4.15. Comparison between the energies dissipated during crack propagation in the localization band (W_{lb}^{p}) and in the entire volume (W^{p})

4.3.5 Effect of different material parameters

Influence of hardening exponent n on global response

In this part, the hardening parameter κ_0 remains constant. Figure 4.16(a) shows the J resistance curves for different values of n. It is seen that n can affect crack tip blunting, crack initiation toughness J_c and tearing behavior. Larger values of n lead to steeper blunting lines. In particular, if $\sigma_Y = (\sigma_0 + \sigma_{UTS})/2$, with $\sigma_{UTS} = \sigma_0(n/\kappa_0)^n e^{-n+\kappa_0}$ for the selected hardening law, is used for the normalization of J, the blunting lines for different n would overlap. This result is in accordance with the ASTM E1820 standard which uses σ_Y to define the blunting line. In addition, crack appears earlier with a smaller value of n. On the contrary, the tearing modulus ($T_{ear} = \Delta J/(\sigma_0 \Delta a)$) decreases for increasing values of n. One can notice that the simulations are performed for $n \geq 0.12$ as crack bifurcation is observed for $n < 0.12$ as shown in Figure 4.16(b). This could correspond to the competition between crack normal opening and shear cracking. Further investigations on crack bifurcation will be conducted in the future work.

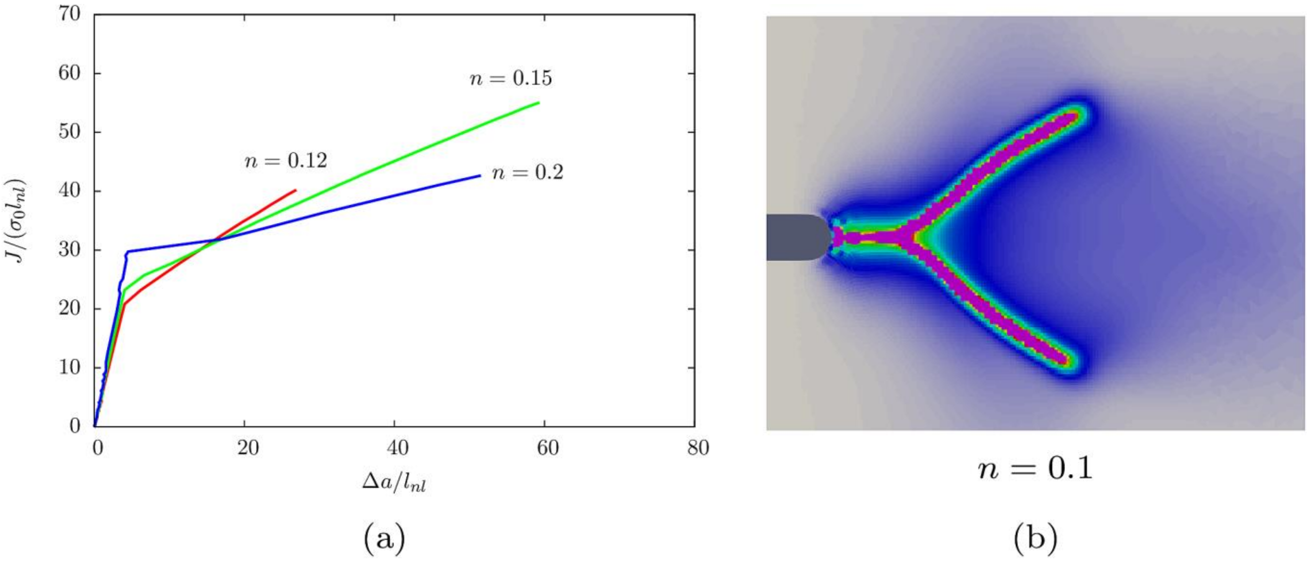

Figure 4.16. (a) J resistance curve for different n>0.1; (b) crack bifurcation for n=0.1 in the undeformed configuration

Influence of f_0 and f_c on global response

Figure 4.17 (a) plots the J resistance curves for different initial porosity f_0. It shows that f_0 affects both crack initiation and tearing behavior. To propagate the same crack length Δa, the smaller f_0 is, the more energy should be provided. Indeed, the normal stress required to achieve material separation is high when f_0 is low, so that a fully developed plastic zone is formed in front of the crack tip leading to large plastic dissipation as the crack advances (Xia and Shih, 1995) . On the contrary, if the value of f_0 is high enough, the J resistance curve during crack propagation becomes flat and crack extension may become unstable. Like in the case with $n < 0.12$ and $f_0 = 0.001$ (see above), crack bifurcation is also observed for the case with $f_0 \sim 10^{-4}$ and $n = 0.15$. In the work of (Hütter et al., 2013), this bifurcation was not observed as large values for f_0 ($f_0 \geq 0.01$) were used.

The J resistance curves with different f_c are depicted in Figure 4.17 (b). From the obtained results, one can observe that the value of f_c has influence on both crack initiation and tearing behavior: On the one hand, the critical toughness J_c increases with f_c as the void coalescence (so the failure) is postponed with the increase of f_c. On the other hand, the slope of J resistance curve, i.e., tearing modulus $T_{ear} = \Delta J/(\sigma_0 \Delta a)$ increases with f_c during crack propagation.

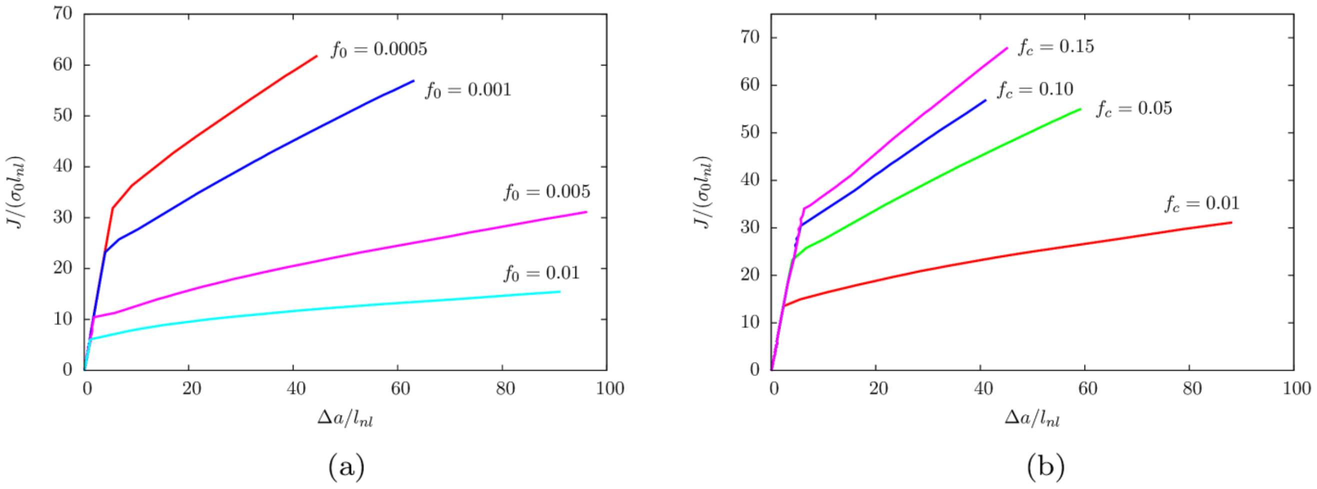

Figure 4.17. J resistance curves for (a) different f_0; (b) different f_c

4.4 Summary

In this chapter, the nonlocal GTN model is used to simulate crack extension over relatively long distances (> 200 elements) in the case of small scale yielding using the boundary layer model where the material is loaded applying a remote stress intensity factor. The use of the boundary layer model allows defining non dimensional quantities.

This technique is first used to study the numerical stability (see Appendix A5). The effect of the penalty parameters r_{nl} and r_{inco} on the $J - \Delta a$ curves and on the local values of plastic strain, damage and stresses is investigated. This allows defining ranges for both parameters so that they solve the purely numerical issues without affecting the computed physical quantities of interest. It is also shown that the mesh size in the crack propagation area must be at least three times smaller than the model intrinsic length defined as $l_{nl} = \sqrt{c/\sigma_0}$ to obtain mesh independency.

Using these optimal numerical parameters, a systematic study of the properties of the proposed model is carried out. The highly damaged zone surrounding the crack defined as the area where $f > 2f_c$ a thickness which is about has $1.3l_{nl}$. After an initial stage corresponding to blunting and initiation of crack growth, a stabilized crack propagation stage is reached with damage and stress gradients (Figure 4.11) much sharper than during initiation. The non-local framework can nevertheless describe these gradients. This steady state also corresponds to a constant cumulated plastic strain at failure (Figure 4.12). Plastic dissipation in the highly damage zone ($\mathcal{W}_{lb}^p$) is evaluated as a function of crack advance and compared to the total dissipated energy ($\mathcal{W}^p$). Both quantities increase as a function of crack advance and it is shown that $\mathcal{W}_{lb}^p$ is much smaller than $\mathcal{W}^p$. Their ratio tends to be constant for large crack advance which corresponds to steady state crack propagation. The effect of model parameters such as f_c or f_0 is also studied. Standard evolutions (Hütter et al., 2013) are obtained. Increasing f_0 or decreasing f_c leads to lower values of $J/(\sigma_0 l_{nl})$ for a given crack advance as well as to lower values of the tearing modulus $\Delta J/(\sigma_0\ \Delta a)$. Finally crack bifurcation is observed when the hardening exponent, n, decreases. The same phenomenon is observed when the initial porosity f_0 is decreased. The question of whether the effect is a purely numerical artefact or reflects some reality remains open. The simulated bifurcation could possibly represent the observed zigzagging cracks observed after blunting (see e.g. (Beachem and Yoder, 1973; Handerhan and Garrison Jr, 1992)).

5 Industrial applications

> *我们可以体验的最美丽的东西是神秘的，它是所有真正的艺术和科学的源泉*
>
> *La plus belle chose que nous puissions éprouver, c'est le côté mystérieux de la vie. C'est le sentiment profond qui se trouve au berceau de l'art et de la science véritable.*
>
> *The most beautiful thing we can experience is the mysterious. It is the source of all true art and science.*
>
> 阿尔伯特•爱因斯坦 Albert Einstein

Résumé

Ce chapitre est dédié aux applications industrielles du modèle GTN nonlocal dans le cadre du projet ATLAS+.

Le but de ce chapitre est de voir si notre modèle est d’une part, capable de prédire le comportement du matériau et d’autre part, assez robuste pour pouvoir simuler une grande propagation de fissure dans une structure industrielle.

La première partie de ce chapitre se concentre sur différents essais qui ont été réalisés dans différents laboratoires dont EDF et ARMINES, ainsi que les résultats expérimentaux obtenus (courbes de « force-déplacement », « force-réduction de diamètre », « force – COD », fractographies, etc). Pour la propagation de fissure dans le tube, un mode mixte (propagation dans le plan et bifurcation hors-plan) a été observé en début de la propagation. Puis la bifurcation complète de la fissure a eu lieu.

Une partie de ces résultats expérimentaux (à savoir, AE2) sont utilisés pour identifier les paramètres du modèle de GTN nonlocal. Ces paramètres sont ensuite utilisés pour prédire les AE4, AE10, AE20, SENT et le tube FP1. Selon les résultats obtenus, avec les paramètres identifiés, les comportements globaux de AE4, AE10 et CT20 sont bien prédits alors qu’une surestimation de force est observée pour les SENT. Quant à la prédiction du tube, le comportement global est bien prédit jusqu’à une ouverture de 8 mm. Par ailleurs, on a bien prédit une propagation hors plan.

Ainsi, notre modèle est assez robuste pour pourvoir être appliqué aux cas industriels.

5.1 Introduction to European project ATLAS+

The European project ATLAS+ (Advanced Structural Integrity Assessment Tools for Safe Long Term Operation) has been launched in June 2017. The main mission of this project is to develop advanced structural assessment tools to address technological improvements for the safe and long term operation of nuclear reactor pressure vessels (Lindqvist et al., 2018). To this end, it is required to study the transferability of the properties of ductile materials from small-scale specimens to large-scale structures.

Figure 5.1. Ferritic pipe provided by Framatome GmbH

The fracture experiments were thus decided to be conducted on the ferritic steel 15NiCuMoNb5 (WB36) that is used in the secondary feed-water line in German PWR reactors. The material was supplied as a 30 mm thick pipe (internal diameter 318 mm and external diameter 378 mm) provided by Framatome GmbH (see Figure 5.1). In order to characterize the WB36 material, several specimens, which are extracted from the ferritic pipe, were tested. The location of each specimen is shown in Figure 5.2. A summary of some ductile fracture tests on small specimens (smooth tensile specimens ST, notched tensile specimens NT, compact tension specimens CT, single edge notch tension specimen SENT) is given in Table 5.1.

After material characterization, the 4-point bending tests on three large-scale pre-cracked pipes will be done at room temperature. Like the small specimens, these pipes are also made from the pipe provided by Framatome GmbH. They have the same geometry and are subjected to the same loading. The difference is that they have different initial defects. The bending tests were planned to be done so as to investigate the effect of the crack tip constraint at a structural scale. The results will be used to develop and validate advanced tools for structural integrity assessment.

Table 5.1. Ductile fracture tests for material characterization

Test (20°)	Specimen	Orientation (see Figure 5.2)	Company
Tensile tests	ST6	L	BZN, EDF, KIWA
Notched tensile tests	NT2, NT4, NT10	L	ARMINES, CEA, EDF
$J - \Delta a$	CT20	LT	ARMINES, EDF, KIWA
$J - \Delta a$	SENT20	LS	ARMINES, EDF

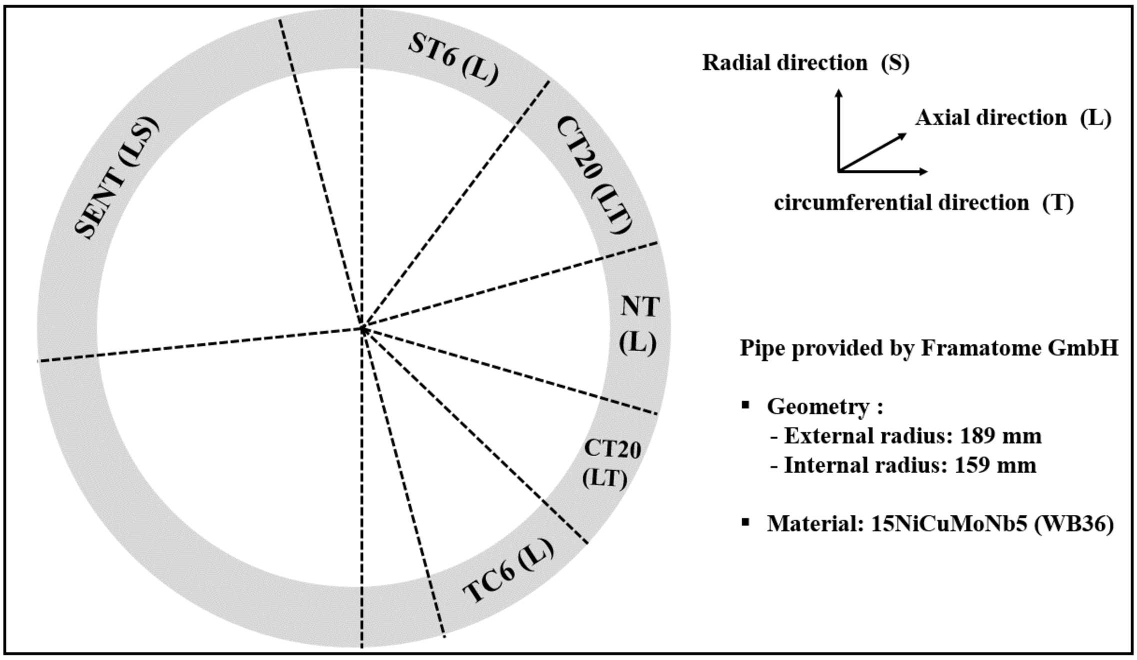

Pipe provided by Framatome GmbH

- **Geometry :**
  - **External radius: 189 mm**
  - **Internal radius: 159 mm**
- **Material: 15NiCuMoNb5 (WB36)**

Figure 5.2. Location of each specimen (ST, NT, CT, SENT) in the pipe

5.2 Experimental results

5.2.1 Chemical composition

The analysis of the chemical composition of the WB36 material was performed in the laboratory of the French company EDF. Results are shown in Table 5.2.

Table 5.2. Chemical composition of the ferritic steel 15NiCuMoNb5

Elements	C	Si	Mn	P	S	Cr	Mo	Ni
Content (%)	0.14	0.31	0.94	0.009	0.02	0.4	0.35	1.14
Elements	Al	Sn	Cu	As	N	V	Nb	O
Content (%)	0.15	0.13	0.62	-	0.013	-	0.03	0.003

5.2.2 Smooth tensile specimens

The simple tensile tests were conducted at room temperature (around 20°C). The geometry of the tensile bar is shown in Figure 5.3(a).

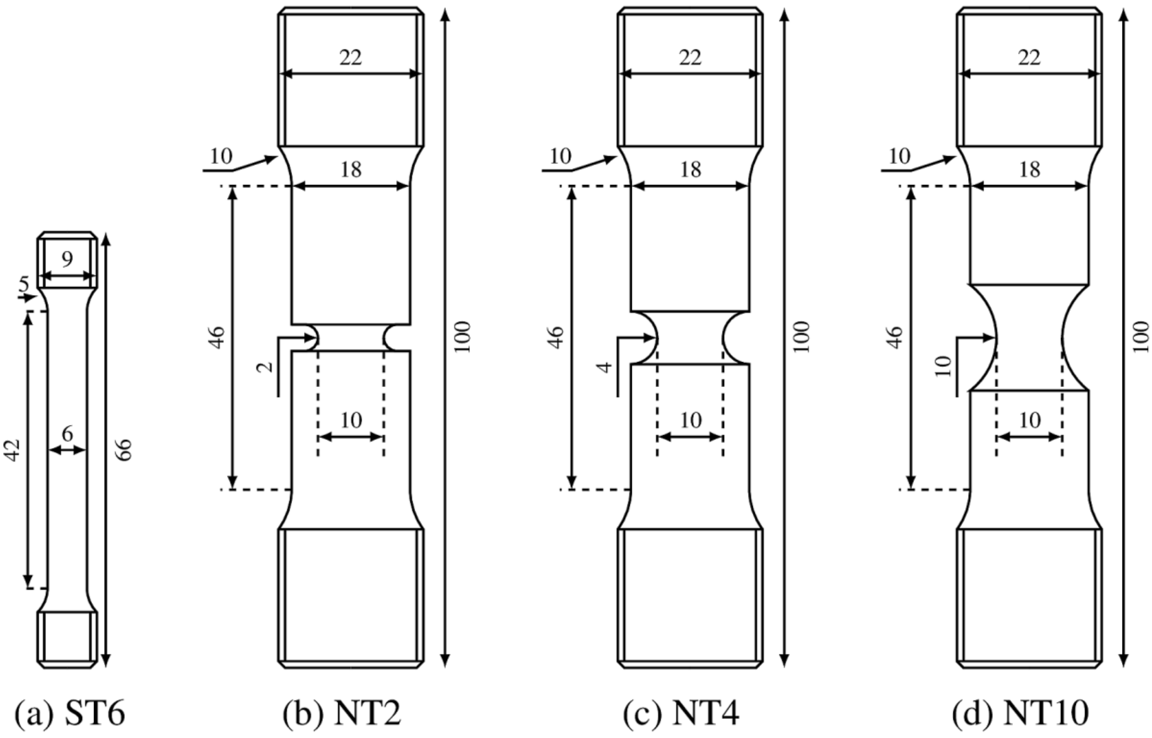

(a) ST6 (b) NT2 (c) NT4 (d) NT10

Figure 5.3. Geometries of the ST6, NT2, NT4 and NT10 (unit: mm)

Figure 5.4(a) shows the true stress-strain curves of the material. In total, 17 smooth tensile specimens were tested. Figure 5.4(b) plots the corresponding upper, average and lower values. These results show the inhomogeneity of the tensile properties of the material (the Relative Average Deviation[9] is around 3%).

---

[9] Relative average deviation (RAD) of a data set is a percentage that tells how much, on average, each measurement differs from the arithmetic mean of the data.

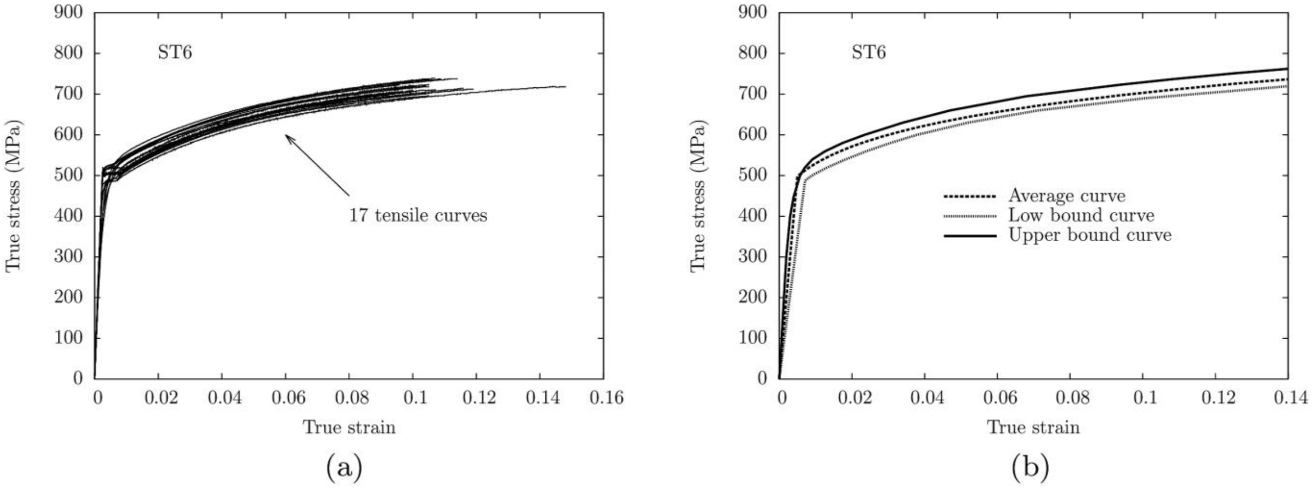

Figure 5.4. Tensile curves of the material WB36

5.2.3 Notch tensile specimens

Three types of notched tensile specimens (NT2, NT4 and NT10) were tested at room temperature (around 20°C). For each specimen, three tests were performed by different laboratories (ARMINES, CEA and EDF). The geometries of the three NT are respectively shown in Figure 5.3(b) (c) and (d). Note that the index x of $\mathrm{NT_x}$ is computed as $x = 10R/\Phi_0$ with R the initial notch radius and Φ_0 the initial minimum diameter.

Figure 5.5 (a) plots the obtained normalized force-displacement curves by ARMINES (S_0 refers to the initial cross section). The longitudinal displacement is measured using an extensometer (gage length 27 mm) located on both sides of the notch. Figure 5.5 (b) plots the obtained normalized force-diameter reduction curves by ARMINES, CEA and EDF. It shows a good agreement among the results obtained by different laboratories. Moreover, the effect of geometry is clearly illustrated by the maximum force and the diameter reduction at failure. Note that the sudden load drop in these two figures corresponds to crack initiation at the center of the specimens. This point will be called “fracture point” in the following.

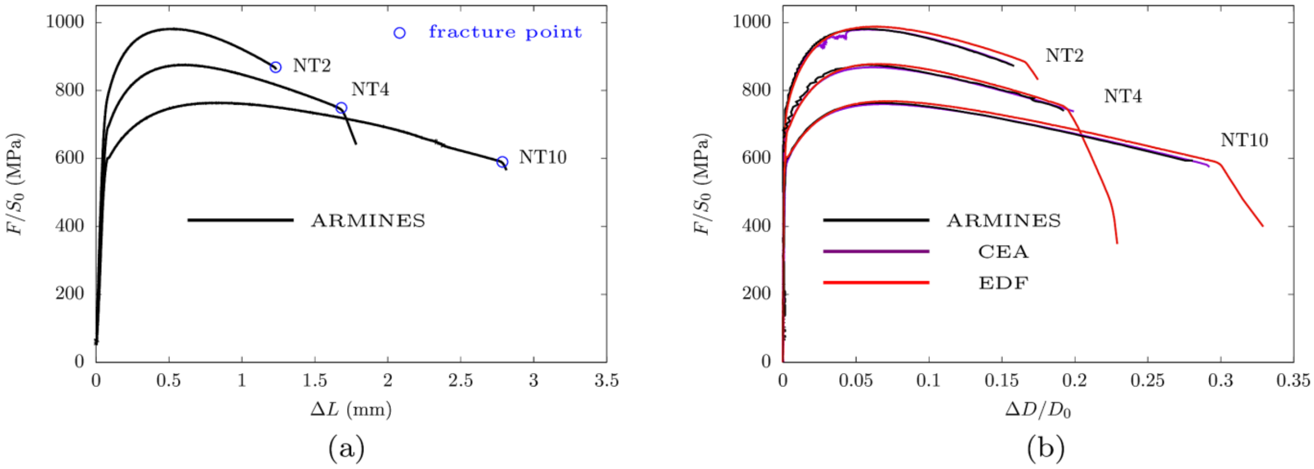

Figure 5.5. (a) Force-Displacement curves and (b) force-diameter reduction curves for different NT

Scanning electron microscope (SEM) fractographs at the center (crack-initiation area) of the fracture surface of NT2, NT4 and NT10 samples at magnification 100X and 500X are shown in Figure 5.6. Fracture Mode is ductile since lots of large (MnS) and fine (Fe_3C) dimples are visible. The proportions of large and fine dimples on fracture surface depends on stress state (triaxiality). The triaxiality level in $\mathrm{NT_x}$ decreases with increasing notch radius, i.e., $\mathrm{T}_r(NT2) > \mathrm{T}_r(NT4) > \mathrm{T}_r(NT10)$ with T_r the triaxiality. It is observed that the size of large dimples does not appear to be significantly modified by triaxiality in the present case. Inclusions tend to be aligned. In addition, cup-cone fracture is observed in certain NT specimen: very fine dimples and limited void growth are observed in the slanted region (an example of cup-cone on NT2 is shown in Figure 5.7).

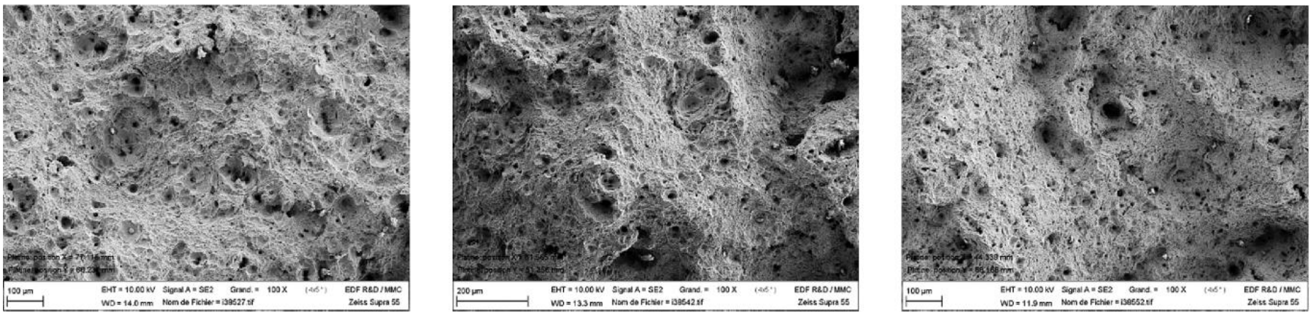

(a) Fracture surface of NT2, NT4 and NT10 at magnification 100X

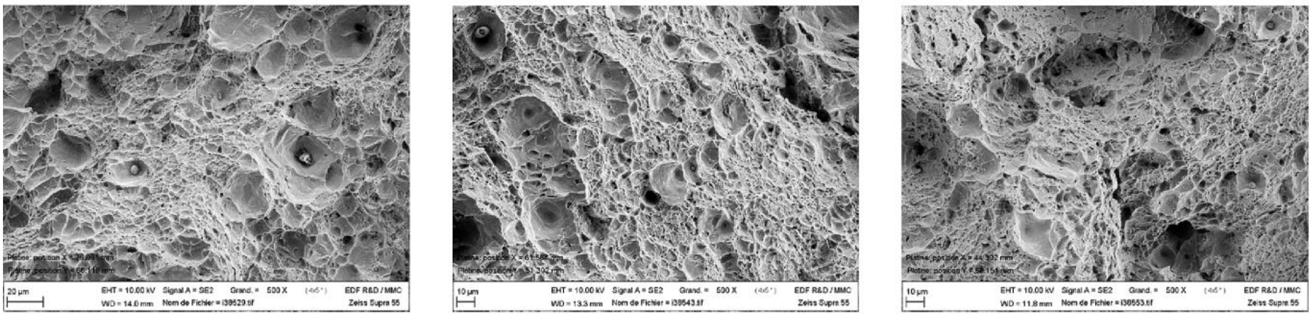

(b) Fracture surface of NT2, NT4 and NT10 at magnification 500X

Figure 5.6. Fracture surface of NT2, NT4 and NT10 at magnification (a) 100X; (b) 500X

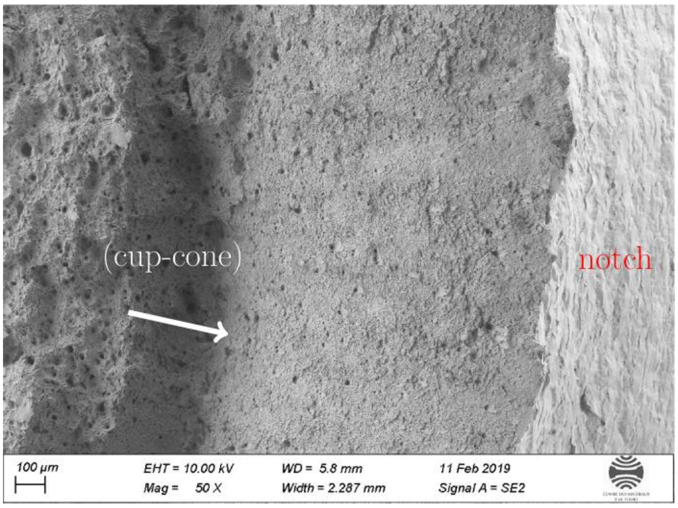

Figure 5.7. Cup-cone fracture observed in NT2

5.2.4 Compact tension specimens

The first ductile tearing tests were conducted on compact tension specimens (CT) with different sizes (CT10, CT20), different a_0/W ratios and different orientations (LT or LS, see Figure 5.2 for the orientation) at room temperature (around 20°C). All specimens are side-grooved. For each specimen, the tests were done by different laboratories (EDF, ARMINES).

Here we only present the results on CT20 (LT) with $B = 20$ mm, $B_N = 16$ mm and $a_0/W = 0.6$. Here, B is the specimen thickness, B_N is the net specimen thickness ($B_N = B$ if no side grooves), a_0 is the initial crack length (precracked by fatigue) and $W - a_0$ is the size of uncracked ligament. The geometry of CT20 is shown in Figure 5.8.

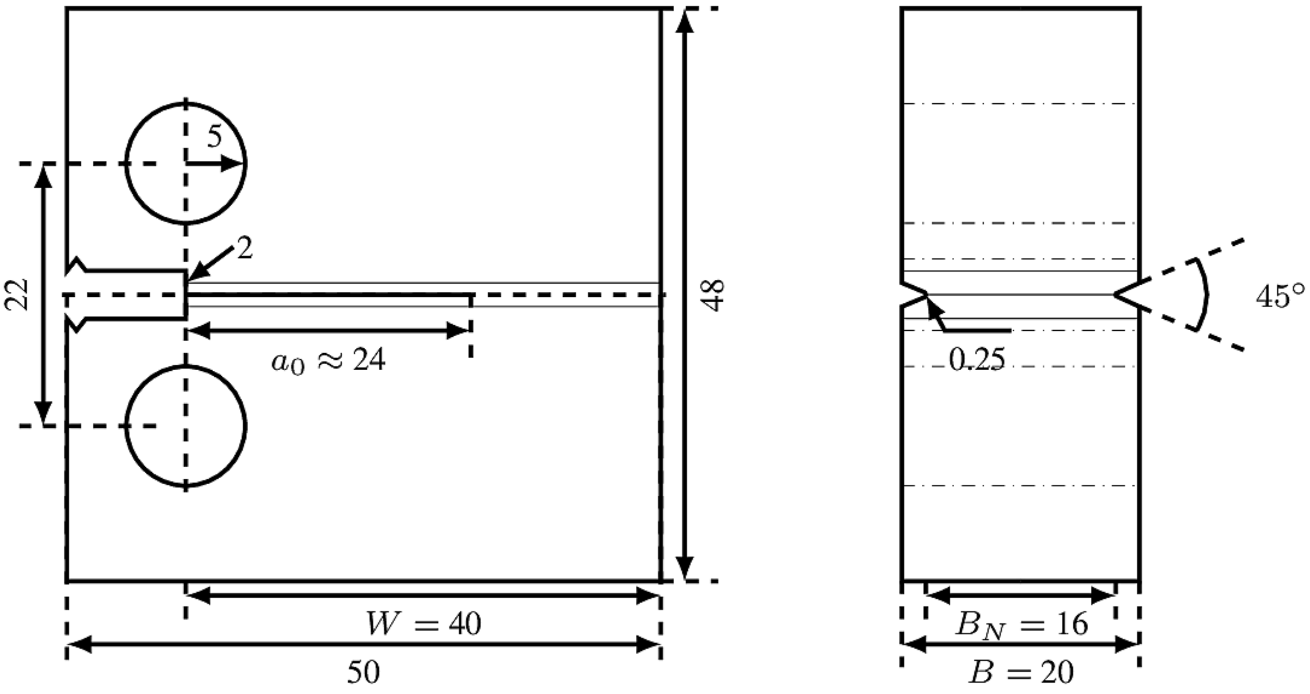

Figure 5.8.geometry of CT20 (unit: mm)

Figure 5.9 plots the force-CMOD curves for the nine tests performed on CT20. A difference is observed among the results which is mainly due to slightly different initial crack length (a_0) and possibly to the inhomogeneity of the material.

Figure 5.10 shows the fracture surface of all CT specimens except CT20-4 at the end of loading. The results show that ductile tearing occurs on all specimens. In addition, in most cases, the fracture surface is rather flat.

Scanning electron microscope (SEM) fractographs at the center and near the side-groove of the CT20-1 sample at magnification 100X are shown in Figure 5.11. Fracture Mode is ductile. Large dimples are dominant while fine dimples can still be found. There are lots of inclusions on the fracture surface and these inclusions are aligned along the crack propagation direction. In particular, we estimate that the void distance is about 300 μm (as shown in this figure), which will be considered as the characteristic length in our work. No obvious difference is observed between the center and the side-groove nearby area.

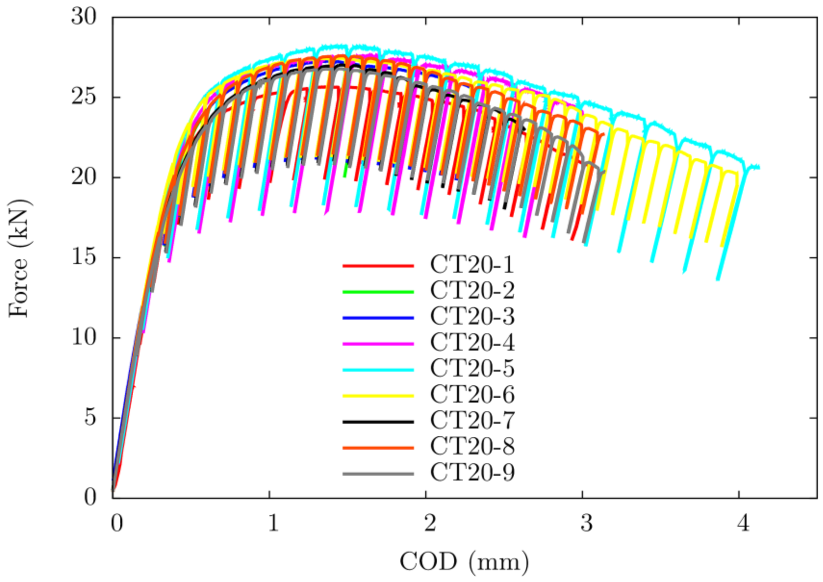

Figure 5.9. Force-COD for CT20

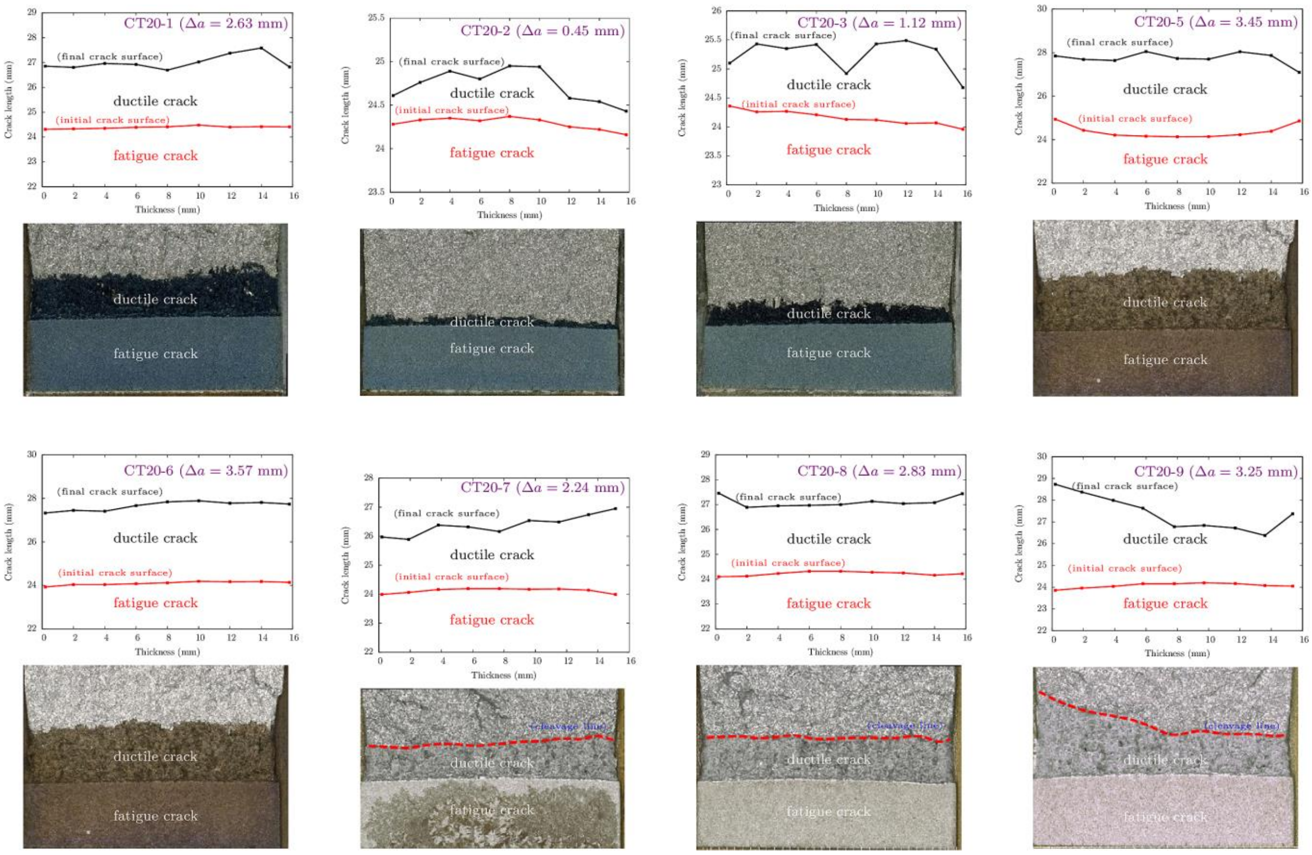

Figure 5.10. Fracture surface on ARMINES and EDF CT20 specimens

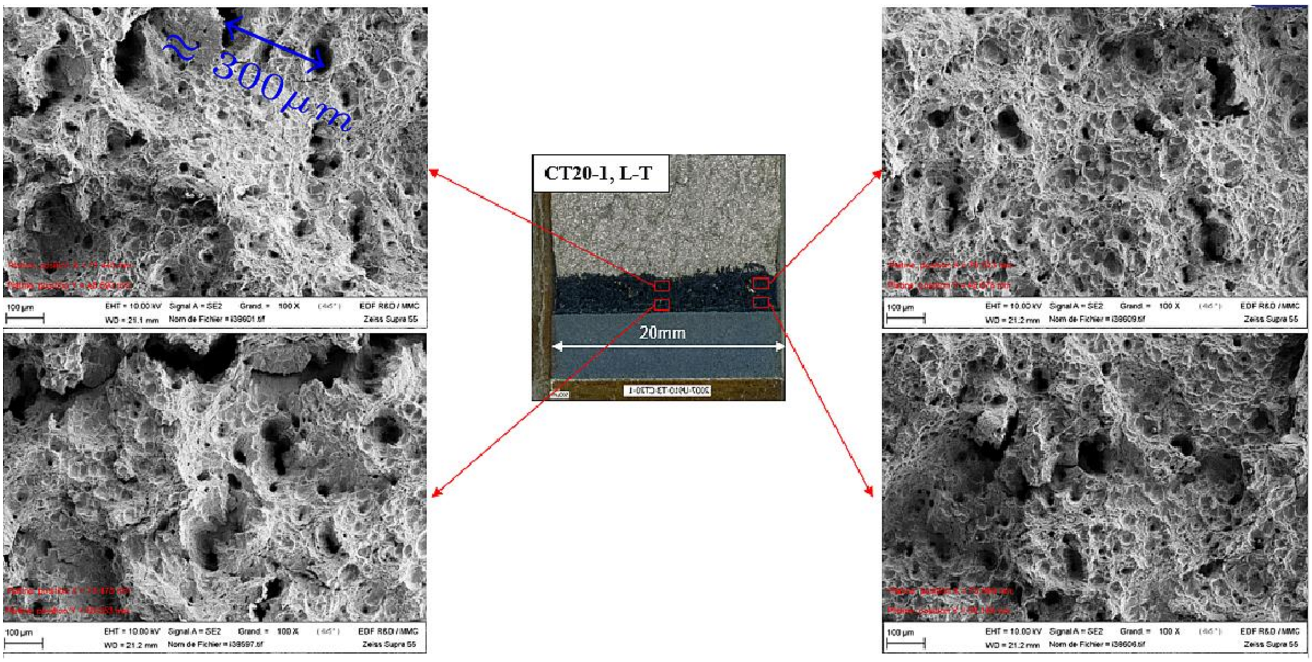

Figure 5.11. Fracture surface at the center and on the two sides of CT20-1 specimen

5.2.5 Single edge notch tension specimens

The second ductile tearing tests were conducted on single edge notch tension specimens (SENT) with the same $a_0/W \approx 0.5$ ($a_0 \approx 7.5$ mm and $W = 15$ mm) and the same orientation (LS) at room temperature (around 20°C). All specimens are side-grooved. The tests were conducted in the laboratory of ARMINES and EDF. The geometry of SENT is shown in Figure 5.12.

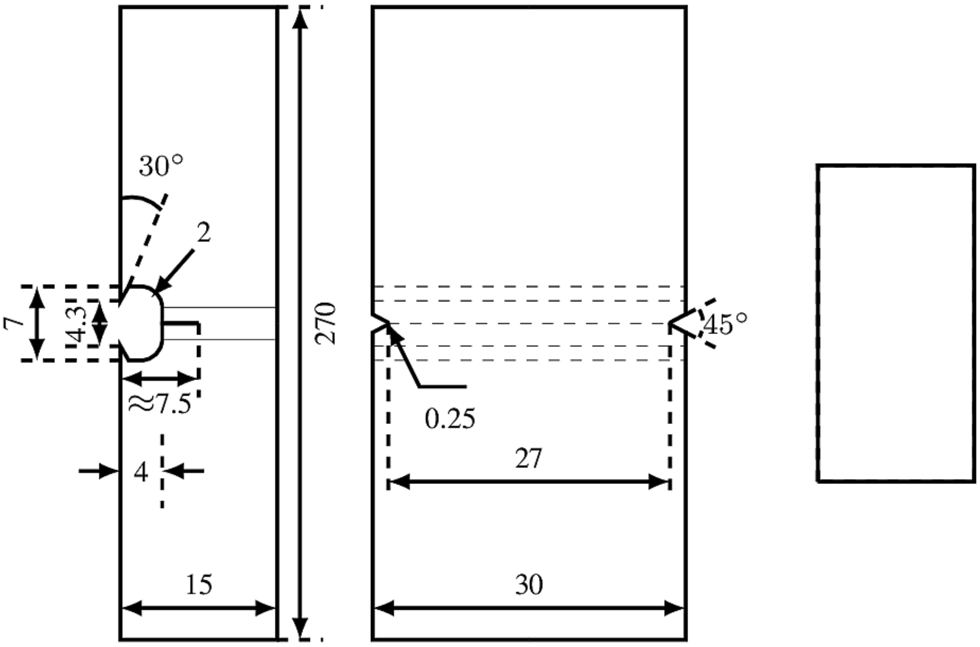

Figure 5.12. Geometry of SENT (from left to right: front view, right view, top view)

Figure 5.13 plots the force-CMOD curves for all SENT specimens. A good agreement among different results is observed.

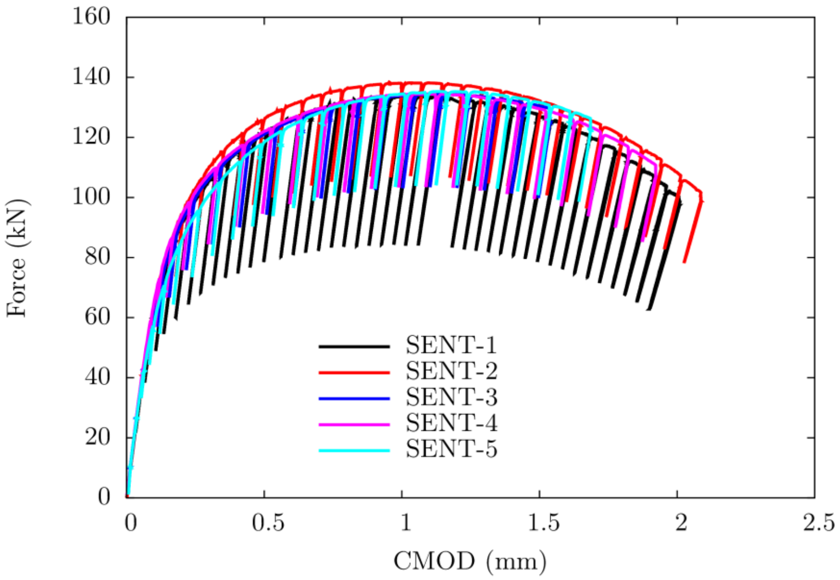

Figure 5.13. Force-CMOD for SENT

Scanning electron microscope (SEM) fractographs of fracture surfaces at the center and near the side-groove of SENT-5 sample at magnification 100X are shown in Figure 5.14. Fracture mode is ductile since as lots of (large and small) dimples are visible. There are lots of inclusions on the fracture surface and these inclusions are perpendicular to the crack propagation direction which is linked to the orientation of the specimens. We estimate that the void distance is about 300 μm (as shown in this figure). No obvious difference is observed between the center area and the side-groove area.

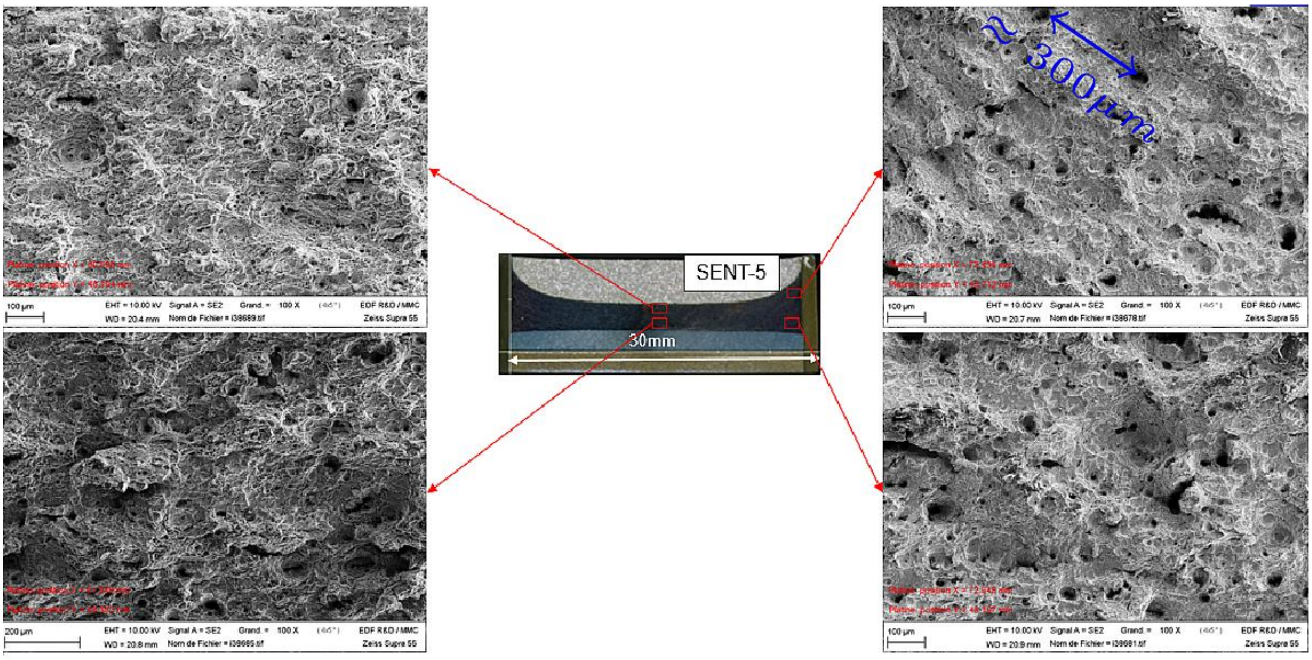

Figure 5.14. Crack surface at the center and near side-groove area of SENT-5 at magnification 100X

Figure 5.15 shows ductile crack growth along the thickness for 4 SENT specimens. It is observed that the maximum ductile crack extension occurs near the side-groove area.

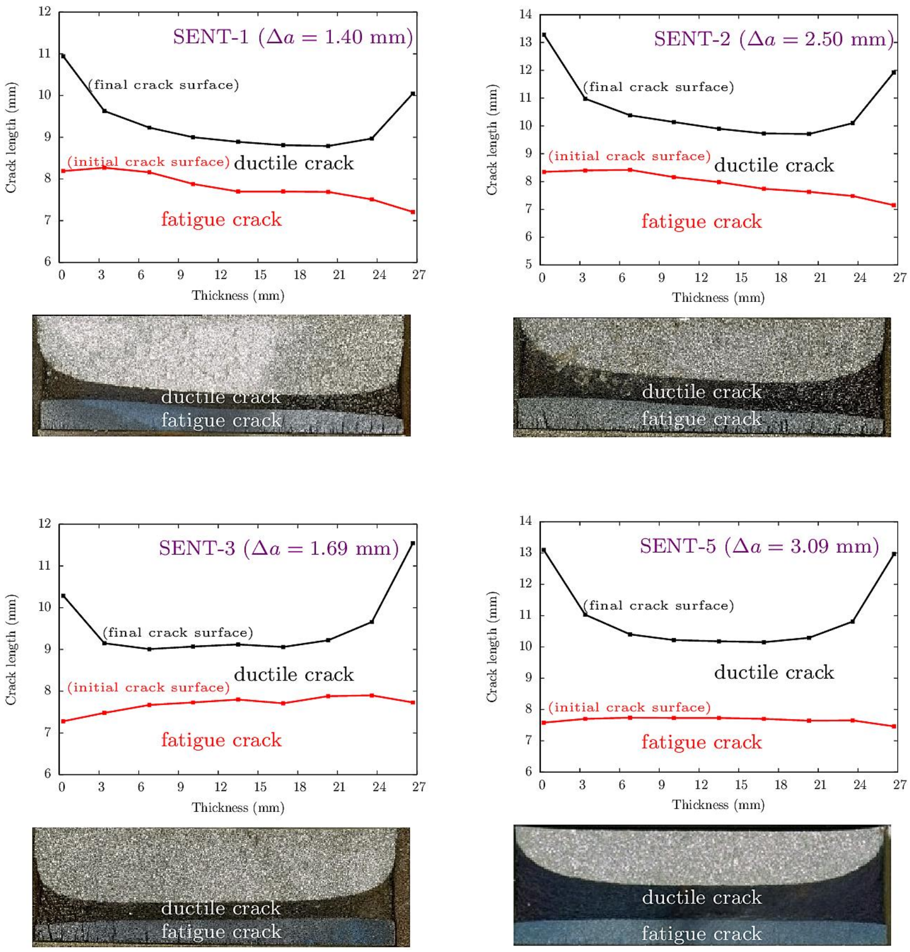

Figure 5.15. Ductile crack growth along the thickness on SENT specimens

5.2.6 Large-scale FP1 pipe

Three pipes (FP1, FP2 and FP3) with the same geometry and loading but with different initial defects were manufactured. The geometry of the pipe FP1 is shown in Figure 5.16. The central section of the pipe FP1 are made of the WB36 material, while the two extensions are made of the E355 steel. The initial through-wall crack created by fatigue is located on the xy cross-section plane (or $z = 0$ plane in cylindrical coordinate system), as shown in the Figure 5.16. Figure 5.17 shows the FP1 pipe before the bending test. The initial through-wall crack is clearly visible in this figure.

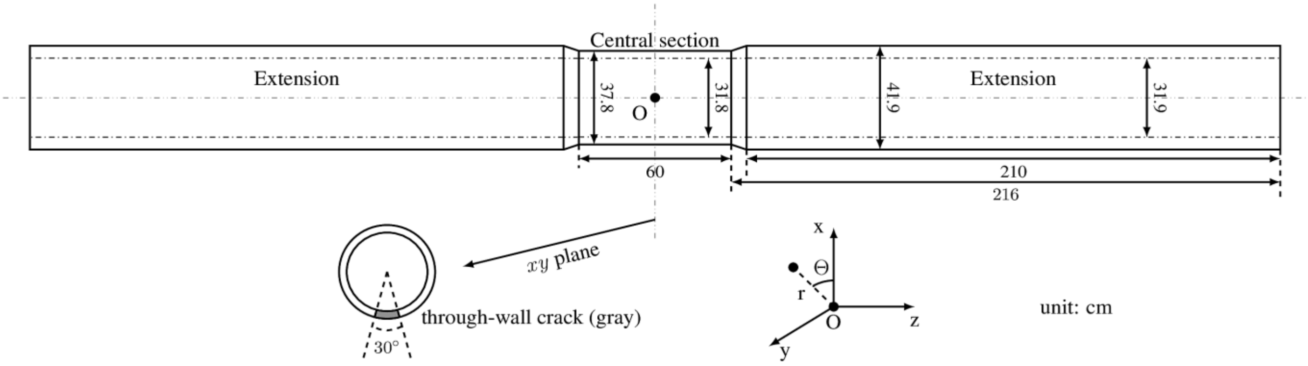

Figure 5.16. Geometry of the pipe FP1 (unit: cm)

Figure 5.17. View of the FP1 pipe

The test on the FP1 setup has been successfully finished in May, 2019 at EDF. Figure 5.18(a) shows the pipe during the test and Figure 5.18(b) shows the corresponding experimental results (force – COD). As shown in this figure, a large ductile crack growth (around 2 cm COD) is realized. Globally, crack bifurcation of about 45° is observed, as shown in Figure 5.19(a). In Figure 5.19(a), we also observe that crack bifurcation occurs along two directions at crack initiation and then only one of them continues to propagate. After the test, post-fatigue was made to propagate the crack so as to facilitate the cutting of the fracture surface. The cut surface is shown in Figure 5.19(b). The different "beach marks" (yellow arrows) can be clearly seen in this figure. The different beach marks correspond to the complete unloading performed during the test. Figure 5.20 shows the beginning of crack propagation. One can observe that there is a flat zone in the center (a triangle shape with a maximal crack propagation of 12 mm (Figure 5.20(a)) or 8 mm (Figure 5.20(b))) oriented in the initial (pre-) crack plan and shear lips on both sides. In particular, the first beach mark ($\mathrm{COD} \approx 6$ mm) is located in this zone. The intersection between the red line and the blue dashed line indicates that the maximum crack propagation is around 4 mm (for Figure 5.20(b)) – 6 mm (for Figure 5.20(a)) in the initial (pre-) crack plane for $\mathrm{COD} = 6$ mm. This is a typical value that can be used to validate the simulated results.

After crack initiation and some crack propagation, the crack goes out of the initial plane, as shown in Figure 5.19. The internal crack length is around 62 mm and the external crack length is around 70 mm.

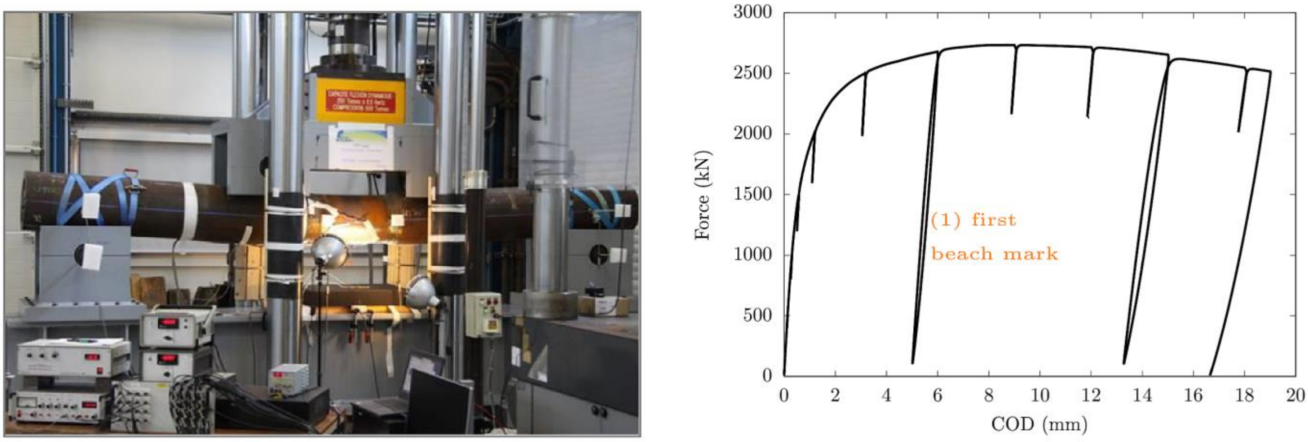

(a)

(b)

Figure 5.18. (a) View of the pipe FP1 during the test (b) Force-CMOD curves

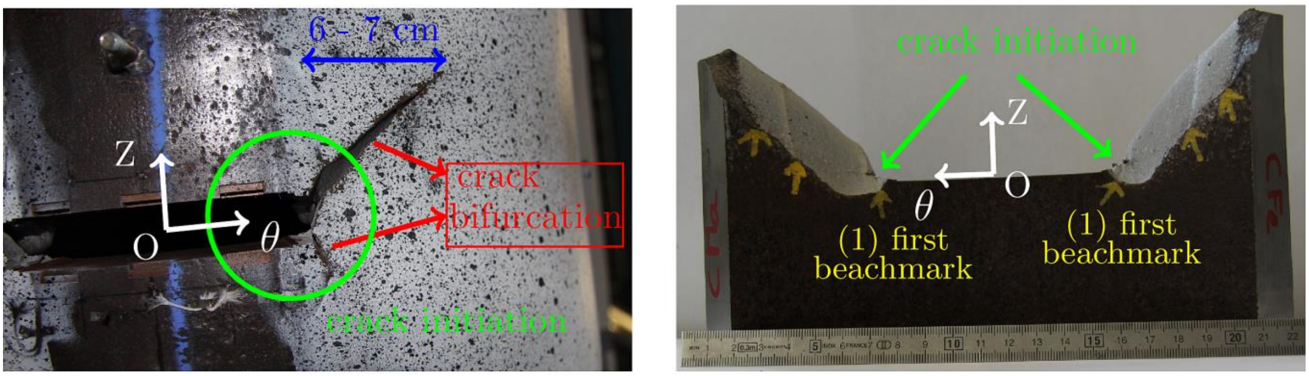

(a) external surface $r = R_{ext}$ (b) internal surface $r = R_{int}$

Figure 5.19. (a) Crack bifurcation; (b) FP1 cut

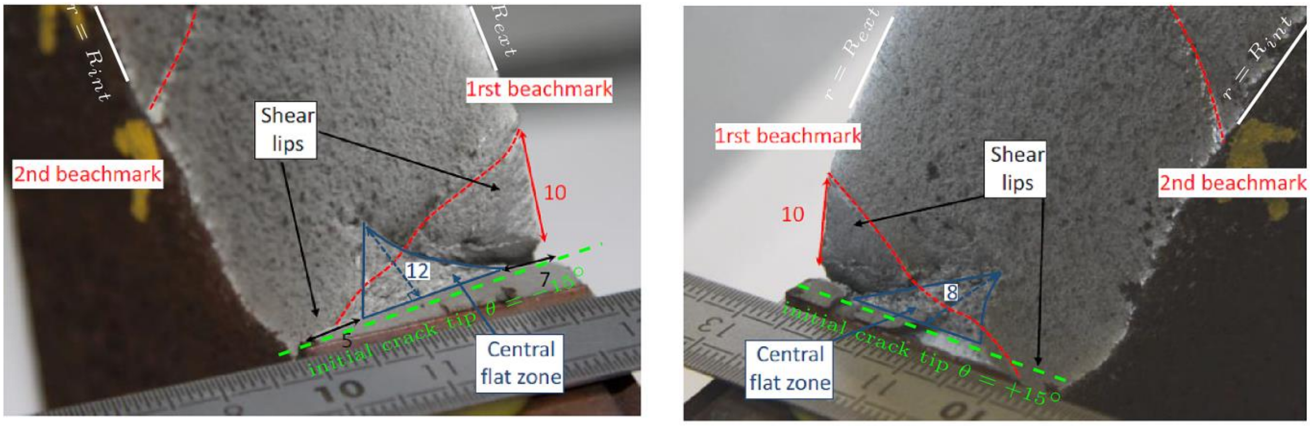

(a) $\theta \leq -15°$ (b) $\theta \geq 15°$

Figure 5.20. Crack initiation and beginning of crack propagation

5.3 Calibration of model parameters

5.3.1 Simulation techniques

In this part, we summarize the simulation techniques that have been already mentioned in the previous chapters and that will be used in the following.

The non-local GTN model was implemented in Code_Aster (software for finite element analyses), developed at EDF (Electricité De France). An implicit time-discretization with respect to $(\boldsymbol{E^p}, \kappa)$ and a staggered update with respect to the porosity f are used to integrate the constitutive equations. A material point is considered as broken when f reaches f_F. In that case, the material behavior is only governed by the viscous-elastic part of the overlay model which consists of an assembly of an elastic spring of stiffness E_v and a viscous dashpot of viscosity η, as introduced in Chapter 3. This viscous model is proposed to deal with the distorted broken elements.

The notched tensile specimens are meshed using axisymmetric elements while other specimens (the compact tension specimen CT20, the single edge notch tension specimen SENT and the large-scale structure – FP1 pipe) are meshed using 3D elements. In all cases, mixed finite elements with 2×2 (quadrilateral elements) or $2 \times 2 \times 2$ (hexahedron elements) integration points by element are used. The mesh size is close to 0.1 mm in areas where cracks propagate.

Meshes of NT, CT20, SENT are shown in Figure 5.21. Usual symmetry conditions are accounted for in order to reduce the size of the simulations. The 5-field finite element is used for the simulation.

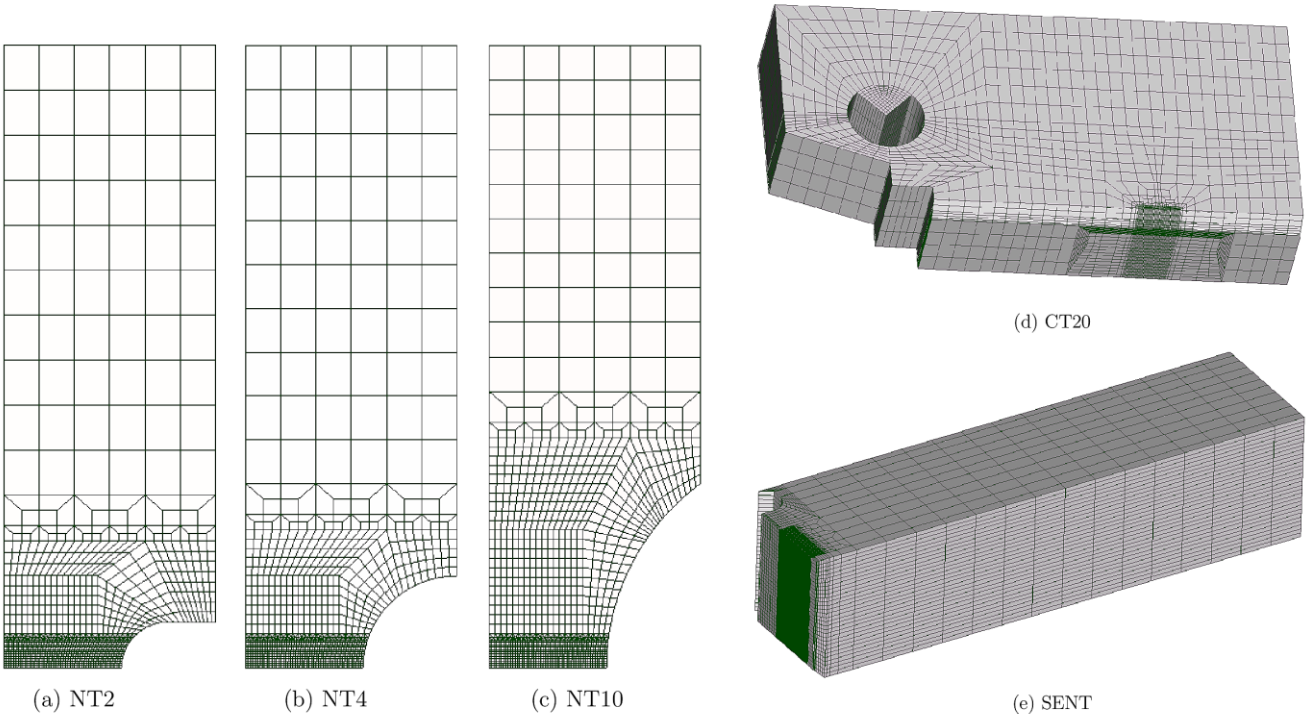
(a) NT2 (b) NT4 (c) NT10 (d) CT20 (e) SENT

Figure 5.21. Meshes for NT, CT20 and SENT

Mesh of pipe is shown in Figure 5.22. Only one quart of the pipe is modeled since crack bifurcation along two directions are observed at crack initiation stage. Usual boundary and loading conditions for 4-point bending tests are accounted for. The central part is modeled by the GTN model while the extension part is assumed to be elastic. The support is modeled by a segment and thus the prescribed displacement loading condition is applied to this segment. But one should notice that the boundary conditions prescribed on a segment is mathematically not correct since it may induce an ill-posed variational problem, one can refer to (Lorentz, 2005) for the detailed explanation. Numerically, this kind of modeling can induce indentation effects which strongly affect computational convergence. In our case, the support is located in the extension parts which are assumed to be elastic, the convergence is thus expected to be unaffected by the modeling of the supports. In practice, loading is achieved though contact between the supports and the pipe. This is neglected in the current simulation.

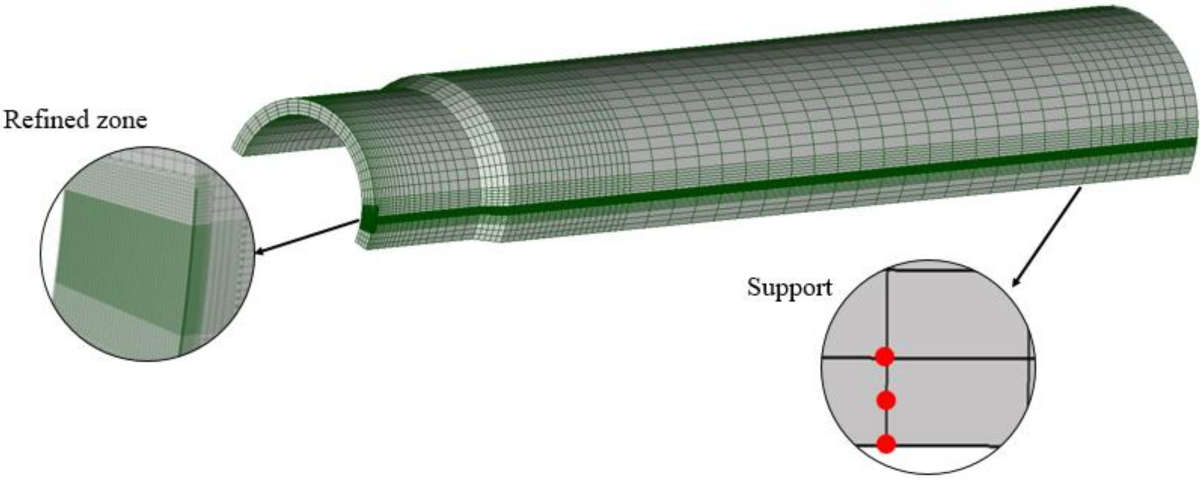

Figure 5.22. Mesh of the FP1 pipe

The goal of our work is to check whether the current model (1) is sufficiently robust so as to be able to simulate crack propagation in small-specimens and in a large industrial structure (over a distance of about 1 cm) (2) is able to predict the mixed mode propagation at crack initiation and the beginning of crack propagation stage. In fact, there is a flat zone in the center (a triangle shape with 12 mm maximal crack propagation) oriented in the initial (pre-) crack plan and shear lips on both sides.

The numbers of degrees of freedoms (DOFs) for each 3D computation are: CT (~400,000 DOFs), SENT (~1,190,000 DOFs), Pipe (~1,810,000 DOFs).

5.3.2 Identification procedure

This section aims at fitting the parameters of the nonlocal GTN model based on some of the experimental results presented in the Section 5.2. In particular, void nucleation is not taken into account in this work. Young modulus is measured by experiment: $E \approx 205000$ MPa. Poisson ratio is set to 0.3 (globally acceptable value for steel). Consequently, the parameters to be calibrated are:

- **Parameters describing plasticity**: the hardening function is assumed to be:

$$\bar{\sigma}(\kappa) = r_0 + r_1(1 - \exp(-g_1\kappa)) + r_2(1 - \exp(-g_2\kappa)) \tag{5.1}$$

  where $(r_0, r_1, g_1, r_2, g_2)$ are five hardening parameters. Note that the nonlinear terms are used to obtain a good fit over the whole plastic strain range. If $g_1 \gg g_2$, then the term $r_1(1 - \exp(-g_1\kappa))$ quickly reaches a plateau and it would be used to fit the early stages of work hardening, while the second term $r_2(1 - \exp(-g_2\kappa))$ is used to fit hardening for high value of plastic strain.
- **Parameters describing damage**: Initial porosity f_0; void growth parameters (q_1, q_2); critical porosity f_c ; porosity at fracture f_F

- **Parameters describing non-locality:** Nonlocal length scale l_{nl}. We recall that the definition of l_{nl} leads to the nonlocal parameter c ($c = \sigma_0 l_{nl}^2$). The yield stress σ_0 is about 500 MPa, according to the tensile curves of the WB36 material (see Figure 5.4).

The following fitting procedure is used in this work:

- Plasticity parameters are fitted using tensile tests on NT2 specimens. An inverse method is applied to match the simulated force-diameter reduction curves with the experiments. Note that this method can be used only when the porosity f is small, in that case, the coupling between plasticity and damage is not significant.
- Initial porosity f_0 can be evaluated using the Franklin formula. In this formula, the chemical contents of the elements Manganese (Mn) and Sulphur (S) are involved:

$$f_0 = 0.54\left(C_S - \frac{0.001}{C_{Mn}}\right) \tag{5.2}$$

  One can refer to Table 5.2 for the value of C_S and C_{Mn}.
- Nonlocal length scale l_{nl} is set to $300\ \mu m$, which is approximatively equal to the void distance shown in Figure 5.11 and Figure 5.14. This l_{nl} leads to a nonlocal parameter $c \approx 50\ N$. In particular, it was checked that for $l_{nl} \approx$ 0.3 mm, the mesh size l_e (0.1 mm) is sufficiently small such that the simulation results are mesh-independent. This is in agreement with the results obtained in Chapter 4 and Appendix A5: it is necessary to have $l_e \leq l_{nl}/3$ to have a spatially converged solution.
- Void growth parameter q_1 is set to 1.5, the critical porosity f_c is set to 0.05 and the porosity at fracture f_F is set to 0.25. This is in consistent with the results of unit cell computations obtained in (Koplik and Needleman, 1988; Shinohara et al., 2016).
- Void growth parameter q_2 determines the fracture point in the force-diameter reduction curve of NT2 tests.
- Numerical parameters $r_{nl}, r_{inco}, E_v, t_v$ are given according to the recommendations in Chapter 3.

The obtained parameters are gathered in Table 5.3.

Table 5.3. Calibrated model parameters

Elasticity	Young modulus E	205000 MPa
	Poisson ratio ν	0.3
Plasticity	Hardening law $\bar{\sigma}(\kappa)$	$300 + 207(1 - \exp(-2465\kappa)) + 311(1 - \exp(-9.1\kappa))$
Damage	Initial porosity f_0	0.001
	Critical porosity f_c	0.05
	Porosity at failure f_F	0.25
	Material constants (q_1, q_2)	(1.5,1.14)
Nonlocality	Nonlocal length l_{nl}	0.3 mm
Numerical parameters	Penalty parameter r_{nl}	5000 MPa
	Penalty parameter r_{inco}	5000 MPa
	Viscoelastic modulus E_v/E	0.001
	Viscoelastic time τ_v/T	0.01

In conclusion, only the NT2 specimens are used to calibrate model parameters. The fitting results are given in the Figure 5.23. A very good fit on the plasticity and the fracture point is obtained for NT2.

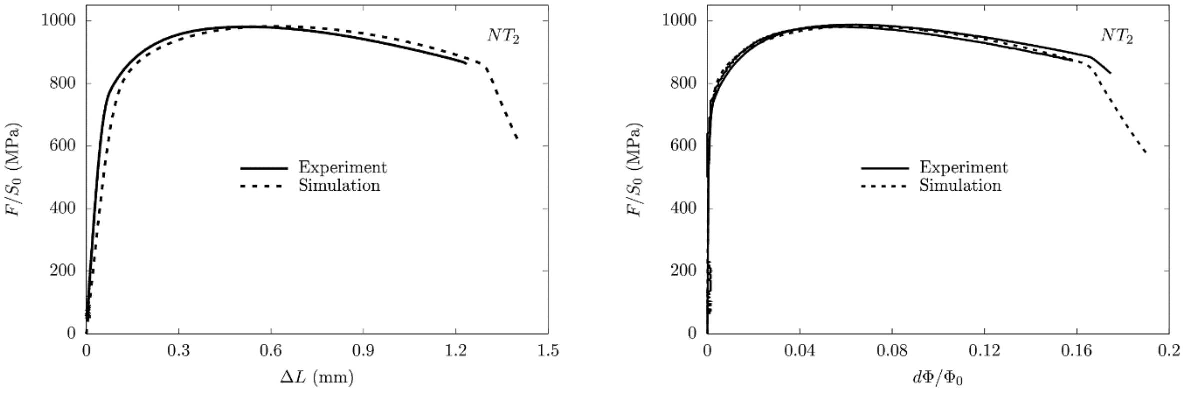

(a) (b)

Figure 5.23. Comparison of experimental and fitted result for NT2 specimen

Figure 5.24 shows the distribution of the hardening variable and the porosity for different loading steps for the NT2 specimen. It is observed that the maximum value of the hardening variable is located at the notched root, while the crack initiates from the center. This is in agreement with experimental observations. Besides, a clear “nonlocal zone” can be seen in the porosity field. Strain/damage localization is well controlled. Similar tendency can be observed for NT4 and NT10 except that the plasticity level increases with the notch radius.

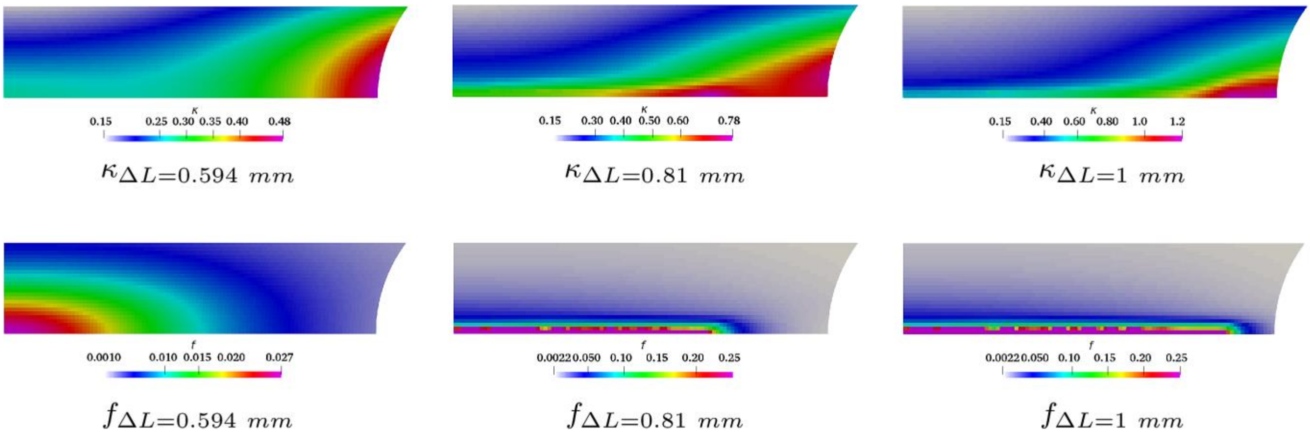

Figure 5.24. Distribution of the hardening variable κ and the porosity f for NT2 (undeformed configuration)

To further investigate this nonlocal zone, Figure 5.25 plots the profiles of κ and f in the ligament at different load levels for NT2. The x-axis stands for the distance to the center point in the initial configuration. According to Figure 5.25(a), the hardening variable increases with x when no point is broken. After crack initiation, the hardening parameter firstly decreases and then increases with x in front of the crack tip. According to Figure 5.25(b), unlike crack propagation in small-scale yielding where the profile of the porosity shifts along the ligament, here the profile of porosity slightly changes during crack propagation. The main difference between crack propagation in NT and small-scale yielding is that the ligament length in NT becomes comparable with the crack length, thus, the boundary (geometry constraint) has a significant effect on crack propagation in NT which never reaches a steady-state.

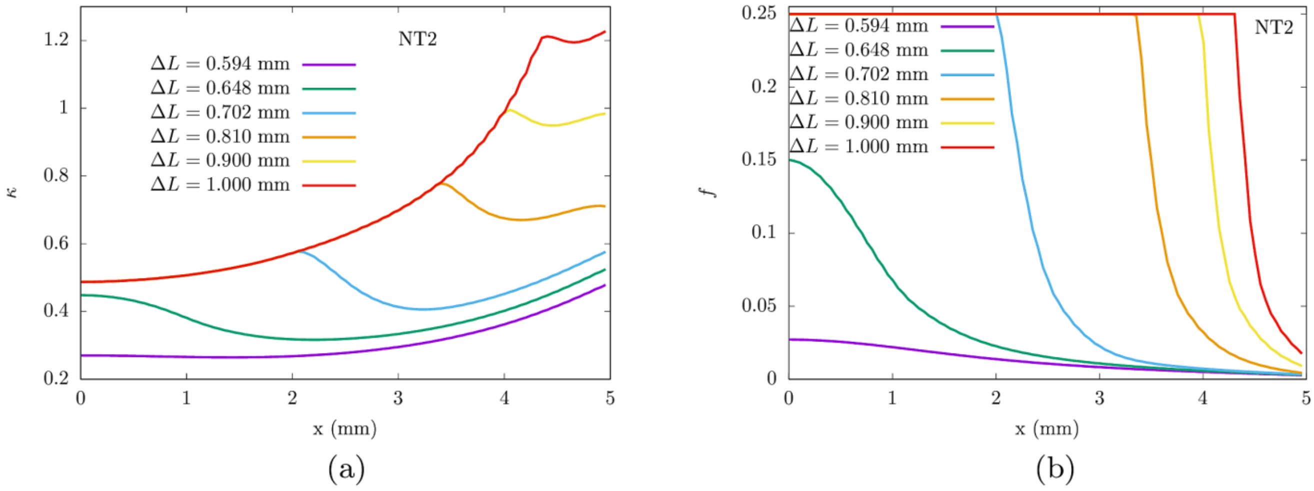

Figure 5.25. Profiles of (a) the hardening parameter and (b) the porosity in the ligament for NT2

5.4 Model validation on small specimens

As said in the previous part, the experimental results on NT2 were used to fit the plasticity parameters and the damage parameter q_2. These parameters were then used to predict plasticity and the fracture points for NT4 and NT10, as well as the global behavior of CT20 and SENT.

5.4.1 Prediction for notch tensile specimens

Figure 5.26 compares the experimental and simulated force-displacement and force-diameter reduction curves for NT4 and NT10 specimens. As can be seen in this figure, a very good fit on the plasticity is obtained. As for the fracture points, the parameters predict a slightly later crack initiation than that in experiments.

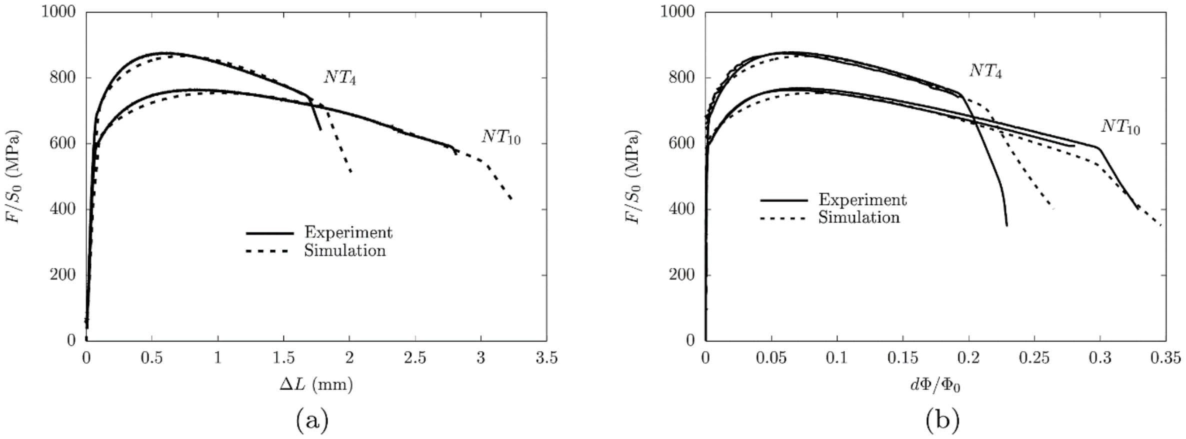

Figure 5.26. Comparison of experimental and simulated force-displacement and force-diameter reduction curves for NT4 and NT10

5.4.2 Prediction for compact tension specimens

The length of the initial crack a_0 obtained by fatigue was set to 24.3 mm (corresponding to CT20-5 in Figure 5.10) in the simulation of CT20. The comparison between the experimental and the simulated force-CMOD (crack mouth opening displacement) is shown in Figure 5.27. The simulated result agrees very well with the experiment result.

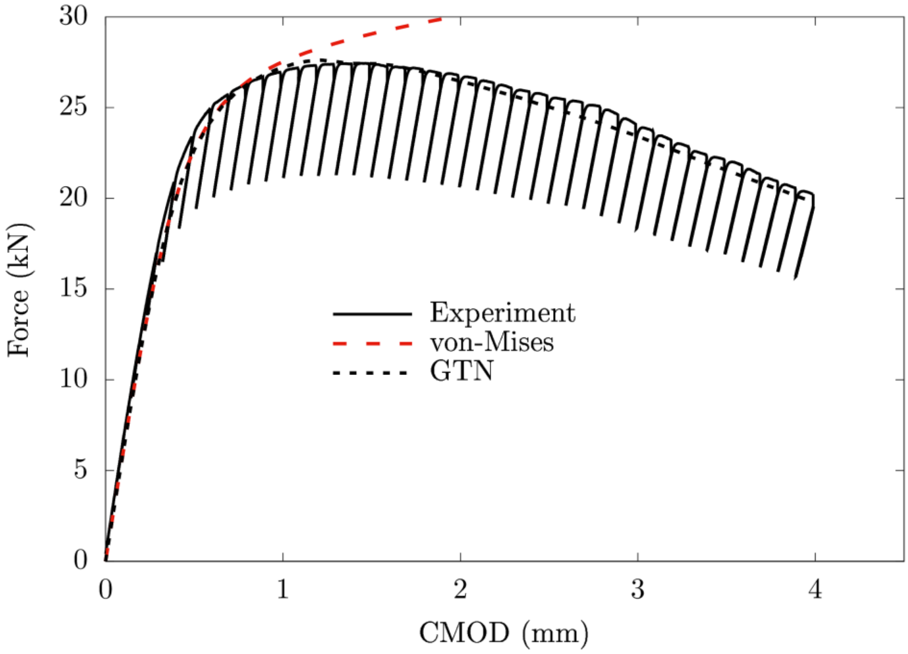

Figure 5.27. Comparison of the experimental and simulated force-CMOD curves for compact tension specimens test (F: Force, Δa: crack length)

In experiments, the crack was determined using the unloading compliance technique. In simulations, the crack is defined as the zone where $f = f_F$ (fully broken material). Figure 5.28(a) plots the crack surface at different load levels. It can be seen that crack growth is more important in the center than that in the lateral side-groove area. This observation is different from the experimental observation in which the fracture surface has a rather straight front. The difference may be linked to the fact that void nucleation is not taken into account in the simulations. The ASTM-1820 9-point method to define crack propagation is then used to post-process the simulations to compute a mean simulated crack propagation. Note that the crack length is computed in deformed configuration. Figure 5.28(b) compares the experimental and simulated CMOD-Δa curves. A good agreement is obtained.

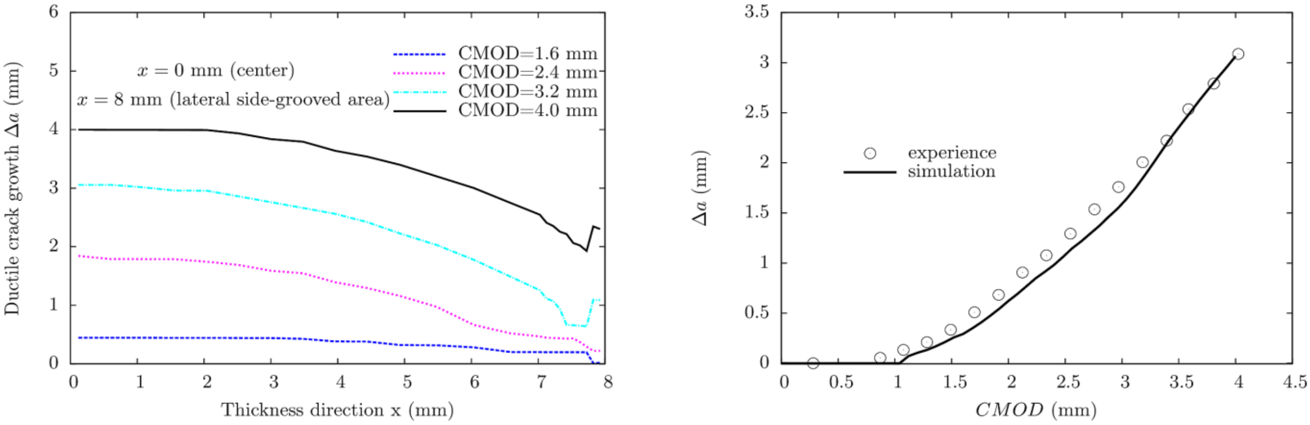

Figure 5.28. Comparison of crack propagation between the simulation and the experiment for CT20 (CMOD: crack mouth opening displacement, Δa: crack length)

5.4.3 Prediction for single edge notched tension specimens

To further verify the model parameters fitted through the experimental results of NT2, the SENT specimen with a different crack tip constraint compared to CT20 was analyzed. However, as shown in Figure 5.29 the calibrated parameters overestimate the force, even in the plasticity-dominated phase. Then crack initiates much later than that observed in experiments. The discrepancy on plasticity between simulation and experiment can be explained by the inhomogeneity of material. The calibrated parameters should be further optimized to well predict the damage bahavior in SENT. For example, it may be better to fit at the same time (q_1, q_2) instead of only fitting q_2. It is also possible to slightly modify the value of l_{nl}, etc.

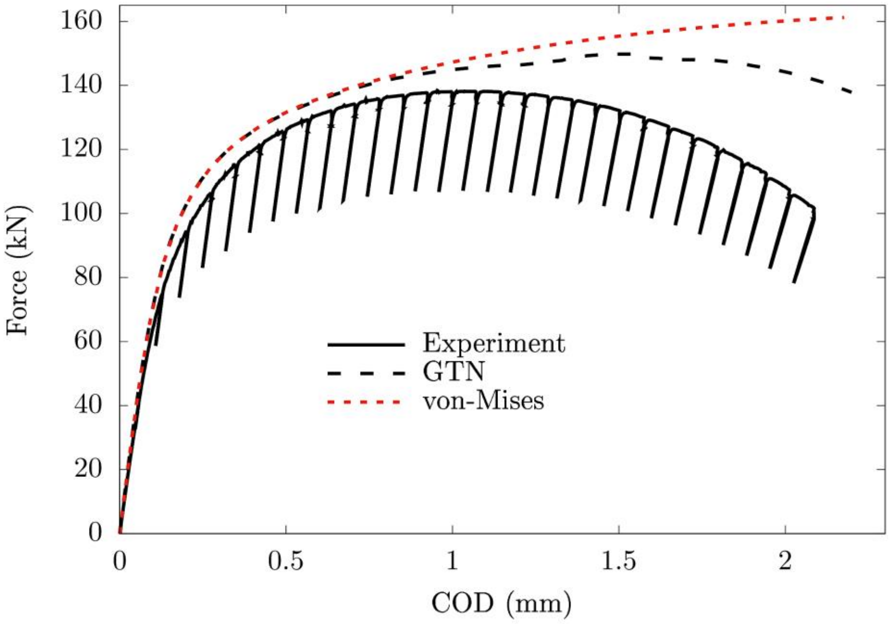

Figure 5.29. Force-COD curves for SENT

5.5 Model validation on a large-scale structure (FP1 pipe)

Even if the fitted parameters are not well predictive for SENT, we still used them to predict the behavior of the FP1 pipe. By doing so, firstly, we would like to check if the prediction on the FP1 pipe is similar to that on SENT knowing that the triaxaility state in pipe is close to that in SENT and thus we may propose some possible ways to improve the calibration procedure. Secondly, we want to see whether the nonlocal GTN model can be used in one industrial case knowing that nonlocal models were rarely used in industrial 3D cases in the literature. Thirdly, it is expected to obtain the mixed mode crack propagation at crack initiation and the beginning of crack propagation stage.

Figure 5.30 plots the experimental and simulated (with GTN and von-Mises) force-COD curves for the FP1 pipe. Firstly, we compare the simulated curves with the GTN and von-Mises models. Their diffence is not significant since crack only propages over a short distance. Then we compare the simulated GTN curve to the experimental curve. It can be seen that the simulated result agrees well with the experimental results up to a COD ≈ 8 mm: the predicted force is just slightly higher than that measured in experiment, this difference can be linked to the modeling strategy (the extension arms are assumed to be elastic) or the inhomogeneity of the material. Simulation was not performed for $\mathrm{COD} > 10$ mm since the crack already “escapes” the mesh refined zone, as will be shown later. Besides, simulation predicts a crack initiation when $\mathrm{COD} \approx 2.2$ mm, as shown in this figure, which is in agreement with the experimental measure ($\mathrm{COD_{exp}} \approx 2.3$ mm).

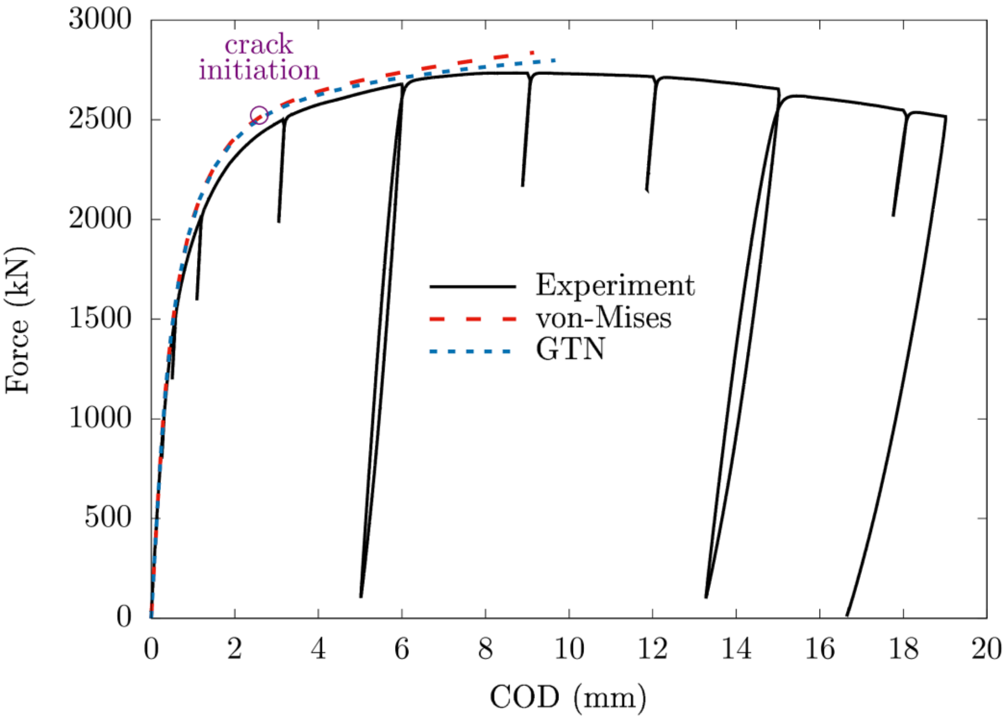

Figure 5.30. Force-COD curves for the FP1 pipe (COD: crack opening displacement)

Now we focus on the predicted crack path. According to the simulation results, the crack is not completely located on the symmetry plane ($z = 0$ plane in cylindrical coordinate system or initial pre-cracked plane). For this, we examine the evolutions of different parameter fields on the quasi-symmetry plane. We will explain latter why we use “quasi-symmetry plane” instead of “symmetry plane”. Figure 5.31 shows the distribution of porosity, hardening variable κ, crack opening stress and triaxiality (defined by T_h/T_*) on the quasi-symmetry plane when COD ≈ 6 mm. This COD corresponds to the first beach mark in the experiment. Several information can be obtained:

- Figure 5.31(a) shows that crack growth is much more significant in the center than on both sides along the circumferential direction. In particular, in the center along the circumferential direction, there are around 120 broken finite elements, that corresponds to a crack length of about 5.5 mm in the deformed configuration. This result agrees well with the experimental observation where a crack propagation around 4-6 mm (in deformed configuration) in the center along the circumferential direction was observed. A nonlocal zone is obviously seen in front of the current crack tip.
- Figure 5.31(b) shows that the hardening variable is around 0.45 in front of the current crack tip. In addition, in the initial crack tip nearby zone, plasticity is more important compared to that in other areas which causes a high gradient of plastic strains.
- Figure 5.31(c) shows that in front of the current crack tip and along the circumferential direction, the crack-opening stress σ_{zz} first increases then decreases. Besides, as mentioned in Appendix A5.6, the spurious and extremely high crack opening stresses are observed in the vicinity of the initial crack tip which is linked to the very high gradient of plastic deformation, this gradient leads to additional hardening in the yield function ($c\Delta\kappa$).
- Figure 5.31(d) shows that in front of the current crack tip, the triaxiality on both sides is much lower than that in the center (about 1.8). This explains why damage growth is more significant in the center than on both sides.
- A very special zone (in blue) is observed in Figure 5.31(a). In this zone, the triaxiality is negative and the crack opening stress is not zero. It implies that in this zone, the crack is already out of plane. To further confirm this conclusion, we plot the projection of the porosity field on the quasi-symmetry plane in Figure 5.32. From this figure, it is clear that near this special zone, crack already deviates from the symmetry plane.

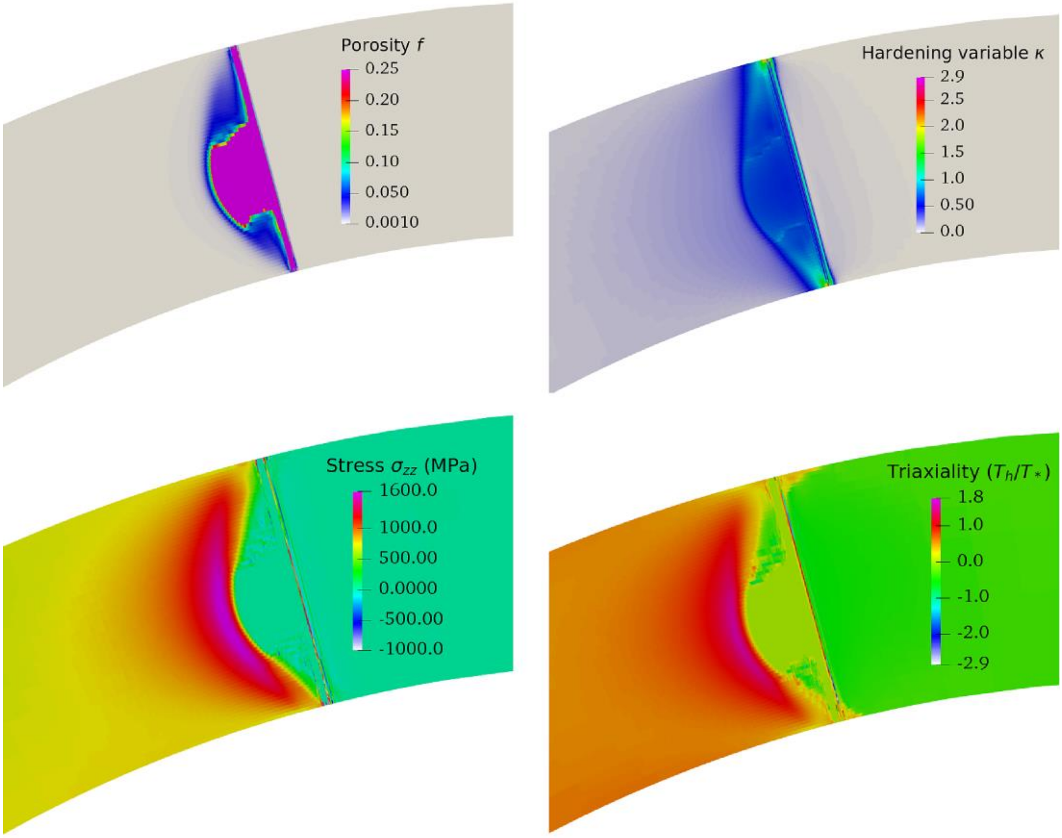

Figure 5.31. Distribution of the porosity, the hardening variable, the stress σ_{zz} and the generalized triaxiality on the symmetry plane when COD=6 mm

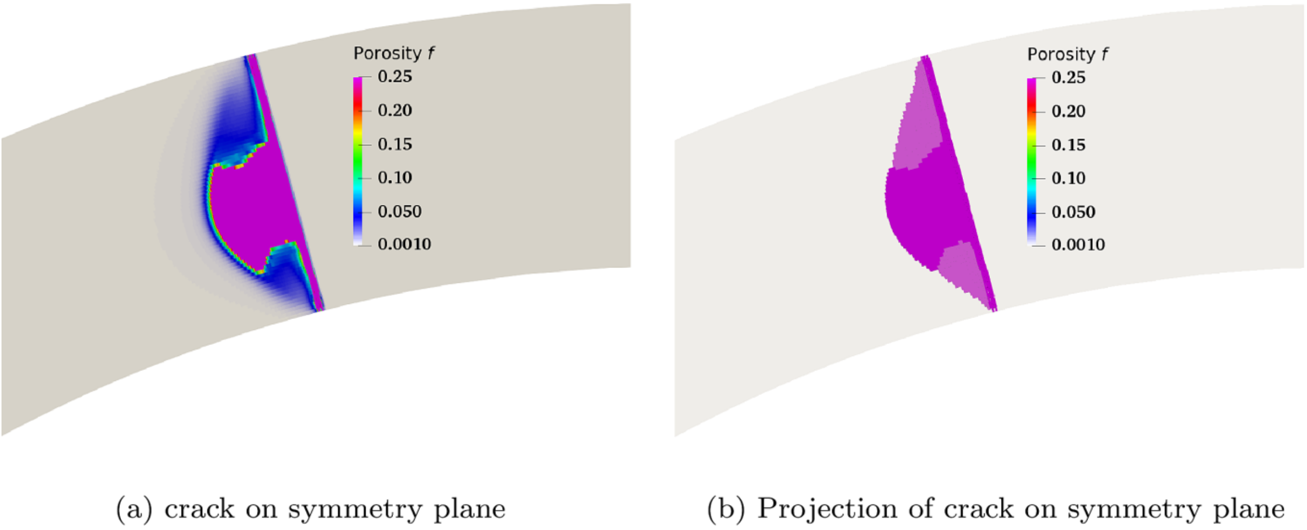

(a) crack on symmetry plane (b) Projection of crack on symmetry plane

Figure 5.32. (a) Distribution of porosity on crack plane; (b) Projection of porosity on symmetry plan

Figure 5.33 shows the fields of the porosity in θz plane for $r = 160, 164, 169, 174, 179, 184, 188$ mm (see Figure 5.16 for the convention of the cylindrical coordinate system). Each quadrangle corresponds to an integration point. We also recall that $R_{int} = 159$ mm and $R_{ext} = 189$ mm.

From this figure, it can be seen that:

- The crack tends to leave from the symmetry plane when $r \rightarrow R_{int} = 159$ mm or $r \rightarrow R_{ext} = 189$ mm while for $r \rightarrow (R_{int} + R_{ext})/2 = 174$ mm (i.e., center of the thickness), the crack initiates at the initial crack tip and then propagate along the circumferential direction while remaining in the symmetry plane.
- For $r = 174$ mm, due to an unknown reason (probably due to the fact that the value of r_{nl} is not large enough), a slight oscillation of damage is observed such that the first layer of the integration points are not broken. The results presented above (i.e., Figure 5.31) are extracted from the second layer of integration points. That explains why we earlier said “quasi-symmetry plane” instead of “symmetry plane”.
- The localization band is clearly illustrated in Figure 5.33, we also observe here that the gradient of the porosity exists in the crack propagation direction and in the band thickness direction. It is thus suggested to use the same mesh size in both directions.
- When $r \rightarrow R_{int}$ or $r \rightarrow R_{ext}$, crack deviation is observed. This figure is plotted in initial configuration (crack propagation in deformed configuration is still too short), so it is difficult to figure out the deviation angle. However, the “a-priori” refinement along the axial direction (i.e., z direction) is not far enough so that the crack propagates again in a plane parallel to the symmetry plane, as shown in the figure for $r = 184$ mm. We recall that according to the study of small-scale yielding in Chapter 4 and Appendix A5, it is necessary to have $l_e \leq l_{nl}/3$ with l_e the mesh size and l_{nl} the nonlocal length so as to have a spatial converged solution. This implies that a high number of elements is required to mesh the slanted crack path. Such a high number of elements, considering the highly non-linear behavior, is out of reach for the time being.

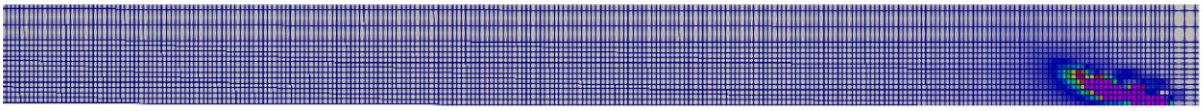

(a) $r = 160$ mm (near internal surface)

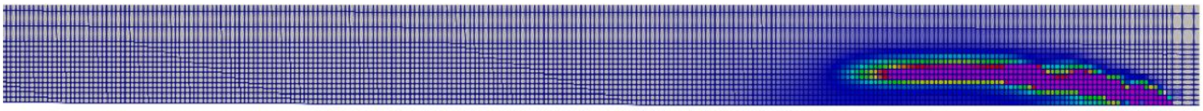

(b) $r = 164$ mm

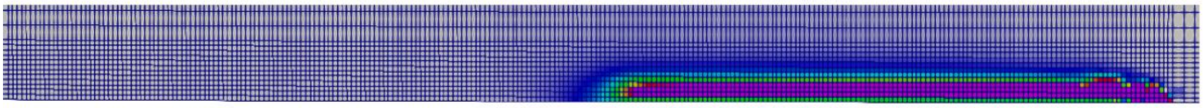

(c) $r = 169$ mm

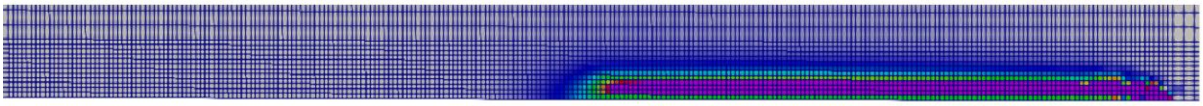

(d) $r = 174$ mm (half thickness cutting plane))

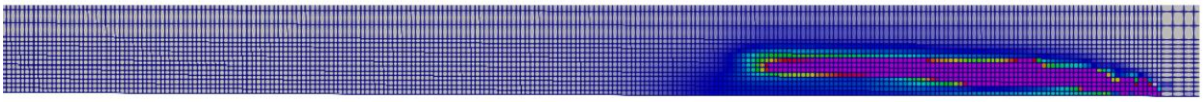

(e) $r = 179$ mm

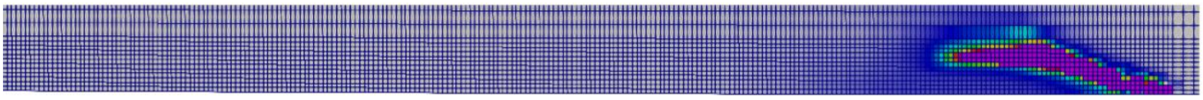

(f) $r = 184$ mm

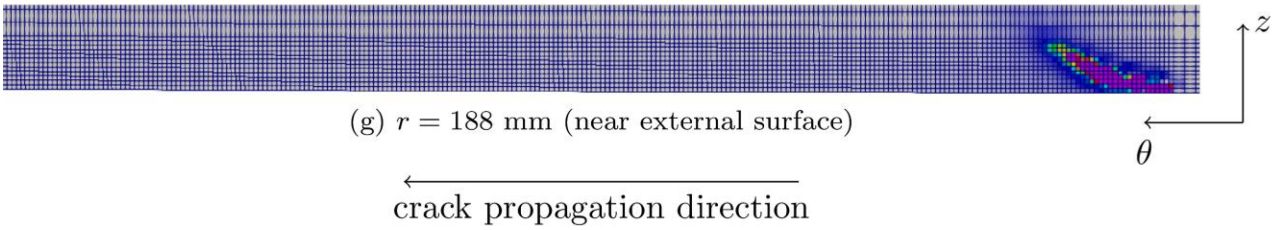

(g) $r = 188$ mm (near external surface)

Figure 5.33. The distribution of the porosity f along the circumferential direction for different radius r when COD=6 mm (integration points view)

In conclusion, we are able to capture the mixed mode crack propagation observed in experiment with the use of the nonlocal GTN model. Before closing this chapter, we would like to give the results obtained by the local GTN model. The simulation with the local GTN model was performed using the finite element software Z-set. Figure 5.34 shows the distribution of the porosity f and the crack opening stress σ_{zz} on the symmetry plane. For the field of crack opening stress, the distribution in front of crack tip are rather similar to that obtained with the nonlocal model. For the field of porosity, compared to Figure 5.31, one can see that here the crack remains on the symmetry plane without any deviation. Besides, the gradient of the porosity in front of the current crack tip is much sharper than that obtained with the nonlocal GTN model. This emphasizes the importance of nonlocal models.

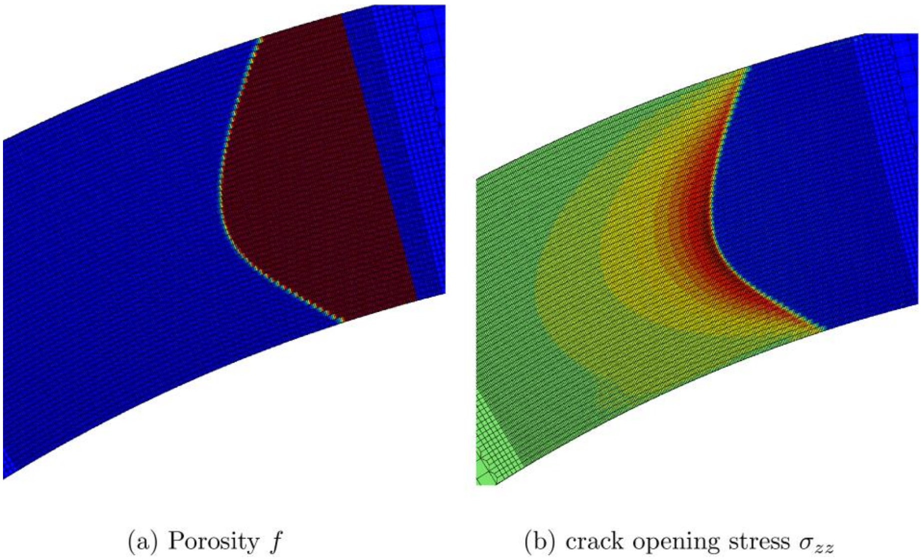

(a) Porosity f (b) crack opening stress σ_{zz}

Figure 5.34. Distribution of the porosity f and crack opening stress σ_{zz} *(results obtained with the local GTN model by Z-set)*

5.6 Summary

In this chapter, the nonlocal GTN model is applied to simulate several tests on small-scale specimens (notched tensile (NT), compact tension (CT) and single edge notched tension (SENT) pre-cracked specimens) and on large-scale industrial structure (pre-cracked pipe). These fracture tests were conducted within the framework of the UE project named ATLAS+. Some experimental results, including the chemical contents of the WB36 material, the global response (force-displacement, force-CMOD or force-diameter reduction) and fractographs, are shortly summarized in the first part. Then, the model parameters are calibrated according to the experimental results on NT2. They are used to predict the behavior of other small-scale specimens and the large-scale FP1 pipe. The results indicate that the GTN model can well predict the global behavior of NT and CT. However, these parameters cannot give a satisfactory result neither on the plasticity nor on the damage for SENT. In spite of that, simulation of the FP1 pipe was performed using these parameters. The results are in good agreement with the experimental results until a CMOD ≈ 8 mm. Besides, a mixed mode crack propagation is obtained thanks to the nonlocal effect, which agrees well with the experimental observation.

6 Conclusion and Future work

6.1 Summary

The major goal of this work was to propose and establish a robust, reliable and efficient modeling strategy for the prediction of crack propagation in three-dimensional industrial cases with a crack extension length equal to few centimeters.

The GTN damage model was chosen in this work for the modeling of ductile fracture. This model is a "local approach to fracture" type model. It is well known that this approach leads to a problematic localization of strain and damage. Indeed, damage at the continuum level results in strain-softening, which is the source of spatial localization of the strain, plastic strain and damage. However using "standard" constitutive equations, the width of the localization band remains undetermined whereas it should be related to some material characteristic length (i.e., distance between defects). Thus, nonlocal constitutive relations are required so as to be able to explicitly introduce a characteristic length in the model. These equations account for a spatial coupling of neighboring material points by introducing an interaction distance. Due to some mathematical, numerical reasons, the gradient enhanced energy (GEE) approach is used in this work. The hardening variable is regularized to simultaneously control plastic localization and damage localization.

Numerically, the use of local approach leads to a spurious mesh-sensitivity in finite element simulations. It is demonstrated in (Zhang, 2016) and in our work that the nonlocal modification of local approach can effectively reduce mesh-sensitivity.

Another numerical problem is volumetric locking which leads to strong oscillations of stress fields in finite element simulations. In this work, the mixed element formulation is used since the robustness of this method has already been demonstrated in the PhD work of (Zhang, 2016) in the case of ductile damage. As shown in (Zhang, 2016), the proposed finite element formulation can lead to very heterogeneous plastic strain fields. The method proposed in (Zhang, 2016) was thus improved in our work.

Besides, highly distorted elements are observed in the simulations of large crack extensions (Zhang, 2016). This may strongly affect the computational convergence. In this work, a viscous-elastic regularization is proposed to avoid excessively distorted elements. An additional stiffness and a characteristic time are introduced in the model. It is seen that the stiffness can preclude distortion, resulting in (small) viscous stresses which vanish with time.

In order to characterize the improved GTN model, to optimize parameters preventing stress and strain oscillations and thus to perform reliable simulations, systematic numerical analyses of the model were conducted. Theses analyses include:

- The study of the augmentation terms introduced in the nonlocal locking-free formulation: Two penalty parameters (r_{nl}, r_{inco}) are introduced. Some parametric studies allow giving an appropriate range for each penalty parameter. Finally, it is suggested that $r_{nl} \geq 10\sigma_0$ and $r_{inco} \sim 10\sigma_0$.
- The study of the viscous-elastic parameters: Two parameters (E_v, τ_v) are introduced. It is suggested to use: $E_v = 0.001E$ and $\tau_v = 0.01\Delta t$.
- The comparison between the staggered scheme and the implicit scheme for the update of the porosity (damage variable in GTN model): These two schemes lead to the same level of error on the prediction of local and global responses. In this work, the staggered scheme is adopted.
- The global and local sub-stepping methods: in order to control the error introduced by the large load-increment, the global/local sub-stepping methods based on $\Delta \ln f$ are proposed. The global method may be computationally expensive, especially when it comes to three-dimensional industrial simulations. The local method can effectively reduce the computational cost. But it requires to well evaluate the

tangent stiffness matrices for the points at which the local adaptation is activated so as to avoid the global non-convergence of Newton-Raphson algorithm due to a poor estimate of the global stiffness matrix.

In order to study the properties of the improved GTN model, large crack propagation under small-scale yielding and plane-strain mode I conditions were simulated. A linear relationship between the non-local intrinsic length and the width of the computed damage/strain localization band is established. Crack tip blunting, crack initiation and large crack propagation are well captured with the improved model. Wide ranges for the plasticity and damage parameters can be used in a reliable way so that toughness at crack initiation as well as ductile tearing behavior can be thoroughly studied. All these results highlight the robustness of the improved model.

In the framework of the UE project ATLAS+, fracture tests are performed on several small-scale specimens (notched tensile (NT), compact tension (CT) and single edge notched tensile (SENT) pre-cracked specimens) and on large-scale industrial structures (pre-cracked pipes). The parameters are fitted according to the experimental results on some of the small-scale specimens. They are used to predict the behavior of other small-scale specimens. According to the obtained results, the improved GTN model is able to predict crack initiation and crack propagation in two-dimensional (NT) and three-dimensional (CT) simulations in a correct way. Simulation of large scale test on pipe FP1 confirms again this conclusion. It should be noticed that more than one million degrees of freedom can be involved in the simulations of pipe. The robustness, the reliability and the performance of the improved model are thus demonstrated once again.

6.2 Future work

Recalibration of model parameters for ATLAS+ project

It was mentioned in chapter 5 that the calibrated parameters cannot well predict the plastic and the damage behaviors of SENT specimens. Discrepancy in the plastic regime may be due to the inhomogeneity of the material, Discrepancy for the cracking behavior may be linked to the calibration of the model parameters. Therefore, it is necessary to recalibrate the parameters with an optimized fitting procedure. We propose the following ways for the improvement:

- Modification of c to have a better result on SENT: the nonlocal parameter c is one parameter that is not fitted. Since the influence of this parameter on NT is very small, it is possible to slightly decrease this value to increase the damage rate in SENT. Attention should be paid to the following two points: (1) the nonlocal length l_{nl}, which is derived from c, should be at least 3 times larger than the mesh size to have a spatially converged solution; (2) The damage rate in CT can also be affected by c.
- Parameter fitting on (q_1, q_2): in our fitting procedure, the value of q_1 is fixed to 1.5. It may be better to fit at the same time (q_1, q_2) using NT, CT and/or SENT specimens.
- Activation of void nucleation: in this work, void nucleation is deactivated since there was no evidence of nucleation (possibly on iron carbides). In spite of this, the consideration of void nucleation may give a better result.

Once the optimized parameters are found, the simulation of the pipe FP1 should be performed again.

Modeling of crack initiation

A special attention is paid to the spurious and extremely high crack opening stress in the vicinity of the initial crack tip in the case of CT, SENT, Pipe and small-scale yielding simulations. One example can be found in Appendix A5.5 in the case of small-scale yielding simulations. It is observed that the crack opening stress at the initial crack tip is large compared to that at other positions with the use of the GTN model when strain nucleation is not activated. This result is due to the very high gradient of plastic deformation which causes additional hardening in the yield function ($c\Delta\kappa$). In addition, the material point (in the ligament) located at the initial crack tip never fails. This is mainly related to the low triaxiality at the initial crack tip. The illustration of this problem can be found in Appendix A5.6 in the case of small-scale yielding simulations. A strain-controlled nucleation was introduced to break these crack-tip nearby unbroken material points and thus avoid the large crack opening stress. Its efficiency is demonstrated in the small-scale yielding simulations. However, this nucleation formulation introduces one additional parameter, i.e., the critical equivalent plastic strain $E^p_{eq,c}$ which needs to be adjusted. It should not be too small, otherwise other undesired points may fail and the crack path may be physically incorrect; on the other hand, it should not be too large as the deformation of the desired point may be too large before its failure.

Another possible solution to solve the problem of the large crack-opening stresses induced by the additional hardening $c\Delta\kappa$ in the yield function is to eliminate this additional term by regularizing $E_h = \mathrm{tr}(\boldsymbol{E^p})$, in that case, the yield function does not depend on $c\Delta\kappa$. Note that E_h is directly linked to f_g. The Helmholtz free energy is:

$$\mathcal{F}(\boldsymbol{E}, \boldsymbol{E^p}, \kappa, f) = \mathcal{F}_\ell(\boldsymbol{E}(\underline{u}), \boldsymbol{E^p}, \kappa) + \int_{\Omega_0} \left(\frac{1}{2} c_2 \boldsymbol{\nabla} E_h \, . \boldsymbol{\nabla} E_h\right) d\Omega_0 \tag{6.1}$$

However, with this formulation, it is necessary to check whether the strain localization and the plastic strain localization still exist or not. It is also possible to control at the same time κ and ε_h,

$$\mathcal{F}(\boldsymbol{E},\boldsymbol{E^p},\kappa) \;=\; \mathcal{F}_\ell(\boldsymbol{E}(\underline{u}),\boldsymbol{E^p},\kappa) \;+\int_{\Omega_0}\left(\frac{1}{2}c\boldsymbol{\nabla}\kappa.\boldsymbol{\nabla}\kappa\right)d\Omega_0+\int_{\Omega_0}\left(\frac{1}{2}c_2\boldsymbol{\nabla}E_h.\boldsymbol{\nabla}E_h\right)d\Omega_0 \tag{6.2}$$

where $c < c_2$ so as to reduce the effect of $c\Delta\kappa$ in the yield function. This formulation shares some similarities with certain formulations of phase-field in which the plasticity and the damage are regularized at the same time (see Chapter 1).

Besides, we could also use a convex function of $\boldsymbol{\nabla}\kappa.\boldsymbol{\nabla}\kappa$ in the Helmholtz free energy such that when $\boldsymbol{\nabla}\kappa$ is too large, the term $c\Delta\kappa$ tends to zero or at least tends to a value comparable to σ_0. But in that case, the nonlocality effect is lost when $\boldsymbol{\nabla}\kappa$ is large.

Modeling of void coalescence

As stated in Chapter 1, the critical porosity f_c in the GTN model is often considered as a material constant. However, according to the results of some RVE simulations presented in Appendix A6, it is observed that the critical porosity f_c depends on the stress triaxiality T_r and the initial porosity f_0. Therefore, it may be[10] preferable (1) to predict the value of f_c using RVE simulations or other criteria such as the Thomason-type criterion and (2) to take into account the change of the plastic flow direction during void coalescence, as mentioned in Chapter 1.

Shear failure

Within the range of high levels of stress triaxialities, the GTN model has very good predictive performance. However, as shown in Section 2.6.1, the GTN model predicts no damage growth under zero or negative mean stress. To describe damage and failure due to shear deformation, some rather phenomenological models have been proposed to represent the mechanism of shear softening (Chen et al., 2017; Malcher et al., 2014; Nahshon and Hutchinson, 2008; Xue, 2008). In their work, the Lode angle is used to describe the combined stress state. A second-phase nucleation mechanism due to void sheeting and localization under shear condition is proposed. The acceleration of void growth and coalescence by shear softening and localization are taken into account. These models have shown great improvement in predicting the damage and failure of ductile materials, especially in the case of simple shear loading.

For example, in the work of (Xue, 2008), the void growth is described by an additional term:

$$\dot{f}_g = (1-f)\mathrm{tr}\big(\dot{\boldsymbol{E}}^p\big) + gq_3f^{q_4}E_{eq}\dot{E}_{eq} \tag{6.3}$$

where $(q_3, q_4) = (3.72, 0.5)$ for the 2D case and $(q_3, q_4) = (3.79, 0.33)$ for the 3D case, E_{eq} is the equivalent strain and g is the normalized Lode angle:

$$g = 1-\frac{6}{\pi}\left|\tan^{-1}\left(\frac{1}{\sqrt{3}}\left(2\left(\frac{s_2-s_3}{s_1-s_3}\right)-1\right)\right)\right| \tag{6.4}$$

with s_1, s_2, s_3 the principal deviatoric stress components and $s_1 \geq s_2 \geq s_3$. The value of g can vary from 0 to 1: $g = 0$ for tensile stress state, $g = 1$ for pure shear state and $0 < g < 1$ for combined stress states.

---

[10] It should still be noticed that the conclusions obtained from the RVE simulations are sometimes not suitable for the structural simulations. So it is possible that the value of f_c does not depend on stress triaxiatliy or initial porosity. That is why we use the word “may be” instead of using “is”.

Numerical implementation of the model of (Xue, 2008) is very simple since the porosity is updated using an explicit scheme in our work. Thus, we just need to add an additional term in the evolution equation of void growth.

Adaptive mesh refinement with remeshing technique

It is well known that the accuracy of finite element analysis is directly related to the finite element mesh: The computed solution will approach the exact solution as the mesh is refined. To avoid too large computing size, local refinement is attractive but the preferential mesh refinement zone must be known a priori, otherwise global refinement is required. This is typically problematic when it comes to industrial three-dimensional simulations where the zone of interest remains unknown or large compared to the desired mesh size. In this case, the required computational complexity would be very large. For example, for the mesh of the FP1 pipe in ATLAS+, in our work, one quarter of the geometry is discretized: in the area of interest, there are 6 elements in axial direction, around 140 elements in circumferential direction and 64 elements in radial directions, thus in total, there are $2 \times 6 \times 140 \times 64 \approx 106{,}000$ 3D elements (the total number of element to discretize the entire structure is two times larger), which corresponds to about 450,000 nodes. The computing time that we use for the propagation of 1cm CTOD is already around 1-2 months. However, this mesh is not really suitable for the prediction of 45° crack bifurcation observed in experiments: firstly, due to crack bifurcation, we lost one symmetric plane (i.e., the plane at which the initial fatigue crack is located); secondly, the mesh should be further refined along the axial direction. Assume that we still have 64 elements in the radial direction, while along the circumferential and axial direction, we refine 1.4 cm with a mesh size 0.1 mm. In this case, the area of interest contains about $140 \times 140 \times 64 > 1.25$ millions 3D elements. The total number of element to discretize the entire structure can even reach 2 million elements. The required computing time can be more than 1 year for a propagation of just $1.4\sqrt{2} \approx 2$ cm.

One way to deal with this problem is to use remeshing technique. The basic process of this technique can be found in Chapter 1. With this technique, the fine mesh is only used in a small area of interest (i.e., in front of the current crack tip) while the coarse mesh is used far from the crack front. This can significantly reduce the problem size.

Besides, the remeshing strategy can also avoid large element distortion, as mentioned in Chapter 1. The idea is to replace the distorted elements by some new elements using remeshing. Particularly, the element-deletion method or crack insertion can be used in combination with the remeshing technique so as to obtain a smooth boundary.

7 Appendices

A1 Class of Generalized standard materials

The concept of Generalized Standard Materials (GSM) was initially introduced in (Halphen and Nguyen, 1975) as a type of elastic-plastic models and was then extended to several dissipative phenomena (Nguyen, 1993). Assume that the material state is simply described by $(\boldsymbol{\varepsilon}, \underline{\alpha})$. The concept of GSM is based on the following four hypotheses:

- The Helmholtz free energy $\Phi(\boldsymbol{\varepsilon}, \underline{\alpha})$ is convex with respect to each internal variable belong to $\underline{\alpha}$.
- The Helmholtz free energy $\Phi(\boldsymbol{\varepsilon}, \underline{\alpha})$ can be divided into two parts:

  $$\Phi(\boldsymbol{\varepsilon}, \underline{\alpha}) = \Phi_1(\boldsymbol{\varepsilon}) + \Phi_2(\underline{\alpha}) \tag{7.1}$$

  where Φ_1 is a quadratic function and Φ_2 is a function strictly convex with respect to each internal variable belong to $\underline{\alpha}$.
  The stress tensor $\boldsymbol{\sigma}$ and the driving force $\underline{A}$ associated to $\underline{\alpha}$ are given by the state equations which derive from the second principle of thermodynamics under the form of the Clausius-Duhem inequality:

  $$\boldsymbol{\sigma} = \frac{\partial \Phi}{\partial \boldsymbol{\varepsilon}}(\boldsymbol{\varepsilon}, \underline{\alpha}), \qquad \underline{A} = -\frac{\partial \Phi}{\partial \underline{\alpha}}(\boldsymbol{\varepsilon}, \underline{\alpha}) \tag{7.2}$$

  With these definitions, the dissipation becomes:

  $$\mathcal{D} = \boldsymbol{\sigma} : \dot{\boldsymbol{\varepsilon}} - \dot{\Phi} = \underline{A} . \underline{\dot{\alpha}} \tag{7.3}$$

  In particular, it can be demonstrated that the driving force associated to $\boldsymbol{\varepsilon}^{\boldsymbol{p}} \in \underline{\alpha}$ is the stress tensor $\boldsymbol{\sigma}$.
- The driving forces $\underline{A}$ govern $\underline{\dot{\alpha}}$ through flow rules

  $$\underline{\dot{\alpha}} \in \frac{\partial \Phi}{\partial \underline{A}}(\underline{A}) \tag{7.4}$$

  If we note F the yield function and λ the Lagrange multiplier, then the flow rule can be written as:

  $$\underline{\dot{\alpha}} = \lambda \frac{\partial F}{\partial \underline{A}}(\underline{A}), F \leq 0, \lambda \geq 0, \lambda F = 0 \tag{7.5}$$
- The yield function F is convex with respect to $\underline{A}$.

A constitutive law can be classified into the GSM if the third hypothesis is fulfilled. Moreover, the solution is unique if all hypotheses are satisfied. The GTN damage model can be classified into the GSM if the porosity is integrated in an explicit manner, i.e., we “forget” the evolution of porosity during the integration of the GTN constitutive law. One can refer to (Enakoutsa et al., 2007) for more detail.

A2 Stiffness matrix for Newton algorithm at global level

A2.1 Continuum level

The partial derivatives of the function $\delta_{\underline{u}}\mathcal{L}$ with regard to $(\underline{u}, a, l, P, \theta)$ are:

$$\begin{cases} \dfrac{\partial(\delta_{\underline{u}}\mathcal{L})}{\partial \boldsymbol{E}} = \displaystyle\int_{\Omega_0} \left(\delta\boldsymbol{E}\colon\left(\frac{\partial \overline{\boldsymbol{T}}_{\boldsymbol{D}}}{\partial \overline{\boldsymbol{E}}} : (\mathbb{I} - \frac{1}{3}\boldsymbol{I}\otimes\boldsymbol{I}) + r_{inco}\boldsymbol{I}\otimes\boldsymbol{I}\right) : \delta\boldsymbol{E}\right) d\Omega_0 \\ \dfrac{\partial(\delta_{\underline{u}}\mathcal{L})}{\partial a} = \displaystyle\int_{\Omega_0} \left(\left(\delta\boldsymbol{E}\colon\frac{\partial \overline{\boldsymbol{T}}_{\boldsymbol{D}}}{\partial a}\right)\delta a\right) d\Omega_0 \\ \dfrac{\partial(\delta_{\underline{u}}\mathcal{L})}{\partial l} = \displaystyle\int_{\Omega_0} \left(\left(\delta\boldsymbol{E}\colon\frac{\partial \overline{\boldsymbol{T}}_{\boldsymbol{D}}}{\partial l}\right)\delta l\right) d\Omega_0 \\ \dfrac{\partial(\delta_{\underline{u}}\mathcal{L})}{\partial P} = \displaystyle\int_{\Omega_0} \left((\delta\boldsymbol{E}\colon\boldsymbol{I})\delta p\right) d\Omega_0 \\ \dfrac{\partial(\delta_{\underline{u}}\mathcal{L})}{\partial \theta} = \displaystyle\int_{\Omega_0} \left(\left(\delta\boldsymbol{E}\colon\left(\frac{\partial \overline{\boldsymbol{T}}_{\boldsymbol{D}}}{\partial \overline{\boldsymbol{E}}} : \frac{1}{3}\boldsymbol{I} - r_{inco}\boldsymbol{I}\right)\right)\delta\theta\right) d\Omega_0 \end{cases} \tag{7.6}$$

The partial derivatives of the function $\delta_a\mathcal{L}$ with regard to $(\underline{u}, a, l, P, \theta)$ are:

$$\begin{cases} \dfrac{\partial(\delta_a\mathcal{L}\,)}{\partial \boldsymbol{E}} = \displaystyle\int_{\Omega_0} \left(\left(\left(-r_{nl}\frac{\partial\kappa}{\partial\boldsymbol{E}}\right) : \delta\boldsymbol{E}\right)\delta a\right) d\Omega_0 \\ \dfrac{\partial(\delta_a\mathcal{L}\,)}{\partial a} = \displaystyle\int_{\Omega_0} \left(\left(c\delta a\boldsymbol{\nabla}\delta a + \delta a r_{nl}\left(1 - \frac{\partial\kappa}{\partial a}\right)\delta a\right)\right) d\Omega_0 \\ \dfrac{\partial(\delta_a\mathcal{L}\,)}{\partial l} = \displaystyle\int_{\Omega_0} \left(\delta a\left(1 - r_{nl}\frac{\partial\kappa}{\partial l}\right)\delta l\right) d\Omega_0 \\ \dfrac{\partial(\delta_a\mathcal{L}\,)}{\partial P} = 0 \\ \dfrac{\partial(\delta_a\mathcal{L}\,)}{\partial \theta} = \displaystyle\int_{\Omega_0} \left(\delta a\left(-r_{nl}\frac{\partial\kappa}{\partial\overline{\boldsymbol{E}}} : \left(\frac{1}{3}\boldsymbol{I}\right)\right)\delta\theta\right) d\Omega_0 \end{cases} \tag{7.7}$$

The partial derivatives of the function $\delta_l\mathcal{L}$ with regard to $(\underline{u}, a, l, P, \theta)$ are:

$$\begin{cases} \dfrac{\partial(\delta_l\mathcal{L})}{\partial \boldsymbol{E}} = \displaystyle\int_{\Omega_0} \left(\delta l\left(-\frac{\partial\kappa}{\partial\boldsymbol{E}}\right) : \delta\boldsymbol{E}\right) d\Omega_0 \\ \dfrac{\partial(\delta_l\mathcal{L})}{\partial a} = \displaystyle\int_{\Omega_0} \left(\delta l\left(-\frac{\partial\kappa}{\partial a}\right)\delta a\right) d\Omega_0 \\ \dfrac{\partial(\delta_l\mathcal{L})}{\partial l} = \displaystyle\int_{\Omega_0} \left(\delta l\left(-\frac{\partial\kappa}{\partial l}\right)\delta l\right) d\Omega_0 \\ \dfrac{\partial(\delta_l\mathcal{L})}{\partial P} = 0 \\ \dfrac{\partial(\delta_l\mathcal{L})}{\partial \theta} = \displaystyle\int_{\Omega_0} \left(\delta l\left(-\frac{\partial\kappa}{\partial\overline{\boldsymbol{E}}} : \frac{1}{3}\boldsymbol{I}\right)\delta\theta\right) d\Omega_0 \end{cases} \tag{7.8}$$

The partial derivatives of the function $\delta_P \mathcal{L}$ with regard to $(\underline{u}, a, l, P, \theta)$ are:

$$\begin{cases} \dfrac{\partial(\delta_P \mathcal{L})}{\partial \boldsymbol{E}} = \displaystyle\int_{\Omega_0} (\delta P \boldsymbol{I} : \delta \boldsymbol{E}) d\Omega_0 \\ \dfrac{\partial(\delta_P \mathcal{L})}{\partial a} = 0 \\ \dfrac{\partial(\delta_P \mathcal{L})}{\partial l} = 0 \\ \dfrac{\partial(\delta_P \mathcal{L})}{\partial P} = 0 \\ \dfrac{\partial(\delta_P \mathcal{L})}{\partial \theta} = \displaystyle\int_{\Omega_0} (\delta P(-1)\delta\theta) d\Omega_0 \end{cases} \tag{7.9}$$

The partial derivatives of the function $\delta_\theta \mathcal{L}$ with regard to $(\underline{u}, a, l, P, \theta)$ are:

$$\begin{cases} \dfrac{\partial(\delta_\theta \mathcal{L})}{\partial \boldsymbol{E}} = \displaystyle\int_{\Omega_0} \left(\delta\theta \left(\dfrac{\partial \overline{\boldsymbol{T}}_{\boldsymbol{H}}}{\partial \overline{\boldsymbol{E}}} : \left(\mathbb{I} - \dfrac{1}{3}\boldsymbol{I} \otimes \boldsymbol{I}\right) - r_{inco}\boldsymbol{I}\right) : \delta\boldsymbol{E}\right) d\Omega_0 \\ \dfrac{\partial(\delta_\theta \mathcal{L})}{\partial a} = \displaystyle\int_{\Omega_0} \left(\delta\theta \left(\dfrac{\partial \overline{\boldsymbol{T}}_{\boldsymbol{H}}}{\partial a}\right) \delta a\right) d\Omega_0 \\ \dfrac{\partial(\delta_\theta \mathcal{L})}{\partial l} = \displaystyle\int_{\Omega_0} \left(\delta\theta \left(\dfrac{\partial \overline{\boldsymbol{T}}_{\boldsymbol{H}}}{\partial l}\right) \delta l\right) d\Omega_0 \\ \dfrac{\partial(\delta_\theta \mathcal{L})}{\partial P} = \displaystyle\int_{\Omega_0} (\delta\theta(-1)\delta P) d\Omega_0 \\ \dfrac{\partial(\delta_\theta \mathcal{L})}{\partial \theta} = \displaystyle\int_{\Omega_0} \left(\delta\theta \left(\dfrac{\partial \overline{\boldsymbol{T}}_{\boldsymbol{H}}}{\partial \overline{\boldsymbol{E}}} : \left(\dfrac{1}{3}\boldsymbol{I}\right) + r_{inco}\right) \delta\theta\right) d\Omega_0 \end{cases} \tag{7.10}$$

A2.2 Discretized level

In discretized space, the partial derivatives of the function $\underline{F}^{\underline{u}}$ with regard to $(\underline{u}, a, l, P, \theta)$ are:

$$\begin{cases} \dfrac{\partial \underline{F}^{\underline{u}}}{\partial \boldsymbol{E}} = \displaystyle\sum_g w_g \left(\mathbb{P}_{\boldsymbol{g}} : \left(\boldsymbol{F}_{\boldsymbol{g}}^{\boldsymbol{\Gamma}} . \underline{\boldsymbol{B}}_g^{\underline{u}}\right) : \left(\dfrac{\partial \overline{\boldsymbol{T}}_{\boldsymbol{D,g}}}{\partial \overline{\boldsymbol{E}}_g} : \left(\mathbb{I} - \dfrac{1}{3}\boldsymbol{I} \otimes \boldsymbol{I}\right) + r_{inco}\boldsymbol{I} \otimes \boldsymbol{I}\right)\right) : \mathbb{P}_g : \left(\boldsymbol{F}_{\boldsymbol{g}}^{\boldsymbol{\Gamma}} . \underline{\boldsymbol{B}}_g^{\underline{u}}\right) \\ \dfrac{\partial \underline{F}^{\underline{u}}}{\partial a} = \displaystyle\sum_g w_g \left(\mathbb{P}_g : \left(\boldsymbol{F}_{\boldsymbol{g}}^{\boldsymbol{\Gamma}} . \underline{\boldsymbol{B}}_g^{\underline{u}}\right) : \dfrac{\partial \overline{\boldsymbol{T}}_{\boldsymbol{D,g}}}{\partial a_g}\right) N_g^a \\ \dfrac{\partial \underline{F}^{\underline{u}}}{\partial l} = \displaystyle\sum_g w_g (\mathbb{P}_g : \left(\boldsymbol{F}_{\boldsymbol{g}}^{\boldsymbol{\Gamma}} . \underline{\boldsymbol{B}}_g^{\underline{u}}\right) : \dfrac{\partial \overline{\boldsymbol{T}}_{\boldsymbol{D,g}}}{\partial l_g}) \, N_g^l \\ \dfrac{\partial \underline{F}^{\underline{u}}}{\partial P} = \displaystyle\sum_g w_g (\mathbb{P}_g : \left(\boldsymbol{F}_{\boldsymbol{g}}^{\boldsymbol{\Gamma}} . \underline{\boldsymbol{B}}_g^{\underline{u}}\right) : \boldsymbol{I}) \, N_g^P \\ \dfrac{\partial \underline{F}^{\underline{u}}}{\partial \theta} = \displaystyle\sum_g w_g \left(\mathbb{P}_g : \left(\boldsymbol{F}_{\boldsymbol{g}}^{\boldsymbol{\Gamma}} . \underline{\boldsymbol{B}}_g^{\underline{u}}\right) : \left(\dfrac{\partial \overline{\boldsymbol{T}}_{\boldsymbol{D,g}}}{\partial \overline{\boldsymbol{E}}_g} : \left(\dfrac{1}{3}\boldsymbol{I}\right) - r_{inco}\boldsymbol{I}\right)\right) N_g^\theta \end{cases} \tag{7.11}$$

The partial derivatives of the function F^a with regard to $(\underline{u}, a, l, P, \theta)$ are:

$$\begin{cases} \dfrac{\partial F^a}{\partial \boldsymbol{E}} = \displaystyle\sum_g w_g \left(N_g^a \left(-r_{nl} \frac{\partial \kappa_g}{\partial \boldsymbol{E}_g} \right) : \mathbb{P}_g : \left(\boldsymbol{F}_{\boldsymbol{g}}^{\boldsymbol{\Gamma}} . \underline{\boldsymbol{B}}_g^u \right) \right) \\ \dfrac{\partial F^a}{\partial a} = \displaystyle\sum_g w_g \left(N_g^a r_{nl} \left(1 - \frac{\partial \kappa_g}{\partial a_g} \right) N_g^a + c \underline{B}_g^a . \underline{B}_g^a \right) \\ \dfrac{\partial F^a}{\partial l} = \displaystyle\sum_g w_g \left(N_g^a \left(1 - r_{nl} \frac{\partial \kappa_g}{\partial l_g} \right) N_g^l \right) \\ \dfrac{\partial F^a}{\partial P} = 0 \\ \dfrac{\partial F^a}{\partial \theta} = \displaystyle\sum_g w_g \left(N_g^a \left(-r_{nl} \frac{\partial \kappa_g}{\partial \overline{\boldsymbol{E}}_{\boldsymbol{g}}} : \frac{1}{3} \boldsymbol{I} \right) N_g^\theta \right) \end{cases} \tag{7.12}$$

The partial derivatives of the function F^l with regard to $(\underline{u}, a, l, P, \theta)$ are:

$$\begin{cases} \dfrac{\partial F^l}{\partial \boldsymbol{E}} = \displaystyle\sum_g w_g \left(N_g^l \left(- \frac{\partial \kappa_g}{\partial \boldsymbol{E}_g} \right) : \mathbb{P}_g : \left(\boldsymbol{F}_{\boldsymbol{g}}^{\boldsymbol{\Gamma}} . \underline{\boldsymbol{B}}_g^u \right) \right) \\ \dfrac{\partial F^l}{\partial a} = \displaystyle\sum_g w_g \left(N_g^l \left(- \frac{\partial \kappa_g}{\partial a_g} \right) N_g^a \right) \\ \dfrac{\partial F^l}{\partial l} = \displaystyle\sum_g w_g \left(N_g^l \left(- \frac{\partial \kappa_g}{\partial l_g} \right) N_g^l \right) \\ \dfrac{\partial F^l}{\partial P} = 0 \\ \dfrac{\partial F^l}{\partial \theta} = \displaystyle\sum_g w_g \left(N_g^l \left(- \frac{\partial \kappa_g}{\partial \overline{\boldsymbol{E}}_{\boldsymbol{g}}} : \frac{1}{3} \boldsymbol{I} \right) N_g^\theta \right) \end{cases} \tag{7.13}$$

The partial derivatives of the function F^P with regard to $(\underline{u}, a, l, P, \theta)$ are:

$$\begin{cases} \dfrac{\partial F^P}{\partial \boldsymbol{E}} = \displaystyle\sum_g w_g \left(N_g^P \boldsymbol{I} : \mathbb{P}_g : \left(\boldsymbol{F}_{\boldsymbol{g}}^{\boldsymbol{\Gamma}} . \underline{\boldsymbol{B}}_g^u \right) \right) \\ \dfrac{\partial F^P}{\partial a} = 0 \\ \dfrac{\partial F^P}{\partial l} = 0 \\ \dfrac{\partial F^P}{\partial P} = 0 \\ \dfrac{\partial F^P}{\partial \theta} = \displaystyle\sum_g w_g \left(N_g^P (-1) N_g^\theta \right) \end{cases} \tag{7.14}$$

The partial derivatives of the function F^{θ} with regard to $(\underline{u}, a, l, P, \theta)$ are:

$$\begin{cases} \dfrac{\partial F^{\theta}}{\partial \boldsymbol{E}} = \sum\limits_{g} w_g \left(N_g^{\theta} \left(\dfrac{\partial \bar{T}_{H,g}}{\partial \bar{\boldsymbol{E}}_g} : \left(\mathbb{I} - \dfrac{1}{3} \boldsymbol{I} \otimes \boldsymbol{I} \right) - r_{inco} \boldsymbol{I} \right) \right) : \mathbb{P}_g : (\boldsymbol{F}_{\boldsymbol{g}}^{\boldsymbol{\Gamma}} . \underline{\boldsymbol{B}}_g^{u})) \\ \dfrac{\partial F^{\theta}}{\partial a} = \sum\limits_{g} w_g \left(N_g^{\theta} \left(\dfrac{\partial \bar{T}_{H,g}}{\partial a_g} \right) N_g^{a} \right) \\ \dfrac{\partial F^{\theta}}{\partial l} = \sum\limits_{g} w_g \left(N_g^{\theta} \left(\dfrac{\partial \bar{T}_{H,g}}{\partial l_g} \right) N_g^{l} \right) \\ \dfrac{\partial F^{\theta}}{\partial P} = \sum\limits_{g} w_g \left(N_g^{\theta} (-1) N_g^{P} \right) \\ \dfrac{\partial F^{\theta}}{\partial \theta} = \sum\limits_{g} w_g \left(N_g^{\theta} \left(\dfrac{\partial \bar{T}_{H,g}}{\partial \bar{\boldsymbol{E}}_g} : \dfrac{1}{3} \boldsymbol{I} + r_{inco} \right) N_g^{\theta} \right) \end{cases} \tag{7.15}$$

A3 Integration of the von-Mises 5-field law

In chapter 2, the von-Mises constitutive relations have already been shown, we recall here the main equations:

$$\begin{cases} \boldsymbol{T} = \mathbb{E}:(\boldsymbol{E} - \boldsymbol{E^p}) \\ V \equiv T_{eq} - T_* = 0 \\ \Delta\boldsymbol{E^p} = \lambda \dfrac{\partial T_*}{\partial \boldsymbol{T}} \\ \Delta\kappa = \lambda \geq 0 \\ F = T_* - \bar{\sigma}(\kappa) + l + r_{nl}a - r_{nl}\kappa \leq 0 \\ \lambda F = 0 \\ \Delta f_n = B_n(\kappa)\Delta\kappa \\ \Delta f_g = (1-f)\mathrm{tr}(\Delta\boldsymbol{E^p}) \\ \Delta f = \Delta f_n + \Delta f_g \end{cases} \tag{7.16}$$

The input data consists of $(\boldsymbol{E}, a, l)$ and the output data are $(\boldsymbol{T}, \kappa)$. Here and subsequently, unless otherwise stated, we note z^-, z and Δz the values of the quantity z at the beginning of the current time step, at the end of the current time step and its increment during the current time step.

A3.1 Solution algorithm

Elasticity

We focus on the case corresponding to $T_* \neq 0$. The trial stress tensor is computed as followed:

$$\boldsymbol{T^e} = \mathbb{E}:(\boldsymbol{E} - \boldsymbol{E^{p-}}) \tag{7.17}$$

The value of T_* can be obtained using $G(T_*, \boldsymbol{T^e}) = 0$. If $F(\kappa^-, T_*) \leq 0$, then the solution corresponds to the elastic domain characterized by $\lambda = 0$.

Plasticity

Now consider the case $F(\kappa^-, T_*) > 0$. The consistency condition shows that $\lambda > 0, F = 0$. In this case, the Equation (7.16) can be reduced to:

$$\begin{cases} T_H = T_H^e \\ \boldsymbol{T_D} = \boldsymbol{T_D^e} - 2\mu\Delta\boldsymbol{E^p} \\ \Delta\boldsymbol{E^p} = 1.5\Delta\kappa \dfrac{\boldsymbol{T_D^e}}{T_{eq}^e} \\ 0 = T_{eq}^e - 3\mu\Delta\kappa - \bar{\sigma}(\kappa) - r_{nl}\kappa + ra + l \end{cases} \tag{7.18}$$

where $\kappa = \kappa^- + \Delta\kappa$. This set of equations can be easily solved: firstly, the value of $\Delta\kappa$ can be obtained through the equation $T_{eq}^e - 3\mu\Delta\kappa - \bar{\sigma}(\kappa) - r\kappa + ra + l = 0$. Then $\Delta\boldsymbol{E^p}$ can be easily computed once $\Delta\kappa$ is known. Finally, $\boldsymbol{T_D}$ can be derived from $\Delta\boldsymbol{E^p}$.

Singularity

The solution algorithm described above relies on the assumption that $T_* \neq 0$, which is used in the derivation of the flow rule for $\boldsymbol{E^p}$. This assumption holds in the case of local models with nonlocal modification. But for the nonlocal model, the elastic domain can reduce to a point due to the term $l + ra$ in the yield function. Indeed, if $T_* = 0$, then $\boldsymbol{T} = \boldsymbol{0}$ and thus $\boldsymbol{E} = \boldsymbol{E^p}$ according to the Hooke law. The singularity occurs if and only if

$$\pi_\mathrm{N}(\Delta E^p, f) = \sup_{\boldsymbol{\sigma}, \sigma_* \leq 1} \{\boldsymbol{\sigma} : \Delta \boldsymbol{E^p}\} \leq \Delta\kappa \tag{7.19}$$

where the function π_N is strictly positive, homogeneous of degree one and $\pi_\mathrm{N}(\Delta E^p) = 0 \Leftrightarrow \Delta E^p = 0$. In the case of the von-Mises law, it can be demonstrated that:

$$\pi_N(\Delta \boldsymbol{E^p}) = \Delta E^p_{eq} \tag{7.20}$$

It can be demonstrated that in singular case, Equation (7.16) can be reduced to:

$$\begin{cases} \boldsymbol{0} = \boldsymbol{T^e_D} - 2\mu\Delta\boldsymbol{E^p_D} \\ T_H = T^e_H \\ 0 = \bar{\sigma}(\kappa) - r_{nl}\kappa + r_{nl}a + l \end{cases} \tag{7.21}$$

where $\kappa = \kappa^- + \Delta\kappa$ with $\Delta\kappa$ a value fulfilling Equation (7.19).

A3.2 Tangent matrix

In the following, for the enhanced strain tensor and the corresponding stress tensor, instead of noting $\overline{\boldsymbol{E}}$ and $\overline{\boldsymbol{T}}$, we note $\boldsymbol{E}$ and $\boldsymbol{T}$. If we note $m = l + ra$, then the tangent matrix is

$$\mathbb{J} = \begin{pmatrix} \dfrac{\partial \boldsymbol{T}}{\partial \boldsymbol{E}} & \dfrac{\partial \boldsymbol{T}}{\partial m} \\ \dfrac{\partial \kappa}{\partial \boldsymbol{E}} & \dfrac{\partial \kappa}{\partial m} \end{pmatrix} \tag{7.22}$$

Elasticity

In elastic case, the only non-zero term is $\frac{\partial \boldsymbol{T}}{\partial \boldsymbol{E}} = \mathbb{E}$ with $\mathbb{E}$ the Hooke's matrix which is:

$$\mathbb{E} = \begin{pmatrix} \lambda + 2\mu & \lambda + 2\mu & \lambda + 2\mu & 0 & 0 & 0 \\ \lambda + 2\mu & \lambda + 2\mu & \lambda + 2\mu & 0 & 0 & 0 \\ \lambda + 2\mu & \lambda + 2\mu & \lambda + 2\mu & 0 & 0 & 0 \\ 0 & 0 & 0 & 2\mu & 2\mu & 2\mu \\ 0 & 0 & 0 & 2\mu & 2\mu & 2\mu \\ 0 & 0 & 0 & 2\mu & 2\mu & 2\mu \end{pmatrix} \tag{7.23}$$

where $\lambda = (3\mathrm{K} - 2\mu)/3$ with λ Lamé's first parameter, K bulk modulus and μ shear modulus.

Plasticity

In plastic case, the expression of $\partial \boldsymbol{T}/\partial \boldsymbol{E}$ is:

$$\frac{\partial \boldsymbol{T}}{\partial \boldsymbol{E}} = \frac{\partial (T_H I + \boldsymbol{T_D})}{\partial \boldsymbol{E}} = \mathbb{E} - 3\mu \frac{\boldsymbol{T_D^e} \otimes \frac{\partial \kappa}{\partial \boldsymbol{E}}}{T_{eq}^e} + 3\mu\Delta\kappa \frac{\boldsymbol{T_D^e} \otimes \frac{\partial T_{eq}}{\partial \boldsymbol{E}}}{{T_{eq}^e}^2} - 3\mu \frac{\Delta\kappa}{T_{eq}^e} \frac{\partial \boldsymbol{T_D^e}}{\partial \boldsymbol{E}} \tag{7.24}$$

The expression of $\partial \boldsymbol{T}/\partial m$ is:

$$\frac{\partial \boldsymbol{T}}{\partial m} = \frac{\partial (T_H I + \boldsymbol{T_D})}{\partial m} = -3\mu \frac{\boldsymbol{T_D^e}}{T_{eq}^e} \frac{\partial \kappa}{\partial m} \tag{7.25}$$

The expression of $\partial \kappa/\partial \boldsymbol{E}$ is:

$$\frac{\partial \kappa}{\partial \boldsymbol{E}} = \frac{\partial \kappa}{\partial T_{eq}^e} \frac{\partial T_{eq}^e}{\partial \boldsymbol{E}} \tag{7.26}$$

The expression of $\partial \kappa/\partial m$ is:

$$\frac{\partial \kappa}{\partial m} = -\frac{\partial \bar{F}}{\partial m} \left(\frac{\partial \bar{F}}{\partial \kappa} \right)^{-1} \tag{7.27}$$

The terms appeared in Equations (7.24)(7.25)(7.26)(7.27) are listed in the following:

- The expression of $\frac{\partial \boldsymbol{T_D^e}}{\partial \boldsymbol{E}}$

$$\frac{\partial \boldsymbol{T_D^e}}{\partial \boldsymbol{E}} = \begin{pmatrix} \lambda' + 2\mu' & \lambda' + 2\mu' & \lambda' + 2\mu' & 0 & 0 & 0 \\ \lambda' + 2\mu' & \lambda' + 2\mu' & \lambda' + 2\mu' & 0 & 0 & 0 \\ \lambda' + 2\mu' & \lambda' + 2\mu' & \lambda' + 2\mu' & 0 & 0 & 0 \\ 0 & 0 & 0 & 2\mu' & 2\mu' & 2\mu' \\ 0 & 0 & 0 & 2\mu' & 2\mu' & 2\mu' \\ 0 & 0 & 0 & 2\mu' & 2\mu' & 2\mu' \end{pmatrix} \tag{7.28}$$

where $\lambda' = -2\mu/3, 2\mu' = 2\mu$ with K bulk modulus and μ shear modulus.

- Function $\bar{F}$ and its partial derivatives

$$\begin{cases} \bar{F} = T_{eq}^e - 3\mu\Delta\kappa - \bar{\sigma}(\kappa) - r\kappa + m \\ \dfrac{\partial \bar{F}}{\partial \kappa} = -3\mu - \dfrac{\partial \bar{\sigma}}{\partial \kappa}(\kappa) - r \\ \dfrac{\partial \bar{F}}{\partial T_{eq}^e} = 1 \\ \dfrac{\partial \bar{F}}{\partial m} = 1 \end{cases} \tag{7.29}$$

- Derivatives of T_h^e, T_{eq}^e with respect to $\boldsymbol{E}$

$$\begin{cases} \dfrac{\partial T_h^e}{\partial \boldsymbol{E}} = K\boldsymbol{I} \\ \dfrac{\partial T_{eq}^e}{\partial \boldsymbol{E}} = 3\mu \dfrac{\boldsymbol{T_D^e}}{T_{eq}^e} \end{cases} \tag{7.30}$$

- Derivatives of κ with respect to T_{eq}^e, m

$$\begin{cases} \dfrac{\partial \kappa}{\partial T_{eq}^e} = -\dfrac{\partial \bar{F}}{\partial T_{eq}^e}\left(\dfrac{\partial \bar{F}}{\partial \kappa}\right)^{-1} \\ \dfrac{\partial \kappa}{\partial m} = -\dfrac{\partial \bar{F}}{\partial m}\left(\dfrac{\partial \bar{F}}{\partial \kappa}\right)^{-1} \end{cases} \tag{7.31}$$

Singularity

In singular case, $T_* = 0$ and thus $T_{eq} = 0$ for any input $(\boldsymbol{E}, m)$. The tangent matrix can be directly computed:

$$\begin{cases} \dfrac{\partial \boldsymbol{T}}{\partial \boldsymbol{E}} = \dfrac{\partial T_h^e}{\partial \boldsymbol{E}}\boldsymbol{I} \\ \dfrac{\partial \boldsymbol{T}}{\partial m} = \boldsymbol{0} \\ \dfrac{\partial \kappa}{\partial \boldsymbol{E}} = 0 \\ \dfrac{\partial \kappa}{\partial m} = -\dfrac{\partial \bar{T}_*}{\partial m}\left(\dfrac{\partial \bar{T}_*}{\partial \kappa}\right)^{-1} \end{cases} \tag{7.32}$$

The terms appeared in Equations (7.32) are listed in the following:

- The expression of $\frac{\partial T_h^e}{\partial \boldsymbol{E}}$

$$\frac{\partial T_h^e}{\partial \boldsymbol{E}} = \begin{pmatrix} \lambda' + 2\mu' & \lambda' + 2\mu' & \lambda' + 2\mu' & 0 & 0 & 0 \\ \lambda' + 2\mu' & \lambda' + 2\mu' & \lambda' + 2\mu' & 0 & 0 & 0 \\ \lambda' + 2\mu' & \lambda' + 2\mu' & \lambda' + 2\mu' & 0 & 0 & 0 \\ 0 & 0 & 0 & 2\mu' & 2\mu' & 2\mu' \\ 0 & 0 & 0 & 2\mu' & 2\mu' & 2\mu' \\ 0 & 0 & 0 & 2\mu' & 2\mu' & 2\mu' \end{pmatrix} \tag{7.33}$$

where $\lambda' = K, 2\mu' = 0$ with K bulk modulus and μ shear modulus.

- Function $\bar{T}_*$ and its derivatives with respect to (κ, m)

$$\begin{cases} \bar{T}_*\,(\kappa) = \bar{\sigma}(\kappa) + r_{nl}\kappa - m \\ \dfrac{\partial \bar{T}_*}{\partial \kappa}(\kappa) = \dfrac{\partial \bar{\sigma}}{\partial \kappa}(\kappa) + r_{nl} \\ \dfrac{\partial \bar{T}_*}{\partial m}(\kappa) = -1 \end{cases} \tag{7.34}$$

A4 Integration of the GTN 5-field law (implicit scheme)

In chapter 2, the GTN constitutive relations have already been shown, we recall here the main equations:

$$\begin{cases} \boldsymbol{T} = \mathbb{E} : (\boldsymbol{E} - \boldsymbol{E^p}) \\ G \equiv \left(\dfrac{T_{eq}}{T_*}\right)^2 + 2q_1 f^* \cosh\left(\dfrac{3}{2} q_2 \dfrac{T_H}{T^*}\right) - 1 - (q_1 f^*)^2 = 0 \\ \Delta\boldsymbol{E^p} = \dfrac{\lambda}{J} \dfrac{\partial T_*}{\partial \boldsymbol{T}} \\ \Delta\kappa = \lambda \geq 0 \\ F = \dfrac{T_*}{J} - \bar{\sigma}(\kappa) + l + r_{nl} a - r_{nl} \kappa \leq 0 \\ \lambda F = 0 \\ \Delta f_n = B_n(\kappa) \Delta\kappa \\ \Delta f_g = (1 - f) \mathrm{tr}(\Delta\boldsymbol{E^p}) \\ \Delta f = \Delta f_n + \Delta f_g \end{cases} \tag{7.35}$$

The input data consists of $(\boldsymbol{E}, a, l)$ and the output data are $(\boldsymbol{T}, \kappa)$. The internal variables are $(f, \boldsymbol{E^p})$. Here and subsequently, unless otherwise stated, we note z^-, z and Δz the values of the quantity z at the beginning of the current time step, at the end of the current time step and its increment during the current time step. To obtain the solutions of Equation (7.35), as mentioned in previous sections, a semi-explicit scheme with respect to the porosity f is possible. The solution algorithm of this scheme has already been described in (Zhang et al., 2018). In this section, we will describe the solution algorithm of the fully implicit scheme with respect to $(f, \boldsymbol{E^p}, \kappa)$.

A4.1 Solution algorithm

Elasticity

We focus on the case corresponding to $T_* \neq 0$ and $q_1 f^* < 1$. The trial stress tensor is computed as followed:

$$\boldsymbol{T^e} = \mathbb{E} : (\boldsymbol{E} - \boldsymbol{E^{p-}}) \tag{7.36}$$

The value of T_* can be obtained using $G(T_*, \boldsymbol{T^e}, f^-) = 0$. If $F(\kappa^-, T_*) \leq 0$, then the solution corresponds to the elastic domain characterized by $\lambda = 0$. Another method is that we compute T_* using $F(\kappa^-, T_*) = 0$. Then we evaluate $G(T_*, \boldsymbol{T^e}, f^-)$, if $G \leq 0$, then the solution corresponds to the elastic domain characterized by $\lambda = 0$. This method is simpler than the previous one.

Plasticity

Now consider the case $F(\kappa^-, T_*) > 0$. The consistency condition shows that $\lambda > 0, F = 0$. In this case, the Equation (7.35) can be reduced to:

$$\begin{cases} \bar{G}(p, T_*, f) = \left(\dfrac{T_{eq}^e \bar{q}(p, T_*, f)}{T_*}\right)^2 + 2q_1 f^* \cosh\left(\dfrac{3}{2} q_2 \dfrac{T_H^e p}{T^*}\right) - 1 - (q_1 f^*)^2 = 0 \\ \bar{M}(p, T_*, f) = -\bar{T}_*\left(\bar{\lambda}(p, T_*, f)\right) + T^* = 0 \\ \bar{N}(p, T_*, f) = \Delta f - \dfrac{1 - f}{J} \bar{\lambda}(p, T_*, f) \mathrm{tr}\left(\dfrac{\partial T_*}{\partial \boldsymbol{T}}\right) - \bar{B}_n\left(\bar{\lambda}(p, T_*, f)\right) \bar{\lambda}(p, T_*, f) = 0 \end{cases} \tag{7.37}$$

where (p, q) are defined by $(T_h = pT_h^e, T_{eq} = qT_{eq}^e)$ and

$$\left\{\begin{aligned} \bar{q}(p,T_*,f) &= \frac{T_*\bar{\Lambda}\left(\frac{T_h^e p}{T_*},f\right)}{T_*\bar{\Lambda}\left(\frac{T_h^e p}{T_*},f\right)+\frac{\mu}{\kappa}T_h^e(1-p)} \\ \bar{\lambda}(p,T_*,f) &= \frac{JT_h^e(1-p)}{3K\bar{\Lambda}\left(\frac{T_h^e p}{T_*},f\right)\bar{\Theta}\left(\frac{T_h^e p}{T_*},\frac{T_{eq}^e\bar{q}(p,T_*,f)}{T_*},f\right)} \\ \frac{\partial T_*}{\partial \boldsymbol{T}}(p,T_*,f) &= \bar{\Theta}\left(\frac{T_h^e p}{T_*},\frac{T_{eq}^e\bar{q}(p,T_*,f)}{T_*},f\right)\left[\frac{3}{2}\frac{\boldsymbol{T_D}}{T_*}+\bar{\Lambda}\left(\frac{T_h^e p}{T_*},f\right)\boldsymbol{I}\right] \end{aligned}\right. \tag{7.38}$$

The hardening function can be assumed to be:

$$\overline{\sigma}(\kappa) = r_0 + r_h\kappa + r_1(1 - e^{-g_1\kappa}) + r_2(1 - e^{-g_2\kappa}) + r_3(\kappa + \kappa_0)^{g_3} \tag{7.39}$$

where $\mathrm{r}_0, r_h, r_1, r_2, r_3, g_1, g_2, g_3, \kappa_0$ are the hardening parameters.

The Equation (7.37) can be solved using Newton-Raphson algorithm. We note $\underline{x} = (p, T_*, f)$ and $\underline{R} = (\bar{G}, \bar{M}, \bar{N})$. In the current time step, at iteration $j + 1$, we have $\underline{x}^{j+1} = \underline{x}^j - \left(\mathbb{J}_R^j\right)^{-1}\underline{R}^j$ with $\mathbb{J}_R^j = \frac{\partial \underline{R}}{\partial \underline{x}}(\underline{x}^j)$. The solution is convergent when $||\underline{R}^n|| < \underline{\epsilon}$ with n the total iteration numbers and $\underline{\epsilon}$ a value near $\underline{0}$. The Jacobian matrix $\mathbb{J}_R^j$ is defined as:

$$\mathbb{J}_R^j = \begin{pmatrix} \dfrac{\partial \bar{G}}{\partial p} & \dfrac{\partial \bar{G}}{\partial T_*} & \dfrac{\partial \bar{G}}{\partial f} \\ \dfrac{\partial \bar{M}}{\partial p} & \dfrac{\partial \bar{M}}{\partial T_*} & \dfrac{\partial \bar{M}}{\partial f} \\ \dfrac{\partial \bar{N}}{\partial p} & \dfrac{\partial \bar{N}}{\partial T_*} & \dfrac{\partial \bar{N}}{\partial f} \end{pmatrix} \tag{7.40}$$

The partial derivatives of the function $\bar{G}$ with regard to (p, T_*, f) are:

$$\left\{\begin{aligned} \frac{\partial \bar{G}}{\partial p}(p,T_*,f) &= \frac{\partial G}{\partial p} + \frac{\partial G}{\partial q}\frac{\partial \bar{q}}{\partial p} \\ \frac{\partial \bar{G}}{\partial T_*}(p,T_*,f) &= \frac{\partial G}{\partial T_*} + \frac{\partial G}{\partial q}\frac{\partial \bar{q}}{\partial T_*} \\ \frac{\partial \bar{G}}{\partial f}(p,T_*,f) &= \frac{\partial G}{\partial f} + \frac{\partial G}{\partial q}\frac{\partial \bar{q}}{\partial f} \end{aligned}\right. \tag{7.41}$$

The partial derivatives of the function $\bar{M}$ with regard to (p, T_*, f) are:

$$\left\{\begin{aligned} \frac{\partial \bar{M}}{\partial p}(p,T_*,f) &= -\frac{\partial \bar{T}_*}{\partial \kappa}\frac{\partial \bar{\lambda}}{\partial p} \\ \frac{\partial \bar{M}}{\partial T_*}(p,T_*,f) &= -\frac{\partial \bar{T}_*}{\partial \kappa}\frac{\partial \bar{\lambda}}{\partial T_*} + 1 \\ \frac{\partial \bar{M}}{\partial f}(p,T_*,f) &= -\frac{\partial \bar{T}_*}{\partial \kappa}\frac{\partial \bar{\lambda}}{\partial f} \end{aligned}\right. \tag{7.42}$$

The partial derivatives of the function $\bar{N}$ with regard to (p, T_*, f) are:

$$\begin{cases} \dfrac{\partial \bar{N}}{\partial p}(p, T_*, f) = -\left(\dfrac{\partial \bar{N}_g}{\partial p} + \dfrac{\partial \bar{N}_n}{\partial p}\right) \\ \dfrac{\partial \bar{N}}{\partial T_*}(p, T_*, f) = -\left(\dfrac{\partial \bar{N}_g}{\partial T_*} + \dfrac{\partial \bar{N}_n}{\partial T_*}\right) \\ \dfrac{\partial \bar{N}}{\partial f}(p, T_*, f) = -\left(\dfrac{\partial \bar{N}_g}{\partial f} + \dfrac{\partial \bar{N}_n}{\partial f}\right) + 1 \end{cases} \tag{7.43}$$

where $(\bar{N}_g, \bar{N}_n)$ correspond to the evolution of the porosity due to void growth and void nucleation, respectively.

The terms appeared in Equations (7.41)(7.42)(7.43) are listed in the following:

- Function G and its partial derivatives

$$\begin{cases} G(p, q, T_*, f) = \left(\dfrac{T_{eq}}{T_*}\right)^2 + 2q_1 f^* \cosh\left(\dfrac{3}{2} q_2 \dfrac{T_H}{T^*}\right) - 1 - (q_1 f^*)^2 = 0 \\ \dfrac{\partial G}{\partial p}(p, q, T_*, f) = 3q_1 q_2 f_* \dfrac{T_h^e}{T_*} \sinh\left(\dfrac{3}{2} q_2 \dfrac{T_h^e p}{T_*}\right) \\ \dfrac{\partial G}{\partial q}(p, q, T_*, f) = 2\left(\dfrac{T_{eq}^e}{T_*}\right)^2 q \\ \dfrac{\partial G}{\partial T_*}(p, q, T_*, f) = -2\dfrac{\left(T_{eq}^e q\right)^2}{T_*^3} - 3q_1 q_2 f^* \dfrac{T_h^e p}{T_*^2} \sinh\left(\dfrac{3}{2} q_2 \dfrac{T_h^e p}{T_*}\right) \\ \dfrac{\partial G}{\partial f}(p, q, T_*, f) = 2q_1 \cosh\left(\dfrac{3}{2} q_2 \dfrac{T_h^e p}{T_*}\right) \dfrac{\partial f^*}{\partial f} - 2q_1^2 f^* \dfrac{\partial f^*}{\partial f} \end{cases} \tag{7.44}$$

- Hardening function $\bar{\sigma}$ and its derivatives

$$\begin{cases} \bar{\sigma}(\kappa) = r_0 + r_h \kappa + r_1(1 - e^{-g_1 \kappa}) + r_2(1 - e^{-g_2 \kappa}) + r_3(\kappa + \kappa_0)^{g_3} \\ \dfrac{\partial \bar{\sigma}}{\partial \kappa}(\kappa) = r_h + r_1 g_1 e^{-g_1 \kappa} + r_2 g_2 e^{-g_2 \kappa} + r_3 g_3 (\kappa + \kappa_0)^{g_3 - 1} \end{cases} \tag{7.45}$$

- Function B_n and its derivatives

$$\begin{cases} B_n(\kappa) = \dfrac{f_N}{s_N \sqrt{2\pi}} e^{-\frac{1}{2}\left(\frac{(\kappa - \kappa_N)}{s_N}\right)^2} \\ \dfrac{\partial B_n}{\partial \kappa}(\kappa) = -f_N \dfrac{(\kappa - \kappa_N)}{s_N^2 \sqrt{2\pi}} e^{-\frac{1}{2}\left(\frac{(\kappa - \kappa_N)}{s_N}\right)^2} \end{cases} \tag{7.46}$$

- Function T_* and its derivatives

$$\begin{cases} \bar{T}_*(\kappa) = J(\bar{\sigma}(\kappa) + r_{nl}\kappa - l - r_{nl} a) \\ \dfrac{\partial \bar{T}_*}{\partial \kappa} = J\left(\dfrac{\partial \bar{\sigma}}{\partial \kappa}(\kappa) + r_{nl}\right) \end{cases} \tag{7.47}$$

- Function $\mathit{\Lambda}$ and its partial derivatives

$$\begin{cases} \mathit{\Lambda}(x,f) = \dfrac{1}{2} q_1 q_2 f^* \sinh\left(\dfrac{3}{2} q_2 x\right) \\ \dfrac{\partial \mathit{\Lambda}}{\partial x}(x,f) = \dfrac{3}{4} q_1 q_2^2 f^* \sinh\left(\dfrac{3}{2} q_2 x\right) \\ \dfrac{\partial \mathit{\Lambda}}{\partial f}(x,f) = \dfrac{1}{2} q_1 q_2 \dfrac{\partial f^*}{\partial f} \sinh\left(\dfrac{3}{2} q_2 x\right) \end{cases} \tag{7.48}$$

- Function $\bar{\mathit{\Lambda}}$ and its partial derivatives

$$\begin{cases} \bar{\mathit{\Lambda}}(x,f) = \mathit{\Lambda}\left(\dfrac{T_h^e p}{T_*}, f\right) \\ \dfrac{\partial \bar{\mathit{\Lambda}}}{\partial p}(x,f) = \dfrac{T_h^e}{T_*} \dfrac{\partial \mathit{\Lambda}}{\partial x}\left(\dfrac{T_h^e p}{T_*}, f\right) \\ \dfrac{\partial \bar{\mathit{\Lambda}}}{\partial f}(x,f) = \dfrac{\partial \mathit{\Lambda}}{\partial f}\left(\dfrac{T_h^e p}{T_*}, f\right) \end{cases} \tag{7.49}$$

- Function $\mathit{\Theta}$ and its partial derivatives

$$\begin{cases} \mathit{\Theta}(x,y,f) = \left(y^2 + 3x\mathit{\Lambda}(x,f)\right)^{-1} \\ \dfrac{\partial \mathit{\Theta}}{\partial x}(x,y,f) = \dfrac{-3\mathit{\Lambda} + 3x\dfrac{\partial \mathit{\Lambda}}{\partial x}}{(y^2 + 3x\mathit{\Lambda})^2} \\ \dfrac{\partial \mathit{\Theta}}{\partial y}(x,y,f) = \dfrac{-2y}{(y^2 + 3x\mathit{\Lambda})^2} \\ \dfrac{\partial \mathit{\Theta}}{\partial f}(x,y,f) = \dfrac{-3x\dfrac{\partial \mathit{\Lambda}}{\partial f}}{(y^2 + 3x\mathit{\Lambda})^2} \end{cases} \tag{7.50}$$

- Function $\bar{\mathit{\Theta}}$ and its partial derivatives

$$\begin{cases} \bar{\mathit{\Theta}} = \mathit{\Theta}\left(\dfrac{T_h^e p}{T_*}, \dfrac{T_{eq}^e \bar{q}}{T_*}, f\right) \\ \dfrac{\partial \bar{\mathit{\Theta}}}{\partial p} = \dfrac{T_h^e}{T_*} \dfrac{\partial \mathit{\Theta}}{\partial x}\left(\dfrac{T_h^e p}{T_*}, \dfrac{T_{eq}^e \bar{q}}{T_*}, f\right) + \dfrac{T_{eq}^e}{T_*} \dfrac{\partial \mathit{\Theta}}{\partial y}\left(\dfrac{T_h^e p}{T_*}, \dfrac{T_{eq}^e \bar{q}}{T_*}, f\right) \dfrac{\partial \bar{q}}{\partial p} \\ \dfrac{\partial \bar{\mathit{\Theta}}}{\partial q} = \dfrac{T_{eq}^e}{T_*} \dfrac{\partial \mathit{\Theta}}{\partial y}\left(\dfrac{T_h^e p}{T_*}, \dfrac{T_{eq}^e \bar{q}}{T_*}, f\right) \\ \dfrac{\partial \bar{\mathit{\Theta}}}{\partial f} = \dfrac{\partial \mathit{\Theta}}{\partial f}\left(\dfrac{T_h^e p}{T_*}, \dfrac{T_{eq}^e \bar{q}}{T_*}, f\right) + \dfrac{T_{eq}^e}{T_*} \dfrac{\partial \mathit{\Theta}}{\partial y}\left(\dfrac{T_h^e p}{T_*}, \dfrac{T_{eq}^e \bar{q}}{T_*}, f\right) \dfrac{\partial \bar{q}}{\partial f} \end{cases} \tag{7.51}$$

- Function $\bar{q}$ and its partial derivatives

$$\begin{cases} \bar{q}(p,T_*,f) = \dfrac{T_*\bar{\Lambda}}{T_*\bar{\Lambda} + \frac{\mu}{\kappa}T_h^e(1-p)} \\ \dfrac{\partial\bar{q}}{\partial p}(p,T_*,f) = \dfrac{T_h^e\frac{\partial\bar{\Lambda}}{\partial x}\left(T_*\bar{\Lambda} + \frac{\mu}{\kappa}T_h^e(1-p)\right) - T_*\bar{\Lambda}\left(T_h^e\frac{\partial\bar{\Lambda}}{\partial x} - \frac{\mu}{K}T_h^e\right)}{\left(T_*\bar{\Lambda} + \frac{\mu}{\kappa}T_h^e(1-p)\right)^2} \\ \dfrac{\partial\bar{q}}{\partial T_*}(p,T_*,f) = \dfrac{\left(\bar{\Lambda} - \frac{T_h^e p}{T_*}\frac{\partial\bar{\Lambda}}{\partial x}\right)\left(T_*\bar{\Lambda} + \frac{\mu}{\kappa}T_h^e(1-p)\right) - T_*\bar{\Lambda}\left(\bar{\Lambda} - \frac{T_h^e p}{T_*}\frac{\partial\bar{\Lambda}}{\partial x}\right)}{\left(T_*\bar{\Lambda} + \frac{\mu}{\kappa}T_h^e(1-p)\right)^2} \\ \dfrac{\partial\bar{q}}{\partial f}(p,T_*,f) = \dfrac{T_*\frac{\partial\bar{\Lambda}}{\partial f}\left(T_*\bar{\Lambda} + \frac{\mu}{\kappa}T_h^e(1-p)\right) - T_*\bar{\Lambda}\left(T_*\frac{\partial\bar{\Lambda}}{\partial f}\right)}{\left(T_*\bar{\Lambda} + \frac{\mu}{\kappa}T_h^e(1-p)\right)^2} \end{cases} \tag{7.52}$$

- Function $\bar{\lambda}$ and its partial derivatives

$$\begin{cases} \bar{\lambda}(p,T_*,f) = \dfrac{JT_h^e(1-p)}{3K\bar{\Lambda}\bar{\Theta}} \\ \dfrac{\partial\bar{\lambda}}{\partial p}(p,T_*,f) = \dfrac{-\frac{J}{3K}T_h^e(1-p)\left(\frac{\partial\bar{\Lambda}}{\partial p}\bar{\Theta} + \bar{\Lambda}\frac{\partial\bar{\Theta}}{\partial p}\right) - \frac{J}{3K}T_h^e\bar{\Lambda}\bar{\Theta}}{(\bar{\Lambda}\bar{\Theta})^2} \\ \dfrac{\partial\bar{\lambda}}{\partial T_*}(p,T_*,f) = \dfrac{-\frac{J}{3K}T_h^e(1-p)\left(\frac{\partial\bar{\Lambda}}{\partial T_*}\bar{\Theta} + \bar{\Lambda}\frac{\partial\bar{\Theta}}{\partial T_*}\right)}{(\bar{\Lambda}\bar{\Theta})^2} \\ \dfrac{\partial\bar{\lambda}}{\partial f}(p,T_*,f) = \dfrac{-\frac{J}{3K}T_h^e(1-p)\left(\frac{\partial\bar{\Lambda}}{\partial f}\bar{\Theta} + \bar{\Lambda}\frac{\partial\bar{\Theta}}{\partial f}\right)}{(\bar{\Lambda}\bar{\Theta})^2} \end{cases} \tag{7.53}$$

- Function $\boldsymbol{v} = \partial\bar{T}_*/\partial\boldsymbol{T}$ and its partial derivatives

$$\begin{cases} \boldsymbol{v}(p,T_*,f) = \bar{\Theta}\left(\dfrac{3}{2}\dfrac{\boldsymbol{T_D}}{T_*} + \bar{\Lambda}\boldsymbol{I}\right) \\ \dfrac{\partial\bar{\boldsymbol{v}}}{\partial p}(p,T_*,f) = \dfrac{\partial\bar{\Theta}}{\partial p}\left(\dfrac{3\boldsymbol{T_D^e}\bar{q}}{2T_*} + \bar{\Lambda}\boldsymbol{I}\right) + \bar{\Theta}\left(\dfrac{\partial\bar{\Lambda}}{\partial p}\boldsymbol{I} + \dfrac{3\boldsymbol{T_D^e}}{2T_*}\dfrac{\partial\bar{q}}{\partial p}\right) \\ \dfrac{\partial\bar{v}}{\partial T_*}(p,T_*,f) = \dfrac{\partial\bar{\Theta}}{\partial T_*}\left(\dfrac{3\boldsymbol{T_D^e}\bar{q}}{2T_*} + \bar{\Lambda}\boldsymbol{I}\right) + \bar{\Theta}\left(\dfrac{\partial\bar{\Lambda}}{\partial T_*}\boldsymbol{I} + \dfrac{3\boldsymbol{T_D^e}}{2T_*}\dfrac{\partial\bar{q}}{\partial T_*} - \dfrac{3\boldsymbol{T_D^e}\bar{q}}{2T_*^2}\right) \\ \dfrac{\partial\bar{\boldsymbol{v}}}{\partial f}(p,T_*,f) = \dfrac{\partial\bar{\Theta}}{\partial f}\left(\dfrac{3\boldsymbol{T_D^e}\bar{q}}{2T_*} + \bar{\Lambda}\boldsymbol{I}\right) + \bar{\Theta}\left(\dfrac{\partial\bar{\Lambda}}{\partial f}\boldsymbol{I} + \dfrac{3\boldsymbol{T_D^e}}{2T_*}\dfrac{\partial\bar{q}}{\partial f}\right) \end{cases} \tag{7.54}$$

- Function $\bar{N}_g$ and its derivatives

$$\begin{cases} \bar{N}_g(p,T_*,f) = \dfrac{1-f}{J}\bar{\lambda}(\boldsymbol{v}:\boldsymbol{I}) \\ \dfrac{\partial \bar{N}_g}{\partial p}(p,T_*,f) = \dfrac{1-f}{J}\left(\dfrac{\partial \bar{\lambda}}{\partial p}(\boldsymbol{v}:\boldsymbol{I}) + \bar{\lambda}\left(\dfrac{\partial \boldsymbol{v}}{\partial p}:\boldsymbol{I}\right)\right) \\ \dfrac{\partial \bar{N}_g}{\partial T_*}(p,T_*,f) = \dfrac{1-f}{J}\left(\dfrac{\partial \bar{\lambda}}{\partial T_*}(\boldsymbol{v}:\boldsymbol{I}) + \bar{\lambda}\left(\dfrac{\partial \boldsymbol{v}}{\partial T_*}:\boldsymbol{I}\right)\right) \\ \dfrac{\partial \bar{N}_g}{\partial f}(p,T_*,f) = \dfrac{1-f}{J}\left(\dfrac{\partial \bar{\lambda}}{\partial f}(\boldsymbol{v}:\boldsymbol{I}) + \bar{\lambda}\left(\dfrac{\partial \boldsymbol{v}}{\partial f}:\boldsymbol{I}\right)\right) - \dfrac{1}{J}\bar{\lambda}(\boldsymbol{v}:\boldsymbol{I}) \end{cases} \tag{7.55}$$

- Function $\bar{N}_n$ and its derivatives ($B_n = B_n(\kappa^- + \bar{\lambda})$ and $\frac{\partial \bar{B}_n}{\partial \kappa} = \frac{\partial \bar{B}_n}{\partial \kappa}(\kappa^- + \bar{\lambda})$)

$$\begin{cases} \bar{N}_n(p,T_*,f) = B_n\bar{\lambda} \\ \dfrac{\partial \bar{N}_n}{\partial p}(p,T_*,f) = \dfrac{\partial \bar{\lambda}}{\partial p}\left(\dfrac{\partial \bar{B}_n}{\partial \kappa}\bar{\lambda} + \bar{B}_n\right) \\ \dfrac{\partial \bar{N}_n}{\partial T_*}(p,T_*,f) = \dfrac{\partial \bar{\lambda}}{\partial T_*}\left(\dfrac{\partial \bar{B}_n}{\partial \kappa}\bar{\lambda} + \bar{B}_n\right) \\ \dfrac{\partial \bar{N}_n}{\partial f}(p,T_*,f) = \dfrac{\partial \bar{\lambda}}{\partial f}\left(\dfrac{\partial \bar{B}_n}{\partial \kappa}\bar{\lambda} + \bar{B}_n\right) \end{cases} \tag{7.56}$$

Singularity

The solution algorithm described above relies on the assumption that $T_* \neq 0$, which is used in the derivation of the flow rule for $\boldsymbol{E^p}$. This assumption holds in the case of the local GTN model. But for the nonlocal model, the elastic domain can reduce to a point due to the term $l + ra$ in the yield function. Indeed, according to (Zhang et al., 2018), if $q_1 f^* < 1$ and $T_* = 0$, then $\boldsymbol{T} = \boldsymbol{0}$ and thus $\boldsymbol{E} = \boldsymbol{E^p}$ according to the HOOKE law. The singularity occurs if and only if

$$\pi_{\mathrm{N}}(\Delta\boldsymbol{E^p}, f) = \sup_{\boldsymbol{\sigma},\sigma_* \leq 1}\{\boldsymbol{\sigma}:\Delta\boldsymbol{E^p}\} \leq \frac{\Delta\kappa}{J} \tag{7.57}$$

where the function π_{N} is strictly positive, homogeneous of degree one and $\pi_{\mathrm{N}}(\Delta\boldsymbol{E^p}) = 0 \Leftrightarrow \Delta\boldsymbol{E^p} = 0$:

$$\pi_N(\Delta\boldsymbol{E^p}, f) = \frac{2}{q_2}\operatorname{arccosh}(1 + C^*)\left|\Delta E_H^p\right| + \frac{2}{3}(1 - q_1 f^*)\sqrt{1 - \gamma C^*}\Delta E_{eq}^e \tag{7.58}$$

with

$$\begin{cases} C^* = -s + \sqrt{s^2 + \dfrac{2}{\gamma}(s-1)} = \dfrac{2\left(1-\frac{1}{s}\right)}{\gamma\left(1+\sqrt{1+\frac{2}{\gamma}\left(\frac{1}{s}-\frac{1}{s^2}\right)}\right)} \\ s^{-1} = \left(\dfrac{q_2^2 {\Delta E_{eq}^p}^2 + \dfrac{9\left|\Delta E_H^p\right|^2}{q_1 f^*}}{q_2^2 {\Delta E_{eq}^p}^2}\right)^{-1} \\ \gamma^{-1} = \dfrac{(1-q_1 f^*)^2}{2 q_1 f^*} \end{cases} \tag{7.59}$$

It can be demonstrated that in singular case, Equation (7.35) can be reduced to:

$$\begin{cases} \bar{T}_*(\kappa) = 0 \\ \quad \Delta f = (1 - f^- + \Delta f)(\Delta \boldsymbol{E}{:}\boldsymbol{I}) + B_n(\kappa)\Delta\kappa \end{cases} \tag{7.60}$$

where $\kappa = \kappa^- + \Delta\kappa$ with $\Delta\kappa$ a value fulfilling Equation (7.57).

A4.2 Tangent matrix

In the following, for the enhanced strain tensor and the corresponding stress tensor, instead of noting $\overline{\boldsymbol{E}}$ and $\overline{\boldsymbol{T}}$, we note $\boldsymbol{E}$ and $\boldsymbol{T}$. If we note $m = l + ra$, then the tangent matrix is

$$\mathbb{J} = \begin{pmatrix} \dfrac{\partial \boldsymbol{T}}{\partial \boldsymbol{E}} & \dfrac{\partial \boldsymbol{T}}{\partial m} \\ \dfrac{\partial \kappa}{\partial \boldsymbol{E}} & \dfrac{\partial \kappa}{\partial m} \end{pmatrix} \tag{7.61}$$

Elasticity

In elastic case, the only non-zero term is $\frac{\partial \boldsymbol{T}}{\partial \boldsymbol{E}} = \mathbb{E}$ with $\mathbb{E}$ the Hooke's matrix which is:

$$\mathbb{E} = \begin{pmatrix} \lambda+2\mu & \lambda+2\mu & \lambda+2\mu & 0 & 0 & 0 \\ \lambda+2\mu & \lambda+2\mu & \lambda+2\mu & 0 & 0 & 0 \\ \lambda+2\mu & \lambda+2\mu & \lambda+2\mu & 0 & 0 & 0 \\ 0 & 0 & 0 & 2\mu & 2\mu & 2\mu \\ 0 & 0 & 0 & 2\mu & 2\mu & 2\mu \\ 0 & 0 & 0 & 2\mu & 2\mu & 2\mu \end{pmatrix} \tag{7.62}$$

where $\lambda = (3K - 2\mu)/3$ with λ Lamé's first parameter, K bulk modulus and μ shear modulus.

Plasticity

In plastic case, the expression of $\partial \boldsymbol{T}/\partial \boldsymbol{E}$ is:

$$\frac{\partial \boldsymbol{T}}{\partial \boldsymbol{E}} = \frac{\partial (T_h^e p \boldsymbol{I} + \bar{q} \boldsymbol{T}_{\boldsymbol{D}}^{\boldsymbol{e}})}{\partial \boldsymbol{E}} = T_h^e \boldsymbol{I} \otimes \frac{\partial p}{\partial \boldsymbol{E}} + \boldsymbol{T}_{\boldsymbol{D}}^{\boldsymbol{e}} \otimes \frac{\partial \bar{q}}{\partial \boldsymbol{E}} + \mathbb{E}' \tag{7.63}$$

The expression of $\partial \boldsymbol{T}/\partial m$ is:

$$\frac{\partial \boldsymbol{T}}{\partial m} = \frac{\partial (T_h^e p \boldsymbol{I} + \bar{q} \boldsymbol{T_D^e})}{\partial m} = T_h^e \frac{\partial p}{\partial m} \boldsymbol{I} + \frac{\partial \bar{q}}{\partial m} \boldsymbol{T_D^e} \tag{7.64}$$

The expression of $\partial \kappa/\partial \boldsymbol{E}$ is:

$$\frac{\partial \kappa}{\partial \boldsymbol{E}} = \frac{\partial \kappa}{\partial J} \frac{\partial J}{\partial \boldsymbol{E}} + \frac{\partial \kappa}{\partial T_h^e} \frac{\partial T_h^e}{\partial \boldsymbol{E}} + \frac{\partial \kappa}{\partial T_{eq}^e} \frac{\partial T_{eq}^e}{\partial \boldsymbol{E}} = \frac{\partial \bar{\lambda}}{\partial J} \frac{\partial J}{\boldsymbol{E}} + \frac{\partial \bar{\lambda}}{\partial T_h^e} \frac{\partial T_h^e}{\partial \boldsymbol{E}} + \frac{\partial \bar{\lambda}}{\partial T_{eq}^e} \frac{\partial T_{eq}^e}{\partial \boldsymbol{E}} \tag{7.65}$$

The expression of $\partial \kappa/\partial m$ is:

$$\frac{\partial \kappa}{\partial m} = \frac{\partial \kappa}{\partial T_*} \frac{\partial T_*}{\partial m} + \frac{\partial \kappa}{\partial f} \frac{\partial f}{\partial m} + \frac{\partial \kappa}{\partial p} \frac{\partial p}{\partial m} = \frac{\partial \bar{\lambda}}{\partial T_*} \frac{\partial T_*}{\partial m} + \frac{\partial \bar{\lambda}}{\partial f} \frac{\partial f}{\partial m} + \frac{\partial \bar{\lambda}}{\partial p} \frac{\partial p}{\partial m} \tag{7.66}$$

The terms appeared in Equations (7.63)(7.64)(7.65) (7.66) are listed in the following:

- The matrix $\mathbb{E}'$

$$\mathbb{E}' = \begin{pmatrix} \lambda' + 2\mu' & \lambda' + 2\mu' & \lambda' + 2\mu' & 0 & 0 & 0 \\ \lambda' + 2\mu' & \lambda' + 2\mu' & \lambda' + 2\mu' & 0 & 0 & 0 \\ \lambda' + 2\mu' & \lambda' + 2\mu' & \lambda' + 2\mu' & 0 & 0 & 0 \\ 0 & 0 & 0 & 2\mu' & 2\mu' & 2\mu' \\ 0 & 0 & 0 & 2\mu' & 2\mu' & 2\mu' \\ 0 & 0 & 0 & 2\mu' & 2\mu' & 2\mu' \end{pmatrix} \tag{7.67}$$

where $\lambda' = (3pK - 2q\mu)/3, 2\mu' = 2q\mu$ with K bulk modulus and μ shear modulus.

- Function G and its partial derivatives

$$\begin{cases} G = \left(\dfrac{T_{eq}^e q}{T_*}\right)^2 + 2q_1 f^* \cosh\left(\dfrac{3}{2} q_2 \dfrac{T_H^e p}{T^*}\right) - 1 - (q_1 f^*)^2 \\ \dfrac{\partial G}{\partial T_h^e} = 3q_1 q_2 f_* \dfrac{p}{T_*} \sinh\left(\dfrac{3}{2} q_2 \dfrac{T_h^e p}{T_*}\right) \\ \dfrac{\partial G}{\partial T_{eq}^e} = 2\left(\dfrac{q}{T_*}\right)^2 T_{eq}^e \end{cases} \tag{7.68}$$

- Function T_* and its derivatives

$$\begin{cases} \bar{T}_*(\kappa) = J(\bar{\sigma}(\kappa) + r_{nl}\kappa - m) \\ \dfrac{\partial \bar{T}_*}{\partial J} = \bar{\sigma}(\kappa) + r_{nl}\kappa - m \\ \dfrac{\partial \bar{T}_*}{\partial m} = -J \end{cases} \tag{7.69}$$

- Function $\bar{\Lambda}$ and its partial derivatives

$$\begin{cases} \bar{\Lambda} = \Lambda\left(\dfrac{T_h^e p}{T_*}, f\right) \\ \dfrac{\partial \bar{\Lambda}}{\partial T_h^e} = \dfrac{p}{T_*}\dfrac{\partial \Lambda}{\partial x}\left(\dfrac{T_h^e p}{T_*}, f\right) \end{cases} \tag{7.70}$$

- Function $\bar{\Theta}$ and its partial derivatives

$$\begin{cases} \bar{\Theta} = \Theta\left(\dfrac{T_h^e p}{T_*}, \dfrac{T_{eq}^e \bar{q}}{T_*}, f\right) \\ \dfrac{\partial \bar{\Theta}}{\partial T_h^e} = \dfrac{p}{T_*}\dfrac{\partial \Theta}{\partial x}\left(\dfrac{T_h^e p}{T_*}, \dfrac{T_{eq}^e \bar{q}}{T_*}, f\right) + \dfrac{T_{eq}^e}{T_*}\dfrac{\partial \Theta}{\partial y}\left(\dfrac{T_h^e p}{T_*}, \dfrac{T_{eq}^e \bar{q}}{T_*}, f\right)\dfrac{\partial \bar{q}}{\partial T_h^e} \\ \dfrac{\partial \Theta}{\partial T_{eq}^e} = \dfrac{\bar{q}}{T_*}\dfrac{\partial \Theta}{\partial y}\left(\dfrac{T_h^e p}{T_*}, \dfrac{T_{eq}^e \bar{q}}{T_*}, f\right) \end{cases} \tag{7.71}$$

- Function $\bar{q}$ and its partial derivatives

$$\begin{cases} \bar{q} = \dfrac{T_* \bar{\Lambda}}{T_* \bar{\Lambda} + \frac{\mu}{\kappa} T_h^e (1-p)} \\ \dfrac{\partial \bar{q}}{\partial T_h^e} = \dfrac{T_* \dfrac{\partial \bar{\Lambda}}{\partial T_h^e}\left(T_* \bar{\Lambda} + \frac{\mu}{\kappa} T_h^e (1-p)\right) - T_* \bar{\Lambda}\left(T_* \dfrac{\partial \bar{\Lambda}}{\partial T_h^e} + \frac{\mu}{K}(1-p)\right)}{\left(T_* \bar{\Lambda} + \frac{\mu}{\kappa} T_h^e (1-p)\right)^2} \\ \dfrac{\partial \bar{q}}{\partial \boldsymbol{E}} = \dfrac{\partial \bar{q}}{\partial J}\dfrac{\partial J}{\partial \boldsymbol{E}} + \dfrac{\partial \bar{q}}{\partial T_h^e}\dfrac{\partial T_h^e}{\partial \boldsymbol{E}} + \dfrac{\partial \bar{q}}{\partial T_{eq}^e}\dfrac{\partial \bar{q}}{\partial \boldsymbol{E}} = \dfrac{\partial \bar{q}}{\partial T_h^e}\dfrac{\partial T_h^e}{\partial \boldsymbol{E}} \\ \dfrac{\partial \bar{q}}{\partial m} = \dfrac{\partial \bar{q}}{\partial T_*}\dfrac{\partial T_*}{\partial m} + \dfrac{\partial \bar{q}}{\partial p}\dfrac{\partial p}{\partial m} + \dfrac{\partial \bar{q}}{\partial f}\dfrac{\partial f}{\partial m} + \dfrac{\partial \bar{q}}{\partial m} = \dfrac{\partial \bar{q}}{\partial T_*}\dfrac{\partial T_*}{\partial m} + \dfrac{\partial \bar{q}}{\partial p}\dfrac{\partial p}{\partial m} + \dfrac{\partial \bar{q}}{\partial f}\dfrac{\partial f}{\partial m} \end{cases} \tag{7.72}$$

- Function $\bar{\lambda}$ and its partial derivatives

$$\begin{cases} \bar{\lambda} = \dfrac{J T_h^e (1-p)}{3K\bar{\Lambda}\bar{\Theta}} \\ \dfrac{\partial \bar{\lambda}}{\partial T_h^e} = \dfrac{-\frac{J}{3K} T_h^e (1-p)\left(\frac{\partial \bar{\Lambda}}{\partial T_h^e}\bar{\Theta} + \bar{\Lambda}\frac{\partial \bar{\Theta}}{\partial T_h^e}\right) - \frac{J}{3K}(1-p)\bar{\Lambda}\bar{\Theta}}{(\bar{\Lambda}\bar{\Theta})^2} \\ \dfrac{\partial \bar{\lambda}}{\partial T_{eq}^e} = \dfrac{-\frac{J}{3K} T_h^e (1-p)\left(\frac{\partial \bar{\Lambda}}{\partial T_{eq}}\bar{\Theta} + \bar{\Lambda}\frac{\partial \bar{\Theta}}{\partial T_{eq}}\right)}{(\bar{\Lambda}\bar{\Theta})^2} \\ \dfrac{\partial \bar{\lambda}}{\partial J} = \dfrac{T_h^e (1-p)}{3K\bar{\Lambda}\bar{\Theta}} \end{cases} \tag{7.73}$$

- Function $\boldsymbol{v} = \frac{\partial \bar{T}_*}{\partial \boldsymbol{T}}$ and its partial derivatives

$$\begin{cases} \boldsymbol{v} = \bar{\Theta}(\frac{3}{2}\frac{\boldsymbol{T_D}}{T_*} + \bar{\Lambda}\boldsymbol{I}) \\ \frac{\partial \bar{\boldsymbol{v}}}{\partial T_h^e} = \frac{\partial \bar{\Theta}}{\partial T_h^e}\left(\frac{3\boldsymbol{T_D^e}\bar{q}}{2T_*} + \bar{\Lambda}\boldsymbol{I}\right) + \bar{\Theta}\left(\frac{\partial \bar{\Lambda}}{\partial T_h^e}\boldsymbol{I} + \frac{3\boldsymbol{T_D^e}}{2T_*}\frac{\partial \bar{q}}{\partial T_h^e}\right) \\ \frac{\partial \bar{v}}{\partial T_{eq}^e} = \frac{\partial \bar{\Theta}}{\partial T_{eq}^e}\left(\frac{3\boldsymbol{T_D^e}\bar{q}}{2T_*} + \bar{\Lambda}\boldsymbol{I}\right) \end{cases} \tag{7.74}$$

- Function $\bar{N}_g$ and its derivatives

$$\begin{cases} \bar{N}_g(p, T_*, f) = \frac{1-f}{J}\bar{\lambda}(\boldsymbol{v}:\boldsymbol{I}) \\ \frac{\partial \bar{N}_g}{\partial T_h^e}(p, T_*, f) = \frac{1-f}{J}\left(\frac{\partial \bar{\lambda}}{\partial T_h^e}(\boldsymbol{v}:\boldsymbol{I}) + \bar{\lambda}\left(\frac{\partial \boldsymbol{v}}{\partial T_h^e}:\boldsymbol{I}\right)\right) \\ \frac{\partial \bar{N}_g}{\partial T_{eq}^e}(p, T_*, f) = \frac{1-f}{J}\left(\frac{\partial \bar{\lambda}}{\partial T_{eq}^e}(\boldsymbol{v}:\boldsymbol{I}) + \bar{\lambda}\left(\frac{\partial \boldsymbol{v}}{\partial T_{eq}^e}:\boldsymbol{I}\right)\right) \\ \frac{\partial \bar{N}_g}{\partial J}(p, T_*, f) = 0 \end{cases} \tag{7.75}$$

- Function $\bar{N}_n$ and its derivatives ($B_n = B_n\left(\kappa^- + \bar{\lambda}\right)$ and $\frac{\partial \bar{B}_n}{\partial \kappa} = \frac{\partial \bar{B}_n}{\partial \kappa}(\kappa^- + \bar{\lambda})$)

$$\begin{cases} \bar{N}_n = B_n\bar{\lambda} \\ \frac{\partial \bar{N}_n}{\partial T_h^e} = \frac{\partial \bar{\lambda}}{\partial T_h^e}\left(\frac{\partial \bar{B}_n}{\partial \kappa}\bar{\lambda} + \bar{B}_n\right) \\ \frac{\partial \bar{N}_n}{\partial T_{eq}^e} = \frac{\partial \bar{\lambda}}{\partial T_{eq}^e}\left(\frac{\partial \bar{B}_n}{\partial \kappa}\bar{\lambda} + \bar{B}_n\right) \\ \frac{\partial \bar{N}_n}{\partial J} = \frac{\partial \bar{\lambda}}{\partial J}\left(\frac{\partial \bar{B}_n}{\partial \kappa}\bar{\lambda} + \bar{B}_n\right) \end{cases} \tag{7.76}$$

- Function $\bar{G}$ and its partial derivatives

$$\begin{cases} \bar{G} = \left(\frac{T_{eq}^e\bar{q}}{T_*}\right)^2 + 2q_1 f^* \cosh\left(\frac{3}{2}q_2\frac{T_H^e p}{T^*}\right) - 1 - (q_1 f^*)^2 \\ \frac{\partial \bar{G}}{\partial T_h^e} = \frac{\partial G}{\partial T_h^e} + \frac{\partial G}{\partial q}\frac{\partial \bar{q}}{\partial T_h^e} \\ \frac{\partial \bar{G}}{\partial T_{eq}^e} = \frac{\partial G}{\partial T_{eq}^e} + \frac{\partial G}{\partial q}\frac{\partial \bar{q}}{\partial T_{eq}^e} \\ \frac{\partial \bar{G}}{\partial J} = 0 \\ \frac{\partial \bar{G}}{\partial m} = 0 \end{cases} \tag{7.77}$$

- Function $\bar{M}$ and its partial derivatives ($\bar{T}_* = \bar{T}_*(\bar{\lambda})$)

$$\begin{cases} \bar{M} = T_* - \bar{T}_* \\ \dfrac{\partial \bar{M}}{\partial T_h^e} = -\dfrac{\partial \bar{T}}{\partial \kappa}\dfrac{\partial \bar{\lambda}}{\partial T_h^e} \\ \dfrac{\partial \bar{M}}{\partial T_{eq}^e} = -\dfrac{\partial \bar{T}}{\partial \kappa}\dfrac{\partial \bar{\lambda}}{\partial T_{eq}^e} \\ \dfrac{\partial \bar{M}}{\partial J} = -\dfrac{\partial \bar{T}}{\partial \kappa}\dfrac{\partial \bar{\lambda}}{\partial J} - \dfrac{\partial \bar{T}}{\partial J} \\ \dfrac{\partial \bar{M}}{\partial m} = J \end{cases} \tag{7.78}$$

- Function $\bar{N}$ and its partial derivatives

$$\begin{cases} \bar{N} = \Delta f - \bar{N}_g - \bar{N}_n \\ \dfrac{\partial \bar{N}}{\partial T_h^e} = -\left(\dfrac{\partial \bar{N}_g}{\partial T_h^e} + \dfrac{\partial \bar{N}_n}{\partial T_h^e}\right) \\ \dfrac{\partial \bar{N}}{\partial T_{eq}^e} = -\left(\dfrac{\partial \bar{N}_g}{\partial T_{eq}^e} + \dfrac{\partial \bar{N}_n}{\partial T_{eq}^e}\right) \\ \dfrac{\partial \bar{N}}{\partial J} = -\left(\dfrac{\partial \bar{N}_g}{\partial J} + \dfrac{\partial \bar{N}_n}{\partial J}\right) \\ \dfrac{\partial \bar{N}}{\partial m} = 0 \end{cases} \tag{7.79}$$

- Derivatives of p, T_*, f with respect to T_h^e, T_{eq}^e, J, m
  According to the theorem of implicit function, we have

$$\begin{pmatrix} \dfrac{\partial p}{\partial T_h^e} & \dfrac{\partial p}{\partial T_{eq}^e} & \dfrac{\partial p}{\partial J} & \dfrac{\partial p}{\partial m} \\ \dfrac{\partial T_*}{\partial T_h^e} & \dfrac{\partial T_*}{\partial T_{eq}^e} & \dfrac{\partial T_*}{\partial J} & \dfrac{\partial T_*}{\partial m} \\ \dfrac{\partial f}{\partial T_h^e} & \dfrac{\partial f}{\partial T_{eq}^e} & \dfrac{\partial f}{\partial J} & \dfrac{\partial f}{\partial m} \end{pmatrix} = -\mathbb{J}_{\mathrm{R}}^{-1}\mathbb{J}_I \tag{7.80}$$

where $\mathbb{J}_R$ can be found in Equation (7.40) and

$$\mathbb{J}_I = \begin{pmatrix} \dfrac{\partial \bar{G}}{\partial T_h^e} & \dfrac{\partial \bar{G}}{\partial T_{eq}^e} & \dfrac{\partial \bar{G}}{\partial J} & \dfrac{\partial \bar{G}}{\partial m} \\ \dfrac{\partial \bar{M}}{\partial T_h^e} & \dfrac{\partial \bar{M}}{\partial T_{eq}^e} & \dfrac{\partial \bar{M}}{\partial J} & \dfrac{\partial \bar{M}}{\partial m} \\ \dfrac{\partial \bar{N}}{\partial T_h^e} & \dfrac{\partial \bar{N}}{\partial T_{eq}^e} & \dfrac{\partial \bar{N}}{\partial J} & \dfrac{\partial \bar{N}}{\partial m} \end{pmatrix} \tag{7.81}$$

- Derivatives of J, T_h^e, T_{eq}^e with respect to $\boldsymbol{E}$

$$\begin{cases} \dfrac{\partial J}{\partial \boldsymbol{E}} = J\boldsymbol{I} \\ \dfrac{\partial T_h^e}{\partial \boldsymbol{E}} = K\boldsymbol{I} \\ \dfrac{\partial T_{eq}^e}{\partial \boldsymbol{E}} = 3\mu \dfrac{\boldsymbol{T_D^e}}{T_{eq}^e} \end{cases} \tag{7.82}$$

- Derivatives of p with respect to $\boldsymbol{E}$

$$\frac{\partial p}{\partial \boldsymbol{E}} = \frac{\partial p}{\partial J}\frac{\partial J}{\partial \boldsymbol{E}} + \frac{\partial p}{\partial T_h^e}\frac{\partial T_h^e}{\partial \boldsymbol{E}} + \frac{\partial p}{\partial T_{eq}^e}\frac{\partial T_{eq}^e}{\partial \boldsymbol{E}} \tag{7.83}$$

Singularity

In singular case, we have directly:

$$\begin{cases} \dfrac{\partial \boldsymbol{T}}{\partial \boldsymbol{E}} = 0 \\ \dfrac{\partial \boldsymbol{T}}{\partial m} = 0 \\ \dfrac{\partial \kappa}{\partial \boldsymbol{E}} = \dfrac{\partial \kappa}{\partial J}\dfrac{\partial J}{\partial \boldsymbol{E}} = -\dfrac{\partial \bar{T}_*}{\partial J}\left(\dfrac{\partial \bar{T}_*}{\partial \kappa}\right)^{-1}\dfrac{\partial J}{\partial \boldsymbol{E}} \\ \dfrac{\partial \kappa}{\partial m} = -\dfrac{\partial \bar{T}_*}{\partial m}\left(\dfrac{\partial \bar{T}_*}{\partial \kappa}\right)^{-1} \end{cases} \tag{7.84}$$

A5 Numerical stability (small-scale yielding)

In this section, the influence of different numerical parameters on the global response (J resistance curve) is investigated. The *proposed new method*, which is presented in Chapter 4, will be used to compute the crack length Δa. The main numerical parameters involved are: the mesh size in the process zone, the non-local penalty parameter, the incompressibility penalty parameter, two artificial nucleation parameters, the external radius of the boundary layer model and the initial notch radius. The aim of these studies is to choose an appropriate (range of) value(s) for each numerical parameter, then these values will be used in the simulations presented in Chapter 4.

A5.1 Element size

The boundary layer model is spatially meshed. Different element sizes l_e are used to discretize the process zone so as to find out a critical one below which the global response is spatially converged. Figure 7.1 shows the J resistance curves when $l_e \in [0.35l_{nl}, 0.70l_{nl}]$ with l_{nl} the non-local length scale. On the one hand, crack initiation can be well captured for $l_e < 0.63l_{nl}$, on the other hand, the curves overlap for $l_e \leq 0.42l_{nl}$. Thus, it is convenient to take $0.35l_{nl}$ for the mesh size in the process zone for the study of crack propagation. This value is retained in the following study.

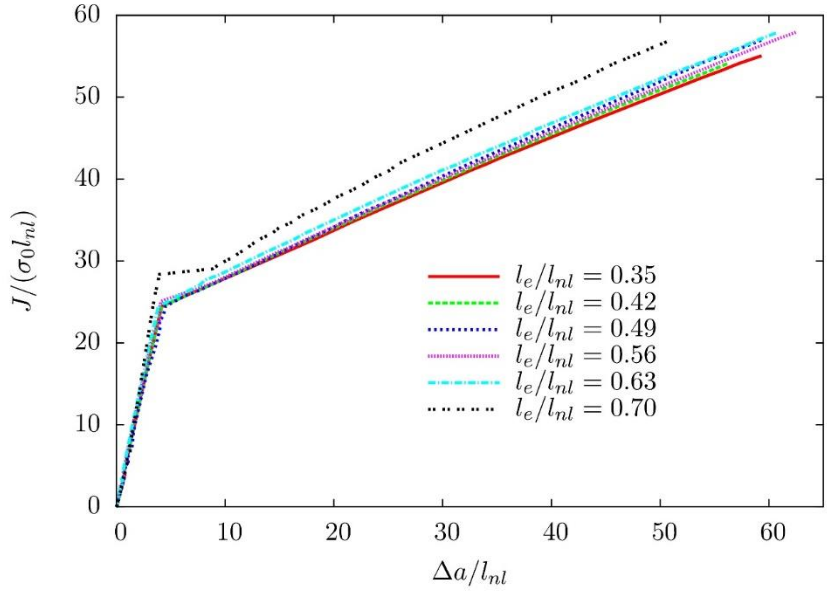

Figure 7.1. J resistance curves for different mesh sizes

A5.2 Nonlocal penalty parameter

As mentioned in Chapter 2, a purely numerical parameter r_{nl} is introduced in the non-local discretized formulation to enforce the equality between a and κ. Obviously, the value of r_{nl} should not be too small, otherwise, its effect becomes negligible. (Zhang et al., 2018) observed oscillations on the κ field when r_{nl} is not large enough in spite of the effect of the Lagrange multiplier l. On the contrary, one can take any large value for r_{nl} as it will not affect the computational precision on $a - \kappa$.

Since the influence of r_{nl} on local responses has already been studied in the work of (Zhang et al., 2018), we only focus on the influence of r_{nl} on the J resistance curves. Four values of r_{nl} ($r_{nl}/\sigma_0 = 0.1, 1, 10, 100$) are studied and no difference is found among the corresponding J resistance curves. It can be concluded that the value of r_{nl} does not affect the global response. In view of the local/global response and the computational convergence, the value of r_{nl}/σ_0 is set to 10 from now on.

A5.3 Incompressibility penalty parameter

In the locking-free mixed element formulation, we also added a purely numerical parameter r_{inco} to add a control on the value of $\theta - tr(\boldsymbol{E})$ through a penalty. Its effects on global and local responses are studied in this part.

Five values of r_{inco} ($r_{inco}/\sigma_0 = 0, 0.1, 1, 10, 100$) are used to perform the simulations. No difference is found among the corresponding J resistance curves. Figure 7.2 plots the porosity (f) profile along the ligament in the deformed configuration at a load level of $J/(\sigma_0 l_{nl}) \approx 28$. Spurious oscillations of f are observed for $r_{inco}/\sigma_0 = 0$ and $r_{inco}/\sigma_0 = 0.1$, they disappear for larger values of r_{inco}. Figure 7.3 plots the field of the crack opening stress σ_{yy} for different r_{inco}. It can be observed that stress oscillations are very important in case of $r_{inco}/\sigma_0 = 100$, especially in the initial crack tip nearby zone. They are much less pronounced for small values of r_{inco}. In view of the local/global responses, r_{inco} should not be too small neither too large since on the one hand, a too small value for r_{inco} can lead to an incorrect local response (for instance the f field in our case) and can hinder the computational convergence, on the other hand, a too large value for r_{inco} prescribes $\theta - tr(\mathbf{E}) \approx 0$ at each integration point, resulting in volumetric locking again. In the following study, the value of r_{inco}/σ_0 is set to 10.

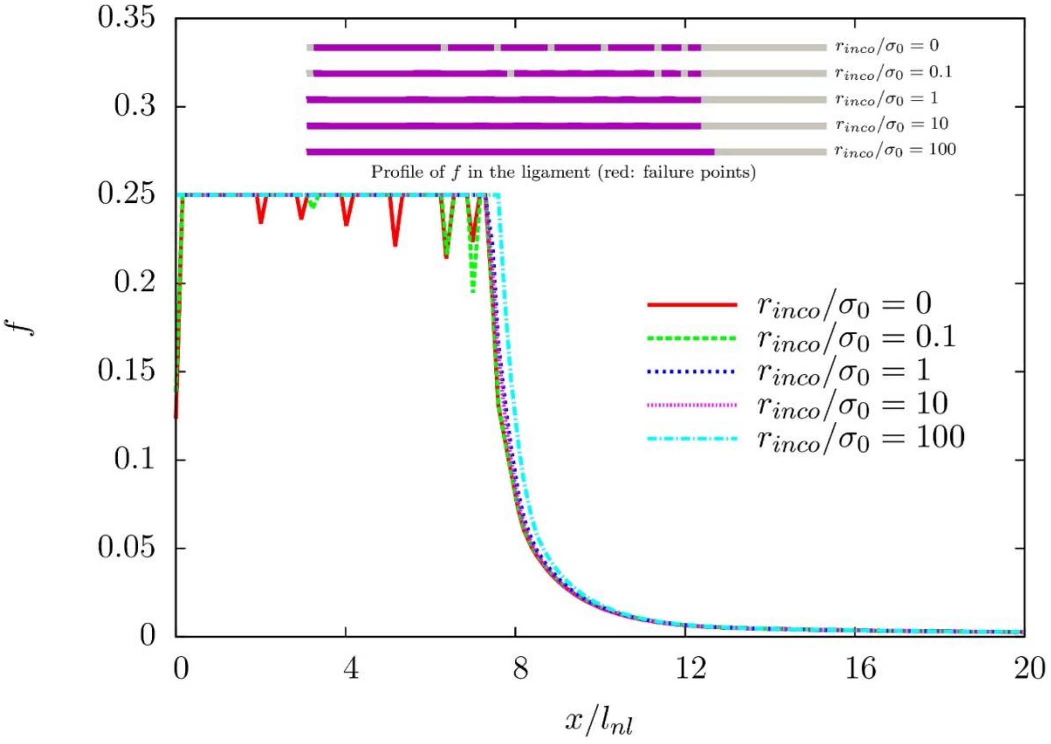

Figure 7.2. Evolution of porosity f in the ligament for different r_{inco} when $J/(\sigma_0 l_{nl}) \approx 28$

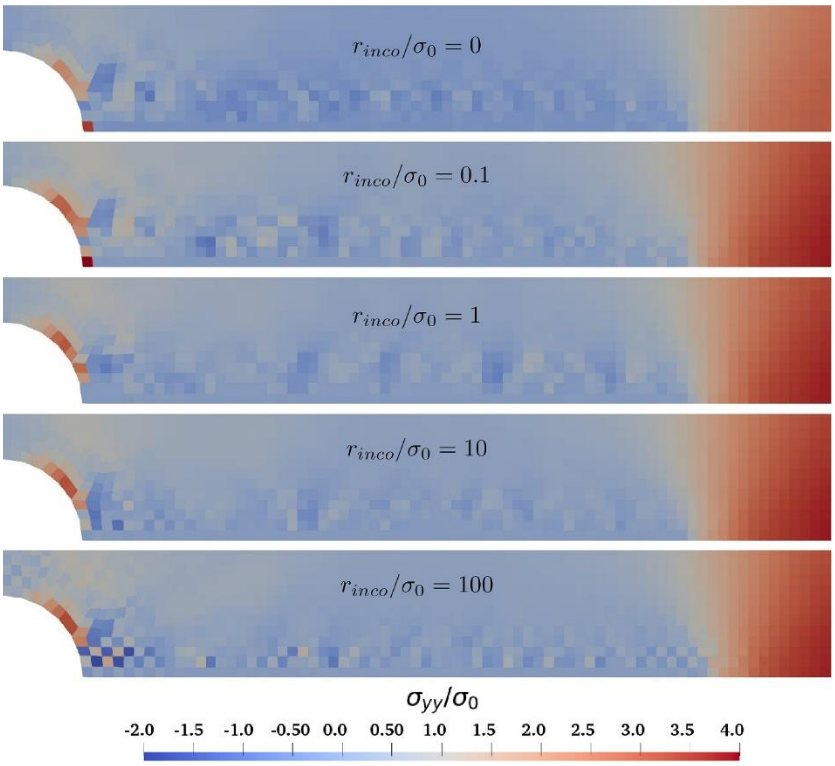

Figure 7.3. Crack opening stress field for different r_{inco} *when* $J/(\sigma_0 l_{nl}) \approx 28$

A5.4 External radius

As said before, small-scale yielding condition requires that the size of the plastic zone R_p be much smaller than the outer radius R_{ext} ($R_{ext}\ /R_p \geq\ 20$) . To check this requirement and choose a convenient value for R_{ext}, we set a value for the maximal load level $J/\sigma_0 l_{nl} \approx 58$. In this case, the final size of the plastic zone is $R_p \approx 2700 l_{nl}$. Five values of R_{ext} are studied ($R_{ext}/R_p\ =\ 0.25, 2.5, 25, 250, 2500$). Figure 7.4 shows the J resistance curves for different R_{ext}. The global response does not depend on the value of R_{ext} for $R_{ext}/R_p \geq 25$. On the contrary, for $R_{ext}/R_p < 25$, the curve becomes steeper and steeper with the decrease of R_{ext} as the small-scale yielding condition is not fulfilled anymore. Therefore, in the following study, in order to respect the SSY condition, R_{ext}/R_p is set to 25 with R_p is obtained at maximal load level.

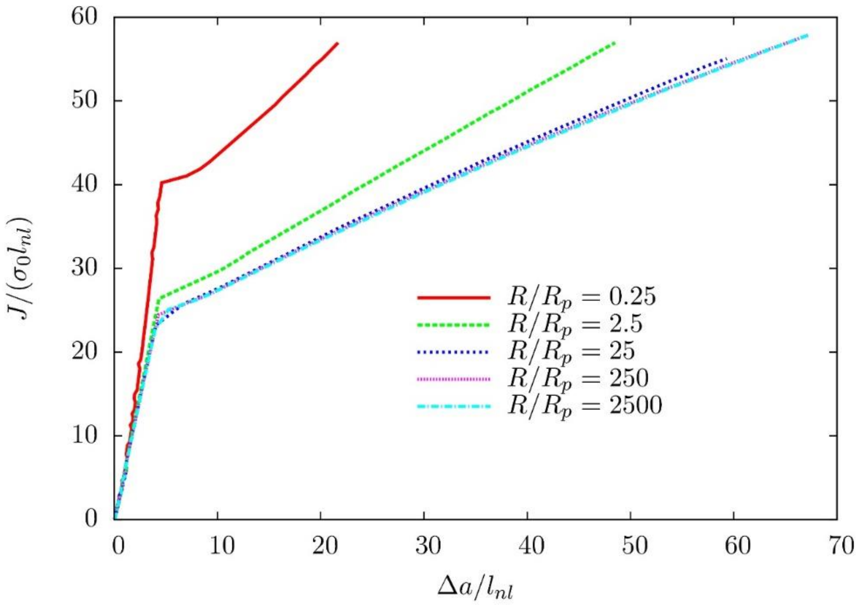

Figure 7.4. . J resistance curve for different R_{ext}

A5.5 Initial notch radius

As stated in (Hütter et al., 2013), pure crack tip blunting is expected in the initial stage of loading, this phenomenon leads to element distortion (Linse et al., 2012; M. Samal et al., 2008a, 2008b). To overcome this difficulty, (McMeeking, 1977) suggested to introduce an initial notch radius R_n at the crack. This study showed that the introduction of R_n only has little influence on the final results provided that $\delta/R_n \geq 5$ (where δ is the crack tip blunting radius) as the theoretical solution for an ideal sharp crack tip can be obtained for this condition. This conclusion will be shown again in this part with a mesh size much smaller than that in the work of (McMeeking, 1977).

Unlike in the other sections where the GTN damage law is used, the von-Mises law is used in this part, following the work of (McMeeking, 1977). Several initial notch radii R_n are studied: $R_n/l_{nl} = 1.4, 2.1, 2.8, 3.5$.

The evolution of the maximum opening stress in the ligament σ_{yy}^{max} as a function of δ/R_n is illustrated in Figure 7.5(a). This figure shows that an asymptotic value is reached when $\delta/R_n \approx 8$. This conclusion is in accordance with (McMeeking, 1977) as the asymptotic value is almost reached for $\delta/R_n \geq 5$. In addition, σ_{yy}^{max} belongs to the range from $4\sigma_0$ to $5\sigma_0$, a value increasing with the hardening level n. This observation agrees with the result obtained in (McMeeking and Parks, 1979), who applied the slip line theory to estimate the stresses under plane-strain small-scale yielding conditions.

However, it is observed that the stress tends to a very large value at the initial crack tip. This problem will be analyzed in the next part. In Figure 7.5(a), the stress in the vicinity of the crack tip was not accounted for.

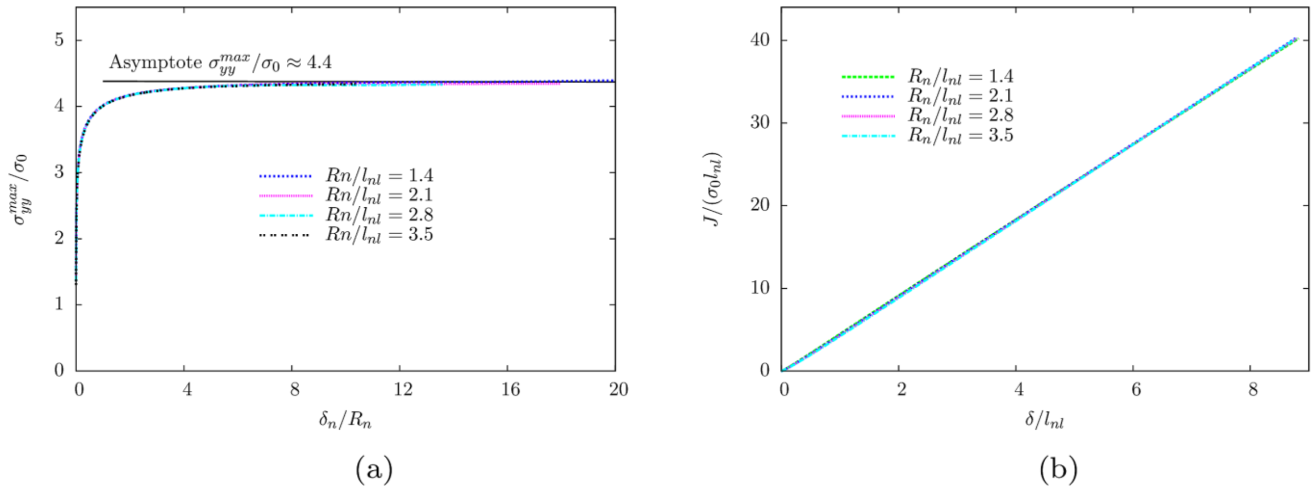

Figure 7.5. (a) Evolution of the maximum opening stress in the ligament; (b) J-δ curves

A5.6 Additional void nucleation

In this part, a special attention is paid to the spurious and extremely high crack opening stress in the vicinity of the initial crack tip, as mentioned in the previous part. It is observed that the crack opening stress at the initial crack tip is large compared to that at other positions when von-Mises law is used. This result is due to the very high gradient of plastic deformation which causes additional hardening in the yield function ($c\Delta\kappa$). The same problem can be found with the use of the GTN model when strain nucleation is not active. In addition, the material point (in the ligament) located at the initial crack tip never fails. This is mainly related to the low triaxiality at the initial crack tip. To illustrate it, a simulation without void nucleation is performed using the GTN damage model. Figure 7.6(a) plots the evolution of the extended triaxiality $T_r = T_H/T^*$ against the equivalent plastic strain defined as $E_{eq}^p = \sqrt{2/3\boldsymbol{E^p}:\boldsymbol{E^p}}$ (including both volumetric and deviatoric parts) at four material points near the crack tip. It shows that at the beginning of loading, triaxiality is very low at the material point located just against the crack tip ($X = 0.07l_{nl}$) and it increases along the ligament. Figure 7.6(b) plots the hardening variable κ against the equivalent plastic strain E_{eq}^p, it indicates that:

- Within a certain range for E_{eq}^p, the equivalent plastic strain E_{eq}^p is very close to the hardening variable κ.
- For the material point which never fails at the end of loading ($X = 0.07l_{nl}$), κ increases much more slowly than E_{eq}^p when $\mathrm{E}_{\mathrm{eq}}^{\mathrm{p}} > 2.3$.
- For the material points near the initial crack tip, the deformation level at fracture decreases along the ligament.

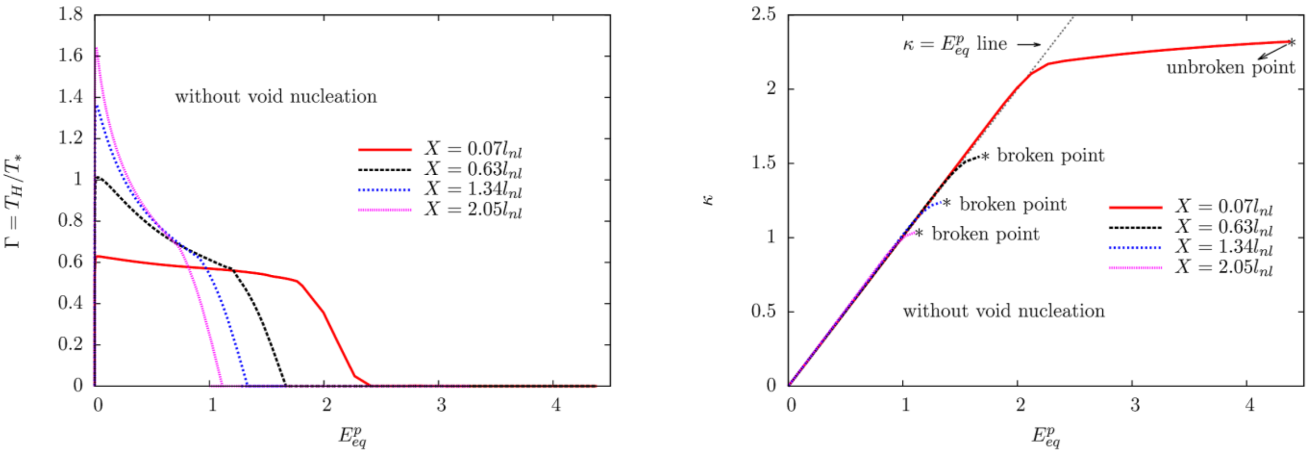

(a) (b)

Figure 7.6. Evolution of (a) the extended triaxiality ; (b) the hardening variable κ *as a function of equivalent plastic strain* E_{eq}^p *for the materials points located at X in the ligament when* $J/(\sigma_0 l_{nl}) \approx 58$

In some cases, for example when an element deletion technique is used, it is imperative that all the material points located in front of the current crack tip in the ligament be in failure. Indeed, with an element deletion technique, elements are removed when the necessary condition for element deletion is met, which would be for instance $f = f_F$ for all material points of an element. So it is interesting to introduce an artificial void nucleation $f_{n,a}$. As regards the form of $f_{n,a}$, a very simple formulation is used as below:

$$f_{n,a} = \begin{cases} 0 & \text{if } E_{eq}^p < E_{eq,c}^p \\ b_0(E_{eq}^p - E_{eq,c}^p) & \text{otherwise} \end{cases} \tag{7.85}$$

where b_0 is a constant and $E_{eq,c}^p$ is the critical equivalent plastic strain. Note that instead of using κ, we use E_{eq}^p as the argument of the function $f_{n,a}$ since κ is likely to be bounded, as shown in Figure 7.6(b).

This formulation enables the material point near the crack tip to locally fail. Attention should be paid to the choice of b_0 and $E_{eq,c}^p$. The coefficient b_0 should be large enough so that the material points can quickly fail and the deformation of the element containing these points would not be too large. Regarding $E_{eq,c}^p$, on the one hand, it should not be too small, otherwise other undesired points may fail and the crack path may be physically incorrect; on the other hand, it should not be too large as the deformation of the desired point may be too large before its failure.

In order to check whether the artificial nucleation affects the global material response, three complementary simulations are performed with $E_{eq,c}^p = 100\%, 200\%, 300\%$ and with the same value $b_0 = 0.25$. The case without nucleation can be seen as $b_0 = 0.25, E_{eq,c}^p = \infty$. No significant discrepancy has been observed. In this paper, we set $b_0 = 0.25$ and $E_{eq,c}^p = 2$.

A6 Influence of initial porosity and stress triaxiality on critical porosity

In this part, we aims at studying the effects of stress triaxiality T_r and the initial porosity f_0 on the critical porosity f_c using the simulations of the representative material volume element RVE.

It is assumed that the solid is made of an array of cylindrical unit cells. Each unit cell is considered as a RVE of initial height $2H_0$ and initial radius $2L_0$ containing a spherical void of radius R_0. The initial porosity is thus $f_0 = 2R_0^3/3H_0L_0^2$.

A6.1 Constant triaxiality

In order to study the effect of the triaxiality T_r on the critical porosity f_c, it is necessary to know how to prescribe a constant triaxiality to RVE.

It is assumed that the deformed boundaries of RVE remain parallel to the undeformed boundaries. Under this assumption, the macroscopic logarithmic principal strains and effective strain are given by:

$$E_x = E_z = \ln\left(\frac{L}{L_0}\right), \qquad E_y = \ln\left(\frac{H}{H_0}\right), \qquad E_e = \frac{2}{3}|E_y - E_x| \tag{7.86}$$

where H is the current height and L is the current radius of RVE. The stresses conjugate to (E_x, E_y, E_z) are $(\Sigma_x, \Sigma_y, \Sigma_z)$. These stresses represent the average reaction forces per unit area of the deformed cell boundary. It can be demonstrated that the hydrostatic stress Σ_h and the effective stress Σ_e are:

$$\Sigma_h = \frac{1}{3}\left(\Sigma_y + 2\Sigma_x\right);\ \Sigma_e = |\Sigma_y - \Sigma_x| \tag{7.87}$$

The stress triaxiality is:

$$T = \frac{\Sigma_h}{\Sigma_e} = \frac{\Sigma_y + 2\Sigma_x}{3|\Sigma_y - \Sigma_x|} = \frac{1 + 2\rho}{3|1 - \rho|} \ \text{ with } \rho = \frac{\Sigma_x}{\Sigma_y} \tag{7.88}$$

If F_x denotes the resultant of all traction t_x acting on the lateral surface of RVE and F_y the resultant of all traction t_y acting on the top surface, according to (Lin et al., 2006), we have

$$\Sigma_y = \frac{2\pi L t_y}{\pi L^2} = \frac{F_y}{\pi L^2}, \qquad \Sigma_x = \Sigma_z = \frac{2\pi L t_x}{2\pi H L} = \frac{F_x}{2\pi H L} \tag{7.89}$$

Note that all shear stress components on RVE are zero to keep symmetry conditions and uniform deformation on RVE's surfaces. According to (Lin et al., 2006), replacing the edge traction t_x and t_y by the axial and radial tractions, T_x and T_y, distributed uniformly on the top and the lateral surfaces, we have:

$$\Sigma_y = T_y, \qquad \Sigma_x = \Sigma_z = T_x \tag{7.90}$$

These relations are quite useful for the traction control technique for constant triaxiality (Lin et al., 2006). This strategy is set up by prescribing the dependency between the uniform radial and axial tractions acted on the lateral and top surfaces, respectively. That is to say, uniform radial and axial tractions should be prescribed such that $\rho = \Sigma_x/\Sigma_y$ remains constant during the loading history.

A6.2 Numerical strategy

Mesh and boundary conditions

The RVE considered here has the same initial height and radius ($H_0 = L_0$). The axisymmetric modeling is considered. The mesh consists of 480 quadrilateral, axisymmetric elements (with reduced integration) of which 24 elements are located around the void and 20 in the radial direction.

In our work, we slightly modify the traction control technique introduced in (Lin et al., 2006). Here, the constant triaxiality is piloted by the displacement u_{AB}. The tractions T_y and T_x are always respectively $T_y = a\cos(\arctan(\rho))$ and $T_x = a\sin(\arctan(\rho))$ with a a value changing with u_{AB}. This technique is called "PILOTAGE" in Code_Aster. Besides, the deformation of AB, as well as the deformation of BC are uniform. One can refer to Figure 7.7 for more detail.

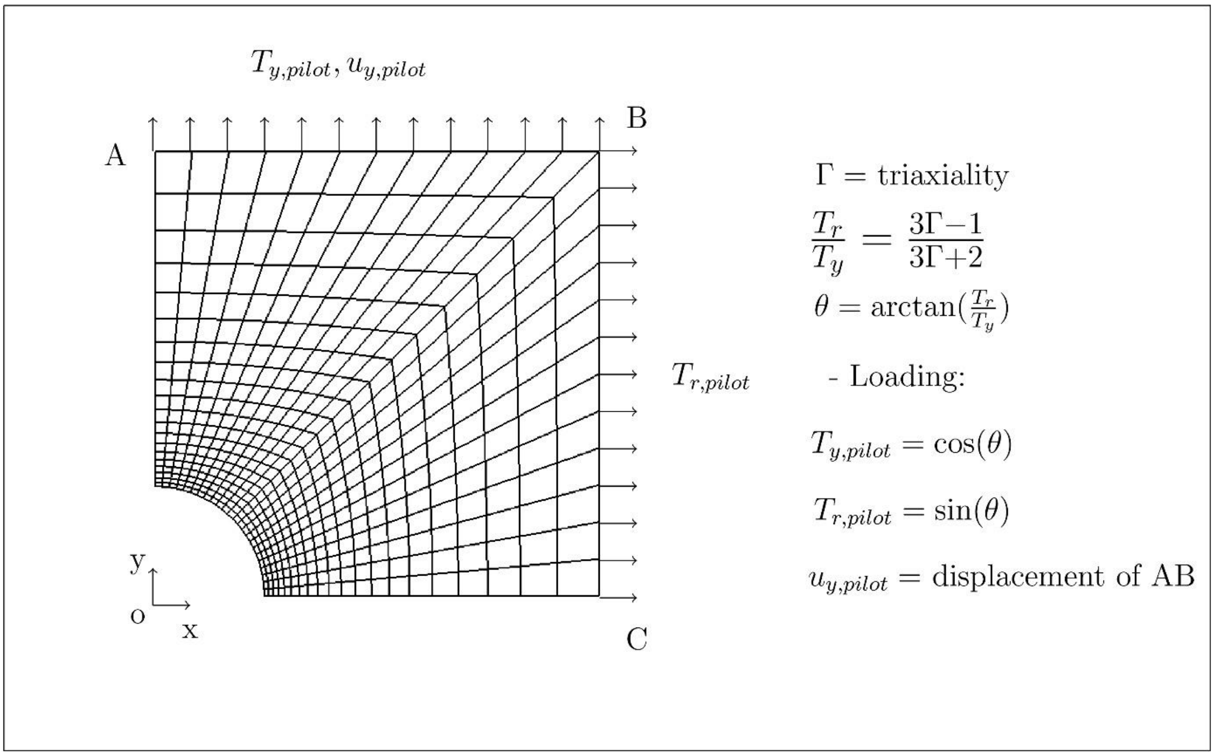

Figure 7.7. Mesh and boundary/loading conditions of RVE

Material properties

The numerical analyses use the standard von-Mises constitutive model following J_2 flow theory. The material is supposed to obey an isotropic hardening (Zhang, 2016):

$$\bar{\sigma}(\kappa) = 545 + 239(1 - e^{-10.3\kappa}) \tag{7.91}$$

For the initial porosity and the stress triaxiality, the following combinations have been investigated.

- $f_0 = 10^{-3}, 5 \times 10^{-3}, 10^{-2}$
- $T_r = 0.7, 0.8, 0.9, 1.0, 1.3, 1.5, 2.0, 2.5, 3.0$

The value of f_0 and T_r cover the range of the initial porosity and the triaxiality in common structural applications.

The current porosity f of RVE can be computed via the condition of plastic incompressibility of the material surrounding the void (Koplik and Needleman, 1988):

$$f = 1 - (1 - f_0)\frac{V_0}{V}\left(1 + \frac{3(1 - 2\nu)}{E}\Sigma_h\right) \tag{7.92}$$

where V_0 and V represent the initial and current volume of RVE.

A6.3 Results

Figure 7.8(a) shows the evolution of the radial stretch $\Delta L/L_0$ with increasing macroscopic effective strain E_e in the case of $f_0 = 0.001, T_r = 3$. It is observed that $\Delta L/L_0$ increases at the beginning since the effect of T_r is larger than the Poisson effect[11] induced by T_y. Then, $\Delta L/L_0$ decreases since the material is assumed to be incompressible. Finally, it becomes a constant which indicates that further deformation takes place in a uniaxial straining mode. This shift to a macroscopic uniaxial strain state indicates the onset of void coalescence.

Figure 7.8(b) shows the corresponding variation of dL/dE_e (i.e., slope of Figure 7.8(a)) with E_e. The critical effective strain E_c is defined as the value of E_e corresponding to $\min_{dL/dE_e=0} E_e$. The corresponding effective stress is T_c and the corresponding porosity is f_c.

These results are in line with the results obtained in (Kim et al., 2004).

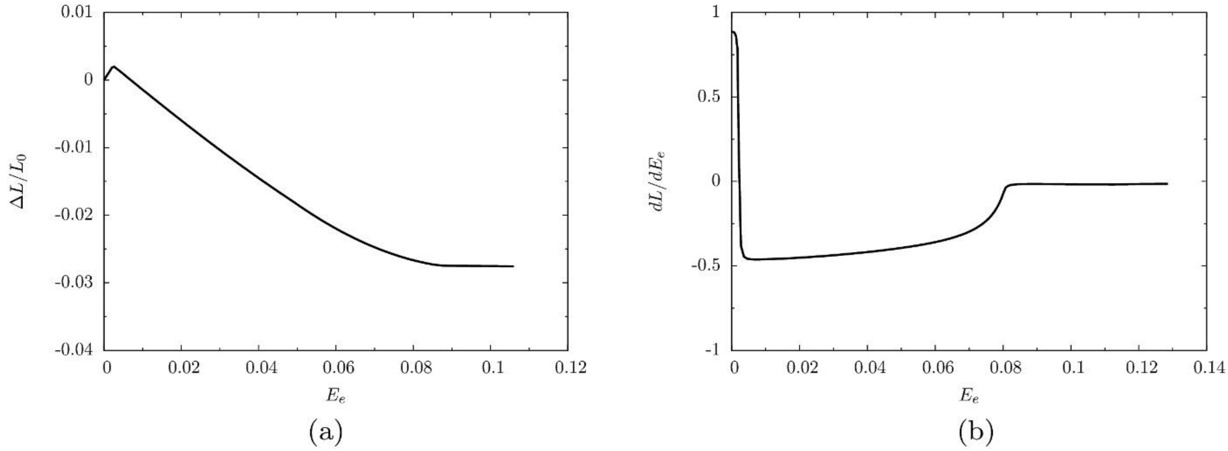

Figure 7.8. (a) Evolution of the radial stretch with equivalent strain; (b) Evolution of dL/dE_{eq} with Ee ($f_0 = 0.001, \Gamma = 3$)

Figure 7.9(a) plots the macroscopic effective stress-strain curve for $f_0 = 0.001$. The competition between strain hardening and porosity-induced softening are clearly illustrated in this figure. The effective stress decreases when the softening is dominant. A rapid drop on T_e is observed once E_e reaches its critical value E_c. Figure 7.9(b) shows the evolution of the porosity f with E_e. It can be seen that f_c depends on Γ.

---

[11] Poisson effect: the phenomenon in which a material tends to expand in directions perpendicular to the direction of compression. Poisson ratio is a measure of the Poisson effect.

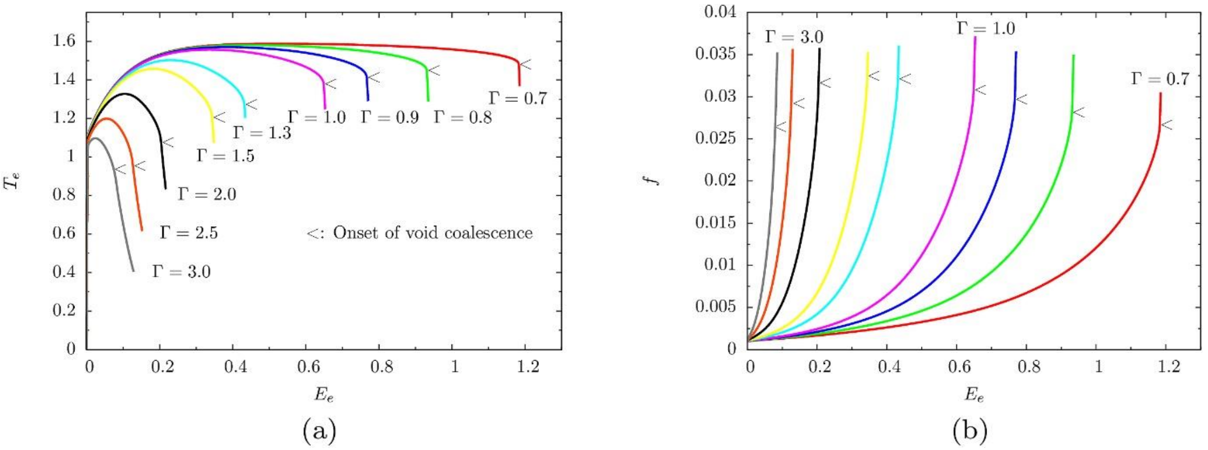

(a) (b)

Figure 7.9. (a) Macroscopic effective stress-strain curve ($f_0 = 0.001$*); (b) Evolution of the porosity with* E_{eq} *(*$f_0 = 0.001$*)*

Similar results were obtained for $f_0 = 0.005$ and 0.01. Figure 7.10 shows the evolution of f_c with the stress triaxiality T_r for different f_0. It can be seen that an increase of T_r leads to an increase of f_c at low triaxiality level and a decrease of f_c at other triaxiality level. Besides, the value of f_c increases with f_0 for a given $T_r s$.

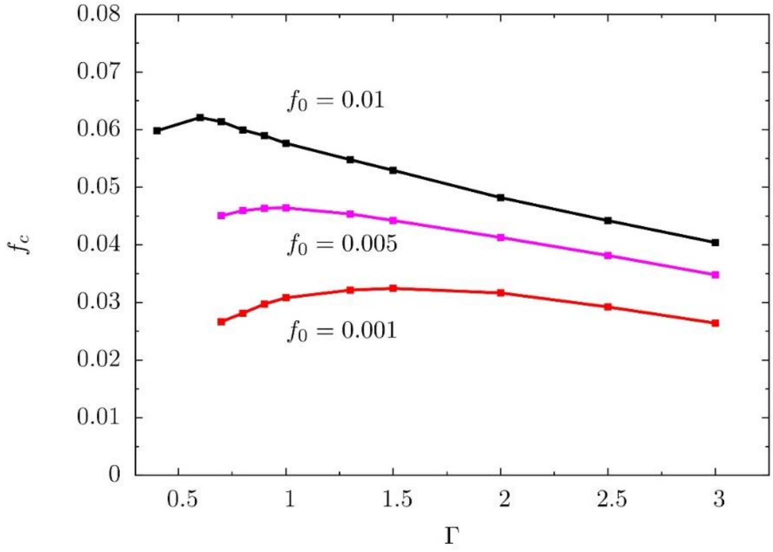

Figure 7.10. Effects of T_r *and* f_0 *on* f_c

Reference

Abbas, M., Ern, A., Pignet, N., 2019a. A Hybrid High-Order method for finite elastoplastic deformations within a logarithmic strain framework.

Abbas, M., Ern, A., Pignet, N., 2019b. A Hybrid High-Order method for incremental associative plasticity with small deformations. Comput. Methods Appl. Mech. Eng. 346, 891–912. https://doi.org/10.1016/j.cma.2018.08.037

Abbas, M., Ern, A., Pignet, N., 2018. Hybrid High-Order methods for finite deformations of hyperelastic materials. Comput. Mech. 62, 909–928. https://doi.org/10.1007/s00466-018-1538-0

Al Akhrass, D., Bruchon, J., Drapier, S., Fayolle, S., 2014. Integrating a logarithmic-strain based hyperelastic formulation into a three-field mixed finite element formulation to deal with incompressibility in finite-strain elastoplasticity. Finite Elem. Anal. Des. 86, 61–70.

Aldakheel, F., 2016. Mechanics of nonlocal dissipative solids: gradient plasticity and phase field modeling of ductile fracture.

Aldakheel, F., Wriggers, P., Miehe, C., 2018. A modified Gurson-type plasticity model at finite strains: formulation, numerical analysis and phase-field coupling. Comput. Mech. 62, 815–833. https://doi.org/10.1007/s00466-017-1530-0

Alessi, R., 2018. Coupling damage and plasticity for a phase-field regularisation of brittle, cohesive and ductile fracture: One-dimensional examples. Int. J. Mech. Sci. 18.

Alessi, R., Ambati, M., Gerasimov, T., Vidoli, S., De Lorenzis, L., 2018. Comparison of phase-field models of fracture coupled with plasticity, in: Advances in Computational Plasticity. Springer, pp. 1–21.

Allix, O., 2013. The bounded rate concept: A framework to deal with objective failure predictions in dynamic within a local constitutive model. Int. J. Damage Mech. 22, 808–828. https://doi.org/10.1177/1056789512468355

Allix, O., Feissel, P., Thévenet, P., 2003. A delay damage mesomodel of laminates under dynamic loading: basic aspects and identification issues. Comput. Struct. 81, 1177–1191. https://doi.org/10.1016/S0045-7949(03)00035-X

Ambati, 2016. A phase-field model for ductile fracture at finite strains and its experimental verification. Comput Mech 19.

Ambati, 2015. Phase-field modeling of ductile fracture. Comput Mech 24.

Ambrosio, L., Tortorelli, V.M., 1990. Approximation of functional depending on jumps by elliptic functional via t-convergence. Commun. Pure Appl. Math. 43, 999–1036.

Anderson, T.L., 2017. Fracture mechanics: fundamentals and applications. CRC press.

Andrade, F., de Sá, J.C., Pires, F.A., 2014. Assessment and comparison of non-local integral models for ductile damage. Int. J. Damage Mech. 23, 261–296. https://doi.org/10.1177/1056789513493103

Areias, P.M.A., Belytschko, T., 2005. Analysis of three-dimensional crack initiation and propagation using the extended finite element method. Int. J. Numer. Methods Eng. 63, 760–788. https://doi.org/10.1002/nme.1305

Auricchio, F., Beirão da Veiga, L., Lovadina, C., Reali, A., Taylor, R.L., Wriggers, P., 2013. Approximation of incompressible large deformation elastic problems: some unresolved issues. Comput. Mech. 52, 1153–1167. https://doi.org/10.1007/s00466-013-0869-0

Badel, P., Lorentz, E., 2011. Critères de convergence en mécanique des solides, in: 10e Colloque National En Calcul Des Structures. p. Clé–USB.

Bazant, Z.P., Belytschko, T.B., Chang, T.-P., others, 1984. Continuum theory for strain-softening. J. Eng. Mech. 110, 1666–1692.

Bazant, Z.P., Pijaudier-Cabot, G., 1988. Nonlocal continuum damage, localization instability and convergence. J. Appl. Mech. 55, 287–293.

Beachem, C., Yoder, G., 1973. Elastic-plastic fracture by homogeneous microvoid coalescence tearing along alternating shear planes. Metall. Trans. 4, 1145–1153.

Becker, R., Smelser, R., Richmond, O., 1989. The effect of void shape on the development of damage and fracture in plane-strain tension. J. Mech. Phys. Solids 37, 111–129.

Benallal, A., Billardon, R., Geymonat, G., 1993. Bifurcation and localization in rate-independent materials. Some general considerations, in: Bifurcation and Stability of Dissipative Systems. Springer, pp. 1–44.

Benzerga, A.A., 2002. Micromechanics of coalescence in ductile fracture. J. Mech. Phys. Solids 50, 1331–1362.

Benzerga, A.A., Besson, J., 2001. Plastic potentials for anisotropic porous solids. Eur. J. Mech.-ASolids 20, 397–434.

Bergheau, J.-M., Leblond, J.-B., Perrin, G., 2014. A new numerical implementation of a second-gradient model for plastic porous solids, with an application to the simulation of ductile rupture tests. Comput. Methods Appl. Mech. Eng. 268, 105–125.

Besson, J., 2010. Continuum models of ductile fracture: a review. Int. J. Damage Mech. 19, 3–52.

Besson, J., 2009. Damage of ductile materials deforming under multiple plastic or viscoplastic mechanisms. Int. J. Plast. 25, 2204–2221.

Besson, J., McCowan, C., Drexler, E., 2013. Modeling flat to slant fracture transition using the computational cell methodology. Eng. Fract. Mech. 104, 80–95.

Besson, J., Moinereau, D., Steglich, D., 2006. Local approach to fracture. Presses des MINES.

Besson, J., Steglich, D., Brocks, W., 2003. Modeling of plane strain ductile rupture. Int. J. Plast. 19, 1517–1541.

Besson, J., Steglich, D., Brocks, W., 2001. Modeling of crack growth in round bars and plane strain specimens. Int. J. Solids Struct. 38, 8259–8284.

Billardon, R., Doghri, I., 1989. Prediction of macrocrack initiation by damage localization. Acad. Sci. Comptes Rendus Ser. II-Mec. Phys. Chim. Sci. Univers Sci. Terre 308, 347–352.

Borden, M.J., Hughes, T.J.R., Landis, C.M., Anvari, A., Lee, I.J., 2016. A phase-field formulation for fracture in ductile materials: Finite deformation balance law derivation, plastic degradation, and stress triaxiality effects. Comput Methods Appl Mech Engrg 37.

Boroomand, B., Zienkiewicz, O., 1999. Recovery procedures in error estimation and adaptivity. Part II: Adaptivity in nonlinear problems of elasto-plasticity behaviour. Comput. Methods Appl. Mech. Eng. 176, 127–146.

Bourdin, B., Francfort, G.A., Marigo, J.-J., 2000. Numerical experiments in revisited brittle fracture. J. Mech. Phys. Solids 48, 797–826.

Brach, S., Tanné, E., Bourdin, B., Bhattacharya, K., 2019. Phase-field study of crack nucleation and propagation in elastic–perfectly plastic bodies. Comput. Methods Appl. Mech. Eng. 353, 44–65.

Brepols, T., Wulfinghoff, S., Reese, S., 2017. Gradient-extended two-surface damage-plasticity: Micromorphic formulation and numerical aspects. Int. J. Plast. 97, 64–106.

Brink, U., Stein, E., 1996. On some mixed finite element methods for incompressible and nearly incompressible finite elasticity. Comput. Mech. 19, 105–119.

Bron, F., Besson, J., 2004. A yield function for anisotropic materials application to aluminum alloys. Int. J. Plast. 20, 937–963.

Brown, L., Embury, J., 1973. Initiation and growth of voids at second-phase particles, in: Proc. Conf. on Microstructure and Design of Alloys, Institute of Metals and Iron and Steel Insitute, London. 1973, 1,(33), 164-169.

Brünig, M., 1999. Formulation and numerical treatment of incompressibility constraints in large strain elastic–plastic analysis. Int. J. Numer. Methods Eng. 45, 1047–1068.

Budiansky, B., Hutchinson, J., Slutsky, S., 1982. Void growth and collapse in viscous solids, in: Mechanics of Solids. Elsevier, pp. 13–45.

Cao, T.-S., 2014. Numerical simulation of 3D ductile cracks formation using recent improved Lode-dependent plasticity and damage models combined with remeshing. Int. J. Solids Struct. 51, 2370–2381.

Cao, T.-S., Montmitonnet, P., Bouchard, P.-O., 2013. A detailed description of the Gurson-Tvergaard-Needleman model within a mixed velocity-pressure finite element formulation: GTN MODEL IMPLEMENTATION IN MIXED VELOCITY-PRESSURE FE FORMULATION. Int. J. Numer. Methods Eng. 96, 561–583.

Carroll, W., Barker, R., 1973. A theorem for optimum finite-element idealizations. Int. J. Solids Struct. 9, 883–895.

Cazacu, O., Revil-Baudard, B., Chandola, N., Kondo, D., 2014. New analytical criterion for porous solids with Tresca matrix under axisymmetric loadings. Int. J. Solids Struct. 51, 861–874.

Cazacu, O., Stewart, J.B., 2009. Analytic plastic potential for porous aggregates with matrix exhibiting tension–compression asymmetry. J. Mech. Phys. Solids 57, 325–341.

Cervera, M., Chiumenti, M., Codina, R., 2010. Mixed stabilized finite element methods in nonlinear solid mechanics: Part i: Formulation. Comput. Methods Appl. Mech. Eng. 199, 2559–2570.

Chen, Y., Zhang, C., Varé, C., 2017. An extended GTN model for indentation-induced damage. Comput. Mater. Sci. 128, 229–235.

Chu, C., Needleman, A., 1980. Void nucleation effects in biaxially stretched sheets. J. Eng. Mater. Technol. 102, 249–256.

Crouzeix, M., Mignot, A.L., 1984. Analyse numérique des équations différentielles. Masson.

Dally, J., Sanford, R., 1987. Strain-gage methods for measuring the opening-mode stress-intensity factor, K I. Exp. Mech. 27, 381–388.

Danas, K., Aravas, N., 2012. Numerical modeling of elasto-plastic porous materials with void shape effects at finite deformations. Compos. Part B Eng. 43, 2544–2559.

De Borst, R., Mühlhaus, H.-B., 1992. Gradient-dependent plasticity: formulation and algorithmic aspects. Int. J. Numer. Methods Eng. 35, 521–539.

de Souza Neto, E., Perić, D., Dutko, M., Owen, D., 1996. Design of simple low order finite elements for large strain analysis of nearly incompressible solids. Int. J. Solids Struct. 33, 3277–3296.

de Souza Neto, E.A., Peric, D., Owen, D.R., 2011. Computational methods for plasticity: theory and applications. John Wiley & Sons.

Desmorat, R., Gatuingt, F. (Eds.), 2007. Introduction of an internal time in nonlocal integral theories. CRC Press. https://doi.org/10.1201/b10546

Di Luzio, G., Bažant, Z.P., 2005. Spectral analysis of localization in nonlocal and over-nonlocal materials with softening plasticity or damage. Int. J. Solids Struct. 42, 6071–6100.

Di Pietro, D.A., Ern, A., 2015. A hybrid high-order locking-free method for linear elasticity on general meshes. Comput. Methods Appl. Mech. Eng. 283, 1–21.

Di Pietro, D.A., Ern, A., Lemaire, S., 2014. An arbitrary-order and compact-stencil discretization of diffusion on general meshes based on local reconstruction operators. Comput. Methods Appl. Math. 14, 461–472.

Diamantopoulou, E., Liu, W., Labergere, C., Badreddine, H., Saanouni, K., Hu, P., 2017. Micromorphic constitutive equations with damage applied to metal forming. Int. J. Damage Mech. 26, 314–339.

Dias da Silva, V., 2004. A simple model for viscous regularization of elasto-plastic constitutive laws with softening. Commun. Numer. Methods Eng. 20, 547–568.

Doghri, I., 2013. Mechanics of deformable solids: linear, nonlinear, analytical and computational aspects. Springer Science & Business Media.

Doherty, W.P., Wilson, E.L., Taylor, R.L., 1969. Stress analysis of axisymmetric solids utilizing higher-order quadrilateral finite elements. University of California, Structural Engineering Laboratory.

Elguedj, T., Bazilevs, Y., Calo, V.M., Hughes, T.J., 2008. F-bar projection method for finite deformation elasticity and plasticity using NURBS based isogeometric analysis. Int. J. Mater. Form. 1, 1091–1094.

Elguedj, T., Bazilevs, Y., Calo, V.M., Hughes, T.J., 2007. B and F Projection Methods for Nearly Incompressible Linear and Nonlinear Elasticity and Plasticity using Higher-order NURBS Elements: Defense Technical Information Center, Fort Belvoir, VA. https://doi.org/10.21236/ADA478310

Enakoutsa, K., Leblond, J.-B., 2009. Numerical implementation and assessment of the GLPD micromorphic model of ductile rupture. Eur. J. Mech. - ASolids 28, 445–460.

Enakoutsa, K., Leblond, J.B., Perrin, G., 2007. Numerical implementation and assessment of a phenomenological nonlocal model of ductile rupture. Comput. Methods Appl. Mech. Eng. 196, 1946–1957.

Engelen, R.A.B., Geers, M.G.D., Baaijens, F.P.T., 2003. Nonlocal implicit gradient-enhanced elasto-plasticity for the modelling of softening behaviour. Int. J. Plast. 19, 403–433.

Eringen, A.C., Edelen, D., 1972. On nonlocal elasticity. Int. J. Eng. Sci. 10, 233–248.

Ern, A., Guermond, J.-L., 2013. Theory and practice of finite elements. Springer Science & Business Media.

Espinosa, H.D., Zavattieri, P.D., Emore, G.L., 1998. Adaptive FEM computation of geometric and material nonlinearities with application to brittle failure. Mech. Mater. 29, 275–305.

Faleskog, J., Gao, X., Shih, C.F., 1998. Cell model for nonlinear fracture analysis–I. Micromechanics calibration. Int. J. Fract. 89, 355–373.

Feld-Payet, S., 2010. Amorçage et propagation de fissures dans les milieux ductiles non locaux 171.

Feld-Payet, S., Besson, J., Feyel, F., 2011. Finite Element Analysis of Damage in Ductile Structures Using a Nonlocal Model Combined with a Three-field Formulation. Int. J. Damage Mech. 20, 655–680.

Feld-Payet, S., Chiaruttini, V., Besson, J., Feyel, F., 2015. A new marching ridges algorithm for crack path tracking in regularized media. Int. J. Solids Struct. 71, 57–69.

Flatten, A., Klingbeil, D., Svendsen, B., 2006. Non-local modeling of thermomechanical localization in metals, in: PAMM: Proceedings in Applied Mathematics and Mechanics. Wiley Online Library, pp. 369–370.

Forest, S., 2009. Micromorphic Approach for Gradient Elasticity, Viscoplasticity, and Damage. J. Eng. Mech. 135, 117–131. https://doi.org/10.1061/(ASCE)0733-9399(2009)135:3(117)

Fortin, M., Brezzi, F., 1991. Mixed and hybrid finite element methods. New York: Springer-Verlag.

Fortin, M., Glowinski, R., 1983. Augmented Lagrangian methods: applications to the numerical solution of boundary-value problems. Elsevier.

Francfort, G.A., Marigo, J.-J., 1998. Revisiting brittle fracture as an energy minimization problem. J. Mech. Phys. Solids 46, 1319–1342.

Garrison Jr, W., Moody, N., 1987. Ductile fracture. J. Phys. Chem. Solids 48, 1035–1074.

Geers, M.G.D., 2004. Finite strain logarithmic hyperelasto-plasticity with softening: a strongly non-local implicit gradient framework. Comput. Methods Appl. Mech. Eng. 193, 3377–3401. https://doi.org/10.1016/j.cma.2003.07.014

Geers, M.G.D., Ubachs, R.L.J.M., Engelen, R.A.B., 2003. Strongly non-local gradient-enhanced finite strain elastoplasticity. Int. J. Numer. Methods Eng. 56, 2039–2068. https://doi.org/10.1002/nme.654

Gologanu, M., Leblond, J.-B., Devaux, J., 1994. Approximate models for ductile metals containing nonspherical voids—case of axisymmetric oblate ellipsoidal cavities. J. Eng. Mater. Technol. 116, 290–297.

Gologanu, M., Leblond, J.-B., Devaux, J., 1993. Approximate models for ductile metals containing non-spherical voids—case of axisymmetric prolate ellipsoidal cavities. J. Mech. Phys. Solids 41, 1723–1754.

Gologanu, M., Leblond, J.-B., Perrin, G., Devaux, J., 2007. Recent extensions of Gurson's model for porous ductile metals, in: Continuum Micromechanics. Springer, pp. 61–130.

Gologanu, M., Leblond, J.-B., Perrin, G., Devaux, J., 2001. Theoretical models for void coalescence in porous ductile solids. I. Coalescence "in layers." Int. J. Solids Struct. 38, 5581–5594.

Grassl, P., Xenos, D., Jirásek, M., Horák, M., 2014. Evaluation of nonlocal approaches for modelling fracture near nonconvex boundaries. Int. J. Solids Struct. 51, 3239–3251.

Griffith, A.A., 1921. VI. The phenomena of rupture and flow in solids. Philos. Trans. R. Soc. Lond. Ser. Contain. Pap. Math. Phys. Character 221, 163–198.

Gross, D., Seelig, T., 2017. Fracture mechanics: with an introduction to micromechanics. Springer.

Gross, D., Seelig, T., 2011. Fracture mechanics: with an introduction to micromechanics, 2nd ed. ed, Mechanical engineering series. Springer, Heidelberg ; New York.

Gurson, A.L., 1977. Continuum theory of ductile rupture by void nucleation and growth: Part I—Yield criteria and flow rules for porous ductile media. J. Eng. Mater. Technol. 99, 2–15.

Hadamard, J., 1903. Leçons sur la propagation des ondes et les équations de l'hydrodynamique. A. Hermann.

Hahn, G., Rosenfield, A., 1975. Metallurgical factors affecting fracture toughness of aluminum alloys. Metall. Trans. A 6, 653–668.

Han, X., Besson, J., Forest, S., Tanguy, B., Bugat, S., 2013. A yield function for single crystals containing voids. Int. J. Solids Struct. 50, 2115–2131.

Handerhan, K., Garrison Jr, W., 1992. A study of crack tip blunting and the influence of blunting behavior on the fracture toughness of ultra high strength steels. Acta Metall. Mater. 40, 1337–1355.

Hannard, F., Simar, A., Maire, E., Pardoen, T., 2018. Quantitative assessment of the impact of second phase particle arrangement on damage and fracture anisotropy. Acta Mater. 148, 456–466.

Heerens, J., Schödel, M., 2003. On the determination of crack tip opening angle, CTOA, using light microscopy and δ5 measurement technique. Eng. Fract. Mech. 70, 417–426.

Herrmann, L.R., 1965. Elasticity equations for incompressible and nearly incompressible materials by a variational theorem. AIAA J. 3, 1896–1900.

Hinton, E., Campbell, J., 1974. Local and global smoothing of discontinuous finite element functions using a least squares method. Int. J. Numer. Methods Eng. 8, 461–480.

Hu, H.-C., 1955. On some variational principles in the theory of elasticity and plasticity. Sci Sin 4, 33–54.

Hu, H.-C., 1954. On some variational principles in the theory of elasticity and the theory of plasticity.

Huang, Y., 1991. Accurate dilatation rates for spherical voids in triaxial stress fields. ASME J Appl Mech 58, 1084–1086.

Huespe, A.E., Needleman, A., Oliver, J., Sánchez, P.J., 2012. A finite strain, finite band method for modeling ductile fracture. Int. J. Plast. 28, 53–69. https://doi.org/10.1016/j.ijplas.2011.05.010

Hughes, T.J., 2012. The finite element method: linear static and dynamic finite element analysis. Courier Corporation.

Hughes, T.J., 1980. Generalization of selective integration procedures to anisotropic and nonlinear media. Int. J. Numer. Methods Eng. 15, 1413–1418.

Hutchinson, J., 1968. Singular behaviour at the end of a tensile crack in a hardening material. J. Mech. Phys. Solids 16, 13–31.

Hütter, G., 2017. A micromechanical gradient extension of Gurson's model of ductile damage within the theory of microdilatational media. Int. J. Solids Struct. 110–111, 15–23.

Hütter, G., Linse, T., Mühlich, U., Kuna, M., 2013. Simulation of ductile crack initiation and propagation by means of a non-local Gurson-model. Int. J. Solids Struct. 50, 662–671.

Hütter, G., Linse, T., Roth, S., Mühlich, U., Kuna, M., 2014a. A modeling approach for the complete ductile–brittle transition region: cohesive zone in combination with a non-local Gurson-model. Int. J. Fract. 185, 129–153.

Hütter, G., Zybell, L., Kuna, M., 2014b. Size effects due to secondary voids during ductile crack propagation. Int. J. Solids Struct. 51, 839–847. https://doi.org/10.1016/j.ijsolstr.2013.11.012

Irwin, G.R., 1957. Analysis of stresses and strains near the end of a crack traversing a plate. J Appl Mech.

Jackiewicz, J., Kuna, M., 2003. Non-local regularization for FE simulation of damage in ductile materials. Comput. Mater. Sci. 28, 684–695.

Jirásek, M., 2007. Nonlocal damage mechanics. Rev. Eur. Génie Civ. 11, 993–1021.

Jirásek, M., Rolshoven, S., 2003. Comparison of integral-type nonlocal plasticity models for strain-softening materials. Int. J. Eng. Sci. 41, 1553–1602.

Kasper, E.P., Taylor, R.L., 2000a. A mixed-enhanced strain method Part I: Geometrically linear problems. Comput. Struct. 14.

Kasper, E.P., Taylor, R.L., 2000b. A mixed-enhanced strain method Part II: Geometrically nonlinear problems. Comput. Struct. 10.

Keralavarma, S., Benzerga, A., 2010. A constitutive model for plastically anisotropic solids with non-spherical voids. J. Mech. Phys. Solids 58, 874–901.

Keralavarma, S., Chockalingam, S., 2016. A criterion for void coalescence in anisotropic ductile materials. Int. J. Plast. 82, 159–176.

Kim, D., Barlat, F., Bouvier, S., Rabahallah, M., Balan, T., Chung, K., 2007. Non-quadratic anisotropic potentials based on linear transformation of plastic strain rate. Int. J. Plast. 23, 1380–1399.

Kim, J., Gao, X., Srivatsan, T.S., 2004. Modeling of void growth in ductile solids: effects of stress triaxiality and initial porosity. Eng. Fract. Mech. 71, 379–400.

Ko, D.-C., Kim, B.-M., Choi, J.-C., 1997. Finite-element simulation of the shear process using the element-kill method. J. Mater. Process. Technol. 72, 129–140.

Koplik, J., Needleman, A., 1988. Void growth and coalescence in porous plastic solids. Int. J. Solids Struct. 24, 835–853.

Kröner, E., 1967. Elasticity theory of materials with long range cohesive forces. Int. J. Solids Struct. 3, 731–742.

Kuhn, C., Noll, T., 2016. On phase field modeling of ductile fracture 20.

Ladevèze, P., Pelle, J.P., 2001. La maîtrise du calcul en mécanique linéaire et non linéaire. Hermès Science publ.

Leblond, J., Perrin, G., Devaux, J., 1994. Bifurcation effects in ductile metals with nonlocal damage. J. Appl. Mech. 61, 236–242.

Lee, E., 1981. Some comments on elastic-plastic analysis. Int. J. Solids Struct. 17, 859–872.

Lee, H.C., Choi, J.S., Jung, K.H., Im, Y.T., 2009. Application of element deletion method for numerical analyses of cracking. J. Achiev. Mater. Manuf. Eng. 35, 8.

Lee, N.-S., Bathe, K.-J., 1994. Error indicators and adaptive remeshing in large deformation finite element analysis. Finite Elem. Anal. Des. 16, 99–139.

Lemaitre, J., 1985. Coupled elasto-plasticity and damage constitutive equations. Comput. Methods Appl. Mech. Eng. 51, 31–49.

Lemaitre, J., Chaboche, J.-L., 1978. Aspect phénoménologique de la rupture par endommagement. J Méc Appl 2.

Lemaitre, J., Desmorat, R., Sauzay, M., 2000. Anisotropic damage law of evolution. Eur. J. Mech.-ASolids 19, 187–208.

Li, H., Fu, M.W., Lu, J., Yang, H., 2011. Ductile fracture: Experiments and computations. Int. J. Plast. 27, 147–180. https://doi.org/10.1016/j.ijplas.2010.04.001

Lian, J., Sharaf, M., Archie, F., Münstermann, S., 2013. A hybrid approach for modelling of plasticity and failure behaviour of advanced high-strength steel sheets. Int. J. Damage Mech. 22, 188–218.

Lian, J., Wu, J., Münstermann, S., 2015. Evaluation of the cold formability of high-strength low-alloy steel plates with the modified Bai–Wierzbicki damage model. Int. J. Damage Mech. 24, 383–417.

Lin, R.C., Steglich, D., Brocks, W., Betten, J., 2006. Performing RVE calculations under constant stress triaxiality for monotonous and cyclic loading. Int. J. Numer. Methods Eng. 66, 1331–1360. https://doi.org/10.1002/nme.1600

Lindqvist, S., Wallin, K., Moinereau, D., Smith, M., Marie, S., Dillström, P., Keim, E., Szavai, S., 2018. Advanced Structural Integrity Assessment Tools for Safe Long Term Operation (ATLAS+), in: ASME 2018 Pressure Vessels and Piping Conference. American Society of Mechanical Engineers, p. V06AT06A073–V06AT06A073.

Linse, T., Hütter, G., Kuna, M., 2012. Simulation of crack propagation using a gradient-enriched ductile damage model based on dilatational strain. Eng. Fract. Mech. 95, 13–28. https://doi.org/10.1016/j.engfracmech.2012.07.004

Ljustina, G., Fagerström, M., Larsson, R., 2014. Rate Sensitive Continuum Damage Models and Mesh Dependence in Finite Element Analyses. Sci. World J. 2014, 1–8. https://doi.org/10.1155/2014/260571

Lorentz, E., 2017. A nonlocal damage model for plain concrete consistent with cohesive fracture. Int. J. Fract. 207, 123–159.

Lorentz, E., 2005. Ill-posed boundary conditions encountered in 3D and plate finite element simulations. Finite Elem. Anal. Des. 41, 1105–1117.

Lorentz, E., 1999. Lois de comportement à gradients de variables internes: construction, formulation variationnelle et mise en oeuvre numérique (PhD Thesis). Université Pierre et Marie Curie-Paris VI.

Lorentz, E., Andrieux, S., 2003. Analysis of non-local models through energetic formulations. Int. J. Solids Struct. 40, 2905–2936. https://doi.org/10.1016/S0020-7683(03)00110-0

Lorentz, E., Benallal, A., 2005. Gradient constitutive relations: numerical aspects and application to gradient damage. Comput. Methods Appl. Mech. Eng. 194, 5191–5220. https://doi.org/10.1016/j.cma.2004.12.016

Lorentz, E., Besson, J., Cano, V., 2008. Numerical simulation of ductile fracture with the Rousselier constitutive law. Comput. Methods Appl. Mech. Eng. 197, 1965–1982.

Lorentz, E., Cano, V., 2005. A nonlocal formulation applied to ductile damage. Lat. Am. J. Solids Struct. 2, 17–27.

Lorentz, E., Godard, V., 2011. Gradient damage models: Toward full-scale computations. Comput. Methods Appl. Mech. Eng. 200, 1927–1944. https://doi.org/10.1016/j.cma.2010.06.025

Loubignac, G., Cantin, G., Touzot, G., 1977. Continuous stress fields in finite element analysis. AIAA J. 15, 1645–1647.

Madou, K., Leblond, J.-B., 2013. Numerical studies of porous ductile materials containing arbitrary ellipsoidal voids–I: Yield surfaces of representative cells. Eur. J. Mech.-ASolids 42, 480–489.

Madou, K., Leblond, J.-B., Morin, L., 2013. Numerical studies of porous ductile materials containing arbitrary ellipsoidal voids–II: Evolution of the length and orientation of the void axes. Eur. J. Mech.-ASolids 42, 490–507.

Malcher, L., Andrade Pires, F.M., César de Sá, J.M.A., 2014. An extended GTN model for ductile fracture under high and low stress triaxiality. Int. J. Plast. 54, 193–228.

Marigo, J.-J., Maurini, C., Pham, K., 2016. An overview of the modelling of fracture by gradient damage models. Meccanica 51, 3107–3128. https://doi.org/10.1007/s11012-016-0538-4

McClintock, F.A., 1968. A criterion for ductile fracture by the growth of holes. J. Appl. Mech. 35, 363–371.

McClintock, F.A., 1963. On the plasticity of the growth of fatigue cracks.

McMeeking, R.M., 1977. Finite deformation analysis of crack-tip opening in elastic-plastic materials and implications for fracture. J. Mech. Phys. Solids 25, 357–381.

McMeeking, Rm., Parks, D., 1979. On criteria for J-dominance of crack-tip fields in large-scale yielding, in: Elastic-Plastic Fracture. ASTM International.

McMeeking, R.M., Rice, J., 1975. Finite-element formulations for problems of large elastic-plastic deformation. Int. J. Solids Struct. 11, 601–616.

Mediavilla, J., Peerlings, R.H.J., Geers, M.G.D., 2006. Discrete crack modelling of ductile fracture driven by non-local softening plasticity. Int. J. Numer. Methods Eng. 66, 661–688. https://doi.org/10.1002/nme.1572

Mediavilla, J., Peerlings, R.H.J., Geers, M.G.D., 2006a. A nonlocal triaxiality-dependent ductile damage model for finite strain plasticity. Comput. Methods Appl. Mech. Eng. 195, 4617–4634.

Mediavilla, J., Peerlings, R.H.J., Geers, M.G.D., 2006b. An integrated continuous–discontinuous approach towards damage engineering in sheet metal forming processes. Eng. Fract. Mech. 73, 895–916. https://doi.org/10.1016/j.engfracmech.2005.10.011

Mediavilla, J., Peerlings, R.H.J., Geers, M.G.D., 2006c. A robust and consistent remeshing-transfer operator for ductile fracture simulations. Comput. Struct. 84, 604–623. https://doi.org/10.1016/j.compstruc.2005.10.007

Miehe, C., 2014. Variational gradient plasticity at finite strains. Part I: Mixed potentials for the evolution and update problems of gradient-extended dissipative solids. Comput. Methods Appl. Mech. Eng. 268, 677–703.

Miehe, C., Aldakheel, F., Raina, A., 2016. Phase field modeling of ductile fracture at finite strains: A variational gradient-extended plasticity-damage theory. Int. J. Plast. 84, 1–32. https://doi.org/10.1016/j.ijplas.2016.04.011

Miehe, C., Apel, N., Lambrecht, M., 2002. Anisotropic additive plasticity in the logarithmic strain space: modular kinematic formulation and implementation based on incremental minimization principles for standard materials. Comput. Methods Appl. Mech. Eng. 191, 5383–5425.

Miehe, C., Lambrecht, M., 2001. Algorithms for computation of stresses and elasticity moduli in terms of Seth-Hill's family of generalized strain tensors. Commun. Numer. Methods Eng. 17, 337–353. https://doi.org/10.1002/cnm.404

Monchiet, V., Bonnet, G., 2013. A Gurson-type model accounting for void size effects. Int. J. Solids Struct. 50, 320–327.

Monchiet, V., Cazacu, O., Charkaluk, E., Kondo, D., 2008. Macroscopic yield criteria for plastic anisotropic materials containing spheroidal voids. Int. J. Plast. 24, 1158–1189.

Monchiet, V., Kondo, D., 2013. Combined voids size and shape effects on the macroscopic criterion of ductile nanoporous materials. Int. J. Plast. 43, 20–41.

Morgeneyer, T.F., Besson, J., 2011. Flat to slant ductile fracture transition: Tomography examination and simulations using shear-controlled void nucleation. Scr. Mater. 65, 1002–1005.

Morgeneyer, T.F., Taillandier-Thomas, T., Helfen, L., Baumbach, T., Sinclair, I., Roux, S., Hild, F., 2014. In situ 3-D observation of early strain localization during failure of thin Al alloy (2198) sheet. Acta Mater. 69, 78–91.

Mühlhaus, H.-B., Alfantis, E., 1991. A variational principle for gradient plasticity. Int. J. Solids Struct. 28, 845–857.

Nahshon, K., Hutchinson, J., 2008. Modification of the Gurson model for shear failure. Eur. J. Mech.-ASolids 27, 1–17.

Needleman, A., Tvergaard, V., 1984. An analysis of ductile rupture in notched bars. J. Mech. Phys. Solids 32, 461–490.

Nonn, A., Kalwa, C., 2010. Modeling of damage behaviour of high strength pipeline 8.

Oliver, J., Huespe, A.E., Cante, J.C., Díaz, G., 2010. On the numerical resolution of the discontinuous material bifurcation problem. Int. J. Numer. Methods Eng. n/a-n/a. https://doi.org/10.1002/nme.2870

Oñate, E., Castro, J., 1991. Adaptive mesh refinement techniques for structural problems, in: The Finite Element Method in the 1990's. Springer, pp. 133–145.

Ortiz, M., Quigley Iv, J., 1991. Adaptive mesh refinement in strain localization problems. Comput. Methods Appl. Mech. Eng. 90, 781–804.

Pardoen, T., Delannay, F., 2000. A method for the metallographical measurement of the CTOD at cracking initiation and the role of reverse plasticity on unloading. Eng. Fract. Mech. 65, 455–466. https://doi.org/10.1016/S0013-7944(99)00128-9

Pardoen, T., Hutchinson, J., 2000. An extended model for void growth and coalescence. J. Mech. Phys. Solids 48, 2467–2512.

Paris, P., Tada, H., Zahoor, A., Ernst, H., 1979. The theory of instability of the tearing mode of elastic-plastic crack growth, in: Elastic-Plastic Fracture. ASTM International.

Paux, J., Morin, L., Brenner, R., Kondo, D., 2015. An approximate yield criterion for porous single crystals. Eur. J. Mech.-ASolids 51, 1–10.

PavanaChand, C., KrishnaKumar, R., 1998. Remeshing issues in the finite element analysis of metal forming problems. J. Mater. Process. Technol. 75, 63–74.

Pavankumar, T.V., Samal, M.K., Chattopadhyay, J., Dutta, B.K., Kushwaha, H.S., Roos, E., Seidenfuss, M., 2005. Transferability of fracture parameters from specimens to component level. Int. J. Press. Vessels Pip. 82, 386–399. https://doi.org/10.1016/j.ijpvp.2004.10.003

Peerlings, R.H.J., DE BORST, R., Brekelmans, W.A.M., 1996. Gradient enhanced damage for quasi-brittle materials 13.

Peerlings, R.H.J., Geers, M.G.D., de Borst, R., Brekelmans, W.A.M., 2001. A critical comparison of nonlocal and gradient-enhanced softening continua. Int. J. Solids Struct. 38, 7723–7746. https://doi.org/10.1016/S0020-7683(01)00087-7

Perić, D., Hochard, C., Dutko, M., Owen, D., 1996. Transfer operators for evolving meshes in small strain elasto-placticity. Comput. Methods Appl. Mech. Eng. 137, 331–344.

Phadnis, V.A., Makhdum, F., Roy, A., Silberschmidt, V.V., 2013. Drilling in carbon/epoxy composites: Experimental investigations and finite element implementation. Compos. Part Appl. Sci. Manuf. 47, 41–51. https://doi.org/10.1016/j.compositesa.2012.11.020

Pijaudier-Cabot, G., Bažant, Z.P., 1987. Nonlocal damage theory. J. Eng. Mech. 113, 1512–1533.

Polizzotto, C., 2001. Nonlocal elasticity and related variational principles. Int. J. Solids Struct. 38, 7359–7380. https://doi.org/10.1016/S0020-7683(01)00039-7

Rank, E., 1989. Adaptive h-, p-and hp-versions for boundary integral element methods. Int. J. Numer. Methods Eng. 28, 1335–1349.

Reddi, D., Areej, V., Keralavarma, S., 2019. Ductile failure simulations using a multi-surface coupled damage-plasticity model. Int. J. Plast.

Rice, J., Drugan, W.J., Sham, T.-L., 1980. Elastic-plastic analysis of growing cracks, in: Fracture Mechanics. ASTM International.

Rice, J., Tracey, D.M., 1973. Computational fracture mechanics, in: Numerical and Computer Methods in Structural Mechanics. Elsevier, pp. 585–623.

Rice, J.R., 1968. A path independent integral and the approximate analysis of strain concentration by notches and cracks. J. Appl. Mech. 35, 379–386.

Rice, Jr., Rosengren, G.F., 1968. Plane strain deformation near a crack tip in a power-law hardening material. J. Mech. Phys. Solids 16, 1–12.

Rice, J.R., Tracey, D.M., 1969. On the ductile enlargement of voids in triaxial stress fields. J. Mech. Phys. Solids 17, 201–217.

Rousselier, G., 1981. Finite deformation constitutive relations including ductile fracture damage.

Rudnicki, J.W., Rice, J., 1975. Conditions for the localization of deformation in pressure-sensitive dilatant materials. J. Mech. Phys. Solids 23, 371–394.

Samal, M., Seidenfuss, M., Roos, E., Dutta, B., Kushwaha, H., 2008a. Experimental and numerical investigation of ductile-to-brittle transition in a pressure vessel steel. Mater. Sci. Eng. A 496, 25–35.

Samal, M., Seidenfuss, M., Roos, E., Dutta, B., Kushwaha, H., 2008b. Finite element formulation of a new nonlocal damage model. Finite Elem. Anal. Des. 44, 358–371.

Samal, M.K., Seidenfuss, M., Roos, E., 2009. A new mesh-independent Rousselier’s damage model: Finite element implementation and experimental verification. Int. J. Mech. Sci. 51, 619–630. https://doi.org/10.1016/j.ijmecsci.2009.06.006

Samal, M.K., Seidenfuss, M., Roos, E., Dutta, B.K., Kushwaha, H.S., 2008. Experimental and numerical investigation of ductile-to-brittle transition in a pressure vessel steel. Mater. Sci. Eng. A 496, 25–35. https://doi.org/10.1016/j.msea.2008.06.046

Seidenfuss, M., Samal, M., Roos, E., 2011. On critical assessment of the use of local and nonlocal damage models for prediction of ductile crack growth and crack path in various loading and boundary conditions. Int. J. Solids Struct. 48, 3365–3381.

Seupel, A., Hütter, G., Kuna, M., 2018. An efficient FE-implementation of implicit gradient-enhanced damage models to simulate ductile failure. Eng. Fract. Mech. 199, 41–60. https://doi.org/10.1016/j.engfracmech.2018.01.022

Seupel, A., Kuna, M., 2019. A gradient-enhanced damage model motivated by engineering approaches to ductile failure of steels. Int. J. Damage Mech. 105678951882387. https://doi.org/10.1177/1056789518823879

Shinohara, Y., Madi, Y., Besson, J., 2016. Anisotropic ductile failure of a high-strength line pipe steel. Int. J. Fract. 197, 127–145.

Sidoro, F., Dogui, A., 2001. Some issues about anisotropic elastic±plastic models at ®nite strain. Int. J. Solids Struct. 10.

Siegmund, T., Brocks, W., 1999. Prediction of the Work of Separation and Implications to Modeling 20.

Simo, J., Miehe, C., 1992. Associative coupled thermoplasticity at finite strains: Formulation, numerical analysis and implementation. Comput. Methods Appl. Mech. Eng. 98, 41–104.

Simo, J., Taylor, R.L., Pister, K., 1985. Variational and projection methods for the volume constraint in finite deformation elasto-plasticity. Comput. Methods Appl. Mech. Eng. 51, 177–208.

Simo, J.-C., Armero, F., 1992. Geometrically non-linear enhanced strain mixed methods and the method of incompatible modes. Int. J. Numer. Methods Eng. 33, 1413–1449.

Simo, J.C., Rifai, M.S., 1990. A class of mixed assumed strain methods and the method of incompatible modes. Int. J. Numer. Methods Eng. 29, 1595–1638. https://doi.org/10.1002/nme.1620290802

Sneddon, I.N., 1946. The distribution of stress in the neighbourhood of a crack in an elastic solid. Proc R Soc Lond A 187, 229–260.

Steglich, D., Brocks, W., 1998. Micromechanical modelling of damage and fracture of ductile materials. Fatigue Fract. Eng. Mater. Struct. 21, 1175–1188.

Sun, D.-Z., Siegele, D., Voss, B., Schmitt, W., 1989. Application of local damage models to the numerical analysis of ductile rupture. Fatigue Fract. Eng. Mater. Struct. 12, 201–212. https://doi.org/10.1111/j.1460-2695.1989.tb00527.x

Sussman, T., Bathe, K.-J., 1987. A finite element formulation for nonlinear incompressible elastic and inelastic analysis. Comput. Struct. 26, 357–409.

Tanguy, B., Besson, J., 2002. An extension of the Rousselier model to viscoplastic temperature dependent materials 21.

Tanné, M.E., 2017. Variational phase-field models from brittle to ductile fracture: nucleation and propagation 160.

Taylor, R.L., 2000. A mixed-enhanced formulation tetrahedral finite elements. Int. J. Numer. Methods Eng. 47, 205–227.

Thomason, P., 1985a. A three-dimensional model for ductile fracture by the growth and coalescence of microvoids. Acta Metall. 33, 1087–1095.

Thomason, P., 1985b. Three-dimensional models for the plastic limit-loads at incipient failure of the intervoid matrix in ductile porous solids. Acta Metall. 33, 1079–1085.

Torki, M., Benzerga, A., Leblond, J.-B., 2015. On void coalescence under combined tension and shear. J. Appl. Mech. 82, 071005.

Torki, M.E., 2019. A unified criterion for void growth and coalescence under combined tension and shear. Int. J. Plast.

Turcke, D., McNeice, G., 1974. Guidelines for selecting finite element grids based on an optimization study. Comput. Struct. 4, 499–519.

Tvergaard, V., Hutchinson, J.W., 1992. The relation between crack growth resistance and fracture process parameters in elastic-plastic solids. J. Mech. Phys. Solids 40, 1377–1397.

Tvergaard, V., Needleman, A., 1997. Nonlocal effects on localization in a void-sheet. Int. J. Solids Struct. 34, 2221–2238. https://doi.org/10.1016/S0020-7683(96)00140-0

Tvergaard, V., Needleman, A., 1995. Effects of nonlocal damage in porous plastic solids. Int. J. Solids Struct. 32, 1063–1077. https://doi.org/10.1016/0020-7683(94)00185-Y

Tvergaard, V., Needleman, A., 1984. Analysis of the cup-cone fracture in a round tensile bar. Acta Metall. 32, 157–169.

Vincent, P.-G., Suquet, P., Monerie, Y., Moulinec, H., 2014a. Effective flow surface of porous materials with two populations of voids under internal pressure: I. A GTN model. Int. J. Plast. 56, 45–73.

Vincent, P.-G., Suquet, P., Monerie, Y., Moulinec, H., 2014b. Effective flow surface of porous materials with two populations of voids under internal pressure: II. Full-field simulations. Int. J. Plast. 56, 74–98.

Westergaard, H.M., 1939. Bearing pressures and cracks.

Wriggers, P., 2008. Nonlinear finite element methods. Springer Science & Business Media.

Xia, L., Shih, C.F., 1995. Ductile crack growth-I. A numerical study using computational cells with microstructurally-based length scales. J. Mech. Phys. Solids 43, 233–259.

Xue, L., 2008. Constitutive modeling of void shearing effect in ductile fracture of porous materials. Eng. Fract. Mech. 75, 3343–3366.

Xue, L., Wierzbicki, T., 2009. Numerical simulation of fracture mode transition in ductile plates. Int. J. Solids Struct. 46, 1423–1435. https://doi.org/10.1016/j.ijsolstr.2008.11.009

Zhang, Y., 2016. Modélisation et simulation numérique robuste de l'endommagement ductile 161.

Zhang, Y., Lorentz, E., Besson, J., 2018. Ductile damage modelling with locking-free regularised GTN model. Int. J. Numer. Methods Eng. 113, 1871–1903. https://doi.org/10.1002/nme.5722

Zhang, Z., Niemi, E., 1994a. A new failure criterion for the Gurson-Tvergaard dilational constitutive model. Int. J. Fract. 70, 321–334.

Zhang, Z., Niemi, E., 1994b. Analyzing ductile fracture using dual dilational constitutive equations. Fatigue Fract. Eng. Mater. Struct. 17, 695–707.

Zhang, Z., Thaulow, C., Ødeg\a ard, J., 2000. A complete Gurson model approach for ductile fracture. Eng. Fract. Mech. 67, 155–168.

Zienkiewicz, O., Taylor, R., Too, J., 1971. Reduced integration technique in general analysis of plates and shells. Int. J. Numer. Methods Eng. 3, 275–290.

RÉSUMÉ

Cette étude a pour objectif principal d'établir une stratégie de modélisation robuste, fiable et performante pour décrire des propagations de fissures d'échelle centimétrique en régime ductile dans des composants industriels. Le modèle d'endommagement de GTN écrit en grandes déformations est utilisé pour modéliser l'endommagement ductile. Ce modèle conduit généralement à une localisation de la déformation, conformément à l'expérience. L'échelle caractéristique de ce phénomène est introduite dans les équations de comportement via l'adoption d'une formulation non locale.

Sur le plan numérique, ce modèle non local rend bien compte de la localisation dans une bande d'épaisseur donnée lorsqu'on raffine suffisamment le maillage. Par ailleurs, le problème de verrouillage numérique associé au caractère initialement isochore de la déformation plastique est limité en utilisant une formulation à base d'éléments finis mixtes. Enfin, la distorsion des éléments totalement cassés (i.e. sans rigidité apparente), qui pourrait nuire à la bonne convergence des simulations numériques, est traitée par une régularisation viscoélastique.

L'ensemble de ces ingrédients sont appliqués pour simuler la propagation de fissure dans un milieu infini plasticité confinée), de sorte à établir un lien avec les approches globales en J-Δa. L'émoussement, l'amorçage et la (grande) propagation de fissure sont bien prédits. Le modèle est également appliqué à une tuyauterie métallique testée en grandeur réelle dans le cadre du projet européen Atlas+. Après une phase d'identification des paramètres sur éprouvette, les réponses globales et locales d'autres éprouvettes et du tube sont confrontés aux résultats expérimentaux. Ces résultats illustrent le degré de robustesse, de fiabilité et de performance qu'on peut attendre du modèle.

MOTS CLÉS

Endommagement ductile ; GTN ; Dépendance au maillage ; Verrouillage volumique ; Eléments distordus ; Régularisation nonlocale ; Eléments mixtes ; Modèle viscoélastique ; Plasticité confinée ; Grande propagation ; Simulation ; Essai ; Applications industrielles

ABSTRACT

The major goal of this work is to establish a robust, reliable and efficient modeling technique so as to describe ductile tearing over a distance of several centimeters in industrial cases. The GTN damage model expressed in the context of finite strains is chosen to model ductile damage. Generally, the model leads to strain localization in agreement with experimental observations. The characteristic length scale of this phenomenon is introduced into the constitutive equations through the use of a nonlocal formulation.

On a numerical ground, the nonlocal model controls the width of the localization band as soon as the mesh is sufficiently refined. Besides, the issue of volumetric-locking associated with plastic incompressibility is handled using a mixed finite element formulation. Finally, the distortion of broken elements (i.e. without any stiffness), which may affect the computational convergence of numerical simulations, is treated using a viscoelastic regularization.

The improved GTN model is applied to simulate crack propagation under small-scale yielding conditions, so as to establish a relation with the global (J-Δa) approach. Crack tip blunting, crack initiation and (large) crack propagation are well captured. The model is also applied to a full-scale metallic pipe in the framework of the UE project Atlas+. After a phase of parameter calibration based on the experimental results on some small specimens, the global and local responses of other small specimens and of the full-scale pre-cracked pipe are compared with the experimental results. The results illustrates the robustness, the reliability and the efficiency of the current model.

KEYWORDS

Ductile damage; GTN; Mesh sensitivity; Volumetric-locking; highly distorted elements; Non-local regularization; Mixed finite elements; Viscoelastic model; Small-scale yielding; Large crack propagation; Simulation; Experiment; Industrial applications